

NASA Contractor Report 3869

# Investigations of Flowfields Found in Typical Combustor Geometries

David G. Lilley

GRANT NAG3-74  
FEBRUARY 1985

**NASA**

NASA Contractor Report 3869

# Investigations of Flowfields Found in Typical Combustor Geometries

David G. Lilley  
*Oklahoma State University*  
*Stillwater, Oklahoma*

Prepared for  
Lewis Research Center  
under Grant NAG3-74

**NASA**  
National Aeronautics  
and Space Administration  
**Scientific and Technical  
Information Branch**

1985



## ABSTRACT

This is the Final Report on Grant NAG 3-74 and discussion is on those activities undertaken during the entire course of research from July 1, 1980 to June 30, 1984. Studies were concerned with experimental and theoretical research on 2-D axisymmetric geometries under low speed nonreacting, turbulent, swirling flow conditions typical of gas turbine and ramjet combustion chambers. They included recirculation zone characterization, time-mean and turbulence simulation in swirling recirculating flow, sudden and gradual expansion flowfields, and further complexities and parameter influences. The study included the investigation of: a complete range of swirl strengths; swirler performance; downstream contraction nozzle sizes and locations; expansion ratios; and inlet side-wall angles. Their individual and combined effects on the test section flowfield were observed, measured and characterized.

Experimental methods included flow visualization (with smoke and neutrally-buoyant helium-filled soap bubbles), five-hole pitot probe time-mean velocity field measurements, and single-, double- and triple-wire hot-wire anemometry measurements of time-mean velocities, normal and shear Reynolds stresses. Computational methods included development of the STARPIC code from the primitive-variable TEACH computer code, and its use in flowfield prediction and turbulence model development.





## CONTENTS

ABSTRACT.....	iii
1. <u>INTRODUCTION</u> .....	1
1.1 The Problem.....	1
1.2 Objectives.....	2
1.3 The Present Contribution.....	3
2. <u>REVIEW OF ACTIVITIES</u> .....	5
2.1 Progress During First Year (1980-81).....	5
2.2 Progress During Second Year (1981-82).....	6
2.3 Progress During Third Year (1982-83).....	8
2.4 Progress During Fourth Year (1983-84).....	9
3. <u>FACILITIES AND TECHNIQUES</u> .....	10
3.1 Facilities.....	10
3.2 Flow Visualization.....	11
3.3 Five-Hole Pitot Probe.....	13
3.4 Hot-Wire Anemometer Techniques.....	13
3.5 Computer Code Developments.....	15
4. <u>RESULTS</u> .....	16
4.1 Swirler Performance.....	16
4.2 Gross Flowfield Characterization.....	17
4.3 Time-Mean Flowfield Characterization.....	19
4.4 Turbulence Measurements.....	20
4.5 Turbulence Modeling.....	23
4.6 Computer Predictions.....	24
5. <u>CLOSURE</u> .....	26
6. <u>REFERENCES</u> .....	27

APPENDIXES

A - On the Prediction of Swirling Flowfields Found in Axisymmetric Combustor Geometries.....	31
B - Mean Flowfields in Axisymmetric Combustor Geometries with Swirl.....	39
C - Turbulence Measurements in a Confined Jet Using A Six-Orientation Hot-Wire Probe Technique.....	48
D - Five-Hole Pitot Probe Time-Mean Velocity Measurements in Confined Swirling Flows.....	61
E - Confined Swirling Flow Predictions.....	73
F - Single-Wire Swirl Flow Turbulence Measurements.....	85
G - The Performance of an Annular Vane Swirler.....	98
H - Accuracy and Directional Sensitivity of the Single- Wire Technique.....	112
I - Limitations and Empirical Extensions of the $k-\epsilon$ Model as Applied to Turbulent Confined Swirling Flows.....	129
J - Swirl Flow Turbulence Modeling.....	139
K - Swirl, Confinement and Nozzle Effects on Confined Turbulent Flow.....	152
L - Turbulence Measurements in a Complex Flowfield Using a Crossed Hot-Wire.....	162
M - Five-Hole Pitot Probe Measurements of Swirl, Confinement and Nozzle Effects on Confined Turbulent Flow.....	173

## 1. INTRODUCTION

### 1.1 The Problem

Both experimental and theoretical studies assist in the design and development of gas turbine combustion chambers. Up to now designers have relied heavily on experimental evidence to produce empirical formulas. However, traditional design methods are now being supplemented by analytical methods (numerical solution of the appropriate governing partial differential equations). Computer modeling of combustion processes is now an established fact, but improvements and new developments (both experimental and theoretical) can and should be made, theoretical modeling being aided by carefully chosen experiments.

The accuracy of currently available prediction codes for swirling recirculating confined flows is in doubt because of questionable turbulence models and lack of a suitable experimental data base. A prerequisite to the prediction of more complex turbulent reacting flows is the development of suitable turbulence models and computer programs for flow prediction under nonreacting conditions, with which the present study is concerned.

Progress needs to be made on computational methods. Typically, a computer code of the TEACH-T type is appropriately modified to include swirl and geometric variations and the two-equations  $k-\epsilon$  turbulence model simulates the mixing characteristics. One problem is that a turbulence model whose basis and parameters are adequate for simple flow situations is not adequate for the more complicated swirling recirculating flow situation. There is a need to develop logical extensions of currently available turbulence models to swirling recirculating flows, in the form of modifying their parameters, inclusion of nonisotropic effects, and/or more complex modifications.



## 1.2 Objectives

The recently-completed research encompassed steady turbulent flow in 2-D axisymmetric geometries, under low speed and nonreacting conditions. The particular problem addressed was concerned with turbulent flow in a round pipe entering an expansion into another round pipe. The inlet flow may possess a swirl component of velocity via passage through swirl vanes at an angle  $\phi$ , and the sidewall may slope at an angle  $\alpha$ , to the main flow direction. The resulting main flowfield domain may possess a central toroidal recirculation zone in the middle of the region on the axis, in addition to the possibility of a corner recirculation zone near the upper corner provoked by the rather sudden enlargement of the cross-sectional area. Of special concern was the characterization of flows of this type in terms of the effects of side-wall angle  $\alpha$ , degree of swirl  $\phi$ , inlet expansion ratio  $D/d$ , and downstream contraction area ratio  $A/a$  on the flowfield in terms of its time-mean and turbulence quantities.

The general goal of this study was to perform experiments and complementary computations with the idea of doing the type of research necessary to improve calculation capability. This involved performing experiments where time-mean and turbulence quantities were measured, and taking input conditions and running a suitable computer code for a variety of test cases so as to compare predictions against experiment. Hence the validity of turbulence model modifications could be assessed. In fact modifications were also deduced directly from the measured stresses and velocity gradients. The goals of the research included:

1. Measurements of mean flow patterns and sizes and shapes of the corner and central toroidal recirculation zones.

2. Flowfield mapping of time-mean velocity, normal and shear Reynolds stresses, and hence turbulent viscosities in each (i,j)-orientation.
3. Development of a computer program based on the Imperial College TEACH-T program for two-dimensional axisymmetric, swirling, confined jet flows with recirculation regions.
4. Improvement of turbulence models for general swirling recirculating flows, including nonisotropic simulation.

### **1.3 The Present Contribution**

The present document is the Final Report on Grant NAG 3-74 with discussion on activities undertaken during the entire course of the research project from July 1, 1980, to June 30, 1984. Three Ph.D. theses<sup>1-3</sup> and five M.S. theses<sup>4-8</sup> evolved in connection with this study. In addition, conference papers<sup>9-21</sup> were written and presented on various aspects of the work. Also, one NASA contractor report<sup>22</sup> and one subcontractor report<sup>23</sup> were published during the course of this investigation.

In the experimental portion of the research, a logical sequence of experiments was undertaken to establish the effects on the resulting flowfield of swirler performance and swirl strength, downstream nozzle, expansion ratio, and inlet side-wall angle. Complementary computations were performed corresponding to all the boundary conditions of the experiments so as to provide a thorough evaluation of state-of-the-art predictive capability, with standard and modified turbulence models.

Section 2 contains a general review of activities undertaken, while Section 3 describes facilities and techniques used in the investigation. Section 4 concentrates on results obtained with highlights of recent Ph.D. and M.S. theses being included. Discussion also is on the coverage of relevant conference papers written during the course of the study; these are included

in the present document as Appendixes A through M. A summary is given in Section 5 and a listing of theses and papers appears in Section 6.

## 2. REVIEW OF ACTIVITIES

### 2.1 Progress During First Year (1980-81)

Items addressed during the first year of the study were described in detail by Rhode.<sup>1</sup> They included:

#### 1. Test Facility

The confined jet test facility was designed and constructed, including the specially-shaped nozzle to ensure uniform flow of low turbulence intensity on entry to the test section. A variable-angle swirler was designed as a scale-up of NASA plans and constructed. Expansion blocks of angles  $\alpha = 90, 70$  and 45 deg. were constructed of wood for the large-diameter test section of diameter 30 cm, so as to enable inlet effects to be studied.

#### 2. Experimental Techniques

A flow visualization capability, with a light curtain from a slide projector located far downstream of the test facility, was set up. Marker particles in the form of neutrally-buoyant helium-filled soap bubbles were generated by a Sage Action Inc. bubble generator via an injector located upstream of the test section in the converging section of the wind tunnel. Smoke injection and tufts were also planned for and photographic techniques clarified.

#### 3. Computational Code Development

An advanced version of the Imperial College TEACH-T computer program was developed. This code STARPIC<sup>22</sup> included swirl flow, a stairstep approximation to the sloping wall boundary, and several other features to enhance accuracy and economy of the predictive technique. The standard two-equation  $k-\epsilon$  turbulence model was included at this stage without refinement.



#### 4. Flowfield Characterization

Emphasis was on the character of the flowfield in terms of streamline patterns and recirculation zones, as evidenced by photography and standard predictions, for a variety of parameter settings of inlet swirl strength and side-wall expansion angles.

#### 2.2 Progress During Second Year (1981-82)

During the second year, more definitive results emerged with the finalization of three student theses<sup>1,4,5</sup> with the following topics specifically addressed:

##### 1. Higher Swirl Strengths

Time-mean flowfield measurements were performed with a traversing five-hole pitot probe in the confined jet with downstream blockage. These measurements were performed on a confined nonswirling flow and various swirling flows, with results given in Refs. 10 and 12. It was determined that the downstream blockage had an increasingly significant effect on corner recirculation patterns as the blockage was positioned closer and closer to the inlet. The data obtained from these experiments was important in evaluating the predictive capability of the  $k-\epsilon$  turbulence model and STARPIC computer code flowfield calculations. They also assisted in turbulence model developments.

##### 2. Swirler Effectiveness

As part of this activity, careful measurements of the flowfield of time-mean velocities  $u$ ,  $v$  and  $w$  immediately downstream of the swirl pack were made.<sup>15</sup> These measurements were performed and documented for various blade settings, and showed that the flowfield typically had a swirl flow angle which was a few degrees smaller than the blade angle. Also, the measurements revealed a larger axial flow in the outer annular portion of the duct;

presumably a result of the centrifugal forces associated with the swirl as the flow passed through the swirler.

### 3. Flowfield Predictions

The STARPIC computer code<sup>22</sup> was used to predict confined jet flows corresponding to those studied experimentally. The calculation method included a staircase boundary representation of the expansion flow and a conventional k- $\epsilon$  turbulence model. The predictions included recirculation zone characterization and mean streamline patterns, which were compared with concurrent experimental studies. Predictions were made at this stage with the standard k- $\epsilon$  turbulence model and no downstream blockage.<sup>9,13</sup> These constraints were removed later in the third year of the program.<sup>17,19</sup>

### 4. Turbulence Measurements

A significant effort was made in the application of three hot-wire methods to the measurement of time-mean and turbulence properties. The experiments performed were designed to provide the information necessary for turbulence modeling development in the confined jet facility. In this phase of the study, the capability of making measurements in the nonswirling flow and in one swirling flow with swirl vane angle  $\phi$  of 38 deg. was established.<sup>11</sup>

One-Wire Method. Single normal hot-wire measurements in nonswirling flow have established that the experimental technique was producing reliable results.<sup>11</sup> Six-orientation hot-wire measurements were made from which a method was developed to make estimates of all components of the time-mean velocity vector and the Reynolds stress tensor. A major portion of these measurements were completed for the nonswirling flowfield,<sup>11</sup> and corresponding measurements in swirling flowfields began, to be completed in the third and fourth years,<sup>14</sup> in which the effect of a downstream blockage was also investigated.

Two-Wire Method. Although the single hot-wire (six-orientation) measurements are convenient and provide a great deal of information on the time-mean velocity and on the kinetic energy of turbulence, they have a possible shortcoming in that measurements of the Reynolds shear stresses are less accurate than could be obtained with a crossed hot-wire. Because of this, the latter technique was developed for use in the nonswirling flow with and without a downstream blockage.<sup>20</sup> Application of the crossed-wire method to swirling flowfields would have some difficulty in that prior knowledge of time-mean flow direction may be required prior to measurement, and multiple orientations will also be needed. Further development of this technique was not pursued in the research program.

Three-Wire Method. A series of hot-wire measurements using a three-wire, hot-wire probe with direct computer interface and data reduction were accomplished on a corresponding nonswirling flow and one swirling flow with swirl vane angle  $\phi$  equal to 38 deg. These measurements were performed by subcontractor Dynamics Technology, Inc. under the direction of Dr. Dennis K. McLaughlin, assisted by Salim I. Janjua.<sup>23</sup>

#### 5. Downstream Blockage

The effects of weak and strong downstream contraction nozzles of area ratio  $A/a$  of 2 and 4 located at  $x/D$  values of 1 and 2 were studied via flow visualization, five-hole pitot probe, and corresponding computer predictions.

### **2.3 Progress During Third Year (1982-83)**

Research continued with additional 'production run' activities in both experimental and prediction sections of the program. This involved using a variety of parameter settings for a complete range of swirl strengths with swirl vane angle  $\phi$  from 0 to 70 deg., of side-wall angle  $\alpha$  from 90 to 45 deg., and of location  $x/D$  from 1 to 2 and area ratio  $A/a$  from 2 to 4 of the

downstream contraction nozzle. Additionally, two further test sections with smaller diameters were studied.

## 2.4 Progress During Fourth Year (1983-84)

The fourth year rounded off the tasks identified in the third year, with five student theses emerging.<sup>2,3,6-8</sup> Specifically, research included:

### 1. Smaller Expansion Ratios

Earlier work was done on the large test section of diameter  $D$  of 30 cm with  $D/d$  of 2. Measurements were extended to include smaller expansion ratio of  $D/d$  of 1.5 and 1.<sup>21</sup>

### 2. Turbulence Measurements

Higher swirl strengths were investigated with and without downstream blockages, using the single-wire six-orientation measurement technique. Kinetic energy of turbulence  $k$  and dissipation rate  $\epsilon$  were also measured.<sup>2,14,16</sup>

### 3. Turbulence Modeling

A considerable effort was placed on analyzing the turbulence measurements of Reynolds stresses and time-mean velocity gradients.<sup>3,17,18</sup> This led to information about the turbulent viscosity and models for its specification in confined swirling flows.

### 4. Flowfield Predictions

Corresponding predictions were made for the situations studied experimentally, using standard and modified two-equation  $k-\epsilon$  turbulence models.<sup>13,17,19</sup>



### 3. FACILITIES AND TECHNIQUES

#### 3.1 Facilities

Oklahoma State University has the following facilities which were purchased and/or constructed by students during the project:

1. wind tunnel,
2. one variable-angle vane swirler,
3. three plexiglass test sections of diameters 30, 22.5 and 15 cm,
4. expansion blocks of 90 and 45 deg., for each of the three test sections,
5. weak and strong downstream contraction nozzles, for each of the three test sections.

The experiments were conducted in the confined jet test facility which is described at length in the Appendixes. The facility has an axial-flow fan whose speed can be changed by altering a variable drive mechanism. Numerous fine screens and straws produce flow in the settling chamber of relatively low turbulence intensity. The contraction section leading to the test section has been specially designed to produce a minimum adverse pressure gradient on the boundary layer and thus avoid unsteady problems associated with local separation region. The sudden expansion consists of a 15 cm diameter circular jet nozzle, exiting abruptly into a 30 cm diameter test section of length 125 cm, which is constructed of plexiglass to facilitate flow visualization. Test sections of 22.5 and 15 cm diameter have also been investigated. The side-wall angle  $\alpha$  and swirl vane angle  $\phi$  are variable. The side-wall angle is set by inserting a block with side-wall angle  $\alpha$  of 90 or 45 deg. Typical operating Reynolds numbers (based on inlet average velocity and inlet diameter) are in the range 50,000 to 150,000 depending upon fan speed and aerodynamic blockage of the swirl vanes. It has been observed that this is

approximately in the Reynolds number insensitive range for this facility, in terms of nondimensional flow characteristic further downstream.<sup>1</sup>

The annular vane swirler used has ten vanes which are individually adjustable to any angle  $\phi$ , and a hub with a streamlined upstream nose and a flat downstream face. The hub-to-swirler diameter ratio is 0.25. The nose has a hyperbolic shape with a very smooth surface so as to offer minimal flow interference. The flat blades are wedge-shaped to give a constant pitch-to-chord ratio of 0.68 which gives good turning efficiency.<sup>15</sup> With an expansion block attached to the exit of the swirl pack, the expansion plane ( $x/D = 0$ ) is 3.2 cm downstream of the swirler exit (where  $x/D = -0.11$ ).

The effects of a downstream contraction nozzle on the upstream flow in the test section is important in combustor aerodynamics. Two nozzles of area ratio 2 and 4 were used. The weaker one has its upstream face contoured in a quarter circle as found in practical ramjet combustor. The stronger contraction nozzle has its upstream face in a 45 deg. slope, more typical of gas turbine combustion chamber exits. These blocks may be located at any axial position in the test section. Nozzles of these two types were constructed to fit in each of the 30, 22.5 and 15 cm diameter test sections, and used in the experimental program.

### **3.2 Flow Visualization**

Flow visualization techniques included: neutrally-buoyant helium-filled soap bubbles, smoke-wire, and tufts, with appropriate illumination and photography techniques. These permit a good 'feel' for a particular flowfield to be obtained quickly, and define areas in special need of further, more precise, investigation. The characteristics of the overall flowfield are easily discernable, including time-mean dividing streamline patterns and recirculation zones. Results from the smoke-wire experiment were utilized

near the inlet, whereas tuft and bubble data were best used in approximating the size and shape of the recirculation zones downstream. Also, bubble flow patterns reveal the existence of a precessing vortex core, which occurs downstream of the central region, in many of the swirl flow cases investigated.<sup>10,21</sup>

Tuft visualization is very important in that it supplies an overall view of local flow direction. Photographs at various shutter speeds were obtained. Slower speeds show more of the temporal behavior, although the tufts are sometimes not distinctly visible in portions of the flowfield. Velocities in recirculation zones are often somewhat lower than in other portions of the flowfield, and thus under such conditions there may be insufficient drag on a tuft to align it accurately with the local flow direction.

Local details in the nonswirling flowfields are clearly revealed through the visualization of streaklines from smoke generated from a kerosine-coated wire being suddenly heated via an electric current. In the swirling flow cases, strong mixing diffuses the smoke so that streaklines are not easily distinguishable. However, under such conditions recirculation zone outlines are visible, especially in the region near the smoke-generation wire.

Soap bubbles injected into the flow upstream of the test section trace pathlines clearly when illuminated. In relatively lower turbulence intensity portions of the flowfield mean flow directions can be obtained by ensemble averaging local tangents to pathlines traced out by soap bubbles. This helps define the flowfield geometry in terms of the outline of recirculation regions.

### **3.3 Five-Hole Pitot Probe**

One of the simplest instruments capable of simultaneously sensing both magnitude and direction of the local velocity vector is the five-hole pitot probe, used extensively in this study.<sup>10,12,15,21</sup> The particular probe employed was model DC-125-12-CD from United Sensor and Control Corp. It has a 3.2 mm diameter sensing tip and shaft containing five tubes. The sensing head is hook-shaped to allow probe shaft rotation without altering the probe tip location. The instrumentation system, in addition to the five-hole pitot probe, consists of a manual traverse mechanism, two five-way ball valves, a very sensitive pressure transducer, a power supply, and an integrating voltmeter. The differential pressure transducer is model 590D from Datametrics, Inc. It has a differential pressure range of from 0 to  $1.3 \times 10^3$  N/m<sup>2</sup> (equivalently, 0 to 10 torr). The integrating voltmeter is the TSI model 1076. As auxiliary equipment, a model 631-B strobotac from General Radio Inc. is used to check the fan speed. A pitot-static probe is used to measure the dynamic pressure in the nozzle throat just upstream of the swirler, and therefrom deduce the swirler inlet uniform axial velocity  $u_0$  which is used later for velocity normalizations. Also, a barometer/thermometer unit from Cenco Corp. is used for local pressure and temperature readings.

### **3.4 Hot-Wire Anemometer Techniques**

The second measurement technique used extensively was the six-orientation single-wire hot-wire technique.<sup>11,14,16</sup> When used on a two-dimensional flow with a predominate flow direction, a single hot-wire normal to the main flow can be used to measure the streamwise components of the time-mean velocity and the rms velocity fluctuation, in a standard manner. The six-orientation technique permits time-mean and turbulence data to be taken in general flowfields. The anemometer used in this study was DISA type 55M01, CTA

standard bridge with a normal hot-wire probe, DISA type 55P01. This probe has two prongs set approximately 3 mm apart which support a 5  $\mu\text{m}$  diameter wire which is gold plated near the prongs to reduce end effects and strengthen the wire. The six-orientation technique permits measurements of time-mean velocity components and turbulence quantities in complex three-dimensional flowfields. Applied in this study to nonreacting axisymmetric flowfields, measurements of time-mean and root-mean-square voltages at six different orientations (each separated by a 30 deg. probe support rotation) contain enough information to obtain the three time-mean velocities, the three normal and three shear Reynolds stresses. At each location in the flow, there are six different values of each of the above quantities that can be obtained using six sets of measurements of three adjacent orientations. Ensemble averages of the output quantities from the six combinations of data appear to produce estimates with the best agreement with independent measurements. The mean voltage is measured with a Hickok Digital Systems, Model DP100, integrating voltmeter and the root-mean square voltage fluctuation is measured using a Hewlett Packard, Model 400 HR, AC voltmeter.

Hot-wire anamometry with multi-wire probes have also been used in the study. A crossed hot-wire technique was used in the nonswirling flow.<sup>20</sup> Background to its operation need not be included here. A triple-wire hot-wire technique was developed under subcontract activity by Dynamics Technology, Inc., using a three-wire hot-wire probe with direct computer interface and data reduction. The raw data from the three sensors were digitized using A to D converters and stored on a Tektronix 4051 computer. The data were further reduced on the computer to obtain time-series for the three instantaneous velocity components in the flowfield. Finally, the time-mean velocities and the turbulence quantities were deduced.

### 3.5 Computer Code Development

A primitive pressure-velocity variable finite difference computer code was developed to predict swirling recirculating inert turbulent flows in axisymmetric combustors in general, and for application to the present specific idealized combustion chamber with sudden or gradual upstream expansions and weak or strong downstream contraction nozzles. The technique involved a staggered grid system for axial and radial velocities, a line relaxation procedure for efficient solution of the equations, a two-equation  $k-\epsilon$  turbulence model, a stairstep boundary representation of the sloping sidewalls, and realistic accommodation of swirl effects. The development was based on the 1974 Imperial College TEACH-T computer code. The finally developed computer program (written in Fortran 4) was code-named STARPIC (mnemonic for swirling turbulent axisymmetric recirculating flows in practical isothermal combustor geometries). The complete report<sup>22</sup> included a program listing and a sample case computation of air flow through a 45 deg. expansion ( $\alpha = 45$  deg.) from an inlet pipe to a larger pipe ( $D/d = 2$ ). The delivered code and description provide computer runs through a range of seven inlet swirl vane angles  $\phi$  equal to 0, 45, 55, 60, 65, 68 and 70 deg. The extensive document presents details of the computational solution procedure. It serves as a user's manual and deals with the computation problem, showing how the mathematical basis and computational scheme may be translated into a computer program. A flow chart, Fortran 4 listing, notes about various subroutines and a user's guide are included as an aid to prospective users of the code.

#### 4. RESULTS

The Ph.D. theses of Rhode,<sup>1</sup> Jackson,<sup>2</sup> and Abujelala<sup>3</sup> and the M.S. theses of Janjua,<sup>4</sup> Yoon,<sup>5</sup> Sander,<sup>7</sup> McKillop,<sup>6</sup> and Scharrer<sup>8</sup> evolved in connection with the investigation. Conference papers<sup>9-21</sup> were written and presented on various aspects of the work. These are attached as Appendixes A through M for completeness, and only highlights of them are cited here in the main text. Several of these papers have also now been published, either in full or abridged form; this is indicated in the reference list in Section 6. Additionally, one NASA contractor report<sup>22</sup> on the STARPIC computer code and one subcontractor report<sup>23</sup> on the triple-wire hot-wire measurement method were written during the course of the study.

##### 4.1 Swirler Performance

Throughout the entire research project, the swirler being used is annular with a hub-to-swirler diameter ratio of 0.25 and ten adjustable vanes of pitch-to-chord ratio 0.68. Measurements of time-mean axial, radial, and swirl velocities were made in Refs. 6 and 15 (see Appendix G) at the swirler exit plane using a five-hole pitot probe technique with computer data reduction. Nondimensionalized velocities from both radial and azimuthal traverses were plotted for a range of swirl vane angles  $\phi$  from 0 to 70 degrees. A theoretical study was included of idealized exit-plane velocity profiles relating the swirl numbers  $S$  and  $S'$  to the ratio of maximum swirl and axial velocities for each idealized case.

Measurements at the swirler exit plane show clearly the effects of centrifugal forces, recirculation zones, and blade wakes on the exit-plane velocity profiles. Assumptions of flat axial and swirl profiles with radial velocity equal to zero were found to be progressively less realistic as the swirler blade angle increases. At low swirl strengths ( $\phi = 38$  deg.), portions

of the  $u$  and  $w$  profiles remain flat while the  $v$ -component is already significant. At moderate swirl  $\phi = 45$  deg., linearly increasing profiles of  $u$  and  $w$  with radius are appropriate with  $v$  nonzero. At stronger swirl  $\phi = 60$  deg., even more spiked profiles are appropriate with most of the flow leaving the swirler near its outer edge, and some reverse flow near the hub. At strong swirl  $\phi = 70$  deg., the profiles are extremely spiked with flow reversal. The central recirculation zone extends upstream of the exit plane, almost to the swirler blades in high-swirl cases. Because of this recirculation, none of the idealizations considered could model strong swirl cases adequately. The flow-turning effectiveness of the flat blades was generally adequate for all vane angles tested. However, the large variations of flow angles and velocities with radius made meaningful comparisons with two-dimensional cascade data impossible. Nonaxisymmetry was found in all swirl cases investigated. It is clear that the investigation of vane swirler performance characteristics served in subsequent parts of the project to aid in computer modeling of gas turbine combustor flowfields, and in the development and evaluation of turbulence models for swirling confined flow.

#### **4.2 Gross Flowfield Characterization**

Recirculation zones are important to combustor designers and the size and location of these regions in the present isothermal flows are readily deduced from flow visualization photographs of tufts, smoke, and bubbles responding to the experimental flowfield patterns. Resulting dividing streamline sketches as well as selected photographs of the visualization experiments are presented and discussed in Refs. 1, 8, 9, 10, and 21 (see Appendixes A, B, and M). In the early part of the study<sup>1,10</sup> a major outcome was the experimental characterization of corner and central recirculation zones in six basic flowfield configurations of an axisymmetric expansion with side-



wall angle  $\alpha = 90$  and  $45$  and swirl vane angle  $\phi = 0$  (swirler removed),  $38$  and  $45$  deg. The size and shape of the recirculation bubbles for each flowfield is illustrated via an artistic impression deduced from a collection of flow visualization photographs of tufts, smoke, and neutrally-buoyant soap bubbles responding to the flow. Increasing swirl vane angle  $\phi$  from  $0$  to  $38$  deg. produces a shortened corner region and the appearance of a central bubble typically extending downstream to approximately  $x/D = 1.7$ , after which a precessing vortex core exists near the axis reaching to the exit of the test section. A further increase in  $\phi$  to  $45$  deg. enlarges the central zone and vortex core with negligible effect on the corner region in those flowfields where it occurs. The effect of side-wall angle  $\alpha$  on the nonswirling flows is negligible. However, a decrease from  $90$  to  $45$  degrees apparently eliminates the corner bubble in the swirling flow cases investigated. This decrease in  $\alpha$  also causes the inlet flow to impinge more severely on the top wall, where larger axial velocities occur.

Later work<sup>8</sup> continued the flow visualization study for higher swirl strengths, smaller diameter tubes, and downstream contraction nozzle effects. Nonswirling and swirling inert flows were investigated in axisymmetric test sections with expansion ratio  $1$  and  $1.5$  and the following geometric parameters: side-wall expansion angle  $\alpha = 45$  and  $90$  degrees, swirl vane angle  $\phi = 0$  (swirler removed),  $45$  and  $70$  degrees, and downstream blockages of area ratios  $2$  and  $4$  located  $2$  and  $4$  diameters from the test section inlet. Significant findings from the flow visualization and pitot probe measurements are discussed in Section 4.3.

### 4.3 Time-Mean Flowfield Characterization

Initial work by Rhode<sup>1,10</sup> utilized the five-hole pitot probe technique to measure time-mean velocities  $u$ ,  $v$ , and  $w$  in the large diameter test section with  $D/d = 2$ , low swirl strengths  $\phi = 0$  (swirler removed), 38 and 45 deg., and no downstream nozzles. Later, Yoon<sup>5,12</sup> (see Appendix D) extended the study to higher swirl strengths  $\phi = 60$  and 70 deg. and downstream nozzle effects with both weak and strong nozzles of area ratios  $A/a = 2$  and 4 located at  $x/D = 1$  and 2. Velocities were extensively plotted and artistic impressions of recirculation zones were presented. Findings included that the nonswirling confined jet possesses a corner recirculation zone extending to just beyond  $x/D = 2$  with no central recirculation zone. The presence of a swirler shortens the corner recirculation zone and generates a central recirculation zone followed by a precessing vortex core. The effect of a gradual inlet expansion is to encourage the flow to remain close to the sidewall and shorten the extent of the corner recirculation zone in all cases investigated. A contraction nozzle of area ratio 2 has little effect on weakly swirling and strongly swirling flows, which are dominated by forward flow and centrifugal forces, respectively. For intermediate swirl cases, the weak downstream nozzle encourages forward movement of otherwise slow-moving air and thereby shortens the central recirculation zone. A strong contraction nozzle of area ratio 4 has a more dramatic effect on the flowfields, particularly affecting both intermediate and strong swirling flow cases. Central recirculation zones are shortened considerably, and axial velocities near the facility axis become highly positive. Core regions become narrower with very strong swirl velocity magnitudes and gradients.

More recently, Scharrer<sup>8,21</sup> (see Appendix M) used the same measurement technique with smaller diameter test section tubes with  $D/d = 1.5$  and 1, again

with downstream nozzles and a full range of swirl strengths. Findings included that the corner recirculation zone is prominent in nonswirling expanding flows, but it decreases when swirl is introduced. The presence of swirl results in the formation of a central recirculation zone. Initially, increases in inlet swirl strength result in an increase in length of this zone. However, increasing to very high swirl strengths results in a shortening and widening of this zone. Placing a downstream nozzle in the flowfield creates an adverse pressure gradient near the wall and a favorable pressure gradient near the centerline. This results in increased axial and swirl velocities near the centerline and decreased velocities near the wall. It also decreases the central recirculation zone length. The degree of the effect increases as the degree of blockage increases. Reduction of the expansion ratio results in a reduction of the central recirculation zone length. The corner recirculation zone length (measured in step heights) does not change appreciably with expansion ratio for ratios greater than 1. Gradual expansion has a minimal effect on the flow.

#### **4.4 Turbulence Measurements**

Major attention was given to the development and application of the six-orientation one-wire hot-wire technique (see Section 3.4) in the present confined jet facility. Applied in this study to nonreacting flowfields, deductions of time-mean velocities, turbulence intensities and shear stresses were possible. The experiments were performed to provide the information necessary for turbulence modeling development in the confined jet facility. Initially, the mathematics and computer reduction code for the technique were developed for the nonswirling flow;<sup>4</sup> later the validity of the technique was established for the swirling flowfield with inlet swirl vane angle of 38 deg.<sup>11</sup> (see Appendix C). Excellent cost-effective results were presented,

with comparisons with independent data illustrating the reliability of the technique. Finally, a sensitivity analysis of the data reduction technique was undertaken which formed the major ingredient of an uncertainty analysis.<sup>11</sup>

Jackson<sup>2</sup> further applied the technique for a full range of swirl strengths in the test section with expansion ratios  $D/d = 1$  and  $2$ , which may be equipped with a strong contraction nozzle of area ratio  $4$  at  $x/D = 2$ . The effect of swirl on time-mean velocities and complete Reynolds stress tensor was investigated, and extensive results were given for swirl vane angles of  $0$  (swirler removed),  $38$ ,  $45$ ,  $60$  and  $70$  deg. Dissipation rates were also measured. Major results were reported for the expansion flowfield in Ref. 14 (see Appendix F). The effect of swirl on the time-mean velocity field was found to shorten the corner recirculation zone length and to generate the existence of a central recirculation zone, which is followed by a precessing vortex core region. As the degree of swirl increases, the length of the central recirculation bubble decreases, whereas its width, and also the width of the precessing vortex core, increases. At the jet inlet to the test section, directional turbulence intensities are found to increase significantly with swirl. Throughout the flowfield, the most dramatic effect of swirl is to increase values of the three turbulent shear stress terms.

Introduction of a strong contraction nozzle at  $x/D = 2$  with an area reduction ratio of  $4$  causes a significant effect on the time-mean swirling flowfield. Central recirculation zones are shortened and axial velocities along the whole jet axis become positive. The core regions become narrow with strong swirl velocities and gradients. Turbulence levels and shear stresses also increase along the jet centerline near the exit of the contraction nozzle.

The accuracy and directional sensitivity of the technique were also assessed, with respect to mean flow velocity orientation to the probe, see Ref. 16 (Appendix H). Results demonstrate relative insensitivity, indicating that the method is a useful cost-effective tool for turbulent flows of unknown dominant flow direction. The technique adequately measures the properties of a flowfield independent of the dominant flow direction except when the flow is predominately in the direction of the probe holder, with the six-orientations of the probe then creating insignificant changes in hot-wire response.

A crossed hot-wire technique has been used for the nonswirling free and confined jet ( $D/d = 2$ ) situations<sup>7,20</sup> (see Appendix L). Axial and radial time-mean velocities, directional turbulence intensities, and main Reynolds stress were measured. Associated turbulent viscosity values were deduced throughout. Investigations were made with and without a downstream contraction nozzle of area ratio 4 located at  $x/D = 2$ . Measurements indicated that the crossed hot-wire used cannot handle axial flow reversal (without prior knowledge and probe reorientation) and that the experimental technique is inadequate for the measurement of time-mean radial velocity. Other quantities show a high level of comparability. In common with previous researchers, time-mean and turbulence characteristics with the contraction nozzle at  $x/D = 2$  show little change from that of the corresponding flowfield with a contraction nozzle, for the nonswirling flow case.

Subcontractor Dynamics Technology, Inc., under the direction of Dr. Dennis K. McLaughlin, completed a series of triple-wire hot-wire measurements,<sup>23</sup> see Section 3.4. Experiments were performed and where possible comparisons were made with the results of independent measurements. For example, the mean velocity components were compared with the results of five-hole pitot probe measurements. The major qualification experiments

involved measurements performed in a nonswirling flow compared with conventional X-wire measurements. In the swirling flowfield with inlet swirl vane angle  $\phi = 38$  deg., advantages and drawbacks of the triple-wire technique over the six-orientation single hot-wire method were discussed.

#### **4.5 Turbulence Modeling**

Abujelala<sup>3</sup> continued the earlier prediction work of Rhode<sup>1</sup> and, additionally, stressed turbulence modeling possibilities. In Ref. 17 (see Appendix I), shortcomings and recommended corrections to the standard two-equation  $k$ - $\epsilon$  turbulence model suggested by previous investigators were presented. They were assessed regarding their applicability to turbulent swirling recirculating flow. Recent experimental data on swirling confined flows, obtained with a five-hole pitot probe and a six-orientation hot-wire probe, were used to obtain optimum values of the turbulence parameters  $C_\mu$ ,  $C_2$ , and  $\sigma_\epsilon$  for swirling flows. General predictions of moderately and strongly swirling flows with these values are more accurate than predictions with the standard or previous simple extensions of the  $k$ - $\epsilon$  turbulence model.

The detailed data base evolved in the course of recent studies, see Section 3.4, were analyzed numerically as a contribution to the turbulence modeling effort<sup>18</sup> (see Appendix J). Swirl strength and a strong contraction nozzle were found to have strong effects on the turbulence parameters. Generally, the most dramatic effect of the increase of swirl is the considerable increase in all the parameters considered - that is, in particular, increase of turbulent viscosity and kinetic energy. The presence of a strong contraction nozzle tends to increase parameter values in regions of acceleration where large radial velocity gradients occur, and to reduce them in the deceleration region near the outer boundary. Based on similarity of viscosity and length scale profiles, a  $C_\mu$  - formulation was deduced which

was shown to improve the predictive capability of the standard  $k-\epsilon$  turbulence model in swirling recirculating flows<sup>19</sup> (see Appendix K).

#### 4.6 Computer Predictions

Application of the STARPIC computer code<sup>22</sup> was made during the first year to the simulation of isothermal airflow in the axisymmetric test facility with diameter expansion ratio  $D/d$  of 2, with two wall expansion angles  $\alpha$  of 90 and 45 deg. and three swirl vane angles  $\phi$  of 0, 45 and 70 deg. All results were obtained via a nonuniform grid system so as to enhance solution accuracy. The inlet profiles of axial velocity  $u$  and swirl velocity  $w$  are idealized as "flat" (that is constant-valued). Predicted  $u$  and  $w$  velocity profiles for the six flowfield configurations are given in Refs. 1 and 9, together with deduced parametric effects on recirculation zone lengths. The general trends are similar to the experimental findings. Note that, in these predictions, the inlet flow angle was taken to be the swirl vane angle  $\phi$ , whereas in reality the blades are not 100% efficient. The experimental inlet data were not available at the time the predictions were made, and the flat inlet profile assumption is now known (see Section 4.1) to be inadequate for precise simulation of the present study, in which the inlet flow conditions are achieved via a ten-blade swirler with pitch/chord ratio of 0.68. As documented in the experimental results, the actual inlet profiles are nonuniform with nonzero radial velocity.

Abujelala<sup>3</sup> continued the theoretical study, and assessed the validity of flowfield predictions resulting from the choice of inlet velocity profiles. Results, see Ref. 13 (Appendix E), demonstrated that realistic predictions are forthcoming only from the inclusion of realistic axial, radial and swirl velocity profiles as inlet conditions. Predictions with either flat inlet profiles, solid body rotation or zero radial velocity are inappropriate.

Predictions were given for a full range of swirl strengths using measured inlet axial, radial and swirl velocity profiles in each case, and predicted velocity profiles, streamline plots and axial velocity representations illustrated the large-scale effects of inlet swirl on flowfields. Predictions were included for the effect of weak and strong downstream contraction nozzles on the flow. In the swirl flow cases, a weak nozzle leads to the discouragement of central recirculation zones with stronger vortex cores downstream possessing negative axial velocities. A strong nozzle has more pronounced effects on swirl flow cases, with discouragement of central recirculation zones, and forward flow in highly swirled vortex core regions further downstream.

Later production runs given in Ref. 19 (see Appendix K) included predictions of swirl, confinement and nozzle effects on confined turbulent flow which were exhibited and compared with five-hole pitot-probe time-mean velocity measurements of Refs. 12 and 21. Two sets of computations were given, one using the standard  $k-\epsilon$  turbulence model and the other using a  $C_{\mu}$ -formulation model deduced from six-orientation single-wire hot-wire measurements, as discussed in Section 4.5. Results confirmed that the accuracy of the latter model is superior. To highlight the effects of confinement and exit nozzle area on this flow, three expansion ratios and two contraction ratios were used. Predictions were given for a full range of swirl strengths using the measured inlet conditions of Ref. 15 for axial, radial and swirl velocity profiles. The predicted velocity profiles illustrate the large-scale effects of inlet swirl on the flowfields. It appears that a strong contraction nozzle has a pronounced effect, on swirl flow cases, with discouragement of central recirculation zones, and forward flow in highly swirled vortex core regions. The expansion ratio value has large-scale effects on the size and location of the recirculation zones.



## 5. CLOSURE

The main objectives of the research program were to determine the effects of swirl and combustor geometry on isothermal flowfield patterns, time-mean velocities and turbulence quantities, and to establish an improved simulation in the form of a computer prediction code equipped with a suitable turbulence model. The study included the investigation of: a complete range of swirl strengths; swirler performance; downstream contraction nozzle sizes and locations; expansion ratios; and inlet side-wall angles. Their individual and combined effects on the test section flowfield were observed, measured and characterized.

This final report concludes the present research on NASA Grant NAG 3-74, summarizing the activities, describing the facilities and techniques, and discussing major results obtained. Further details appear in the Ph.D. and M.S. theses that have evolved, and in the conference research papers that have been written and appended to the present document.

## 6. REFERENCES

The following list of theses and research papers covers research conducted with the support of the grant.

1. Rhode, D. L., "Predictions and Measurements of Isothermal Flowfields in Axisymmetric Combustor Geometries," Ph.D. Thesis, Dept. of Mechanical and Aerospace Engineering, Oklahoma State University, Stillwater, OK, Dec. 1981.
2. Jackson, T. W., "Turbulence Characteristics of Swirling Flowfields", Ph.D. Thesis, Oklahoma State University, Stillwater, Okla., Dec. 1983.
3. Abujelala, M. T., "Confined Turbulent Swirling Recirculating Flow Predictions", Ph.D. Thesis, Oklahoma State University, Stillwater, OK, June 1984.
4. Janjua, S. I., "Turbulence Measurements in a Complex Flowfield Using a Six-Orientation Hot-Wire Probe Technique." M.S. Thesis, Oklahoma State University, Stillwater, OK, Dec. 1981.
5. Yoon, H. K., "Five-Hole Pitot Probe Time-Mean Velocity Measurements in Confined Swirling Flows." M.S. Thesis, Oklahoma State University, Stillwater, OK, July 1982.
6. Sander, G. F., "Axial Vane-Type Swirler Performance Characteristics". M.S. Thesis, Oklahoma State University, Stillwater, OK, May 1983.
7. McKillop, B. E. "Turbulence Measurements in a Complex Flowfield Using a Crossed Hot-Wire". M.S. Thesis, Oklahoma State University, Stillwater, OK, July 1983.
8. Scharrer, G. L., "Swirl, Expansion Ratio and Blockage Effects on Confined Turbulent Flow". M.S. Thesis, Oklahoma State University, Stillwater, OK, May 1984.

9. Rhode, D. L., Lilley, D. G., and McLaughlin, D. K., "On the Prediction of Swirling Flowfields Found in Axisymmetric Combustor Geometries", Proc. ASME Symp. on Fluid Mechanics of Combustion Systems, Boulder, CO, June 22-24, 1981, pp. 257-266. Also ASME Journal of Fluids Engng., Vol. 104, 1982, pp. 378-384.
10. Rhode, D. L., Lilley, D. G., and McLaughlin, D. K., "Mean Flowfields in Axisymmetric Combustor Geometries with Swirl", Paper AIAA-82-0177, Orlando, Florida, January 11-14, 1982. Also AIAA Journal, Vol. 21, No. 4, April 1983, pp. 593-600.
11. Janjua, S. I., McLaughlin, D. K., Jackson, T. W. and Lilley, D. G., "Turbulence Measurements in a Confined Jet Using A Six-Orientation Hot-Wire Probe Technique", Paper AIAA-82-1262, Cleveland, Ohio, June 21-23, 1982. Also AIAA Journal, Vol. 21, No. 12, Dec. 1983, pp. 1609-1610.
12. Yoon, H. K. and Lilley, D. G., "Five-Hole Pitot Probe Time-Mean Velocity Measurements in Confined Swirling Flows", Paper AIAA-83-0315, Reno, Nevada, January 10-13, 1983. Also AIAA Journal, Vol. 22, No. 4, April 1984, pp. 514-515.
13. Abujelala, M. T. and Lilley, D. G., "Confined Swirling Flow Predictions", Paper AIAA-83-0316, Reno, Nevada, January 10-13, 1983.
14. Jackson, T. W. and Lilley, D. G., "Single-Wire Swirl Flow Turbulence Measurements", Paper AIAA-83-1202, Seattle, Washington, June 27-29, 1983.
15. Sander, G. F., and Lilley, D. G., "The Performance of an Annular Vane Swirler", Paper AIAA 83-1326, Seattle, Washington, June 27-29, 1983.
16. Jackson, T. W. and Lilley, D. G., "Accuracy and Directional Sensitivity of the Single-Wire Technique", Paper AIAA-84-0367, Reno, Nevada, January 9-12, 1984.

17. Abujelala, M. T. and Lilley, D. G., "Limitations and Empirical Extensions of the  $k-\epsilon$  Model as Applied to Turbulent Confined Swirling Flows", Paper AIAA-84-0441, Reno, Nevada, January 9-12, 1984. Also Chem. Engng. Comm., (in press), 1984.
18. Abujelala, M. T., Jackson, T. W. and Lilley, D. G., "Swirl Flow Turbulence Modeling", Paper AIAA-84-1376, Cincinnati, Ohio, June 11-13, 1984.
19. Abujelala, M. T. and Lilley, D. G., "Swirl, Confinement and Nozzle Effects on Confined Turbulent Flow", Paper AIAA-84-1377, Cincinnati, Ohio, June 11-13, 1984.
20. McKillop, B. E. and Lilley, D. G., "Turbulence Measurements in a Complex Flowfield Using a Crossed Hot-Wire", Paper AIAA-84-1604, Snowmass, Colorado, June 25-27, 1984.
21. Scharrer, G. L. and Lilley, D. G., "Five-Hole Pitot Probe Measurements of Swirl, Confinement and Nozzle Effects on Confined Turbulent Flow", Paper AIAA-84-1605, Snowmass, Colorado, June 25-27, 1984.
22. Lilley, D. G. and Rhode, D. L., "A Computer Code for Swirling Turbulent Axisymmetric Recirculation Flows in Practical Isothermal Combustor Geometries", NASA CR-3442, Feb., 1982.
23. Janjua, S. I., and McLaughlin, D. K., "Turbulence Measurements in a Swirling Confined Jet Flowfield Using a Triple Hot-Wire Probe", Report DT-8178-02, Dynamics Technology, Inc., Torrance, Calif., Nov., 1982.



APPENDIX A

ON THE PREDICTION OF SWIRLING FLOWFIELDS FOUND IN  
AXISYMMETRIC COMBUSTOR GEOMETRIES

# On the Prediction of Swirling Flowfields Found in Axisymmetric Combustor Geometries

**D. L. Rhode**  
Graduate Student,  
Assistant Professor,  
College Station, Texas

**D. G. Lilley**  
Professor.

**D. K. McLaughlin**  
Professor,  
Group Manager,  
Torrance, Calif.

School of Mechanical  
and Aerospace Engineering,  
Oklahoma State University,  
Stillwater, Okla. 74078

*Combustor modeling has reached the stage where the most useful research activities are likely to be on specific sub-problems of the general three-dimensional turbulent reacting flow problem. The present study is concerned with a timely fluid dynamic research task of interest to the combustor modeling community. Numerical computations have been undertaken for a basic two-dimensional axisymmetric flowfield which is similar to that found in a conventional gas turbine combustor. A swirling nonreacting flow enters a larger chamber via a sudden or gradual expansion. The calculation method includes a stairstep boundary representation of the expansion flow, a conventional  $k-\epsilon$  turbulence model and realistic accommodation of swirl effects. The results include recirculation zone characterization and predicted mean streamline patterns. In addition, an experimental evaluation using flow visualization of neutrally-buoyant helium-filled soap bubbles is yielding very promising results. Successful outcomes of the work can be incorporated into the more combustion- and hardware-oriented activities of gas turbine engine manufacturers, including incorporating the modeling aspects into already existing comprehensive numerical solution procedures.*

## Introduction

The combustor of the gas turbine engine contains high intensity combustion and, as far as possible, must burn fuel completely, cause little pressure drop, produce gases of nearly uniform temperature, occupy small volume, and maintain stable combustion over a wide range of operating conditions [1]. In design situations, the engineer has to seek an optimum path between irreconcilable alternatives of, for example, efficiency and pollution. The general aim of most research investigations is to provide information which is useful to designers by "characterizing" or "modeling" certain features of the phenomenon in question [2]. Up to now designers rely heavily on experimental evidence to produce empirical formulae. However, traditional design methods are now being supplemented by analytical methods (numerical solution of the appropriate governing partial differential equations). Computer modeling of combustion processes is now an established fact, but improvements and new developments (both experimental and theoretical) can and should be made, theoretical modeling being aided by carefully chosen experiments [3].

The present paper addresses research that is restricted to steady turbulent flow in axisymmetric geometries, under low speed and nonreacting conditions – a study area highlighted at a recent workshop [1] as a fundamental research requirement in combustion modeling. The particular problem is concerned with turbulent flow of a given turbulence distribution in a

round pipe entering an expansion into another round pipe, as illustrated in Fig. 1. The in-coming flow may possess a swirl component of velocity via passage through swirl vanes at angle  $\phi$  [equal approximately to  $\tan^{-1}(w_0/u_0)$ ], and the side-wall may slope at an angle  $\alpha$ , to the main flow direction. The resulting flowfield domain may possess a central toroidal recirculation zone CTRZ in the middle of the region on the axis, in addition to the possibility of a corner recirculation zone CRZ near the upper corner provoked by the rather sudden enlargement of the cross-sectional area. Of vital concern is the characterization of flows of this type in terms of the effects of side-wall angle  $\alpha$ , degree of swirl  $\phi$ , turbulence intensity  $k_0$  of the inlet stream and expansion ratio  $D/d$  on the resulting flowfield in terms of its time-mean and

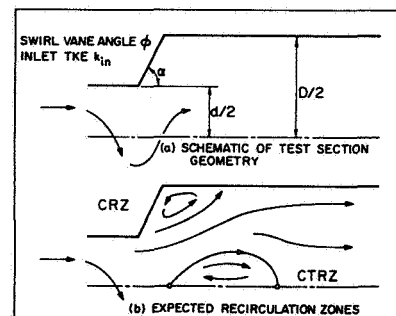


Fig. 1 The flowfield being investigated

Contributed by the Fluids Engineering Division and presented at the Symposium on the Fluid Mechanics of Combustion Systems, Boulder, Colo., Manuscript received by the Fluids Engineering Division, September 2, 1981.

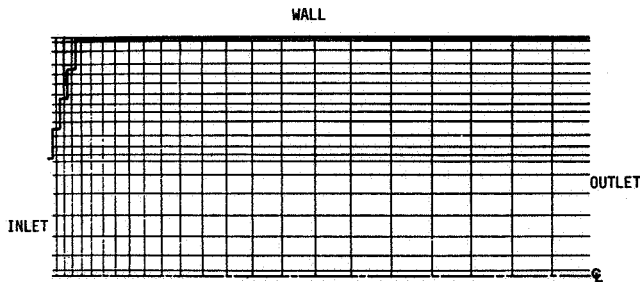


Fig. 2 An example of a coarse grid system being employed to fit the flow domain

turbulence quantities. Such problems have received little attention, yet there is a definite need for work in this area [4-6].

Experimental work in the configuration just described is being complemented by an associated prediction study of the flowfield. Consideration is given to recent work in the finite difference solution, via a primitive variable code, of axisymmetric swirl flow in the combustor geometry of Fig. 1, where the inlet expansion sidewall may slope obliquely to the central axis. Thus a systematic parametric investigation may be contemplated on the effect of sidewall angle  $\alpha$  and degree of swirl  $\phi$  on the resulting flowfield produced. Basic governing equations are presented, together with a brief description of the simulation and solution technique. The equations are elliptic in character and are solved via an advanced version of the Imperial College TEACH-T computer program [7], recently developed at Oklahoma State University [8].

Comparison with available experimental turbulent flow measurements assists in confirming the final predictive capability. One such experiment, underway at Oklahoma State University, is concerned with measuring the effects of swirl and side-wall angle on streamlines, mean flow and turbulence parameters in nonreacting flow. The facility and experimental details are included. For the present paper a preliminary evaluation of the accuracy of the computed flowfields is accomplished by comparison with flow visualization using neutrally-buoyant helium-filled soap bubbles as tracer particles. Photographs of the bubbles can be interpreted to yield time-mean flowfield maps which define approximately the boundaries of recirculation regions and regions of highly turbulent flow. Major features of strongly swirling flow characterization are then presented so as to exemplify the current predictive capability in terms of velocity profiles, streamline patterns and recirculation zone characterization. The final closure summarizes the achievements.

### Theoretical Model

The turbulent Reynolds equations for conservation of mass, momentum (with  $x, r, \theta$  velocity components  $u, v, w$ ),

turbulence kinetic energy  $k$ , and turbulence dissipation rate  $\epsilon$  govern this two-dimensional axisymmetric steady flow. They may be expressed in the general form

$$\frac{1}{r} \left[ \frac{\partial}{\partial x} (\rho u r \phi) + \frac{\partial}{\partial r} (\rho v r \phi) - \frac{\partial}{\partial x} \left( r \Gamma_{\phi} \frac{\partial \phi}{\partial x} \right) - \frac{\partial}{\partial r} \left( r \Gamma_{\phi} \frac{\partial \phi}{\partial r} \right) \right] = S_{\phi}$$

where  $\phi$  represents any of the dependent variables, and the equations differ primarily in their final source terms  $S_{\phi}$  [7-9]. Implicit here is the use of the standard two-equation  $k-\epsilon$  turbulence model, whereby the exchange coefficients  $\Gamma_{\phi}$  may be specified in each equation [10]. All constants appearing in the simulation are given the usual values. The corresponding finite difference equations are solved via an advanced version of the TEACH computer code [7], using a semi-implicit line-by-line method using the tridiagonal matrix algorithm for values at points of a variable size rectangular grid, with variable under-relaxation. A complete description of the finally-developed computer program is now available, with full details in the form of a user's manual about the solution technique, boundary conditions and their implementation, and the iteration scheme and parameters used [8]. A computer program listing and sample output are included for prospective users. Recent advances include revised cell volumes for the axial and radial velocities, swirl effects on wall functions, and incorporation of sloping boundaries. Figure 2 shows an example of grid specification for the present geometry.

### Experimental Approach

Several previous experimenters have investigated nonreacting flows in expansion geometries [11-20]. References [11] and [12] also include flowfield predictions, made with versions of the TEACH-T computer program [7]. These experiments include time-mean velocity measurements [with hot-wire and pitot probes and laser Doppler anemometry], turbulence measurements [with hot-wires and laser anemometers] and flow visualization. The majority of the measurements were made in nonswirling flows [14-20], however some noteworthy experiments were made in swirling confined jets [11, 13]. Direct comparison between the results of the cited experiments and the present experimental results is generally not possible because of differences in geometry. However, in the nonswirling jet comparisons were possible with experiments of Chaturvedi [20], who measured mean and turbulent flow quantities downstream of a sudden expansion of diameter ratio 2.0 and various expansion sidewall angles  $\alpha$ . Measurements of mean velocity in regions of high turbulence intensity and where the direction of the velocity vector is unknown were made with a pitot tube. Mean velocity was also measured with a constant temperature hot-wire anemometer using a single wire. In addition, a cross-wire was used to measure all the Reynolds stresses.

### Nomenclature

$D$ = chamber diameter	$v = (u, v, w)$ = time-mean velocity (in $x, r, \theta$ direction)	$\rho$ = time-mean density
$d$ = nozzle diameter	$x, r, \theta$ = axial, radial, azimuthal cylindrical polar coordinates	$\phi$ = swirl vane angle [ $\tan^{-1}(w_0/u_0)$ ], general dependent variable
$G$ = axial flux of momentum	$\alpha$ = side-wall angle	
$k$ = kinetic energy of turbulence	$\Gamma$ = turbulence exchange coefficient	
$S$ = swirl number = $2(G_{\theta}/G_x d)$ , source term (with subscript)	$\epsilon$ = turbulence energy dissipation rate	<b>Subscripts</b>
		0 = value at inlet to flowfield



The present experiments have been conducted in the Oklahoma State University confined jet facility, and from part of an on-going study aimed at the characterization of time-mean and turbulence quantities in swirling confined flows. It has an axial flow fan whose speed can be changed by altering the varidrive mechanism. Numerous fine screens and straws produce flow in the settling chamber of relatively low turbulence intensity. The contraction section leading to the test section has been designed by the method of Morel [21] to produce a minimum adverse pressure gradient on the boundary layer and thus avoid unsteady problems associated with local separation regions. The sudden expansion consists of a 15 cm diameter circular jet nozzle, exiting abruptly into a 30 cm diameter test section as shown in Fig. 1. The substantial size of this test model provides excellent probe resolution for hot-wire measurements which are currently underway and will be reported in a later paper. The test section is constructed of plexiglas to facilitate flow visualization. The side-wall angle  $\alpha$  and swirl vane angle  $\phi$  are variable. The side-wall angle is set by inserting one of three blocks with a sidewall angle  $\alpha$  of 90, 70, or 45 deg. The swirl vane assembly consists of ten vanes which are individually adjustable to any vane angle  $\phi$ . The pitch/chord ratio at the half radius location is approximately one, and this assures quite high efficiency in generating a swirling motion to the in-coming flow [6]. Typical operating Reynolds numbers [based on inlet average velocity and inlet diameter] are in the range 70,000 to 130,000 depending upon fan speed and aerodynamic blockage of the swirl vanes. It has been observed that this is in the Reynolds number insensitive range for this facility [9], in terms of nondimensional flow characteristics further downstream.

The basic technique for the experiment discussed in this paper involves the visualization of individual neutrally-buoyant helium-filled soap bubbles. The bubbles which are approximately 0.5 to 1 mm diameter are produced by a Sage Action, Inc. generator-injector, which can be located at various positions in the flowfield. Because of the substantial size of the injector itself (1.5 cm in diameter and 6 cm long) it

is not inserted directly into regions of flow interest. Instead it is either mounted upstream in the stilling chamber, or flush mounted to the wall of the large diameter pipe of the test section, to inject bubbles directly into the corner recirculation zone. The bubbles are illuminated by a beam of light from a high-power 35 mm slide projector which is located far downstream of the test facility. Photographs of illuminated bubbles are taken with various shutter speeds and camera positions. At relatively long exposure times (such as 1/8 s) a series of streaks are visible in the field of view corresponding to pathlines of individual bubbles. A 35 mm single lens reflex camera with a 45 mm lens was used. Tri-X Pan black and white film with a normal ASA of 400 was used and developed with a special process which pushed the ASA to 5000. In relatively lower turbulence intensity portions of the flowfield, mean-flow directions can be obtained by ensemble averaging local tangents to pathlines traced out by soap bubbles. This helps to define the gross features of the flowfield in terms of the outline of recirculation regions.

## Results and Discussion

**Computer Code Operation.** The predictions presented here are computer simulations of the isothermal airflow in axisymmetric combustor geometries. As noted earlier diameter expansion ratio  $D/d$  is 2.0, inlet Reynolds number  $Re_d = 1.26 \times 10^5$ , wall expansion angle  $\alpha = 90, 70,$  and 45 deg and swirl vane angle  $\phi$  varies from 0 to 70 deg. All results are obtained via a nonuniform grid system which enhances solution accuracy. In the  $r$ -direction 21 grid lines are employed, and they are clustered near the shear layer region and along the wall and centerline. Cells in the  $x$ -direction are gradually expanding, and from 23 to 35 grid lines are employed as required to produce the desired side-wall angle  $\alpha$ . Some grid independence tests have been undertaken with refined mesh systems up to  $35 \times 55$ ; the present values were found to be adequate in terms of accuracy, and no discernable changes to the mean flow patterns to be presented were found.

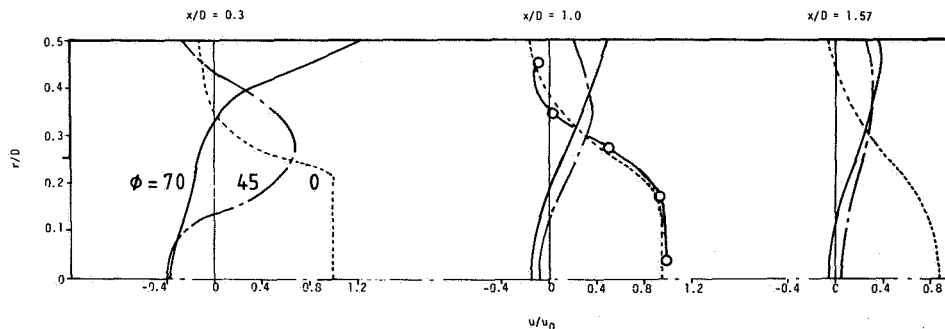


Fig. 3 (a)  $\alpha = 90$  deg

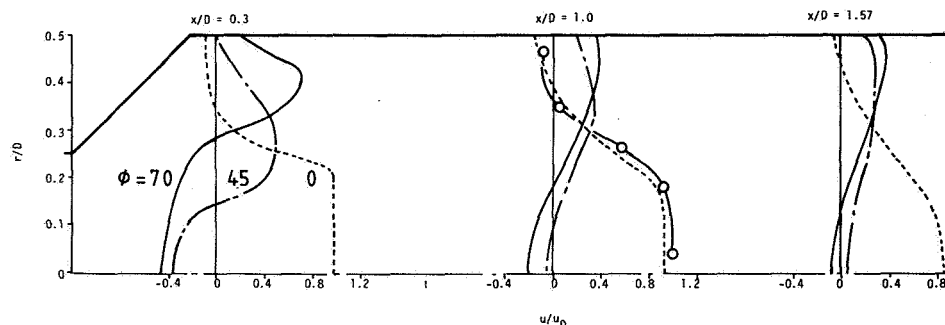


Fig. 3 (b)  $\alpha = 45$  deg

Fig. 3 Predicted axial velocity profiles showing the effect of swirl vane angle  $\phi$  for wall expansion [o-o-o Experiment [20] with  $\phi = 0$ ]

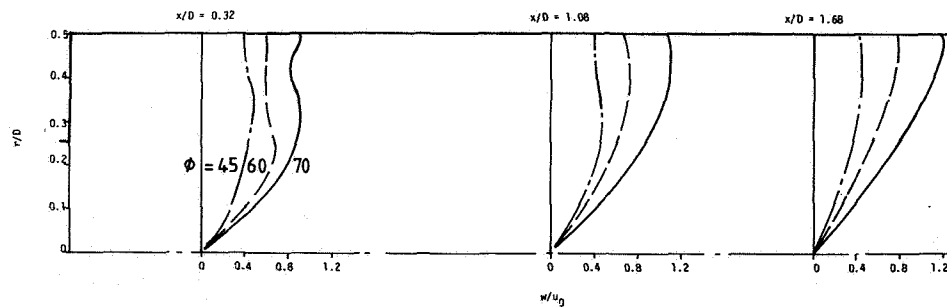


Fig. 4 (a)  $\alpha = 90$  deg

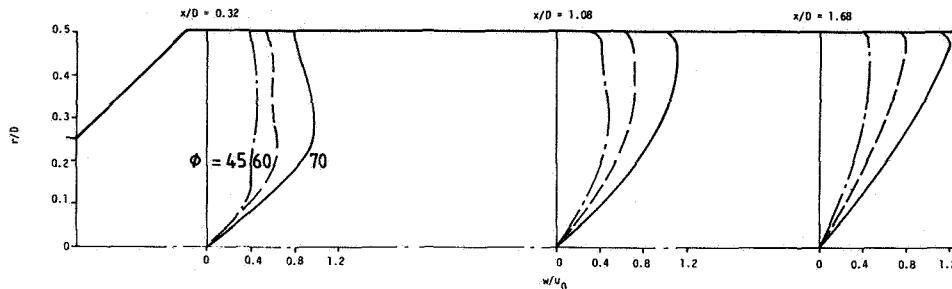


Fig. 4 (b)  $\alpha = 45$  deg

Fig. 4 Predicted swirl velocity profiles showing the effect of swirl vane angle  $\phi$  for wall expansion angles  $\alpha$ :

Computer runs through a range of seven inlet swirl vane angles  $\phi$  equal to 0, 45, 55, 60, 65, 68, and 70 deg are undertaken for each side-wall angle  $\alpha$ . Approximately 200 to 300 iterations [each with 5 field updates for pressure, 4 for axial velocity, and 3 for other primary variables] is needed to converge at each swirl strength, with the solutions for each value of  $\phi$  being used as the initial starting values for the next higher value of  $\phi$  considered. The inlet profiles of axial velocity  $u$  and swirl velocity  $w$  are idealized as flat (that is, constant-valued). This is consistent with the assumption of a one hundred percent efficient swirler, which is a little incorrect at the higher swirl angles. The in-coming nonswirling plug flow [ $u = u_0$  and  $v = w = 0$ ] is turned through an angle  $\phi$  to generate the flat out-going flow [ $u = u_0$ ,  $w = u_0 \tan \phi$  and  $v = 0$ ] with the additional assumption that radial velocity remains zero.

Axial and swirl velocity profiles are presented for the two  $\alpha$  values and three  $\phi$  values, clearly showing details of these parameter influences. Then, streamline plots for each value of  $\phi$ , calculated and drawn by computer for each  $\alpha$ , allow comparison of the shape and size of recirculation zones. Discussion is primarily aimed at guiding designers in judiciously choosing where experimental emphasis should be placed and/or in interpolating results from a limited amount of experimental data. For comparison with other results, it should be noted [6] that swirl number  $S$  and  $\phi$  are related approximately by  $S = 2/3 \tan \phi$ , so that vane angles 45, 60, and 70 deg, for example, correspond to  $S$  values of 0.67, 1.15, and 1.83, respectively.

**Velocity Profiles.** Predicted mean axial velocity profiles for the  $\alpha = 90$  and 45 deg geometries are shown in Figs. 3(a) and 3(b), respectively. The nonswirling case ( $\phi = 0$ ) exhibits good qualitative agreement with measurements of Chaturvedi [20] in a geometrically similar facility. The influence of  $\phi$  is most dramatic near the combustor inlet, where the  $\phi = 0$  profile in Fig. 3(a) shows a large corner recirculation region, provoked by the sudden increase in flow area. A very large value of  $\partial u / \partial r$  occurs near the inlet, which is indicative of high turbulence energy generation in a strong shear layer. Further, the nonswirling centerline velocity exhibits little change in the streamwise direction. With  $\phi = 45$  deg the mean

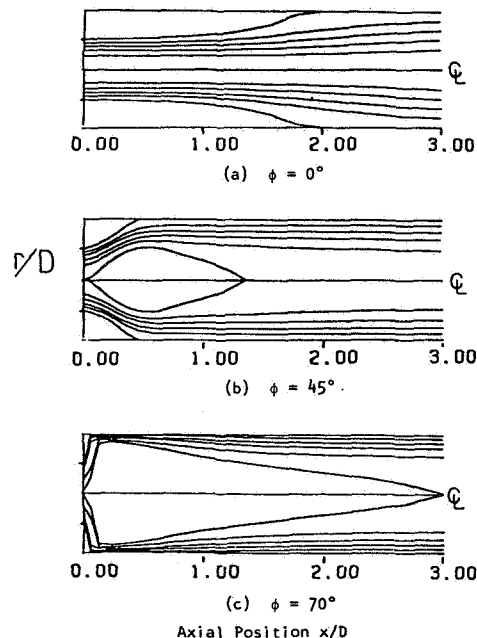


Fig. 5 Predicted streamline plots with wall expansion angle  $\alpha = 90$  deg and various swirl vane angles  $\phi$ : (a) 0 deg, (b) 45 deg, and (c) 70 deg

axial velocity profile is dramatically changed. Near the inlet a central toroidal recirculation zone appears and the corner recirculation zone is considerably smaller. Also, a maximum velocity value occurs in an annular fashion near  $r/D = 0.25$ , although a more flattened shape quickly develops before  $x/D = 1.0$ . It should also be noted that the boundary layer on the outer sidewall is too thin to be seen on the figures. The strong swirl case of  $\phi = 70$  deg shows a much wider central recirculation region at  $x/D = 0.3$ , which is caused by strong centrifugal effects. This promotes a very high forward velocity near the wall rather than a corner recirculation region. This tendency has been qualitatively observed by combustor designers at high degrees of swirl, but little quantitative data are yet available to precisely substantiate

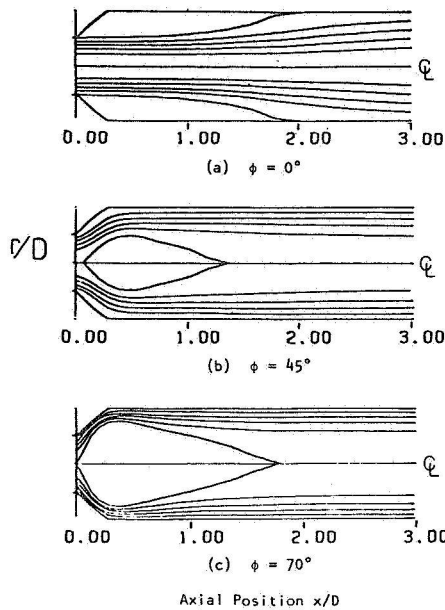


Fig. 6 Predicted streamline plots with wall expansion angle  $\alpha = 45$  deg and various swirl vane angles  $\phi$ : (a) 0 deg, (b) 45 deg, and (c) 70 deg

this phenomenon. The radial extent of the central recirculation zone and the velocity near the wall quickly diminish downstream as swirl strength is dissipated.

The effect of side-wall angle  $\alpha$  is only noticeable on the more strongly swirling flow cases and then only near to the inlet. Figure 3(b) with  $\alpha = 45$  deg shows little effect of  $\alpha$  on the nonswirling flow, but dramatic effects on the  $\phi = 45$  and 70 deg flows. In the former case, no corner recirculation zone is present. In the latter case, the reduction of side-wall angle has greatly reduced the velocity near the confining walls and made the central recirculation zone narrower with higher reverse velocities. It should be noted, however, that only a slight effect of  $\alpha$  (for the range considered here) remains beyond  $x/D$  values of about 1.0.

Figures 4(a) and 4(b) show swirl velocity profiles for the corresponding geometries with vane angles of 45, 60, and 70 deg. All of these profiles show solid-body-rotation behavior near the centerline, even near the inlet where a flat profile is a specified inlet condition. The radial location of the station maximum for  $w$  tends to increase with  $x/D$  in Fig. 4(a). Also irregularities of the profiles at  $x/D = 0.32$  disappear with increasing  $x$ . Hence, swirl as well as axial velocity profiles appear to approach those corresponding to swirling flow in a pipe [22] as  $x$  increases.

Comparing Fig. 4(b) with 4(a), it is the weaker swirl cases which show the most appreciable effect of  $\alpha$  at  $x/D = 0.32$ , and again this diminishes with increasing  $x$ . Profiles near the inlet are a little flatter in the outer part of the flow, with narrower solid-body-rotation regions near the axis. The profiles at  $x/D = 1.68$  exhibit similarity for each geometry and if normalized with respect to their inlet swirl velocity maximum values, the curves will collapse on to a single characteristic curve.

**Streamline Plots.** Figure 5 shows results calculated and plotted by computer to show the combustor designer the sequence of predicted streamline patterns he should expect upon increasing the vane angle for the  $\alpha = 90$  deg combustor. In particular, the size and shape of recirculation bubbles are emphasized. The nonswirling case shown in Fig. 5(a) exhibits a large corner recirculation region as indicated also in Fig. 3(a). As swirl is introduced, a central recirculation region appears in conjunction with a decrease in size of the corner

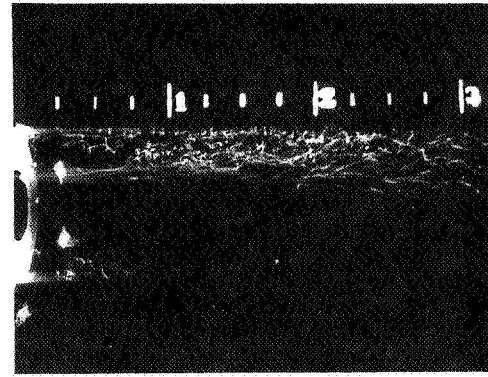


Fig. 7 (a)  $\phi = 0$  deg

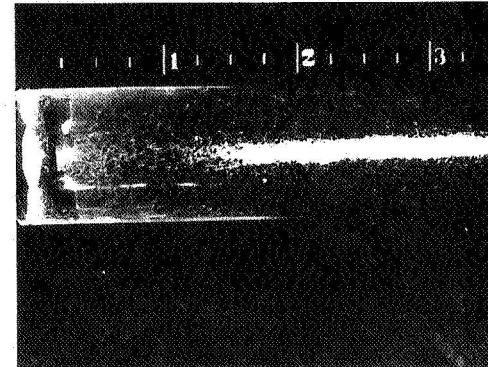


Fig. 7 (b)  $\phi = 45$  deg

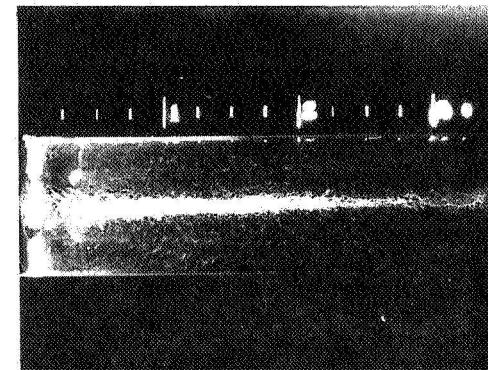


Fig. 7 (c)  $\phi = 70$  deg

Fig. 7 Flow visualization of pathlines produced by helium-filled soap bubbles with wall expansion angle  $\alpha = 90$  deg for various vane swirl angles  $\phi$ :

recirculation region, as seen in the 45 deg swirl angle case. Further increases in swirl vane angle result in continued enlargement of the center zone. Similarly, the corner recirculation zone is gradually reduced in axial extent until it disappears by  $\phi = 70$  deg [see Part (c) of the figure].

The same series of streamline patterns is displayed in Fig. 6 for the 45 deg expansion geometry. The same trend is found as the vane angle is increased, except that in this case the center recirculation zone is generally slightly smaller in both directions. The corner zone is similar in size for nonswirling conditions, but vanishes as swirl strength is increased. Compare, for example, the corresponding Part (b) of Figs. 5 and 6. The combustor designer may obtain further insight by observing a similar series of streamline plots predicted by Novick et al. [23] for an isothermal dump combustor flowfield with the following differences: a 90 deg expansion, an inlet hub, and a constricted exit.

**Flow Visualization.** An indication of the validity of the computations can be obtained by comparing predicted mean

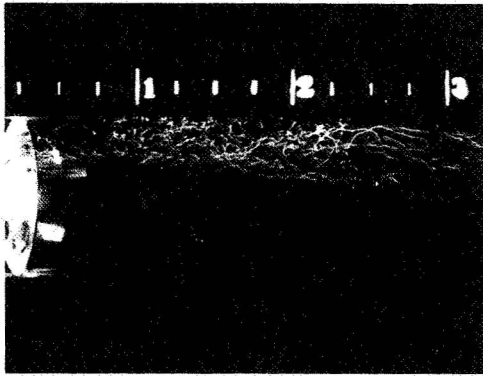


Fig. 8(a)  $\phi = 0$  deg

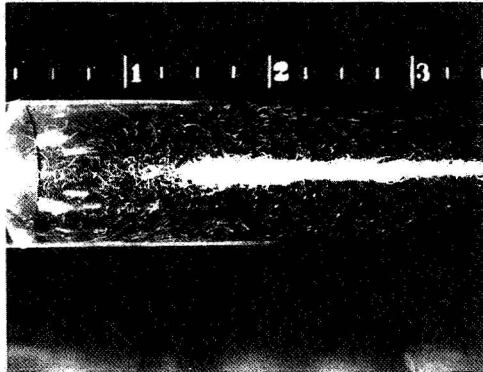


Fig. 8(b)  $\phi = 45$  deg

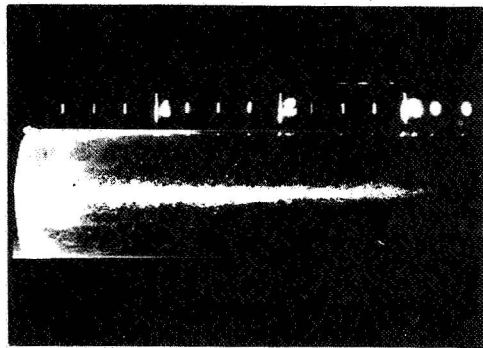


Fig. 8(c)  $\phi = 70$  deg

Fig. 8 Flow visualization of pathlines produced by helium-filled soap bubbles with wall expansion angle  $\alpha = 45$  deg for various vane swirl angles  $\phi$ : (a) 0 deg, (b) 45 deg, and (c) 70 deg

streamline patterns with the pathlines traced out by the soap bubbles in the flow visualization experiments. Generally, a relatively long exposure time of  $1/8$  s is used so as to identify pathlines, and infer streamlines therefrom. A sample flow visualization photograph is presented in Fig. 7(a) corresponding to the zero swirl, 90 deg expansion angle flowfield. The photograph, with the flow from left to right, clearly shows a great number of individual pathlines. Photographs of this type can be used to distinguish regions of highly turbulent flow from smoother regions (for example near the centerline of the flowfield) which have smoother, straighter pathlines. In addition, the outline of the corner recirculation region can be estimated from Fig. 7(a) (and numerous additional photographs taken at the identical run condition). For this geometry the mean stagnation point defining the end of the recirculation zone appears to be at about 2 chamber diameters (8 step heights) downstream of the

sudden enlargement. Examination of Fig. 5(a) shows that this is in quite good agreement with the numerical prediction.

A photograph with  $\phi = 45$  deg is shown in Fig. 7(b), where a precessing vortex core, PVC, is clearly seen extending from  $x/D = 1.25$  to the exit, although its upstream starting location fluctuates from about  $x/D = 1.0$  to 1.5. The PVC is a well-known phenomenon in strongly swirling confined flows, consisting of a central core in the flowfield which exhibits a three-dimensional time-dependent instability. Oscillation is at low frequency [4-6]. A corner recirculation zone is faintly visible in Fig. 7(b), and it seems to extend to about  $x/D = 0.4$ . At stronger swirl  $\phi = 70$  deg, the PVC is even thicker and extends further upstream, merging discretely with the central recirculation zone, see Part (c) of Fig. 7. There is now little evidence of a corner recirculation region. All these effects are in general agreement with the predictions of Figs. 3 and 5.

Figure 8 displays a sequence of photographs corresponding to those of Fig. 7, only now the side-wall angle  $\alpha = 45$  deg. Comparing Parts (a) of the two figures reveals no significant changes, as found in earlier experiments [20], and in the present predictions, there being little predicted effect of the side-wall angle in the range  $\alpha = 90$  to 45 deg on the non-swirling flowfield. The intermediate vane angle case of  $\phi = 45$  deg is visualized in Fig. 8(b), and careful study of this and other photographs is quite revealing. A large concentration of bubbles is seen centered at about  $x/D = 1.5$ , probably corresponding to the location of the time-mean rear stagnation point of the central recirculation zone. The PVC extends from here to the exit. Comparison with Part (b) of Fig. 7 reveals that at  $\phi = 45$  deg the relatively short corner recirculation zone seen with the  $\alpha = 90$  deg geometry does not appear with the  $\alpha = 45$  deg geometry. This is in conformity with the predictions given in Part (b) of Figs. 5 and 6. The  $\phi = 70$  deg flow shown in Fig. 8(c) illustrates no corner recirculation zone as well, with the vortex core being wider and extending even further upstream, again merging almost imperceptibly with the central recirculation zone, as in Fig. 7(c).

The flow visualization photographs in general provide an encouraging base of data for comparison with the computations. Further experimental work is in progress at Oklahoma State University including five-hole pitot probe measurements [24] and single- and multi-wire hot-wire measurements. In all flowfields represented here, the calculation does a reasonable job of predicting the general flow patterns but it is expected that inaccuracies in detail will occur, as has been encountered by others in predicting recirculation zones with the standard  $k-\epsilon$  turbulence model, especially under swirl flow conditions [11, 12]. There are a number of possible reasons for this, but the most likely one is that a turbulence model whose basis and parameters are adequate for simple flow situations is not adequate to handle the more complicated swirling recirculation flow situation.

## Closure

Fundamental theoretical studies are being undertaken on swirling axisymmetric recirculating flows, under low speed and nonreacting conditions. Many factors affect the existence, size and shape of the corner recirculation zone and central toroidal recirculation zone. A major outcome of the current work is the ability to characterize and predict more realistically than previously the existence, size and shape of the corner and central recirculation zones as a function of the angle of the sloping wall, the degree of swirl imparted to the incoming flow, and other swirler and geometric parameters. Computations are made with a suitable computer code which includes several refinements to improve accuracy and economy. A few parameter variations were investigated computationally in order to make combustor design in-

formation available in a directly usable form. Comparison with flow visualization studies reveals that gross features of the flowfield are predicted quite well. A problem in swirling flows is the accuracy with which the details may be predicted. This may be partially attributed to the quality of the turbulence model. Further research should emphasize turbulence model development for swirling recirculating flows.

### Acknowledgment

The authors wish to express their gratitude to NASA Lewis Research Center and Air Force Wright Aeronautical Laboratories for financial support under NASA Grant No. NAG 3-74.

### References

- 1 Gerstein, M. (ed.), "Fundamentals of Gas Turbine Combustion," NASA-CP-2087, 1979, Workshop held at NASA Lewis Research Center, Cleveland, Ohio, Feb. 6-7, 1979.
- 2 Lefebvre, A. H., (ed.), *Gas Turbine Combustion Design Problems*, Hemisphere-McGraw-Hill, New York, 1980.
- 3 Lilley, D. G., "Flowfield Modeling in Practical Combustors: A Review," *Journal of Energy*, Vol. 3, July-Aug. 1979, pp. 193-210.
- 4 Syred, N., and Beér, J. M., "Combustion in Swirling Flows: A Review," *Combustion and Flame*, Vol. 23, 1974, pp. 143-201.
- 5 Lilley, D. G., "Swirl Flows in Combustion: A Review," *AIAA Journal*, Vol. 15, No. 8, Aug. 1977, pp. 1063-1078.
- 6 Gupta, A. K., Lilley, D. G., and Syred, N., *Swirl Flows*, Abacus Press, Tunbridge Wells, England, 1982 (in press).
- 7 Gosman, A. D., and Pun, W. M., "Calculation of Recirculation Flows," Rept. No. HTS/74/2, 1974, Dept. of Mechanical Engineering, Imperial College, London, England.
- 8 Lilley, D. G., and Rhode, D. L., "A Computer Code for Swirling Turbulent Axisymmetric Recirculating Flows in Practical Isothermal Combustor Geometries," NASA CR-3442, Feb. 1982.
- 9 Rhode, D. L., "Predictions and Measurements of Isothermal Flowfields in Axisymmetric Combustor Geometries," Ph.D. thesis, School of Mech. and Aero. Engrg., Okla. State Univ., Stillwater, Okla., 1981.
- 10 Launder, B. E., and Spalding, D. B., "The Numerical Computation of Turbulent Flows," *Comp. Methods in Appl. Mech. and Engrg.*, Vol. 3, Mar. 1974, pp. 269-289.
- 11 Habib, M. A., and Whitelaw, J. H., "Velocity Characteristics of Confined Coaxial Jets With and Without Swirl," ASME Paper No. 79-WA/FE-21, New York, Dec. 2-7, 1979.
- 12 Srinivasan, R., and Mongia, H. C., "Numerical Computations of Swirling Recirculating Flows," Final Report, NASA-CR-165196, Sept. 1980.
- 13 Vu, B. T., and Gouldin, F. C., "Flow Measurement in a Model Swirl Combustor," AIAA Paper No. 80-0076, Jan. 14-16, 1980, Pasadena, Calif.
- 14 Ha Minh, H., and Chassaing, P., "Perturbations of Turbulent Pipe Flow," *Proc. Symposium on Turbulent Shear Flows*, Pennsylvania State University, Apr. 1977, pp. 13.9-13.17.
- 15 Moon, L. F., and Rudinger, G., "Velocity Distribution in an Abruptly Expanding Circular Duct," *ASME JOURNAL OF FLUIDS ENGINEERING*, Mar. 1977, pp. 226-230.
- 16 Phaneuf, J. T., and Netzer, D. W., "Flow Characteristics in Solid Fuel Ramjets," Report No. NPS-57Nt-74081, July 1974, Prepared for the Naval Weapons Center by the Naval Postgraduate School.
- 17 Back, L. H., and Roschke, E. J., "Shear Layer Flow Regimes and Wave Instabilities and Reattachment Lengths Downstream of an Abrupt Circular Channel Expansion," *ASME Journal of Applied Mechanics*, Sept. 1972, pp. 677-781.
- 18 Roschke, E. J., and Back, L. H., "The Influence of Upstream Conditions on Flow Reattachment Lengths Downstream of an Abrupt Circular Channel Expansion," *Journal of Biomech.*, Vol. 9, 1976, pp. 481-483.
- 19 Krall, K. M., and Sparrow, E. M., "Turbulent Heat Transfer in the Separated, Reattached, and Redevelopment Regions of a Circular Tube," *ASME Journal of Heat Transfer*, Feb. 1966, pp. 131-136.
- 20 Chaturvedi, M. C., "Flow Characteristics of Axisymmetric Expansions," *Proceedings Journal Hydraulics Division, ASCE*, Vol. 89, No. HY3, 1963, pp. 61-92.
- 21 Morel, T., "Comprehensive Design of Axisymmetric Wind Tunnel Contractions," ASME Paper 75-FE-17, Minneapolis, Minn., May 5-7, 1975.
- 22 Weske, D. R., and Sturov, G. Ye, "Experimental Study of Turbulent Swirled Flows in a Cylindrical Tube," *Fluid Mechanics - Soviet Research*, Vol. 3, No. 1, Jan.-Feb. 1974, pp. 77-82.
- 23 Novick, A. S., Miles, G. A., and Lilley, D. G., "Numerical Solution of Combustor Flowfields: A Primitive Variable Design Capability," *Journal of Energy*, Vol. 3, No. 2, Mar.-Apr. 1979, pp. 95-105.
- 24 Rhode, D. L., Lilley, D. G., and McLaughlin, D. K., "Mean Flowfields in Axisymmetric Combustor Geometries with Swirl," Paper AIAA 82-0177, Orlando, Fla., Jan. 11-14, 1982.

APPENDIX B

MEAN FLOWFIELDS IN AXISYMMETRIC COMBUSTOR

GEOMETRIES WITH SWIRL

# Mean Flowfields in Axisymmetric Combustor Geometries with Swirl

D.L. Rhode\* and D.G. Lilley†

Oklahoma State University, Stillwater, Oklahoma  
and

D.K. McLaughlin‡

Dynamics Technology, Inc., Torrance, California

A swirling nonreacting flow enters a larger chamber via a sudden or gradual expansion. Six flowfield configurations are investigated with side-wall angles  $\alpha = 90$  and  $45$  deg and swirl vane angles  $\phi = 0, 38,$  and  $45$  deg. Photography of neutrally buoyant helium-filled soap bubbles, tufts, and injected smoke helps to characterize the time-mean streamlines, recirculation zones, and regions of highly turbulent flow. From the photographic evidence, it is found that central recirculation zones occur for the swirling flow cases investigated, after which a relatively narrow precessing vortex core exists near the axis. Five-hole pitot probe pressure measurements allow the determination of time-mean velocities  $u, v,$  and  $w$ . At the inlet, the radial velocity profiles exhibit strong nonuniformity. The time-mean velocity measurements presented here constitute a seriously needed data base for the validation of computer prediction codes and the development of turbulence models for their simulation.

## Nomenclature

$D$	= test section diameter
$d$	= inlet nozzle diameter
$k$	= kinetic energy of turbulence
$p$	= time-mean pressure
$R$	= radius of test chamber
$Re$	= Reynolds number
$u, v, w$	= time-mean velocity (in $x, r, \theta$ direction, respectively)
$V$	= time-mean vector velocity magnitude
$x, r, \theta$	= axial, radial, azimuthal cylindrical polar coordinates, respectively
$\alpha$	= side-wall expansion angle
$\beta$	= yaw angle of flow = $\tan^{-1}(w/u)$
$\delta$	= pitch angle of flow = $\tan^{-1}[v/(u^2 + w^2)^{1/2}]$
$\epsilon$	= turbulence energy dissipation rate
$\rho$	= time-mean density
$\phi$	= swirl vane angle = $\tan^{-1}(w_0/u_0)$

## Subscripts

$d$	= based on inlet nozzle diameter
$p$	= based on probe tip diameter
$0$	= value at inlet to flowfield

## I. Introduction

IN gas turbine and ramjet combustion chamber development, designers are aided by both experimental and theoretical studies.<sup>1</sup> The present research work is concerned with such complementary studies.<sup>2-4</sup> The problem being investigated is concerned with steady turbulent flow in axisymmetric geometries under low speed and nonreacting conditions—a study area which is fundamental to combustor

modeling. The particular problem discussed in this paper is the flow in a round pipe entering an expansion into another round pipe as illustrated in Fig. 1. The incoming flow may possess a swirl component of velocity via passage through swirl vanes at angle  $\phi$  from the axial direction, and the side wall may slope at an angle  $\alpha$ , also from the axial direction. The resulting flowfield domain may possess a central toroidal recirculation zone in the middle of the region on the axis, in addition to the possibility of a corner recirculation zone near the upper corner provoked by the rather sudden enlargement of the cross-sectional area. Of vital importance is the characterization of flows of this type in terms of the effects of side-wall angle  $\alpha$ , degree of swirl  $\phi$ , turbulence intensity of the inlet stream, and expansion ratio  $D/d$  on the resulting flowfield in terms of its time-mean and turbulence quantities. Such problems have received little attention, although they are fundamental to the physical processes occurring in aircraft combustors.

A systematic parametric investigation is being undertaken on the effect of side-wall angle  $\alpha$  and a swirl vane angle  $\phi$  on the resulting flowfield produced. The goals of the ongoing study involve comparison of predictions with experimental turbulent flow measurements so as to assist in evaluating turbulence models and improving the final predictive capability. This paper focuses on the experimental study, with identification of recirculation regions from flow visualization and mean velocity measurements using a five-hole pitot probe, thus providing a useful data base for the later turbulence model development aspects of the study.

## II. Experimental Approach

### A. Previous Studies

There have been several experiments performed with nonreacting flows in expansion geometries that have been reported in the literature, examples of which are contained in Refs. 5,8. References 5-7 also include flowfield predictions, made with versions of the TEACH-T computer program.<sup>9</sup> These experiments include time-mean velocity measurements (with hot-wire and pitot probes and laser Doppler anemometry), turbulence measurements (with hot-wires and laser anemometers) and flow visualization. The majority of the earlier measurements were made in nonswirling flows; however, some noteworthy experiments have been made in swirling confined jets.<sup>5,8</sup> Direct comparison between the results of the cited experiments and the present experimental

Presented as Paper 82-0177 at the AIAA 20th Aerospace Sciences Meeting, Orlando, Fla., Jan. 11-14, 1982; submitted Jan. 22, 1982; revision received June 21, 1982. Copyright © American Institute of Aeronautics and Astronautics, Inc., 1982. All rights reserved.

\*Graduate Student, School of Mechanical and Aerospace Engineering. At present: Assistant Professor, Department of Mechanical Engineering, Texas A&M University, College Station, Texas.

†Professor, School of Mechanical and Aerospace Engineering. Associate Fellow AIAA.

‡Group Manager. Member AIAA.



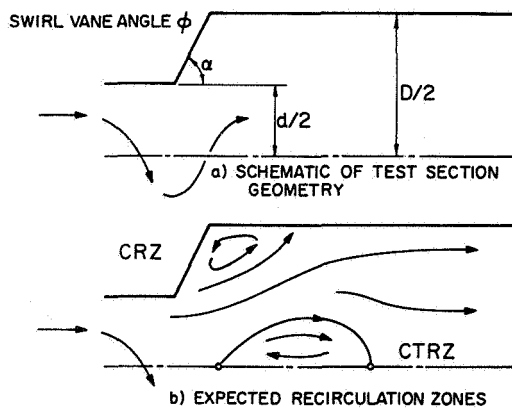


Fig. 1 Schematic of flowfield.

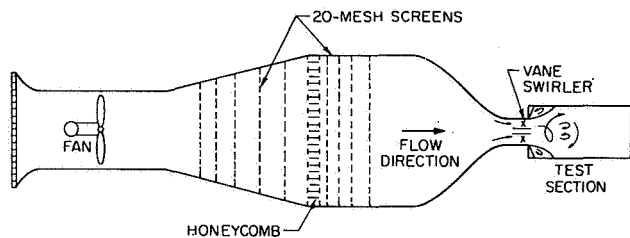


Fig. 2 Schematic of overall flow facility.

results is generally not possible because of differences in geometry. However, in the nonswirling jet, comparisons were possible with experiments of Chaturvedi,<sup>8</sup> who measured time-mean and turbulent flow quantities downstream of a sudden expansion of diameter ratio  $D/d=2$  and various expansion side-wall angles  $\alpha$ .

### B. Test Facility

The present experiments have been conducted in the confined jet facility shown schematically in Fig. 2. The facility has an axial flow fan whose speed can be changed by altering the varidrive mechanism. Numerous fine screens and straws produce flow in the settling chamber of relatively low turbulence intensity. The contraction section leading to the test section has been designed by the method of Morel<sup>10</sup> to produce a minimum adverse pressure gradient on the boundary layer and thus avoid unsteady problems associated with local separation regions.

The test section consists of a swirl vane assembly and an idealized combustion chamber model. The swirl vane assembly contains ten vanes which are individually adjustable for any vane angle  $\phi$ . The pitch/chord ratio of 1 provides good turning efficiency. The hub is located at the center of the swirler with a streamlined nose facing upstream. The downstream end is simply a flat face, simulating the geometric shape of a typical fuel spray nozzle.

The idealized combustion chamber model is composed of an expansion block and a long plexiglass tube. The expansion block is a 30-cm-diam disk with a 15-cm-diam hole centered on its axis through which the air entering the model flows smoothly. The downstream face of the expansion block has been shaped to provide the desired flow expansion angle  $\alpha$  which is shown in Fig. 1. There are currently three interchangeable expansion blocks and the appropriate choice gives  $\alpha=90, 70,$  or  $45$  deg.

There are no film-cooling holes or dilution-air holes in the test facility, and the chamber wall consists of a straight pipe. The inside diameter of the pipe is 30 cm and the length is approximately 125 cm. The substantial size of the test model provides excellent resolution for five-hole pitot probe measurements and flow visualization photography.

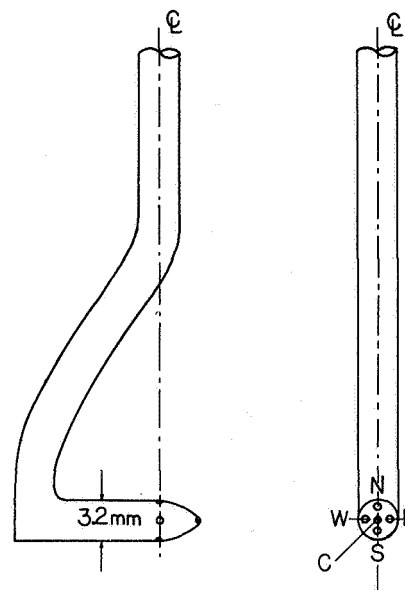


Fig. 3 Five-hole pitot probe.

### C. Flow Visualization Techniques

A slide projector, located downstream of the test facility, served as the light source. A vertical sheet of light 4 cm thick was produced to illuminate the  $rx$  plane of the flow pattern. This was provided by using a slide which is opaque except for a thin slit cut out for light passage to the test section. Tri-X Pan, a very light-sensitive photographic film rated at ASA 400, along with a large camera aperture of  $f 2.0$ , was employed in order to obtain photographs of acceptable contrast. Moreover, the film was substantially overdeveloped to compensate for underexposure; this is equivalent to using an extremely light-sensitive film rated at approximately ASA 6000. Photographs of the bubble streaklines were typically taken at shutter speeds ranging from  $1/60$  to  $1/4$  s. Rhode<sup>4</sup> describes at length the flow visualization studies. Three different techniques are used, including neutrally buoyant helium-filled soap bubbles<sup>11</sup> using a Sage Action, Inc., bubble generator,<sup>12</sup> smoke-wire,<sup>13-15</sup> and tufts.<sup>16,17</sup>

### D. Mean Velocity Measurement

Many instruments are used for separately measuring the magnitude and direction of fluid velocity.<sup>18</sup> However, there are only a few instruments capable of simultaneously sensing both magnitude and direction. One of the simplest of these is the five-hole pitot probe which has been developed and used by various investigators.<sup>19-22</sup> The particular probe employed in this study is model DC-125-12-CD from United Sensor and Control Corp. It is shown schematically in Fig. 3 and has a 3.2-mm-diam sensing tip and shaft containing five tubes. The sensing head is hook-shaped to allow probe shaft rotation without altering the probe tip location.

The instrumentation system, in addition to the five-hole pitot probe, consists of a manual traverse mechanism, two five-way ball valves, a very sensitive pressure transducer, a power supply, and an integrating voltmeter. The differential pressure transducer is model 590D from Datametrics, Inc. The output is read as the dc signal from a TSI model 1076 integrating voltmeter.

Prior to production measurements, the five-hole pitot probe is aerodynamically zeroed for yaw, which is in the horizontal plane of Fig. 4, so that  $x$  and  $\theta$  axes of the measurement coordinate frame coincide with those of the test section. The measurement procedure for each location within a traverse begins with aerodynamically nulling the yaw, and determining the yaw angle  $\beta$ . This is indicated by a zero reading for  $p_w - p_E$ , where the pressures are identified in Fig.



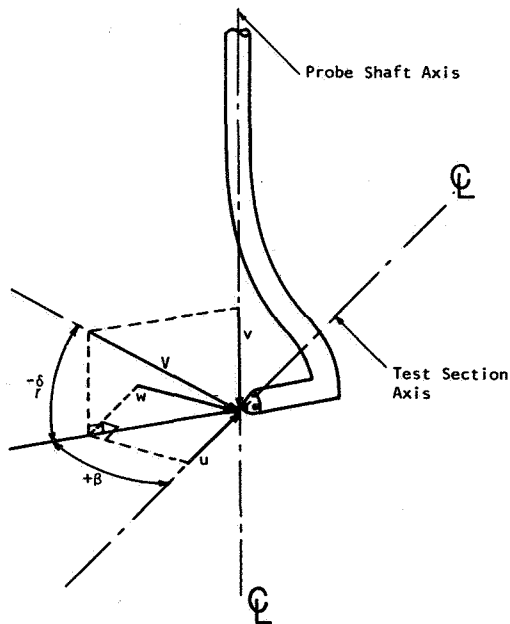


Fig. 4 Velocity components and flow direction angles associated with five-hole pitot measurements (yaw angle  $\beta$  in the horizontal plane and pitch angle  $\delta$  in the vertical plane).

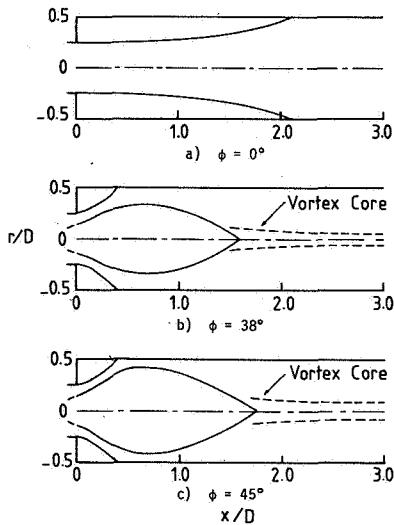


Fig. 5 Artistic impressions of dividing streamlines with wall expansion angle  $\alpha = 90$  deg for swirl vane angles.

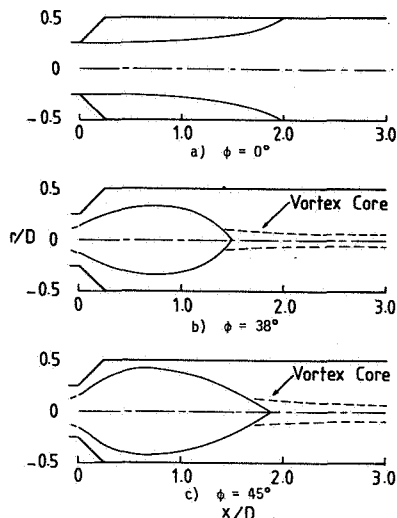


Fig. 6 Artistic impressions of dividing streamlines with wall expansion angle  $\alpha = 45$  deg for swirl vane angles.

3. Then the five-way switching valves are set so that  $p_N - p_S$  is sensed by the transducer. Finally, the reading of  $p_C - p_W$  is similarly obtained.

The data reduction employs two calibration curves which were obtained from a single calibration velocity. The underlying principle is that the calibration is independent of probe Reynolds number  $Re_p$  based on probe tip diameter. Careful calibration experiments reveal that this condition exists for  $Re_p \geq 1090$  corresponding to a local velocity of 5.4 m/s. Hence measurements of such low velocities suffer from a necessary calibration error. However, this error affects the velocity measurements typically by less than 6% for  $Re_p \geq 400$ , corresponding to a local velocity greater than 2 m/s.

The data at each measurement location are reduced using a computer program by first calculating the pitch coefficient  $(p_N - p_S)/(p_C - p_W)$ . From these values an interpolation technique is used to obtain the pitch angle  $\delta$  in the vertical plane from the appropriate calibration characteristic. The resulting value of  $\delta$  is utilized to determine the velocity coefficient  $\rho V^2/[2(p_C - p_W)]$  using the corresponding calibration characteristic.

Values for  $V$  as well as the axial, radial, and swirl velocity components  $u$ ,  $v$ , and  $w$ , shown in Fig. 4, are calculated from the velocity coefficient, pitch angle  $\delta$ , and yaw angle  $\beta$ , which is in the horizontal plane. The magnitude of the velocity vector is given by

$$V = \left[ \frac{2}{\rho} \frac{\rho V^2}{2(p_C - p_W)} (p_C - p_W) \right]^{1/2}$$

and the velocity components are obtained from this magnitude and the pitch and yaw angles.

Elsewhere, Rhode<sup>4</sup> describes the five-hole pitot probe calibration procedure, which is extremely critical to the accuracy of the results, and discusses reliability, since turbulence effects on pressure probes are not well known.<sup>23</sup> A 5% accuracy is expected for most of the measurements, increasing to 10% in regions of low velocity below approximately 2 m/s because of probe insensitivity to low dynamic pressure. It is further asserted that measurements made at flow Reynolds numbers  $Re_d$  (based on inlet pipe diameter) equal to  $1.05 \times 10^5$  and  $7.8 \times 10^4$  for the non-swirling and swirling flows, respectively, are in the Reynolds number invariant regime.

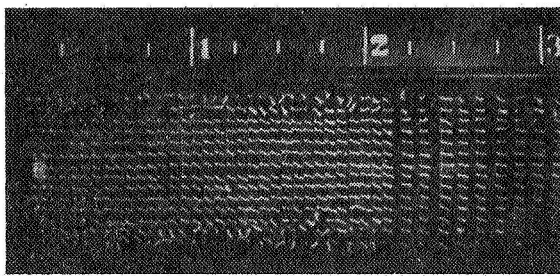
### III. Flow Visualization

Recirculation zones are important to combustor designers. The size and location of these regions in the present isothermal flows are deduced from flow visualization photographs of tufts, smoke, and bubbles responding to the experimental flowfield patterns. Resulting dividing streamline sketches as well as selected photographs of the visualization experiments are now presented and discussed.

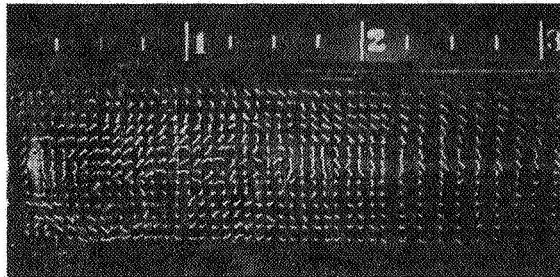
#### A. Artistic Impressions of Streamline Patterns

Photographs of each of the six flowfields resulting from  $\phi = 0, 38,$  and  $45$  deg with  $\alpha = 90$  and  $45$  deg have been examined in detail for each of the three flow visualization methods currently employed. The characteristics of the overall flowfield are illustrated and discussed via the resulting time-mean dividing streamline patterns. These are sketched in Figs. 5 and 6 from information obtained from the entire collection of flow visualization photographs. Results from the smoke-wire experiment are utilized near the inlet, whereas tuft and bubble data are used in approximating the size and shape of the recirculation zones downstream. Also, bubble flow patterns reveal the existence of a precessing vortex core, which occurs downstream of the central region.

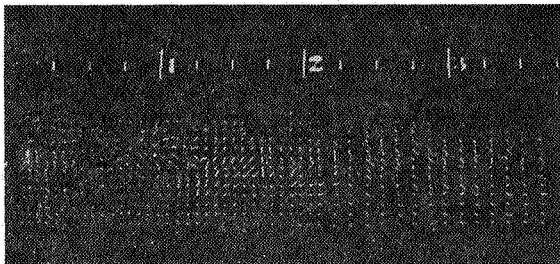
The resulting streamlines for the three swirl cases of the sudden expansion  $\alpha = 90$ -deg geometry are shown in Fig. 5.



a)  $\phi = 0$  deg.



b)  $\phi = 38$  deg.

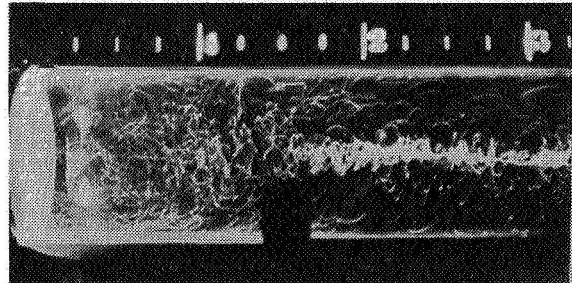


c)  $\phi = 45$  deg.

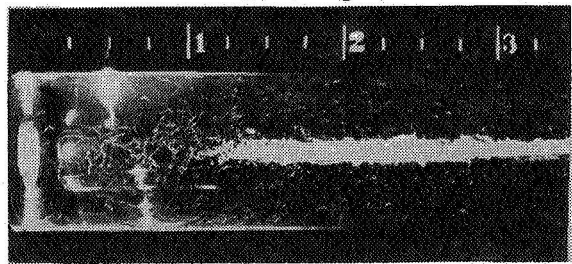
Fig. 7 Flow visualization photographs of tufts in the  $rx$  plane with wall expansion angle  $\alpha = 90$  deg for swirl vane angles.



a)  $\phi = 0$  deg.



b)  $\phi = 38$  deg.

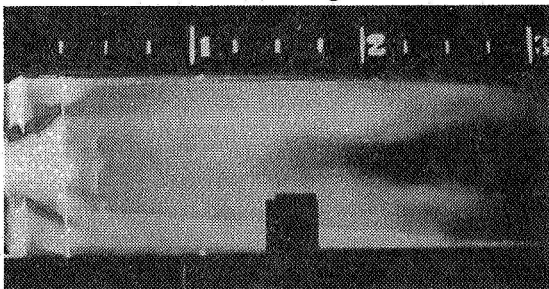


c)  $\phi = 45$  deg.

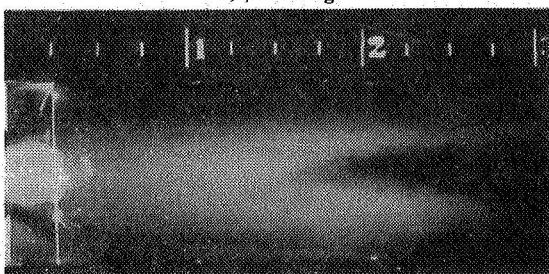
Fig. 9 Flow visualization photographs of pathlines indicated by illuminated neutrally buoyant soap bubbles for wall expansion angle  $\alpha = 90$  deg and swirl vane angles.



a)  $\phi = 0$  deg.



b)  $\phi = 38$  deg.



c)  $\phi = 45$  deg.

Fig. 8 Flow visualization photographs of smoke-wire streaklines with wall expansion angle  $\alpha = 90$  deg for swirl vane angles.

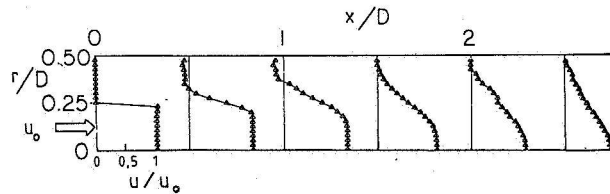


Fig. 10 Measured velocity profiles for wall expansion angle  $\phi = 90$  deg and swirl vane angle  $\phi = 0$  deg.

The nonswirling flow sketch in Fig. 5a exhibits a large corner recirculation zone which is in excellent agreement with the corresponding streamlines from the measurements of Chaturvedi.<sup>8</sup> Appropriate prior measurements for the present swirling flows have not been found. For the moderate swirl vane angle case of  $\phi = 38$  deg a central recirculation region appears in conjunction with a decrease in size of the corner zone. A thin precessing vortex core, discussed at length by Syred and Beer,<sup>24</sup> is observed near the centerline extending from the end of the central region to the test section exit. The axial location where the vortex core begins fluctuates, ranging approximately from  $x/D = 1.25$  to  $1.75$ . This vortex core is essentially a three-dimensional time-dependent phenomenon, which occurs as a swirling region of negligible axial velocity whose center winds around the test section centerline. A further increase in vane angle to  $\phi = 45$  deg results in slight enlargement of the central zone; however, the corner bubble is essentially unaffected. For this flowfield the vortex core is slightly expanded in the radial direction.

The corresponding sequence of dividing streamlines is found in Fig. 6 for the gradual flow expansion case with  $\alpha = 45$  deg. As with Fig. 5, the nonswirling flowfield exhibits excellent agreement with corresponding measurements of

Chaturvedi.<sup>8</sup> No evidence of a corner zone is found from examination of the entire photograph collection for the intermediate vane angle case, although the flow pattern is otherwise very similar to the corresponding flow for  $\alpha=90$  deg. The flowfield with  $\phi=45$  deg produces exactly the same effects as in the abrupt expansion case of Fig. 5.

## B. Flow Visualization

Tuft visualization is very important in that it supplies an overall view of local flow direction. As discussed in Sec. II.C, photographs at various shutter speeds were obtained. Slower speeds show more of the temporal behavior, although the tufts are sometimes not distinctly visible in portions of the flowfield. Some of the more noteworthy photographs are presented here, encompassing a range of shutter speeds. Velocities in recirculation zones are often somewhat lower than in other portions of the flowfield, and thus under such conditions there may be insufficient drag on a tuft to align it accurately with the local flow direction. However, this is taken into consideration in interpreting the photographed results.

The three flowfields for  $\alpha=90$  deg are characterized in Fig. 7 as photographs of the  $rx$ -screen tufts. Figure 7a identifies the corner zone reattachment point for the nonswirling flowfield. It is found to be approximately at  $x/D=2.0$ , wherein tufts showing no air motion are considered stagnation points. Further, an indication of the turbulence level is depicted as the rather slow shutter speed of 1/15 s was used.

For swirl vane angle  $\phi=38$  deg, Fig. 7b is a photograph taken at 1/60 s. The swirl is in the counterclockwise direction when viewed from downstream. There is no evidence of a corner zone and the central region apparently extends to  $x/D=1.5$ . Finally, the  $\phi=45$  deg case shown in Fig. 7c exhibits a central region extending downstream as far as approximately  $x/D=1.85$  for 1/125-s shutter speed.

Local details in the nonswirling flowfields are clearly revealed through the visualization of streaklines indicated from the generation of illuminated smoke. In the swirling flow cases, strong mixing diffuses the smoke so that streaklines are not distinguishable. However, under such conditions recirculation zone outlines are visible, especially in the region near the smoke-generation wire. A selected photograph is exhibited and discussed for each of the three abrupt expansion flowfields.

The corner recirculation bubble in the nonswirling case with wall expansion angle  $\alpha=90$  deg is revealed in Fig. 8a using 1/30-s shutter speed. Also, the radial location of the zero velocity point within the upper and lower corner bubble is estimated to be approximately  $0.15D$  from the respective walls of the test facility. This agrees with the velocity measurements presented later in Sec. IV.

The moderate swirl vane angle flow with a 1/30-s exposure is shown in Fig. 8b. The shortened corner zone is easily identified because the adjacent flow contains no smoke near the inlet. This bubble is seen to extend to approximately  $x/D=0.45$ . The tuft photographs for this case indicate a slightly shorter zone ending at approximately  $x/D=0.4$ . The upstream portion of the central zone is also clearly seen, as low velocity fluid carries a dense mass of smoke which slowly moves upstream of the inlet. Further, the precessing vortex core is seen to contain only slight smoke. Since the core exhibits negligible axial velocity, the smoke is essentially carried around it by the high velocity fluid outside the core.

Figure 8c is a photograph at 1/8-s of the  $\phi=45$  deg case wherein this core is not as distinct. In this case, some smoke has diffused into the core due to a slightly longer delay before activating the camera shutter. Observe that both the corner and central zones near the inlet reveal that the only change from those for  $\phi=38$  deg is a slightly wider central region.

Soap bubbles injected into the flow upstream of the test section trace pathlines clearly when illuminated. In relatively

lower turbulence intensity portions of the flowfield mean-flow directions can be obtained by ensemble averaging local tangents to pathlines traced out by soap bubbles. This helps define the flowfield geometry in terms of the outline of recirculation regions.

A sample flow visualization photograph is presented in Fig. 9a corresponding to the zero swirl, 90-deg expansion angle flowfield. The photograph, taken with a relatively long time exposure (1/8-s), clearly shows a great number of individual pathlines. Photographs of this type can be used to indicate regions of weakly turbulent flow such as that near the centerline of the flowfield which exhibits relatively straight pathlines. In addition, the outline of the corner recirculation region can be estimated from Fig. 9a (and numerous additional photographs taken at the identical run condition). For this geometry the mean stagnation point defining the end of the recirculation zone appears to be at  $x/D=2.0$ .

A photograph with  $\phi=38$  deg and 1/8-s shutter speed is shown in Fig. 9b, where the precessing vortex core is clearly seen extending from  $x/D=1.5$  to the exit. Its upstream extent fluctuates randomly from approximately  $x/D=1.25$  to 1.75. The corner bubble is observed in both the upper and lower portions of the flowfield, extending to approximately  $x/D=0.4$ , which agrees almost exactly with the smoke flow pattern for this flowfield in Fig. 8b. A photograph using 1/8-s shutter speed is presented in Fig. 9c for the  $\phi=45$  deg flowfield where a thicker vortex core is seen. The corner zone is faintly visible here, and its axial length also seems to extend to about  $x/D=0.4$ .

## C. Parametric Effects

Streamline plots allow recirculation zones to be characterized parametrically for the effects of  $\alpha$  and  $\phi$  on the corner and central recirculation zone lengths. Several observations should be noted. First, zone lengths are only slightly affected by  $\alpha$ , as found previously for the corner bubble under isothermal nonswirling conditions.<sup>8,25</sup> Note that, at these high Reynolds numbers, the corner region length is independent of Reynolds number.<sup>26,27</sup> Second, as side-wall angle  $\alpha$  decreases from 90 to 45 deg, the zone lengths typically decrease slightly and the inlet flow is encouraged to impinge on the confining walls. Third, the corner recirculation length decreases upon increasing the swirl vane angle  $\phi$  from 0 to 38 deg, a parameter change which also provokes the existence of a central recirculation bubble and precessing vortex core. Increasing the vane angle further only slightly enlarges the central zone and the vortex core.

## IV. Velocity Measurements

### A. Sudden Expansion, $\alpha=90$ deg

Figures 10-12 show the axial and swirl time-mean velocity profiles, for swirl vane angles  $\phi=0, 38,$  and 45 deg with a sudden expansion (side-wall angle  $\alpha=90$  deg). Measurements are obtained with the five-hole pitot probe in the manner discussed in Sec. II.D. Note that in these and subsequent figures, different scales are used for the normalized axial and swirl velocities. Radial velocities are consistently much smaller than the axial and swirl components, and they may be inferred from the dividing streamline patterns deduced from flow visualization experiments depicted in Figs. 5 and 6. They need not be presented here. Figure 10 shows the corner recirculation region for the nonswirling flow on the verge of reattachment near  $x/D=2.0$ . The corresponding visualization results shown in Fig. 5a give this location as  $x/D=2.1$  and the corresponding measurements of Chaturvedi<sup>8</sup> give a value of  $x/D=2.3$ .

In the absence of pertinent measurements, previous predictions of gas turbine combustor flowfields<sup>2,3,28,29</sup> employed an approximation for inlet velocity boundary conditions. It has generally been assumed that  $v=0$  and that both  $u$  and  $w$  exhibit flat velocity profiles. However, the present



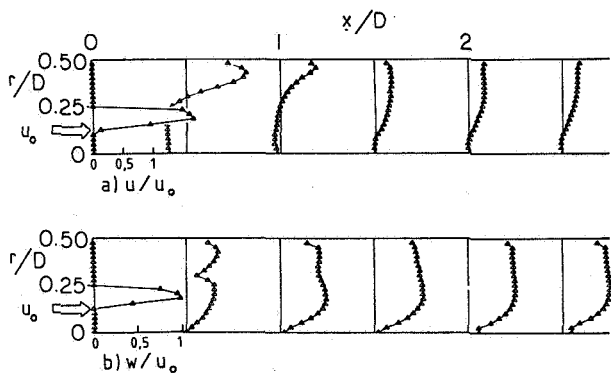


Fig. 11 Measured velocity profiles for wall expansion angle  $\alpha = 90$  deg and swirl vane angle  $\phi = 38$  deg.

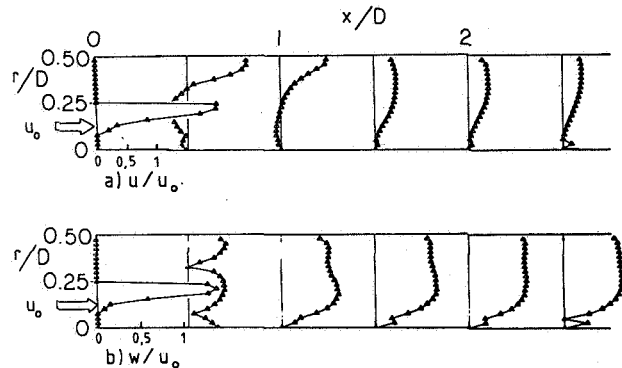


Fig. 12 Measured velocity profiles for wall expansion angle  $\alpha = 90$  deg and swirl vane angle  $\phi = 45$  deg.

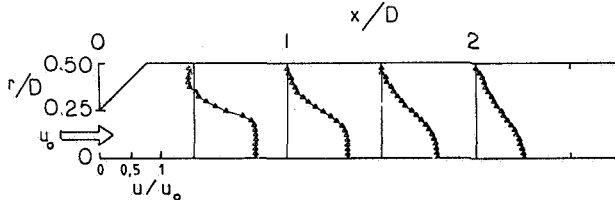


Fig. 13 Measured velocity profiles for wall expansion angle  $\alpha = 45$  deg and swirl vane angle  $\phi = 0$  deg.

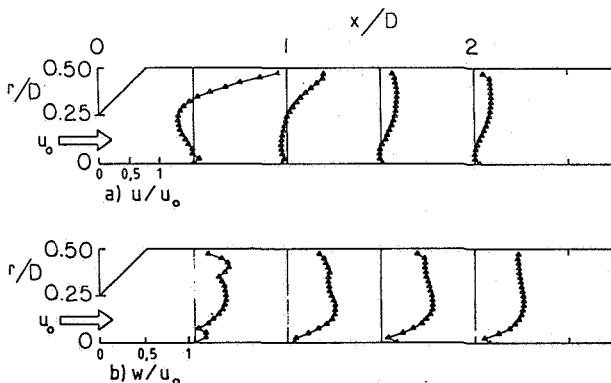


Fig. 14 Measured velocity profiles for wall expansion angle  $\alpha = 45$  deg and swirl vane angle  $\phi = 38$  deg.

measurements, taken 4 cm downstream of the vane swirler, indicate that this is an unrealistic estimate, with sharply peaked  $u$  and  $w$  profiles, as shown in Figs. 11 and 12. The difference results from the use of a swirler with ten flat blades with pitch/chord ratio of unity, imperfect blade efficiency, the existence of a hub, and the fact that the downstream edge of swirl vanes of the test facility is actually located ap-

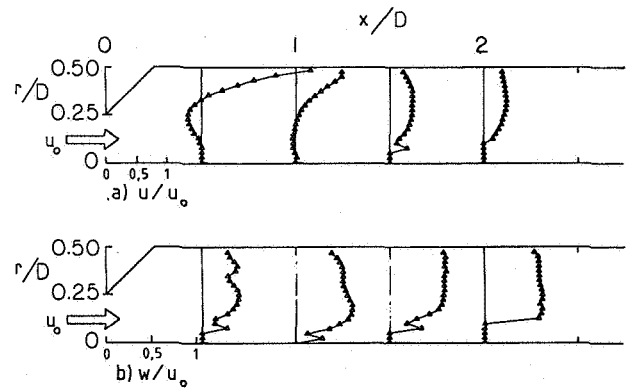


Fig. 15 Measured velocity profiles for wall expansion angle  $\alpha = 45$  deg and swirl vane angle  $\phi = 45$  deg.

proximately 4 cm upstream of the flow expansion corner, where  $x/D = 0$ . This swirler location allows the central recirculation zone to begin upstream of  $x/D = 0$ , thereby changing the velocity profiles there.

Figure 11 also reveals that a 38-deg swirl vane angle produces a maximum swirl flow angle  $[\tan^{-1}(w_0/u_0)]$  of 30 deg at the test chamber inlet. The maximum swirl flow angle for the 45-deg vane angle case shown in Fig. 12 is 34 deg. Thus there is only a slight increase of swirl flow angle, although these two flows are different in that the inlet profiles are considerably more sharply peaked for the latter case. Figures 11 and 12 show zero  $u$  and  $w$  velocity values near the axis at the inlet, but actually the probe was insensitive to the very low velocities there. This is consistent with earlier flow visualization results that the central bubble extends upstream of the inlet. The measurements shown in Fig. 11a provide no evidence regarding the existence of a corner zone. This is expected because flow visualization reveals that the region only extends to  $x/D = 0.4$ . However, there is clear evidence of a rather large central zone whose length is similar to that shown in Fig. 5b. Although the axial velocity profiles are beginning to flatten in the downstream direction, they retain a zero velocity value on the axis, which is consistent with soap bubble flow patterns as seen in Fig. 9b. The early erratic behavior shown by the swirl velocity profiles in Fig. 11b quickly transforms, exhibiting a solid-body-rotation core with a rather flat profile outside this region.

Figure 12 also reveals the discrepancy regarding inlet velocity profiles, this time for the case  $\phi = 45$  deg. The large central recirculation region causes the downstream flow to be accelerated near the top wall. The corresponding swirl velocity component at the  $x/D = 0.5$  axial station typically shows local minima where the mean axial velocity is zero. The accuracy of the velocity measurements at these locations is poor, as discussed in Sec. II.D, so that any physical interpretation here is suspect. Again, the early erratic behavior found in the swirl velocity profile at  $x/D = 0.5$  quickly develops into a shape similar to that seen in Fig. 11b. The precessing vortex core motion discussed in Sec. II.B results in poor measurement repeatability which promotes the irregular behavior within this core region.

#### B. Gradual Expansion, $\alpha = 45$ deg

Figures 13-15 exhibit velocities for the same sequence of flowfields with side-wall angle  $\alpha = 45$  deg. The inlet profiles were not measured in this geometry because the presence of the expansion block interferes with probe positioning. Effects of swirl vane angle  $\phi$  on velocities, similar to those found for the sudden expansion cases, are found in the flowfield sequence for this test section geometry. The major difference is that the sloping wall encourages the inlet flow to accelerate near the top wall. Also, it tends to shorten or obliterate the corner recirculation region.

### C. Comparison of Measurements and Predictions

Flowfield computations have been made<sup>2-4</sup> for a variety of side-wall and swirl vane angles, using the standard  $k-\epsilon$  turbulence model and the technique discussed at length elsewhere.<sup>30</sup> These and other earlier predictions have generally idealized the inlet flow as a plug-flow axial velocity profile with a flat or solid body rotation swirl velocity profile. Though this may be adequate for those applications, it is clearly inadequate for the present study, in which the inlet flow conditions are highly nonuniform. Current work is proceeding with inlet profile effects and turbulence model developments. In this connection, it may be noted that a turbulence model whose basis and parameters are adequate for simple flow situations is not adequate to handle the more complicated swirling recirculating flow situation. Nevertheless, good predictions are available<sup>4</sup> for the case of a less difficult test problem (coswirl and counterswirl flow in a pipe using the data of Ref. 31). This turbulence simulation problem in complex flowfields is clearly an area of current research interest.

### V. Summary

A major outcome of the current study is the experimental characterization of corner and central recirculation zones in six basic flowfield configurations of an axisymmetric expansion with side-wall angle  $\alpha = 90$  and 45 deg and swirl vane angle  $\phi = 0, 38, \text{ and } 45$  deg. The size and shape of the recirculation bubbles for each flowfield is illustrated via an artistic impression deduced from a collection of flow visualization photographs of tufts, smoke, and neutrally buoyant soap bubbles responding to the flow. Increasing swirl vane angle  $\phi$  from 0 to 38 deg produces a shortened corner region and the appearance of a central bubble typically extending downstream to approximately  $x/D = 1.7$ , after which a precessing vortex core exists near the axis reaching to the exit of the test section. A further increase in  $\phi$  to 45 deg enlarges the central zone and vortex core with negligible effect on the corner region in those flowfields where it occurs. The effect of side-wall angle  $\alpha$  on the nonswirling flows is negligible. However, a decrease from 90 to 45 deg apparently eliminates the corner bubble in the swirling flow cases investigated. This decrease in  $\alpha$  also causes the inlet flow to impinge more severely on the top wall, where larger axial velocities occur.

A more detailed experiment consists of the measurement of time-mean velocity components in the axial, radial, and azimuthal directions using a five-hole pitot probe. These measurements generally agree with the flow visualization results and provide a more complete understanding of each flowfield. At the inlet, the axial and swirl velocity profiles exhibit maximum values at approximately  $r/D = 0.2$  in a sharply peaked annular fashion. This nonuniformity arises for several reasons: the use of a ten-blade swirler with pitch/chord ratio of 1, blade inefficiency, the presence of a hub, and the fact that the swirl vane exit station is typically located upstream of the expansion station. This allows the central recirculation zone to begin upstream of the expansion where  $x/D = 0$ .

Clearly, the time-mean velocity measurements presented here contribute to a seriously needed data base for the validation of computer prediction codes and the development of turbulence models for the simulation of complex turbulent swirling flows.

### Acknowledgments

The authors wish to express their sincere gratitude to NASA Lewis Research Center and Air Force Wright Aeronautical Laboratories for support under Grant NAG 3-74.

### References

<sup>1</sup>Lefebvre, A.H., ed., *Gas Turbine Combustor Design Problems*, Hemisphere-McGraw-Hill, New York, 1980.

<sup>2</sup>Rhode, D.L., Lilley, D.G., and McLaughlin, D.K., "On the Prediction of Swirling Flowfields Found in Axisymmetric Combustor Geometries," *Proceedings of ASME Symposium on Fluid Mechanics of Combustion Systems*, Boulder, Colo., June 1981, pp. 257-266; see also *Journal of Fluids Engineering*, Vol. 104, Sept. 1982, pp. 378-384.

<sup>3</sup>Lilley, D.G., Rhode, D.L., and Samples, J.W., "Prediction of Swirling Reacting Flow in Ramjet Combustors," AIAA Paper 81-1485, July 1981.

<sup>4</sup>Rhode, D.L., *Predictions and Measurements of Isothermal Flowfields in Axisymmetric Combustor Geometries*, Ph.D. Thesis, Oklahoma State Univ., Stillwater, Okla., Dec. 1981.

<sup>5</sup>Hajib, M.A. and Whitelaw, J.H., "Velocity Characteristics of Confined Coaxial Jets With and Without Swirl," ASME Paper 79-WA/FE-21, Dec. 1979.

<sup>6</sup>Srinivasan, R. and Mongia, H.C., "Numerical Computations of Swirling Recirculating Flows," Final Report, NASA-CR-165196, Sept. 1980.

<sup>7</sup>Sturgess, G.J., Syed, S.A., and Sepulveda, D., "Application of Numerical Modeling to Gas Turbine Combustor Development Problems," *Proceedings of ASME Symposium on Fluid Mechanics of Combustion Systems*, Boulder, Colo., June 1981, pp. 241-250.

<sup>8</sup>Chaturvedi, M.C., "Flow Characteristics of Axisymmetric Expansions," *Proceedings of the Journal of Hydraulics Division*, ASCE, Vol. 89, HY3, 1963, pp. 61-92.

<sup>9</sup>Gosman, A.D., and Pun, W.M., "Calculation of Recirculating Flows," Report HTS/74/2, Dept. of Mechanical Engineering, Imperial College, London, England, 1974.

<sup>10</sup>Morel, T., "Comprehensive Design of Axisymmetric Wind Tunnel Contractions," ASME Paper 75-FE-17, Minneapolis, Minn. May 1975.

<sup>11</sup>Owen, F.S., Hale, R.W., Johnson, B.V., and Travers, A., "Experimental Investigation of Characteristics of Confined Jet-Driven Vortex Flows," United Aircraft Research Laboratories, East Hartford, Conn., Rept. R-2494-2, Nov. 1961.

<sup>12</sup>Hale, R.W., Tan, P., Stowell, R.C. and Ordway, D.E., "Development of an Integrated System for Flow Visualization in Air Using Neutrally-Buoyant Bubbles," Sage Action, Inc., Ithaca, N.Y., for ONR, Rept. SAI-RR 7107, Dec. 1971.

<sup>13</sup>Corke, T., Koga, D., Drubka, R., and Nagib, H., "A New Technique for Introducing Controlled Sheets of Smoke Streaklines in Wind Tunnels," *Proceedings of International Congress on Instrumentation in Aerospace Simulation Facilities*, IEEE Publ. 77 CH 1251-8 AES, 1974, p. 74.

<sup>14</sup>Nagib, H.M., "Visualization of Turbulent and Complex Flows Using Controlled Sheets of Smoke Streaklines," *Proceedings of International Symposium on Flow Visualization*, Tokyo, Oct. 1977, pp. 181-186; see also Supplement, pp. 29-1 to 29-7.

<sup>15</sup>Cornell, D., "Smoke Generation for Flow Visualization," Aerophysics Research Report 54, Mississippi State Univ., University, Miss., Nov. 1964.

<sup>16</sup>Bird, J.D., "Visualization of Flowfields by Use of a Tuft Grid Technique," *Journal of the Aeronautical Sciences*, Vol. 19, 1952, pp. 481-485.

<sup>17</sup>McMahon, H.M., Hester, D.D., and Palfery, J.G., "Vortex Shedding From a Turbulent Jet in a Cross-Wind," *Journal of Fluid Mechanics*, Vol. 48, 1971, pp. 73-80.

<sup>18</sup>Breyer, D.W. and Pankhurst, R.C., "Pressure-Probe Methods for Determining Wind Speed and Flow Direction," Her Majesty's Stationery Office, London, England, 1971.

<sup>19</sup>Hiatt, G.F. and Powell, G.E., "Three-Dimensional Probe for Investigation of Flow Patterns," *The Engineer*, Vol. 213, Jan. 1962, pp. 165-170.

<sup>20</sup>Pien, P.C., "The Five-Hole Spherical Pitot Tube," David Taylor Model Basin Report 1229, May 1958.

<sup>21</sup>Lee, J.C. and Ash, J.B., "A Three-Dimensional Spherical Pitot Probe," *Transactions of ASME, Journal of Applied Mechanics*, Vol. 23, April 1956, pp. 603-608.

<sup>22</sup>Hale, M.R. and Norrie, D.H., "The Analysis and Calibration of the Five-Hole Spherical Pitot," ASME Paper 67-WA/FE-24, Nov. 1967.

<sup>23</sup>Gupta, A.K. and Lilley, D.G., *Flowfield Modeling and Diagnostics*, Abacus Press, Tunbridge Wells, Kent, England, 1983 (in press).

<sup>24</sup>Syred, N. and Beer, J.M., "Combustion in Swirling Flows: A Review," *Combustion and Flame*, Vol. 23, 1974, pp. 143-201.

<sup>25</sup>Lipstein, N.J., "Low Velocity Sudden Expansion Pipe Flow," Paper presented at ASHRAE 69th Annual Meeting, Miami Beach, Fla., June 1962.

<sup>26</sup>Pratte, B.D. and Keffer, J.R., "The Swirling Turbulent Jet," *Transactions of ASME, Journal of Basic Engineering*, Vol. 94, Dec. 1972, pp. 739-748.

<sup>27</sup>Syred, N. and Dahman, K.R., "Effect of High Levels of Confinement Upon the Aerodynamics of Swirl Burners," *Journal of Energy*, Vol. 2, Jan.-Feb. 1978, pp. 8-15.

<sup>28</sup>Novick, A.S., Miles, G.A., and Lilley, D.G., "Numerical Simulation of Combustor Flowfields," *Journal of Energy*, Vol. 3, March-April 1979, pp. 95-105.

<sup>29</sup>Serag-Eldin, M.A. and Spalding, D.B., "Computations of Three-Dimensional Gas Turbine Combustion Chamber Flows," *Transactions of ASME, Journal of Engineering for Power*, Vol. 101, July 1979, pp. 326-336.

<sup>30</sup>Lilley, D.G. and Rhode, D.L., "A Computer Code for Swirling Turbulent Axisymmetric Recirculating Flows in Practical Isothermal Combustor Geometries," NASA CR-3442, Feb. 1982.

<sup>31</sup>Vu, B.T. and Gouldin, F.C., "Flow Measurements in a Model Swirl Combustor," *AIAA Journal*, Vol. 20, May 1982, pp. 642-651.

*From the AIAA Progress in Astronautics and Aeronautics Series . . .*

**GASDYNAMICS OF DETONATIONS  
AND EXPLOSIONS—v. 75  
and  
COMBUSTION IN REACTIVE SYSTEMS—v. 76**

*Edited by J. Ray Bowen, University of Wisconsin,  
N. Manson, Université de Poitiers,  
A. K. Oppenheim, University of California,  
and R. I. Soloukhin, BSSR Academy of Sciences*

The papers in Volumes 75 and 76 of this Series comprise, on a selective basis, the revised and edited manuscripts of the presentations made at the 7th International Colloquium on Gasdynamics of Explosions and Reactive Systems, held in Göttingen, Germany, in August 1979. In the general field of combustion and flames, the phenomena of explosions and detonations involve some of the most complex processes ever to challenge the combustion scientist or gasdynamicist, simply for the reason that *both* gasdynamics and chemical reaction kinetics occur in an interactive manner in a very short time.

It has been only in the past two decades or so that research in the field of explosion phenomena has made substantial progress, largely due to advances in fast-response solid-state instrumentation for diagnostic experimentation and high-capacity electronic digital computers for carrying out complex theoretical studies. As the pace of such explosion research quickened, it became evident to research scientists on a broad international scale that it would be desirable to hold a regular series of international conferences devoted specifically to this aspect of combustion science (which might equally be called a special aspect of fluid-mechanical science). As the series continued to develop over the years, the topics included such special phenomena as liquid- and solid-phase explosions, initiation and ignition, nonequilibrium processes, turbulence effects, propagation of explosive waves, the detailed gasdynamic structure of detonation waves, and so on. These topics, as well as others, are included in the present two volumes. Volume 75, *Gasdynamics of Detonations and Explosions*, covers wall and confinement effects, liquid- and solid-phase phenomena, and cellular structure of detonations; Volume 76, *Combustion in Reactive Systems*, covers nonequilibrium processes, ignition, turbulence, propagation phenomena, and detailed kinetic modeling. The two volumes are recommended to the attention not only of combustion scientists in general but also to those concerned with the evolving interdisciplinary field of reactive gasdynamics.

*Volume 75—468 pp., 6×9, illus., \$30.00 Mem., \$45.00 List  
Volume 76—688 pp., 6×9, illus., \$30.00 Mem., \$45.00 List  
Set—\$60.00 Mem., \$75.00 List*

TO ORDER WRITE: Publications Dept., AIAA, 1290 Avenue of the Americas, New York, N. Y. 10104

APPENDIX C

TURBULENCE MEASUREMENTS IN A CONFINED JET USING

A SIX-ORIENTATION HOT-WIRE PROBE TECHNIQUE

(AIAA-82-1262)

TURBULENCE MEASUREMENTS IN A CONFINED JET USING A SIX-ORIENTATION HOT-WIRE PROBE TECHNIQUE

S. I. Janjua\* and D. K. McLaughlin\*\*  
Dynamics Technology, Inc., Torrance, California

and

T. Jackson† and D. G. Lilley††  
Oklahoma State University, Stillwater, OK.

Abstract

The six-orientation single hot-wire technique has been applied to the complex flowfield of a swirling, confined jet. This flowfield, which contains a rapid expansion with resulting recirculation regions, is typical of those found in gas turbine engines and ramjet combustors. The present study focusses on turbulence measurements in such a flowfield in the absence of chemical reaction.

A modification to the six-orientation hot-wire technique developed by King has been made, which incorporates the determination of turbulent shear stresses (in addition to normal stresses) and ensemble averaging of redundant turbulence output quantities. With this technique, flowfield surveys have been performed in both swirling and nonswirling axisymmetric confined jets. Where independent data exist, comparisons have been made which demonstrate the reliability of the technique. Finally, a sensitivity analysis of the data reduction technique has been completed which forms the major ingredient in an uncertainty analysis.

Nomenclature

A,B,C	Calibration constants in Equation 1
AO,BO,CO	Cooling velocity functions in Table 1
D	Test section diameter
d	Inlet nozzle diameter
E	Hot-wire voltage
U	Velocity function for axial velocity
W	Velocity function for azimuthal velocity
V	Velocity function for radial velocity
G	Pitch factor
K	Yaw factor
$K_{z_p z_q}$	Covariance for cooling velocities $z_p$ , and $z_q$
P,Q,R	Selected hot-wire probe positions
$Re_d$	Inlet Reynolds number
u	Axial velocity
v	Radial velocity
w	Azimuthal (swirl) velocity
$\tilde{u}, \tilde{w}, \tilde{v}$	Three components of velocity in probe coordinates defined by Figure 5
x,r,θ	Axial, radial, azimuthal cylindrical polar coordinates
Z	Effective cooling velocity acting on a wire

$\alpha$	Side-wall expansion angle
$\gamma_{z_i z_j}$	Correlation coefficient (estimated) between cooling velocities of adjacent wire orientations
$\sigma^2$	Variance of a given quantity
$\phi$	Inverse function of calibration equation
$\Phi$	Swirl vane angle

Subscripts

1,2,3,4,5,6	Refers to the six probe measuring positions
i,j	Dummy indicies which take the values 1 to 3
P,Q,R	Refers to the three selected measuring positions
rms	Root-mean-squared quantity

Superscripts

'	Time-mean average
'	Fluctuating quantity

1. Introduction

1.1 The Gas Turbine Combustor Flowfield

Recent emphasis on fuel economy and pollutant suppression has sparked a renewed interest in gas turbine combustor analysis. A typical axisymmetric gas turbine engine combustor is shown in Figure 1. Flowfields within such combustors typically have a rapid expansion and strong swirl imparted to the incoming air, which result in corner and central recirculation regions. The swirling, recirculating, turbulent flows within combustors present one of the more difficult fluid dynamic problems to analyze. This complexity is increased many fold by the processes of combustion and heat transfer within the flowfield. Despite the complexity of combustor flows, significant progress is being made in their analysis.

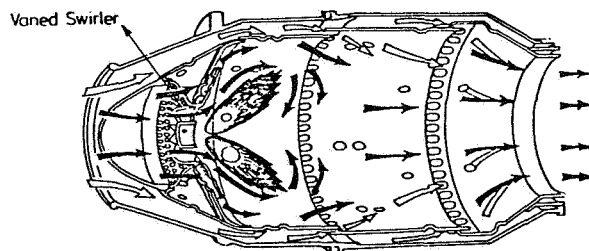


Figure 1. Axisymmetric Combustor of a Gas Turbine Engine

\* Research Engineer, Member AIAA  
\*\* Senior Research Scientist, Member AIAA  
† Graduate Student, Student Member AIAA  
†† Professor, Associate Fellow AIAA



The present paper reports on research which is part of an extensive experimental and computational study of gas turbine flowfields in the absence of combustion. Figure 2 shows the characteristics of the simplified flowfield being investigated. Flow enters through a jet of diameter  $d$  into a tube of diameter  $D$ , after being expanded through an angle  $\alpha$ . Before entering the tube, the flow may be swirled by a swirler located upstream of the inlet plane. Shown schematically are the corner recirculation zone (CRZ) and the central toroidal recirculation zone (CTRZ) which are typically present in these flows.

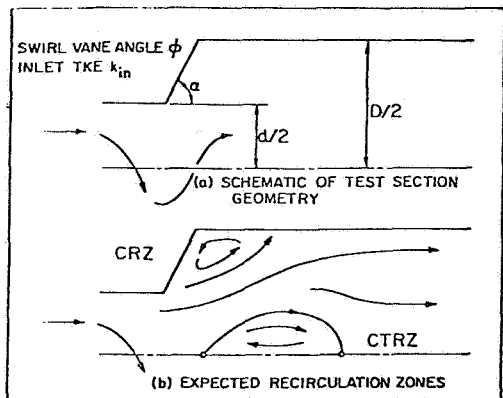


Figure 2. Idealized Combustor Flowfield

The swirling confined jet flowfield shown in Figure 1 is being investigated at Oklahoma State University and at Dynamics Technology, with various methods of approach. Analytically, a computer program (STARPIC) has been assembled which is designed specifically to calculate the swirling confined jet flowfields.<sup>2</sup> Experimentally, a series of flow visualization experiments coupled with 5-hole pitot probe measurements have been used to characterize the time-mean flowfield.<sup>3</sup> Hot-wire measurements of the turbulence properties are also being conducted. This paper reports on the initial results of the hot-wire measurements in the confined jet flowfield.

Several studies on time-mean flowfields of the type just described have been carried out using various turbulence measuring techniques.<sup>4-10</sup> Unfortunately, most of the techniques used do not give complete and detailed information about the flow in terms of all its time-mean and turbulence quantities. In addition, no experiments have been performed on the specific geometry of the present study in the presence of inlet swirl. To develop further the flowfield computational techniques, including the turbulence modeling, there is a strong need to obtain experimental estimates of the turbulence and mean flow quantities in such flows.

## 1.2 The Turbulence Measurement Problem

Turbulence measurement in a complex flowfield has always been a complicated problem encountered by engineers. In the past, turbulence phenomena have been discussed by various authors in detail and various methods of turbulence measurements

have been suggested.<sup>11-13</sup> One of the most widely used instruments to obtain turbulence quantities is the hot-wire anemometer, the most common of which is a single hot-wire. When used at a single orientation and in a two-dimensional flow with a predominant flow direction, a single hot-wire can measure the streamwise components of the time-mean velocity and the root-mean-square velocity fluctuation at a particular location in the flowfield. A two-wire probe can be used to determine the time-mean velocities, streamwise and cross stream turbulence intensities, and the cross correlation between the two components of the velocity fluctuations.<sup>14-15</sup>

Hot-wire measurements in complex three-dimensional flowfields are considerably more difficult than in one- or two-dimensional flowfields in which the mean flow is predominantly in one direction. To measure the three velocities and their corresponding fluctuating components in a three-dimensional flowfield such as encountered in combustor simulators, there are two methods that can be employed at a point in the flowfield:

- 1) A three-wire probe used with a single orientation.
- 2) A single- or double-wire probe used with multi-orientation.

The three-wire probe technique permits the necessary simultaneous measurements from which three instantaneous velocity components can be determined. The appropriate signal processing can produce estimates of mean velocity components and normal and shear turbulent stresses (such as  $\overline{u'^2}$  and  $\overline{u'v'}$ ).

The three-hot-wire probe technique is significantly more complex than the single wire multi-orientation techniques. A multi-dimensional probe drive is required to orient the probe in approximately the mean flow direction. Also, sophisticated signal processing electronics is required to handle the three instantaneous hot-wire voltages. Finally, the three-wire probe typically has less spatial resolution in comparison with a single wire probe.

Multi-orientation of a single hot-wire is a novel way to measure the three components of a velocity vector and their fluctuating components. A method devised by Dvorak and Syred<sup>16</sup> uses a single normal hot-wire oriented at three different positions such that the center one is separated by 45 degrees from the other two. The velocity vector at a location is related to the three orthogonal components using pitch and yaw factors as defined by Jorgensen.<sup>17</sup> The data are obtained in the form of mean and root-mean-square voltages at each orientation. However, the measurements done with a single wire do not supply all the information needed to obtain the turbulence quantities. Therefore, in addition to a single wire, Dvorak and Syred used a cross-wire probe to obtain the covariances between the voltages obtained at adjacent hot-wire orientations.

King<sup>18</sup> modified the technique developed by Dvorak and Syred. His method calls for a normal hot-wire to be oriented through six different positions, each orientation separated by 30 degrees from the adjacent one. Mean and root-mean-square

voltages are measured at each orientation. The data reduction is performed using some assumptions regarding the statistical nature of turbulence, making it possible to solve for the three time-mean velocities, the three normal turbulent stresses, and the three turbulent shear stresses.

### 1.3 The Scope of the Present Study

In the present study, the six-orientation single normal hot-wire technique is being employed to obtain the turbulence quantities in the combustor simulator confined jet flowfield. Measurements have been carried out for both swirling and nonswirling flow with expansion angles of 90 degrees (sudden expansion) and 45 degrees (gradual expansion). Only the 90 degree angle data are presented here and the Reynolds number of the inlet flow is  $= 5 \times 10^4$  which is comparable with aircraft combustor flows (although our experiments are performed in nonreacting flows). The data reduction procedure extends King's technique to obtain turbulent shear and normal stresses using six basic response equations representing the six orientations of a normal hot-wire positioned in the flowfield. Certain modifications are made in the procedure to calculate covariances which are an integral part of the data reduction procedure. An uncertainty analysis is performed on the technique which reveals the sensitivity of this technique to various input parameters discussed in the later parts of this paper. Some of the turbulence quantities obtained are compared with measurements performed by Chaturvedi<sup>5</sup> using a crossed-wire probe in a corresponding flow situation.

## 2. Experimental Facility and Instrumentation

### 2.1 Idealized Flowfield

The facility, designed and built at Oklahoma State University, is a simulation of a typical axisymmetric combustion chamber of a gas turbine engine shown in Figure 1. The schematic of the test facility with the idealized flowfield is shown in Figure 3. Ambient air enters the low-speed wind tunnel through a foam air filter. The air then flows through an axial flow fan driven by a 5 h.p. varidrive motor. Thus, the flow rate can be varied for different test conditions. The flow passes through a turbulence management section which has two fine-mesh screens, a 12.7 cm length of packed straws, and five more fine-mesh screens.

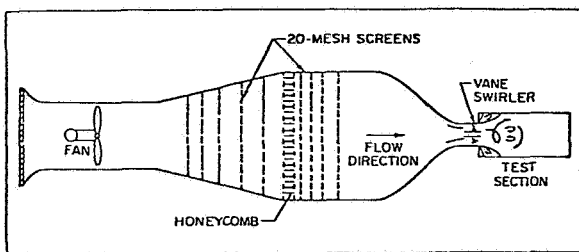


Figure 3. Schematic of the Experimental Facility

The axisymmetric nozzle was designed to produce a minimum adverse pressure gradient on the boundary layer to avoid flow unsteadiness associated with local separation regions. The area ratio of the cross sections of the turbulence management section to that of the nozzle throat is approximately 22.5. The diameter,  $d$ , of the nozzle throat is approximately 15 cm.

The test section is composed of a swirler (optional), an expansion block, and a long plexiglass tube. The expansion block, attached after the swirler, is a 30 cm diameter annular disk of wood. At present, there are three expansion blocks, and the appropriate choice gives  $\alpha = 90, 70, \text{ or } 45$  degrees. The flow is expanded into a plexiglass tube of diameter,  $D$ , of 30 cm, thus giving a diameter expansion ratio ( $D/d$ ) of 2. The test chamber has no film cooling holes or dilution air holes, and the chamber wall of the test section is a constant diameter pipe.

### 2.2 Hot-Wire Instrumentation

The anemometer used for the present study is DISA type 55M01, CTA standard bridge. A normal hot-wire probe, DISA type 55P01, is used in the experiments. This probe has two prongs set approximately 3 mm apart which support a  $5 \mu\text{m}$  diameter wire which is gold plated near the prongs to reduce end effects and strengthen the wire. The mean voltage is measured with a Hickok Digital Systems, Model DP100, integrating voltmeter and the root-mean-square voltage fluctuation is measured using a Hewlett Packard, Model 400 HR, AC voltmeter.

The hot-wire is supported in the facility by a traversing mechanism shown schematically in Figure 4. It consists of a base that is modified to mount on the plexiglass tube of the test section at various axial locations. The hot-wire probe is inserted into the tube through a rotary vernier and the base. The rotary vernier is attached to a slide which can traverse across the flow chamber. Thus, it is possible for the probe to be traversed to any radial location at selected downstream locations in the flowfield and to be rotated through 180 degrees.

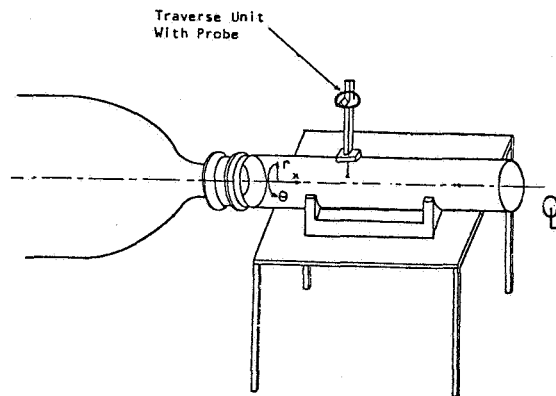


Figure 4. Hot-Wire Probe Mounted on the Test Section

\* Provided for information and not necessarily a product endorsement.

### 2.3 Calibration Nozzle

The hot-wire is calibrated in a small air jet. The facility consists of a compressed air line, which delivers the desired flow rate through a small pressure regulator and a Fisher and Porter Model 10A1735A rotameter. The jet housing consists of an effective flow management section followed by a contoured nozzle with a 3.5 cm diameter throat. A rotary table is used to hold the probe while it is being calibrated in three different orientations.

### 3. Hot-Wire Data Analysis

#### 3.1 Hot-Wire Response Equations

The six-orientation hot-wire technique requires a single, straight, hot-wire to be calibrated for three different flow directions in order to determine the directional sensitivity of such a probe. The three directions and three typical calibration curves are shown in Figure 5. In these relations, tildes signify components of the instantaneous velocity vector in coordinates on the probe. Each of the three calibration curves is obtained with zero velocity in the other two directions. The calibration curves demonstrate that the hot-wire is most efficiently cooled when the flow is in the direction of the  $\tilde{u}$  component, whereas, the wire is most inefficiently cooled when the flow is in the direction of the  $\tilde{w}$  component. Each of the calibration curves follows a second order, least square fit of the form:

$$E_i^2 = A_i + B_i \tilde{u}_i^{1/2} + C_i \tilde{u}_i \quad (1)$$

which is an extension of the commonly used King's law. In this equation,  $A_i$ ,  $B_i$ , and  $C_i$  are calibration constants and  $\tilde{u}_i$  can take on a value of  $\tilde{u}$ ,  $\tilde{v}$ , and  $\tilde{w}$  for the three calibration curves, respectively.

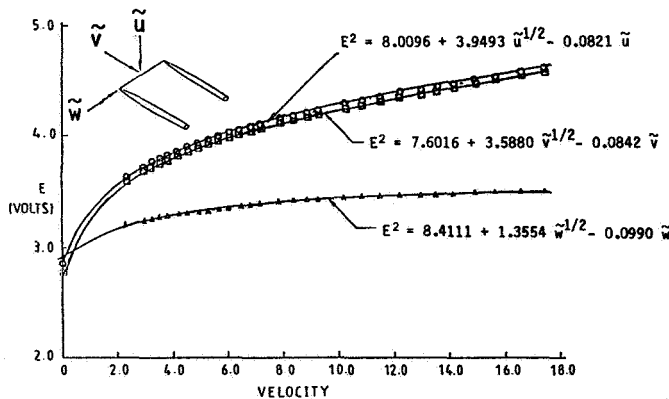


Figure 5. The Three-Directional Hot-Wire Calibration

When the wire is placed in a three dimensional flowfield, the effective cooling velocity experienced by the hot-wire is:

$$Z^2 = \tilde{v}^2 + G^2 \tilde{u}^2 + K^2 \tilde{w}^2 \quad (2)$$

where G and K are the pitch and yaw factors defined by Jorgensen<sup>17</sup> to be:

$$G = \frac{\tilde{v}(\tilde{u} \text{ and } \tilde{w}=0)}{\tilde{u}(\tilde{v} \text{ and } \tilde{w}=0)}, \text{ and}$$

$$K = \frac{\tilde{v}(\tilde{u} \text{ and } \tilde{w}=0)}{\tilde{w}(\tilde{u} \text{ and } \tilde{v}=0)} \quad (3)$$

which are evaluated from the three calibration curves (Figure 5) for a constant value of  $E^2$ . Equation (3) shows that the pitch and yaw factors are calculated with the  $\tilde{v}$  component  $i = 2$  in equation (1) of the effective cooling velocity as the reference. Therefore, the calibration constants used in equation (1) are the coefficients in the E vs.  $\tilde{v}$  calibration of Figure 5, i.e., in a general flowfield:

$$E^2 = A_2 + B_2 Z^{1/2} + C_2 Z$$

with Z as given in Equation (2) above.

Figure 6 shows the pitch and yaw factors as a function of hot-wire voltage determined from the calibration curve of Figure 5. Both factors vary with hot-wire voltage, but the yaw factor is far more sensitive. The sensitivity analysis discussed in the next section demonstrates that uncertainties associated with the varying pitch and yaw factors do not seriously affect the accuracy of the estimated flow quantities.

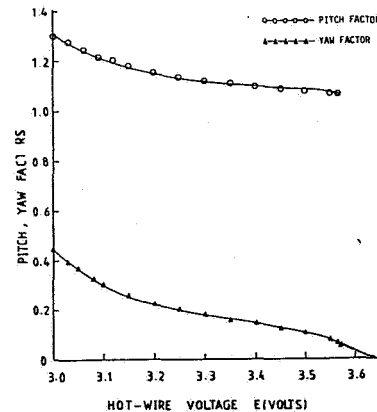


Figure 6. Pitch and Yaw Factors Plotted Against Hot-Wire Mean Effective Voltage

To carry out measurements in the confined jet flowfield, the wire is aligned in the flow in such a way that in the first orientation, the wire is normal to the flow in the axial direction and the probe coordinates coincide with the coordinates of

the experimental facility. Thus, the six equations for the instantaneous cooling velocities at the six orientations, as given by King<sup>18</sup> are:

$$\begin{aligned}
 Z_1^2 &= v^2 + G^2 u^2 + K^2 w^2 \\
 Z_2^2 &= v^2 + G^2(u \cos 30^\circ + w \sin 30^\circ)^2 \\
 &\quad + K^2(w \cos 30^\circ - u \sin 30^\circ)^2 \\
 Z_3^2 &= v^2 + G^2(u \cos 60^\circ + w \sin 60^\circ)^2 \\
 &\quad + K^2(w \cos 60^\circ - u \sin 60^\circ)^2 \\
 Z_4^2 &= v^2 + G^2 w^2 + K^2 u^2 \\
 Z_5^2 &= v^2 + G^2(w \sin 120^\circ + u \cos 120^\circ)^2 \\
 &\quad + K^2(u \sin 120^\circ - w \cos 120^\circ)^2 \\
 Z_6^2 &= v^2 + G^2(w \sin 150^\circ + u \cos 150^\circ)^2 \\
 &\quad + K^2(u \sin 150^\circ - w \cos 150^\circ)^2
 \end{aligned} \tag{4}$$

Solving simultaneously any three adjacent equations provide expressions for the instantaneous values of the three velocity components,  $u$ ,  $w$ , and  $v$  in terms of the equivalent cooling velocities ( $Z_1$ ,  $Z_2$  and  $Z_3$  for example, when the first three equations are chosen). Thus, the general form of the instantaneous velocity components is given as:

$$\begin{aligned}
 U &= \left[ \left\{ AO + \left( AO^2 + \frac{BO^2}{3} \right)^{1/2} \right\} \frac{1}{(G^2 - K^2)} \right]^{1/2} \\
 W &= \left[ \left\{ -AO + \left( AO^2 + \frac{BO^2}{3} \right)^{1/2} \right\} \frac{1}{(G^2 - K^2)} \right]^{1/2} \\
 V &= \left[ CO - \frac{(G^2 + K^2)}{(G^2 - K^2)} \left( AO^2 + \frac{BO^2}{3} \right)^{1/2} \right]^{1/2}
 \end{aligned} \tag{5}$$

The values of  $AO$ ,  $BO$  and  $CO$  depend on the set of the three equations chosen and are given in Table 1 for appropriate equation sets.

TABLE 1  
Values of  $AO$ ,  $BO$ , and  $CO$  in Various Equation Sets

Equation Set P,O,R Choice	AO	BO	CO
1, 2, 3	$(Z_2^2 - Z_3^2)$	$(-2Z_1^2 + 3Z_2^2 - Z_3^2)$	$(Z_1^2 - Z_2^2 + Z_3^2)$
2, 3, 4	$(Z_2^2 - Z_3^2)$	$(-Z_2^2 + 3Z_3^2 - 2Z_4^2)$	$(Z_2^2 - Z_3^2 + Z_4^2)$
3, 4, 5	$(Z_3^2 - 2Z_4^2 + Z_5^2)$	$(Z_3^2 - Z_5^2)$	$(Z_3^2 - Z_4^2 + Z_5^2)$
4, 5, 6	$(-Z_5^2 + Z_6^2)$	$(-2Z_4^2 + 3Z_5^2 - Z_6^2)$	$(Z_4^2 - Z_5^2 + Z_6^2)$
5, 6, 1	$(-Z_5^2 + Z_6^2)$	$(-Z_5^2 + 3Z_6^2 - 2Z_1^2)$	$(Z_5^2 - Z_6^2 + Z_1^2)$
6, 1, 2	$(-Z_6^2 + 2Z_1^2 - Z_2^2)$	$(-Z_6^2 + Z_2^2)$	$(Z_6^2 - Z_1^2 + Z_2^2)$

However, these equations cannot be directly used because it is impossible to obtain  $Z_1$ ,  $Z_2$  and  $Z_3$  at a single instant in time with a single wire

probe. Therefore, Equations (5) must be expressed in terms of mean and root-mean-square values. Equation (1) can be written as:

$$Z_i = [-B_2 + \{B_2^2 + 4C_2(A_2 - E_i^2)\}^{1/2} / 2C_2]^2 \tag{6}$$

The above equation is in terms of instantaneous velocity  $Z_i$  and instantaneous voltage  $E_i$ . In order to obtain an expression for time-mean velocity as a function of time-mean voltage, a Taylor series expansion of Equation (6) can be carried out as follows:

$$Z_i = Z_i(\bar{E}_i + E_i') = \phi(\bar{E}_i) + \frac{E_i'}{1!} \frac{\partial \phi}{\partial E_i} + \frac{E_i'^2}{2!} \frac{\partial^2 \phi}{\partial E_i^2} + \dots \tag{7}$$

where  $\phi = Z_i(\bar{E}_i)$ .

The Taylor series is truncated after second order terms assuming the higher order terms to be relatively small. Time averaging both sides of the above equation and employing the fact that  $E_i' = 0$ , yields:

$$\bar{Z}_i = \phi + \frac{1}{2} \frac{\partial^2 \phi}{\partial E_i^2} \sigma^2 E_i \tag{8}$$

To obtain  $\bar{Z}_i'^2 = \sigma_{Z_i}^2$ , the relationship as given by Hinze<sup>19</sup> is:

$$\bar{Z}_i'^2 = \sigma_{Z_i}^2 = \text{Expec}[Z_i^2] - (\text{Expec}[Z_i])^2 \tag{9}$$

Using Equation (8) as the basis,  $\text{Expec}[Z_i^2]$  and  $(\text{Expec}[Z_i])^2$  can be evaluated and substituted into Equation (8) to get:

$$\bar{Z}_i'^2 = \sigma_{Z_i}^2 = \frac{\partial \phi^2}{\partial E_i} \sigma_{E_i}^2 - \left( \frac{1}{2} \frac{\partial^2 \phi}{\partial E_i^2} \sigma_{E_i}^2 \right)^2 \tag{10}$$

Thus, Equations (8) and (10) give the mean and variance of effective cooling velocities in terms of the mean and variance of the appropriate voltages.

In a 3-dimensional flow, it is usually desirable to obtain the mean and variance for the individual velocity components in axial, azimuthal, and radial directions, and also their cross correlations. The procedure to obtain the mean and variance of the individual velocity components is the same as for the effective cooling velocities except that  $u$ ,  $w$  and  $v$  are functions of three random variables and there are extra terms in the Taylor expansion to account for the covariances of the cooling velocities. Thus, the axial mean velocity component as given by Dvorak and Syred,<sup>16</sup> and King<sup>18</sup> is:

$$\bar{u} = U(\bar{Z}_P, \bar{Z}_Q, \bar{Z}_R) + \frac{1}{2} \sum_{i=1}^3 \frac{\partial^2 U}{\partial Z_i^2} \sigma_{Z_i}^2 + \sum_{i < j}^3 \frac{\partial^2 U}{\partial Z_i \partial Z_j} K_{Z_i Z_j} \tag{11}$$

where  $K_{Z_i Z_j}$  is the covariance of the cooling velocities  $Z_i$  and  $Z_j$  and is defined as:

$$K_{Z_i Z_j} = \frac{1}{T} \int_0^T (Z_i - \bar{Z}_i)(Z_j - \bar{Z}_j) dt \quad (12)$$

Identical expressions for  $\bar{w}$  and  $\bar{v}$  can also be obtained in terms of  $W$  and  $V$ , respectively. Derivatives of the form  $\partial^2 U / \partial Z_i \partial Z_j$  are determined analytically from equations (5) and Table 1.

Also, the normal stresses are given as:

$$\begin{aligned} \overline{u'^2} &= \sum_{i=1}^3 \left( \frac{\partial U}{\partial Z_i} \right)^2 \cdot \sigma_{Z_i}^2 + \sum_{i \neq j}^3 \sum_{j=1}^3 \frac{\partial U}{\partial Z_i} \cdot \frac{\partial U}{\partial Z_j} \cdot K_{Z_i Z_j} \\ &- \left[ \frac{1}{2} \sum_{i=1}^3 \frac{\partial^2 U}{\partial Z_i^2} \cdot \sigma_{Z_i}^2 + \sum_{i < j}^3 \sum_{j=1}^3 \frac{\partial^2 U}{\partial Z_i \partial Z_j} \cdot K_{Z_i Z_j} \right]^2 \quad (13) \end{aligned}$$

with similar expressions for  $\overline{w'^2}$  and  $\overline{v'^2}$ .

Finally, the expressions for shear stresses as given by Dvorak and Syred<sup>16</sup> are of the form:

$$\begin{aligned} \overline{u'v'} &= \sum_{i=1}^3 \frac{\partial U}{\partial Z_i} \frac{\partial V}{\partial Z_i} \sigma_{Z_i}^2 + \sum_{i \neq j}^3 \sum_{j=1}^3 \frac{\partial U}{\partial Z_i} \frac{\partial V}{\partial Z_j} K_{Z_i Z_j} \\ &- \left[ \frac{1}{2} \sum_{i=1}^3 \frac{\partial^2 U}{\partial Z_i^2} \sigma_{Z_i}^2 + \sum_{i < j}^3 \sum_{j=1}^3 \frac{\partial^2 U}{\partial Z_i \partial Z_j} \cdot K_{Z_i Z_j} \right] \\ &\cdot \left[ \frac{1}{2} \sum_{i=1}^3 \frac{\partial^2 V}{\partial Z_i^2} \cdot \sigma_{Z_i}^2 + \sum_{i < j}^3 \sum_{j=1}^3 \frac{\partial^2 V}{\partial Z_i \partial Z_j} \cdot K_{Z_i Z_j} \right] \quad (14) \end{aligned}$$

Expressions for  $\overline{u'w'}$  and  $\overline{v'w'}$  can also be obtained in a similar manner and are given in Reference 22.

### 3.2 Calculation of Covariances

Dvorak and Syred<sup>16</sup> used a DISA time correlator (55A06) to find the correlation coefficients between the velocity fluctuations in the three directions. King's approach is to use the information obtained by all six orientations and devise a mathematical procedure to calculate the covariances.

Covariances are calculated using the relationship:

$$K_{Z_i Z_j} = \gamma_{Z_i Z_j} [\sigma_{Z_i}^2 \sigma_{Z_j}^2]^{1/2} \quad (15)$$

where  $\gamma_{Z_i Z_j}$  is the correlation coefficient between the two cooling velocities  $Z_i$  and  $Z_j$ . By definition, the absolute value of the correlation coefficient  $\gamma_{Z_i Z_j}$  is always less than 1.

King<sup>18</sup> made certain assumptions to calculate the covariances. However, he observed that at times the calculated value of the correlation coefficient is greater than one at which instance he assigned previously fixed values to the correlation coefficients. He argued that if two wires are separated by an angle of 30 degrees, the fluctuating signals from the wires at the two loca-

tions would be such that their contribution to the cooling of the wire would be related by the cosine of the angle between the wires. This assumption leads to the following three values of the correlation coefficients.

$$\gamma_{Z_P Z_Q} = \cos 30 = 0.9 \quad (16)$$

$$\gamma_{Z_Q Z_R} = \cos 30 = 0.9$$

To relate  $\gamma_{Z_P Z_R}$  with  $\gamma_{Z_P Z_Q}$  and  $\gamma_{Z_Q Z_R}$ , King introduced the following relationship:

$$\gamma_{Z_P Z_R} = \eta \gamma_{Z_P Z_Q} \gamma_{Z_Q Z_R} \quad (17)$$

where  $\eta$  is given a value of 0.8. Hence  $\gamma_{Z_P Z_R}$  becomes:

$$\gamma_{Z_P Z_R} = (0.8)(0.9)(0.9) = 0.65 \quad (18)$$

The three covariances are then obtained by substituting the corresponding values of the correlation coefficients into Equation (15).

The present study, however, uses Equations (16) and (18) during the entire data reduction. The reason for this is contained in the results of the sensitivity analysis presented in the next section. This analysis demonstrated that there is not significant error magnification in the data reduction due to the correlation terms.

## 4. Results of Hot-Wire Measurements

The six-orientation hot-wire technique was employed to measure the turbulence quantities for swirling and non-swirling flow conditions in the confined jet facility described earlier. Also, an extensive sensitivity analysis of the data reduction was conducted to assist the estimation of the uncertainties in the output quantities.

### 4.1 Uncertainty Analysis

The uncertainty analysis includes a determination of the sensitivity of the six-orientation hot-wire data reduction to various input parameters which have major contributions in the response equations. Pitch and yaw factors (G and K) are used in the response equations described in Section 3 in order to account for the directional sensitivity of the single hot-wire probe. Figure 6 shows the pitch and the yaw factors plotted against the hot-wire mean effective voltage. Both the pitch and yaw factors are functions of the hot-wire mean effective voltage, but the yaw factor is far more sensitive. A one percent increase in the hot-wire voltage reduces the pitch factor by 1.3 percent and the yaw factor by 56 percent. For the present study, the values of these factors are chosen at an average hot-wire voltage experienced in the flowfield. This was appropriate since the output quantities ( $\bar{u}$ ,  $u'_{rms}$ ,  $u'v'$ , etc) are only weakly dependent on the value of K. This can be seen in the data of Table 2 which summarizes a sensitivity analysis performed on the data reduction program at a

representative position in the flowfield.

Table 2 demonstrates the percent change in the output quantities for a 1 percent change in most of the important input quantities. For the data presented in this table only quantities calculated from the probe orientation combination  $\bar{Z}_5$ ,  $\bar{Z}_6$  and  $\bar{Z}_1$  are used, for simplicity. In this swirling flow  $\bar{Z}_6$  was the minimum of the 6 mean effective cooling velocities. King<sup>18</sup> has argued that the probe orientation combination approximately centered around the minimum effective cooling velocity produces more accurate estimates of calculated turbulence quantities, than do the other orientation combinations.

TABLE 2  
Effect of Input Parameters on Turbulence Quantities

PARAMETER	% CHANGE IN PARAMETER	% CHANGE IN TIME-MEAN AND TURBULENCE QUANTITIES								
		$\bar{u}$	$\bar{v}$	$\bar{w}$	$u'_{rms}$	$v'_{rms}$	$w'_{rms}$	$u'v'$	$u'w'$	$v'w'$
$\bar{Z}_1$	+1	+16.10	+0.66	+4.98	+15.75	-2.06	+2.75	+6.0	+51.43	+11.94
$\bar{Z}_5$	+1	+2.19	-2.21	+11.49	-6.50	+2.42	+12.88	+4.0	+14.29	+7.46
$\bar{Z}_6$	+1	-10.59	-0.36	-8.50	-1.88	+7.07	-9.54	-6.0	-54.29	-11.94
$E'_{1,rms}$	+1	+0.27	-0.06	+0.14	+1.63	+0.13	+0.39	+2.0	+2.86	+1.49
$E'_{5,rms}$	+1	+0.05	0.0	+0.14	0.0	-0.13	+1.57	0.0	0.0	+1.49
$E'_{6,rms}$	+1	-0.16	+0.18	-0.14	-0.63	+1.03	-1.08	-2.0	-5.71	0.0
G	+1	-1.02	0.0	-3.01	-1.0	0.0	-0.98	-2.0	-2.86	-1.49
K	+1	+0.01	-0.04	+0.01	+0.01	0.0	+0.01	0.0	0.0	0.0
$\gamma_{Z_p Z_Q}$	+1	+0.05	0.0	+0.14	-0.13	-0.13	-1.77	0.0	-2.86	+1.49
$\gamma_{Z_0 Z_R}$	+1	+0.21	+0.01	+0.05	-1.63	+0.13	-0.79	0.0	-5.71	+1.49
$\gamma_{Z_p Z_R}$	+1	-0.16	+0.18	-0.08	+0.13	0.0	+0.69	-2.0	+2.86	0.0

It is not unusual in hot-wire anemometry to have the mean velocity components and turbulence quantities that are measured, be quite sensitive to changes in mean hot-wire voltage. For interpretive purposes, the mean hot-wire voltage variations can be thought of as being either errors in measuring the mean voltage, or shifts in the individual wire calibrations due to contamination or strain 'aging' of the wire. The data of Table 2 demonstrate that the most serious inaccuracies in the measurement and data reduction technique will be in the estimates of turbulent shear stresses, the most inaccurate output term being  $u'w'$ .

As already discussed in Section 3, an *ad hoc* assumption is made regarding the numerical values of the correlation coefficients used in the deduction of time-mean and turbulence quantities. The results of the sensitivity analysis (Table 2) show the time-mean and turbulence quantities to be relatively insensitive to variations in the correlation coefficients. Therefore, the major *ad hoc* assumption made in the technique does not seem to have a great effect on the output quantities compared to the effect of other input quantities.

As mentioned earlier, turbulence quantities (the output) can be calculated from six combina-

tions of data from adjacent wire orientations. One measure of the uncertainty in the output quantities can be obtained by examining the variance in these quantities calculated from the six different position combinations. Table 3 shows these comparison data\* for a representative position in the flowfield.\* For each of the output quantities, an ensemble mean  $\bar{x}$  is calculated together with an ensemble standard deviation  $\sigma$ . The ratio  $\sigma/\bar{x}$  is a measure of the uncertainty in the output quantity. In this table, NR stands for 'not resolved', a problem that occurs when the data reduction program attempts to take the square root of a negative quantity. In addition, quantities which are more than three standard deviations outside the mean are rejected as spurious calculations.

TABLE 3  
Scatter Among the Turbulence Quantities When Solved by Six Different Combinations

TURBULENCE QUANTITY	TURBULENCE QUANTITY SOLVED BY SIX COMBINATIONS						MEAN $\bar{x}$	STANDARD DEVIATION $\sigma$	$\sigma/\bar{x}$
	1,2,3	2,3,4	3,4,5	4,5,6	5,6,1	6,1,2			
$\bar{u}/u_0$	0.21	0.20	0.21	0.21	0.19	0.18	0.20	0.01	0.06
$\bar{v}/u_0$	0.10	NR*	0.11	0.17	0.17	0.17	0.14	0.04	0.26
$\bar{w}/u_0$	0.40	0.39	0.39	0.38	0.37	0.40	0.39	0.01	0.03
$u'_{rms}/u_0$	0.14	0.14	0.14	0.07	0.08	0.08	0.11	0.03	0.31
$v'_{rms}/u_0$	0.06	0.11	0.11	0.08	0.08	0.09	0.09	0.02	0.23
$w'_{rms}/u_0$	0.13	0.16	0.10	0.11	0.10	0.12	0.12	0.02	0.20
$u'v'/u_0^2$	NR*	NR*	0.012	NR*	0.005	0.004	0.007	0.004	0.62
$u'w'/u_0^2$	0.002	0.010	0.002	0.004	0.004	0.008	0.005	0.003	0.72
$v'w'/u_0^2$	0.003	NR*	0.003	0.003	0.007	0.001	0.003	0.002	0.58

\* Not Resolved

The data in Tables 2 and 3 can be used to produce estimates in the uncertainties of the calculated turbulence quantities. The data suggest that uncertainties on the order of 5 percent are to be expected in the mean velocity component estimates. Normal turbulent stress estimates ( $u'_{rms}$ , etc.) have uncertainties on the order of 20 to 30 percent and turbulent shear stress estimates are significantly higher, although most of this is a consequence of taking a product of terms such as  $u'$  and  $v'$ .

These uncertainty estimates are considered to be somewhat conservative. More accurate estimates are quite difficult to obtain because, to our knowledge, similar measurements have not been performed with any other instrumentation system in this geometry flowfield. Also, comparisons of several representative points with independent measurements suggest that the ensemble averages estimates are typically in closer agreement than are selected sets of three orientations. Therefore, all turbulence estimates presented in this paper are calculated from ensemble averages of six groups of three adjacent wire orientations. Any data not resolved are not included in this averaging. This approach represents a departure from the technique developed by King<sup>18</sup> who typically

\*  $x/D=1.5$ ,  $r/D=0.25$ ,  $\phi=38$  deg (swirling flow).

selected one group of three orientations from which to calculate his turbulence estimates.

## 4.2 Results of Flowfield Surveys

Radial distributions of time-mean velocities, turbulent normal stresses and shear stresses are obtained for both nonswirling and swirling conditions, at various axial locations in the flowfield.

**Nonswirling Flow.** In the confined jet, the experiments have been conducted with expansion angles of 90 degrees (sudden expansion) and 45 degrees (gradual expansion) and the results for both cases are presented in Reference 22. In the interest of brevity, only the data for a 90 degree expansion are presented here.

Figure 7 shows the radial distribution of time-mean axial and radial velocity components at various axial locations. The axial velocity distributions are compared with a similar study performed by Chaturvedi<sup>5</sup> with a crossed hot-wire probe. Because of the inability of the six-orientation hot-wire technique to determine the sense of the flow direction in a nonswirling flow, the presence of the corner recirculation zone was observed by a sudden increase in the axial velocity closer to the wall.

Figure 8 shows the radial distribution of axial and radial components of the turbulence intensity at various axial locations in the confined jet flowfield. These turbulence intensity components are compared with Chaturvedi's measurements<sup>5</sup> and reasonable agreement is found. In fact, the agreement in most cases is better than the uncertainty estimates derived from the data reduction sensitivity analysis.

Included on Figure 8 are measured turbulent shear stress component ( $\overline{u'v'}/U_0^2$ ) profiles for the nonswirling confined jet. For the most part, these measurements are in reasonable agreement with those made by Chaturvedi<sup>5</sup> with a crossed wire probe. The two significant exceptions to the good agreement occur at the furthest upstream and furthest downstream locations. Upstream, at  $x/D = 0.5$  the shear layer is very thin and, therefore, matching data from several wire orientations obtained at somewhat different times may be practically difficult. We believe the overly large measured turbulent shear stress on the centerline at the furthest downstream station ( $x/D = 3.0$ ) to be a consequence of the transient nature of the flow. The recirculation regions in the confined jet oscillate somewhat at a low frequency, likely characteristic of the main acoustic modes in the tube. These large scale oscillations can have significant correlated velocity fluctuations (such as  $u'v'$ ).

**Swirling Flow** The measurements performed in the swirling flow are with  $\alpha = 90^\circ$ ,  $\phi = 38^\circ$ , and  $x/D = 0.5, 1.0, \text{ and } 1.5$ . The object of these limited number of experiments was to evaluate the reliability and accuracy of the six-orientation hot-wire technique before making extensive use of the technique.

The hot-wire results in the case of time-mean axial and azimuthal (swirl) velocities shown in Figures 9 and 10, are compared with five-hole pitot probe measurements performed by Rhode<sup>3</sup> in the same experimental facility. Agreement among the two studies is fairly good. King<sup>18</sup> suggested a method to determine the sense of the axial velocity. He advised comparing the magnitudes of  $Z_3$  and  $Z_5$  given by Equations 4. In the present flowfield, the swirl velocity is always positive and the two equations giving  $Z_3$  and  $Z_5$  differ only in the sign of axial velocity. Therefore, when  $Z_5$  is greater than  $Z_3$ , the axial velocity is negative, otherwise it is positive. With the proper sense being assigned to the x velocity mean component, the presence of central toroidal recirculation zone is evident in the results of both measurement techniques.

Figure 11 shows the radial distribution of the time-mean radial velocity at various axial locations for a swirl vane angle of 38 degrees and wall expansion angle of 90 degrees. Flow visualization and five-hole pitot probe measurements performed in Rhode's study<sup>3</sup> show the time-mean radial velocity to be negative at axial locations greater than  $x/D = 0.5$ . In spite of the inability of the six-orientation hot-wire technique to determine the sense of the radial velocity, the data are presented with the appropriate sign change. There is a reasonable agreement among the two studies in measurements of time mean radial velocities except at the initial measurement station.

Figure 12 shows the radial distribution of axial, radial and azimuthal turbulent intensities at three axial locations presented. At axial locations closer to the inlet of the confined jet, the axial turbulence intensity is fairly high, up to 32 percent for  $x/D = 0.5$  which is due to the large axial velocity gradients closer to the wall. However, in the case of radial turbulence intensity, the profiles are rather flat. The mean azimuthal velocity also experiences sudden changes in gradients and, hence, the outcome is a large azimuthal turbulence intensity closer to the wall at  $x/D = 0.5$ .

Figure 13 shows the shear stresses  $\overline{u'v'}/U_0^2$ ,  $\overline{u'w'}/U_0^2$ , and  $\overline{v'w'}/U_0^2$  as a function of radial and axial distance. The sensitivity analysis showed that we should expect large uncertainties associated with evaluation of turbulent shear stresses using the six-orientation technique. Therefore, the reliability of the profiles of these shear stresses shown in Figure 13 is uncertain at this time. Nevertheless, stresses  $\overline{u'v'}/U_0^2$  and  $\overline{u'w'}/U_0^2$  are found to have large values closer to the wall that one would expect due to steep axial and azimuthal velocity gradients. The fact that we have found no other measurements of this type in a swirling, recirculating flow attests to the fact that accurate measurements in such a flow are quite difficult.

### Closure

The six-orientation hot-wire technique is a relatively new method to measure time-mean velocity components and turbulence quantities in complex three-dimensional flowfields. Applied in

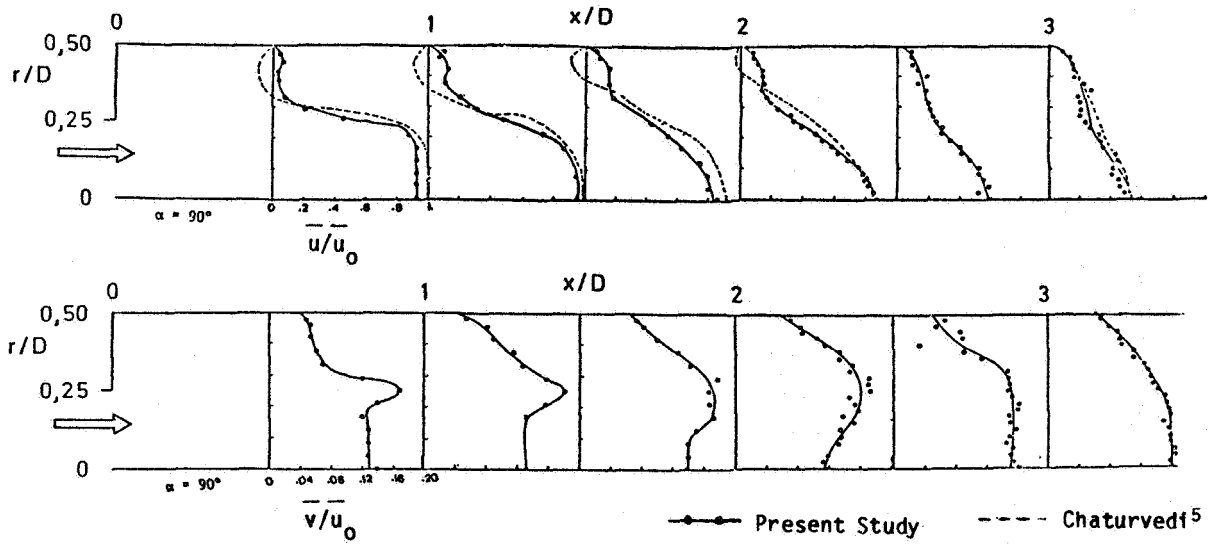


Figure 7. Radial Distributions of Time-Mean Axial and Radial Velocity Components in the Non-Swirling Confined Jet; (Note the Difference in Velocity Scales)

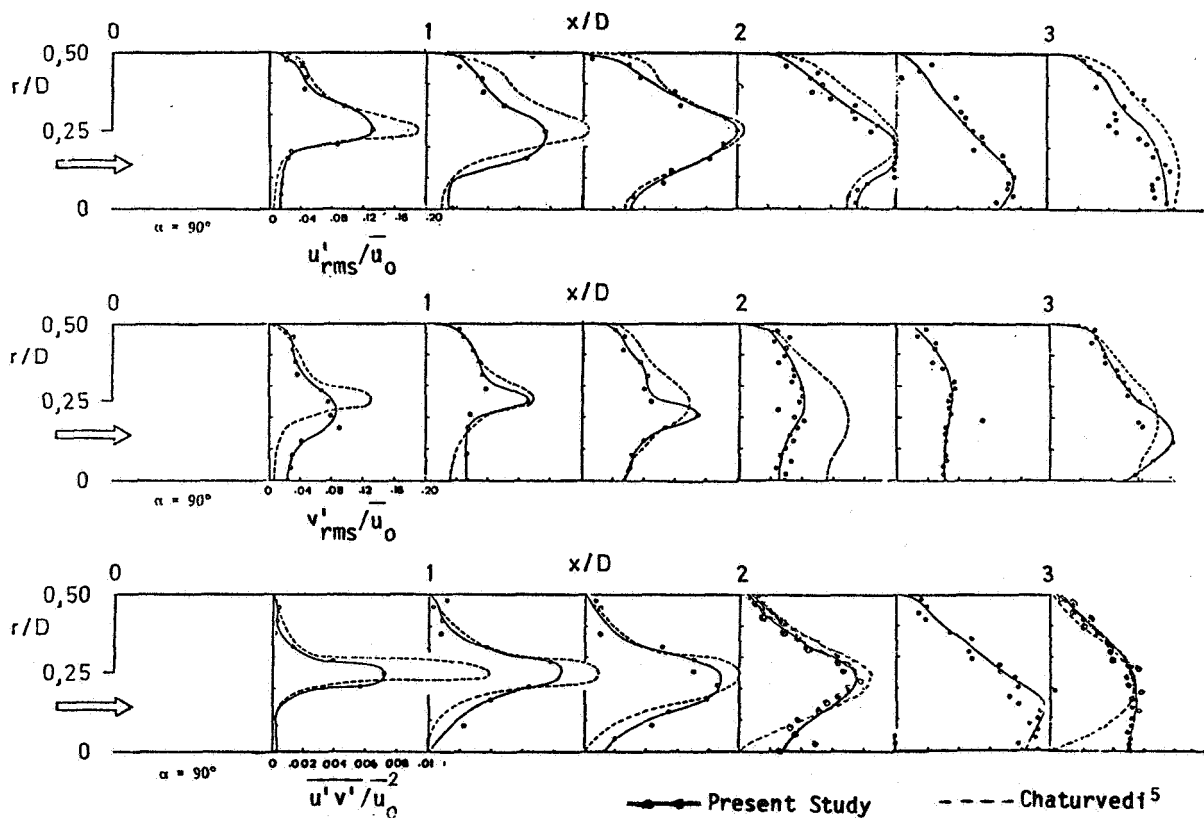


Figure 8. Radial Distributions of Turbulent Intensities  $u'_{rms}/\overline{u}_0$ ,  $v'_{rms}/\overline{u}_0$  and shear stress  $u'v'/\overline{u}_0^2$



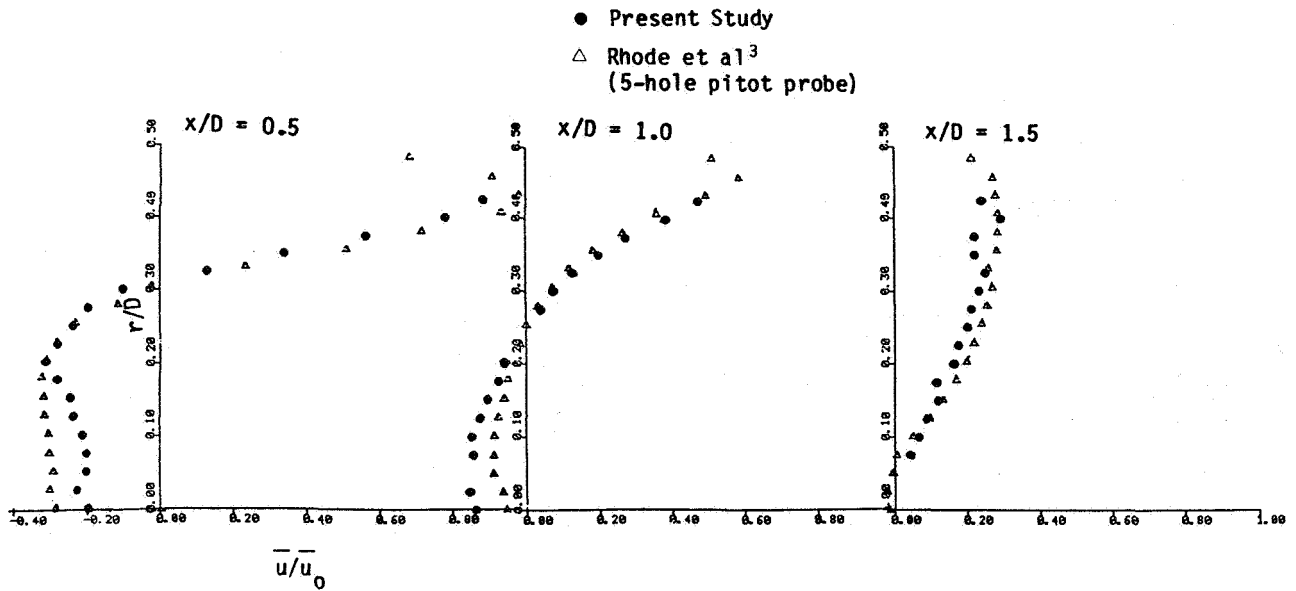


Figure 9. Radial Distribution of Time-Mean Axial Velocity in Swirling Confined Jet for  $\alpha = 90^\circ$  and  $\phi = 38^\circ$

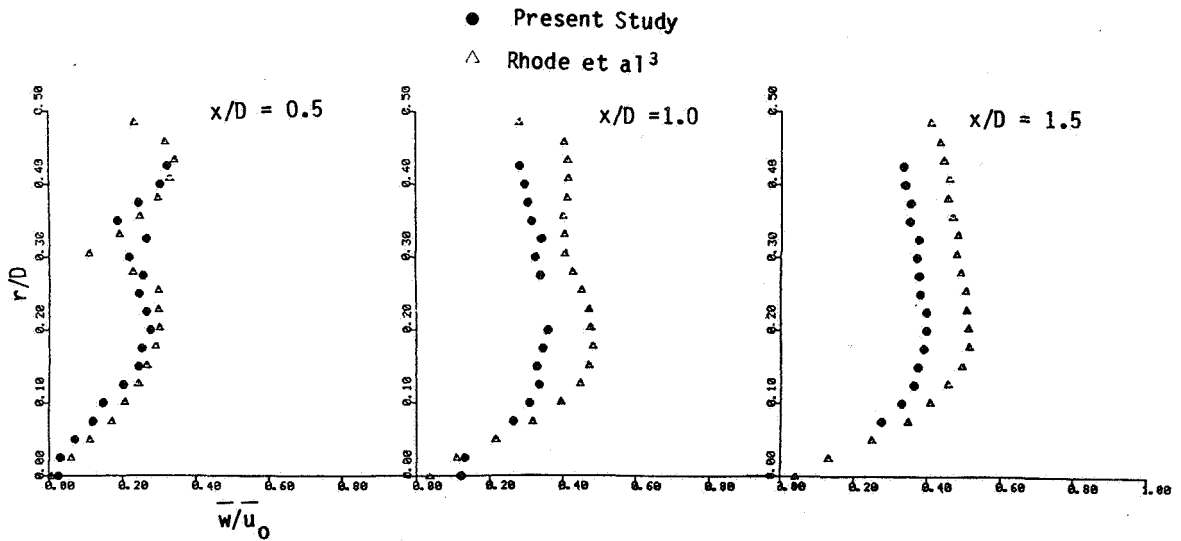


Figure 10. Radial Distribution of Time-Mean Azimuthal Velocity in Swirling Confined Jet for  $\alpha = 90^\circ$  and  $\phi = 38^\circ$

this study to nonreacting axisymmetric flowfields, measurements of time-mean and root-mean-square voltages at six different orientations contain enough information to obtain the time-mean velocities, turbulence intensities and shear stresses. At each location in the flow, there are six different values of each of the above quantities that can be obtained using six sets of measurements of three adjacent orientations. Ensemble averages of the output quantities from the six combinations of data appear to produce estimates with the best agreement with independent measurements.

Flowfield surveys of both swirling and non-swirling confined jets have been made with the six-orientation single hot-wire technique. These measurements have been used to calculate estimates of the mean velocity components and the normal and shear turbulent stresses. Where independent data exist, comparisons have been made which demonstrate the reliability of the technique.

In addition, a sensitivity analysis of the data reduction technique has been conducted which

forms the major ingredient in the uncertainty analysis. It is demonstrated that the largest uncertainties are to be expected in the turbulent shear stress estimates. Nevertheless, in non-swirling flows the measured shear stresses are in reasonable agreement with previous measurements made with a crossed-wire probe. In swirling flow, previous similar measurements have not been found. Consequently, the universal accuracy of the mea-

sured technique applied to swirl flows is still an open question.

Acknowledgement

The authors wish to extend their sincere gratitude to NASA Lewis Research Center and the Air Force Wright Aeronautical Laboratories for support under Grant No. NAG3-74.

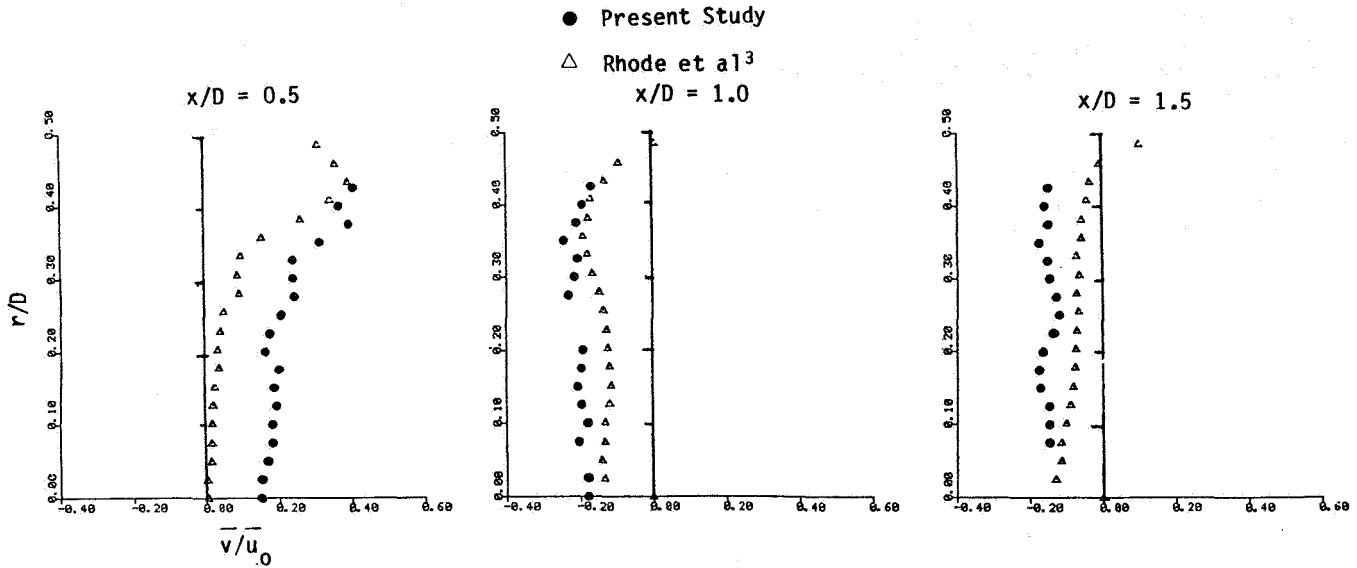


Figure 11. Radial Distribution of Time-Mean Radial Velocity in Swirling Confined Jet for  $\alpha = 90^\circ$  and  $\Phi = 38^\circ$

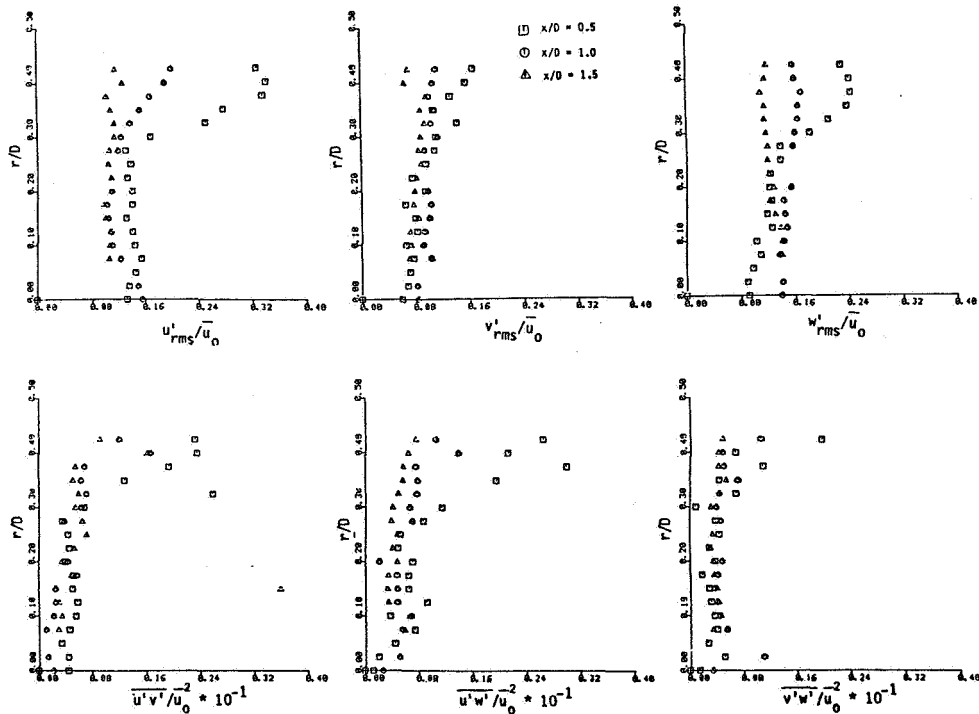


Figure 12. Radial Distribution of Turbulent Shear Stresses  $\overline{u'v'}/u_0^2$ ,  $\overline{u'w'}/u_0^2$ , and  $\overline{v'w'}/u_0^2$  in Swirling Confined Jet for  $\alpha = 90^\circ$  and  $\Phi = 38^\circ$

## References

- <sup>1</sup> Lilley, D.G., "Flowfield Modeling in Practical Combustors: A Review," Journal of Energy, 3, No. 4, 1979.
- <sup>2</sup> Lilley, D.G. and Rhode, D.L., "A Computer Code for Swirling Turbulent Axisymmetric Recirculating Flows in Practical Isothermal Combustor Geometries," NASA Contractor Report 3442, February 1982.
- <sup>3</sup> Rhode, D.L., Lilley, D.G. and McLaughlin, D.K., "Mean Flowfields in Axisymmetric Combustor Geometries with Swirl," AIAA Paper No. 82-0177, 1982, AIAA Journal (in press).
- <sup>4</sup> Krall, K.M. and Sparrow, E.M., "Turbulent Heat Transfer in the Separated, Reattached, and Redevelopment Regions of a Circular Tube," Journal of Heat Transfer, pp. 131-136, February 1966.
- <sup>5</sup> Chaturvedi, M.C., "Flow Characteristics of Axisymmetric Expansions," Proceedings, Journal of the Hydraulic Division, ASCE, 89, No. HY3, pp. 61-92, 1963.
- <sup>6</sup> Phaneuf, J.T. and Netzer, D.W., Flow Characteristics in Solid Fuel Ramjets, Report No. NPS-57Nt74081. Prepared for the Naval Weapons Center by the Naval Postgraduate School, Monterey, California, July 1974.
- <sup>7</sup> Back, L.H. and Roschke, E.J., "Shear Layer Flow Regimes and Wave Instabilities and Reattachment Lengths Downstream of an Abrupt Circular Channel Expansion," Journal of Applied Mechanics pp. 677-681, September 1972.
- <sup>8</sup> Roschke, E.J. and Back, L.H., "The Influence of Upstream Conditions on Flow Reattachment Lengths Downstream of an Abrupt Circular Channel Expansion," Journal of Biomechanics, 9, pp. 481-483, 1976.
- <sup>9</sup> Ha Minh, H. and Chassaing, P., "Perturbations of Turbulent Pipe Flow," Proceedings, Symposium on Turbulent Shear Flows, Pennsylvania State University, pp. 13.9-13.17, April 1977.
- <sup>10</sup> Moon, L.F. and Rudinger, G., "Velocity Distribution in an Abruptly Expanding Circular Duct," Journal of Fluids Engineering, pp. 226-230, March 1977.
- <sup>11</sup> Bradshaw, P., An Introduction to Turbulence and Its Measurement, Pergamon Press, New York, 1971.
- <sup>12</sup> Beer, J.M. and Chigier, N.A. Combustion Aerodynamics, Halsted Press Division, John Wiley & Sons, Inc., New York, 1972.
- <sup>13</sup> Syred, N., Beer, J.M. and Chigier, N.A., "Turbulence Measurements in Swirling Recirculating Flows," Proceedings, Salford Symposium on Internal Flows, London, England: Inst. of Mechanical Engineering, pp. 827-836, 1971.
- <sup>14</sup> Wagnanski, I, and Fiedler, H., "Some Measurements in the Self Preserving Jet," Journal of Fluid Mechanics, 38, p. 577, 1969.
- <sup>15</sup> Pratte, B.D. and Keffer, J.R., "The Swirling Turbulent Jet," Journal of Basic Engineering, 94, pp. 739-748, December 1972.
- <sup>16</sup> Dvorak, K. and Syred, N., "The Statistical Analysis of Hot Wire Anemometer Signals in Complex Flow Fields," DISA Conference, University of Leicester, 1972.
- <sup>17</sup> Jorgensen, F.E., "Directional Sensitivity of Wire and Fiber Film Probes," DISA Information No. 11, Franklin Lakes, N.J., pp. 31-37, May 1971.
- <sup>18</sup> King, C.F., "Some Studies of Vortex Devices - Vortex Amplifier Performance Behavior," Ph.D. Thesis, University College of Wales, Cardiff, Wales, 1978.
- <sup>19</sup> Hinze, J.O. Turbulence, 2nd Edition, McGraw-Hill, New York, 1975.
- <sup>20</sup> Habib, M.A. and Whitelaw, J.H., "Velocity Characteristics of Confined Coaxial Jets With and Without Swirl," ASME Paper 797-WA/FE-21, New York, N.Y., December 2-7, 1979.
- <sup>21</sup> Gupta, A.K. and Lilley, D.G., Flowfield Modeling and Diagnostics, Abacus Press, Tunbridge Wells, England, 1982 (in press).
- <sup>22</sup> Janjua, S.I., "Turbulence Measurements in a Complex Flowfield Using a Six-Orientation Hot-Wire Probe Technique," M.S. Thesis, Oklahoma State University, Stillwater, Oklahoma, December 1981.

APPENDIX D

FIVE-HOLE PITOT PROBE TIME-MEAN VELOCITY

MEASUREMENTS IN CONFINED SWIRLING FLOWS

(AIAA-83-0315)

FIVE-HOLE PITOT PROBE TIME-MEAN VELOCITY  
MEASUREMENTS IN CONFINED SWIRLING FLOWS

H. K. Yoon\* and D. G. Lilley\*\*  
Oklahoma State University, Stillwater, Okla.

Abstract

Nonswirling and swirling nonreacting flows are investigated in an axisymmetric test section with expansion ratio  $D/d = 2$ , which may be equipped with contraction nozzles of area ratios 2 and 4. The effects of several geometric parameters on the flowfield are investigated including: side-wall expansion angle  $\alpha = 90$  and  $45$  deg., swirl vane angle  $\phi = 0, 38, 45, 60,$  and  $70$  deg., and contraction nozzle location  $L/D = 1$  and  $2$  (if present). Data acquisition is via a five-hole pitot probe enabling three time-mean velocity components in the axial, radial, and azimuthal directions to be measured. Velocities are extensively plotted and artistic impressions of recirculation zones are presented.

Nomenclature

C	velocity coefficient = $\rho V^2 / [2(P_C - P_W)]$
D	test section diameter
d	inlet nozzle diameter
L	contraction block downstream distance
p	time-mean pressure
Re	Reynolds number
Q	volume flow rate
$\underline{v} = (u, v, w)$	time-mean velocity (in x-, r-, $\theta$ -directions)
V	time-mean vector velocity magnitude
x, r, $\theta$	axial, radial, azimuthal cylindrical polar coordinates
$\alpha$	side-wall expansion angle
$\beta$	yaw angle of probe = $\tan^{-1}(w/u)$
$\delta$	pitch angle of probe = $\tan^{-1} [v / (\underline{u}^2 + w^2)^{1/2}]$
$\rho$	density
$\phi$	swirl vane angle with respect to facility axis

Subscripts

C	central pitot pressure port
d	relating to inlet nozzle diameter
N, S, E, W	north, south, east, west pitot pressure ports
o	value at inlet to flowfield

1. Introduction

1.1 The Problem

As part of an on-going project at Oklahoma State University, studies are in progress concerned with experimental and theoretical research in 2-D axisymmetric geometries under low speed, nonreacting, turbulent, swirling flow conditions. The flow enters the test section and proceeds into a larger chamber (the expansion ratio  $D/d = 2$ ) via a sudden or gradual expansion (side-wall angle  $\alpha = 90$  and  $45$  degrees). Inlet swirl vanes are adjustable to a variety of vane angles with  $\phi = 0, 38, 45, 60$

and  $70$  degrees being emphasized. A downstream flow contraction nozzle of area ratio 2 or 4 may be located at  $L/D = 1$  or  $2$  and its effect studied. The general aim is to characterize the time-mean and turbulence flowfield, recommend appropriate turbulence model advances, and implement and exhibit results of flowfield predictions. The present contribution concentrates on the time-mean flow characterization via the five-hole pitot probe technique. The paper is based on a recently-completed M.S. Thesis<sup>1</sup> and extends earlier work to higher swirl strengths and downstream nozzle effects.

1.2 Previous Studies

Recent studies on this test facility include:

1. Flow visualization has been achieved via still<sup>2</sup> and movie<sup>3</sup> photography of neutrally-buoyant helium-filled soap bubbles and smoke produced by an injector and a smoke wire.
2. Time-mean velocities have been measured with a five-hole pitot probe at low swirl strengths.<sup>2</sup>
3. Turbulence measurements have recently been completed on swirling (up to  $\phi = 45$  degrees) as well as nonswirling flows using a six-orientation single-wire hot-wire technique,<sup>4</sup> enabling all Reynolds stress components to be deduced.
4. An advanced computer code has been developed to predict corresponding confined swirling flows to those studied experimentally.<sup>5</sup>
5. Tentative predictions<sup>6</sup> have now been supplemented by predictions made from realistic inlet conditions<sup>7</sup> for a complete range of swirl strengths with downstream nozzle effects.<sup>8</sup>

Previous experimenters have described time-mean velocity measurement techniques applicable to both swirling and nonswirling flows. They are extensively surveyed and categorized in a recent Ph.D. Thesis.<sup>9</sup> The most relevant confined flow experiments are discussed in Refs. 10-21. These experiments include time-mean velocity measurements [with hot-wire and pitot probes and laser Doppler anemometry], turbulence measurements [with hot-wires and laser anemometers] and flow visualization. The majority of the measurements were made in nonswirling flows<sup>13-19</sup>, however some noteworthy experiments were made in swirling confined jets.<sup>10,12</sup> Direct comparison between the results of the cited experiments and the present experimental results is generally not possible because of differences in geometry. However, in the nonswirling jet, comparisons are possible with experiments of Chaturvedi<sup>19</sup> who measured mean and turbulent flow quantities downstream of a sudden expansion of diameter ratio 2.0 and various expansion sidewall angles  $\alpha$ . Measurements of mean velocity in regions of high turbulence intensity and where the direction of the velocity vector is unknown were made with a pitot tube. Mean velocity was also measured with a constant temperature hot-wire anemometer using a single wire. In addition, a cross-wire was used to measure all the

\* Graduate Student, School of Mechanical and Aerospace Engineering, Student Member AIAA

\*\* Professor, School of Mechanical and Aerospace Engineering, Associate Fellow AIAA

Reynolds stresses. Recent swirl flow data are now becoming available.<sup>20,21</sup>

### 1.3 The Present Contribution

The objective of the present paper is to characterize the effects of several parameters on the time-mean flowfield including: side-wall expansion angle  $\alpha = 90$  and  $45$  deg., swirl vane angle  $\phi = 0, 38, 45, 60,$  and  $70$  deg., contraction nozzle area ratio  $AR = 2$  and  $4$  and location  $L/D = 1$  and  $2$ . Section 2 describes the facilities and instrumentation employed, along with the procedure for five-hole pitot probe measurements and data reduction. Results are presented and discussed in Section 3, while Section 4 draws conclusions from the study.

## 2. Experimental Approach

### 2.1 The Confined Jet Test Facility

The confined jet facility is described at length elsewhere.<sup>1,9</sup> It has an axial flow fan whose speed can be changed by altering a vari-drive mechanism. Numerous fine screens and straws produce flow in the settling chamber of relatively low turbulence intensity. The contraction section leading to the test section has been designed by the method of Morel<sup>22</sup> to produce a minimum adverse pressure gradient on the boundary layer and thus avoid unsteady problems associated with local separation regions. The sudden expansion consists of a 15 cm diameter circular jet nozzle, exiting abruptly into a 30 cm diameter test section of length 125 cm, which is constructed of plexiglass to facilitate flow visualization. The side-wall angle  $\alpha$  and swirl vane angle  $\phi$  are variable. The side-wall angle is set by inserting a block with side-wall angle  $\alpha$  of  $90$  or  $45$  deg. Typical operating Reynolds numbers [based on inlet average velocity and inlet diameter] are in the range 53,000 to 150,000 depending upon fan speed and aerodynamic blockage of the swirl vanes. It has been observed that this is approximately in the Reynolds number insensitive range for this facility,<sup>9</sup> in terms of nondimensional flow characteristics further downstream.

A schematic of the swirler is shown in Fig. 1. It has ten vanes which are individually adjustable to any angle  $\phi$ , and a hub with a streamlined upstream nose and a flat downstream face. The nose has a hyperbolic shape with a very smooth surface so as to offer minimal flow interference. The flat blades are wedge-shaped to give a constant pitch-to-chord ratio of approximately one which should give good turning efficiency.<sup>2,3</sup> With an expansion block attached to the exit of the swirl pack, the expansion plane [ $x/D = 0$ ] is 3.2 cm downstream of the swirl exit [where  $x/D = -0.11$ ].

The effects of a downstream contraction nozzle on the upstream flow in the test section is important in combustor aerodynamics. Two nozzles of area ratio 2 and 4 are being used. The weaker one is shown diagrammatically in Fig. 2. Its upstream face is contoured in a quarter circle as found in practical ramjet combustors. The stronger contraction nozzle is shown in Fig. 3. Its upstream face is 45 degree slope, more typical of gas turbine combustion chamber exits. These blocks may be located at any axial position in the test section.

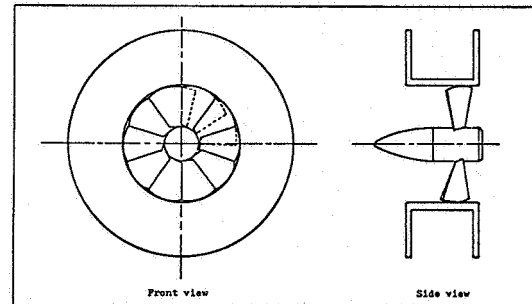


Fig. 1 Annular vane swirler

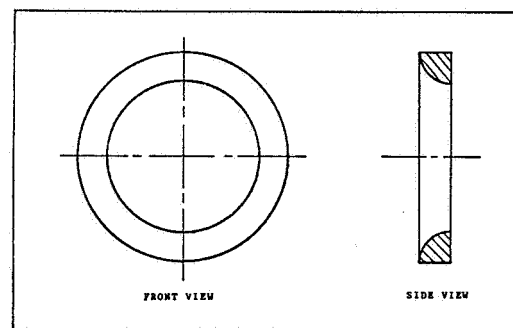


Fig. 2 The weak contraction nozzle with area ratio 2

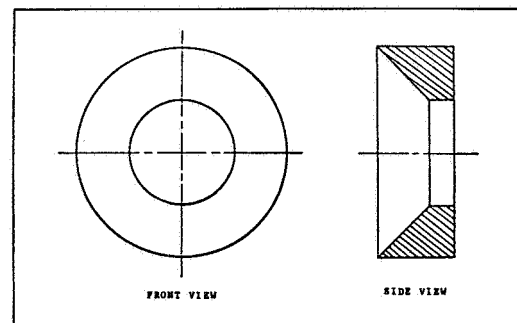


Fig. 3 The strong contraction nozzle with area ratio 4

## 2.2 Five-Hole Pitot Probe Instrumentation

The five-hole pitot probe is one of the few instruments capable of measuring both the magnitude and the direction of fluid velocity simultaneously. The five-hole pitot probe used in this study is a model DC-125-12-CD manufactured by United Sensor and Control Corp. The sensing head is hook-shaped to allow for probe shaft rotation without altering the probe tip location. Little information is available concerning the effects of turbulence on a pressure probe in a swirling flow. However, it is asserted that the five-hole pitot probe is accurate within approximately 5 percent for most of the measurements.<sup>2</sup> This value may increase to 10 percent as the velocity magnitude falls below approximately 2.0 m/s because of the insensitivity of the probe to low dynamic pressure and the dependence of probe calibration on the probe Reynolds number.

The instrumentation assembly, in addition to the five-hole pitot probe, is composed of a manual traverse mechanism, two five-way ball valves, a differential pressure transducer, a power supply, and an integrating digital voltmeter. The differential pressure transducer is model 590D from Data-metrics, Inc. It has a differential pressure range of from 0 to  $1.3 \times 10^3 \text{ N/m}^2$ . The integrating voltmeter is the TSI model 1076. As auxiliary equipment, a model 631-B stroboscopes from General Radio, Inc. is used to check the fan speed. A micro-manometer, along with a pitot-static probe, is used to measure the dynamic pressure in the nozzle throat just upstream of the swirler, and therefrom deduce the swirler inlet uniform axial velocity  $u_0$  which is used later for velocity normalizations. Also, a barometer/thermometer unit from Cenco Corporation is used for local pressure and temperature readings. Measurement apparatus is shown diagrammatically in Fig. 4.

## 2.3 Measurement Procedure and Data Reduction

The measurement procedure involves a five-hole pitot probe. It is aligned with the flow yaw angle  $\beta = \tan^{-1}(w/u)$  in the plane perpendicular to the radius, while the pitch angle  $\delta = \tan^{-1} [v/(u^2 + w^2)^{1/2}]$  and total velocity magnitude  $V$  can then be found from previous corresponding free jet calibrations. The technique, associated computer code and user instructions are documented at length elsewhere.<sup>1,9</sup>

Two kinds of calibration are employed to reduce the raw data from the direct measurements. One is the calibration of the voltmeter, which determines a relationship between the voltmeter output and the velocity magnitude. The other is the calibration of the five-hole pitot probe, which consists of two calibration characteristics: pitch angle  $\delta$  versus differential pressure ratio  $(P_N - P_S)/(P_C - P_W)$ , and velocity coefficient

$$C = \rho V^2 / [2(P_C - P_W)]$$

versus pitch angle  $\delta$ .

In the measurement of the flow in the test section, a series of radial traverses is taken in a vertical line with probe tip pointing horizontally. With obvious compass notation given to the five holes, the first measurement for each location is the yaw angle  $\beta$  for a zero reading of  $(P_W - P_E)$ . This means that the probe tip is aligned with the local flow direction in a horizontal plane. Then the five-way switching valves are set so that  $(P_N - P_S)$  is sensed by the pressure transducer.

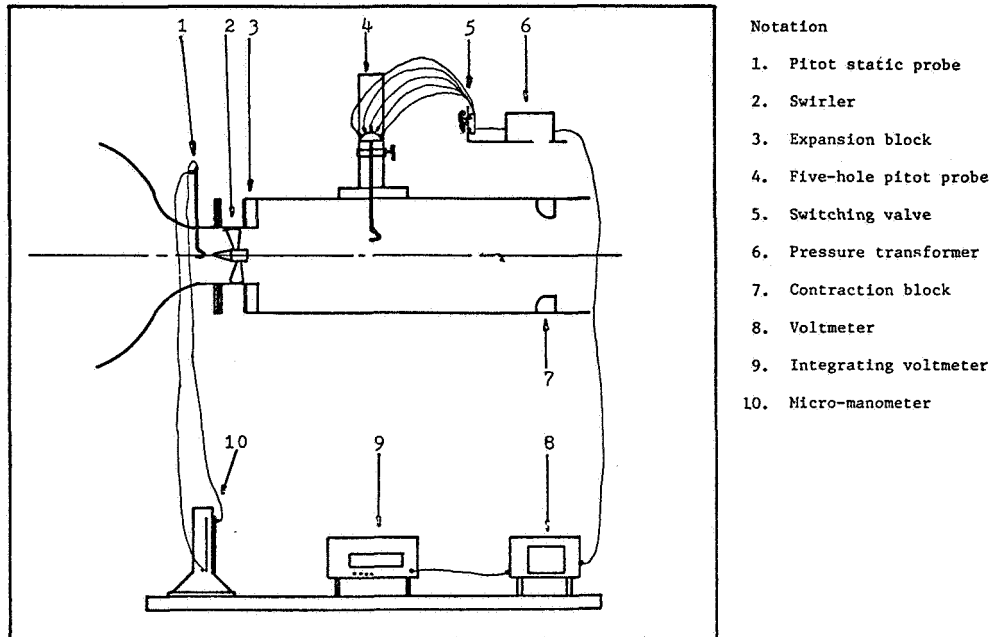


Fig. 4 Apparatus for Mean Velocity Measurements

Finally, the reading of  $(P_C - P_W)$  is similarly measured.

The data reduction employs the two calibration curves, with turbulence effects neglected -- their precise effect on pressure probes in swirl flows is unknown. With the measurement data of the differential pressure ratio  $(P_N - P_C)/(P_C - P_W)$ , the corresponding pitch angle  $\delta$  is obtained with a cubic spline interpolation technique from the appropriate calibration characteristics. The velocity coefficient  $C$  is determined from this value by using the corresponding calibration characteristics. The magnitude of the velocity vector is then calculated from

$$V = \left[ \frac{2}{\rho} (P_C - P_W) \cdot C \right]^{1/2}$$

and the three time-mean velocity components are obtained from this value and the yaw and pitch angles.

### 3. Results and Discussion

Nonswirling and swirling nonreacting flows are investigated in an axisymmetric test section with expansion ratio  $D/d = 2$ , which may be equipped with a contraction nozzle of area ratio 2 and 4. Velocity measurements are made with the five-hole pitot probe as described in Section 2.3. An analysis is made of the effects of various geometric parameters on the extent of the recirculation zones in the flowfield. These parameters include side-wall expansion angle  $\alpha = 90$  and 45 degrees, swirl vane angle  $\phi = 0, 38, 45, 60,$  and 70 degrees, and contraction nozzle location  $L/D = 1$  and 2 (if present). The nozzle inlet velocities and Reynolds numbers employed in this study are high enough to ensure that the flowfields are investigated under conditions independent of Reynolds number variation. All nozzle inlet velocities and Reynolds numbers employed are listed in Table 1. Flow characteristics are extensively tabulated in terms of normalized  $u, v,$  and  $w$  velocity components, yaw angle  $\beta$  and pitch angle  $\delta$  in Ref. 1.

#### 3.1 Effects of Swirl on Sudden Expansion Flows

Swirling flows result from the application of a spiraling motion, with a swirl velocity component being imparted to the flow via the use of swirl vanes. The swirl vane angles employed in this study are 0 (swirler removed), 38, 45, 60, and 70 degrees. Figure 5 parts a through e show the axial and swirl velocity profiles for  $\phi = 0, 38, 45, 60,$  and 70 degrees, respectively, with side-wall expansion angle  $\alpha = 90$  degrees.

The nonswirling flow investigated is obtained with the swirler removed. Figure 5(a) shows a uniform axial velocity entering the test section. The corner recirculation zone extends to just beyond  $x/D = 2.0$ . Measurements for a corresponding flow were taken with a stagnation tube and pitot tube by Chaturvedi.<sup>19</sup> He found the reattachment point to be at  $x/D = 2.3$  which is in good agreement with the present study. Moon and Rudinger<sup>14</sup> located the reattachment point with both theoretical and experimental methods in a similar circular test section with an expansion ratio  $D/d = 1.43$ , which is different from the present study [with  $D/d = 2$ ]. The result yielded a value of  $x/D = 1.25$  as a reattachment point, which corresponds to an attachment point approximately eight step-heights downstream, which is in good agreement with the present study.

The velocity profiles for swirling flows shown in Fig. 5 parts b through e reveal that the flow entering through the swirl vanes is not uniform and has steep velocity gradients in the radial direction especially at high swirl numbers. Furthermore, a considerable back flow around the hub is observed for  $\phi = 70$  degrees, as shown in Fig. 12(e). For all values of swirl vane angle used in this study, the corner recirculation zone does not extend beyond  $x/D = 0.5$ , the closest axial location to the expansion block; instead, the maximum axial velocity is observed close to the top wall at  $x/D = 0.5$ . The effects result from the strong centrifugal forces present in the incoming swirling flow.

The central recirculation zone and precessing vortex core are now discussed. The precessing vortex core is defined as the region of high swirl, low axial velocity flow along the axis, which has a relatively constant small diameter. In flow visualization studies,<sup>2,3</sup> it is seen to precess around the axis of the test section. The central recirculation zone is defined as the wide reverse flow region encountered near the inlet. Articulate impressions are given later in which lines have been drawn connecting the radial positions of zero axial velocity. In case of the vortex core, that region is drawn along the zero axial velocity boundary in the downstream direction after the central recirculation region. The size of the central recirculation zone increases with the increasing swirl vane angle until a certain value of swirl vane angle is reached (around 40 degrees). Then its length begins to decrease under stronger swirl conditions, but its width continues to increase. The core vortex was present at all values of swirl vane angle used in this investigation. In contrast to the central recirculation zone, the vortex core gets continuously wider as the swirl vane angle increases.

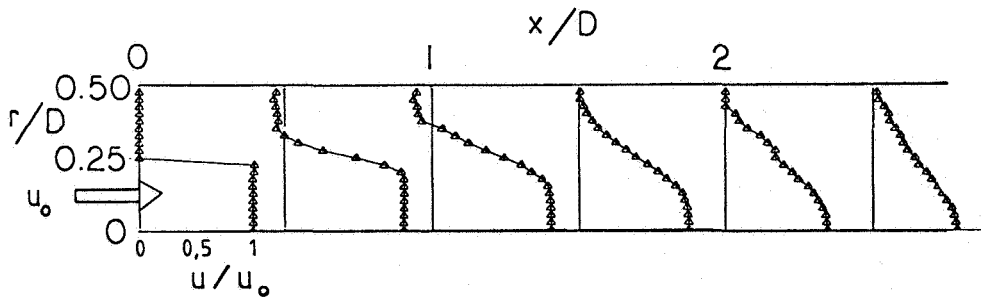
The swirl velocity peaks sharply around the edge of the expansion block before becoming more uniform further downstream as shown in Fig. 15 parts b through e. A considerably nonuniform swirl velocity profile is observed at  $x/D = 0.5$ . Thereafter, relatively steady and uniform velocity profiles are seen, except for the region around the axis. The radial location where the maximum swirl velocity occurs goes up as the swirl vane angle increases. This trend is caused by the increase of centrifugal effects. The swirl velocity along the axis is found to be zero as expected because of symmetry.

#### 3.2 Effects of Gradual Expansion

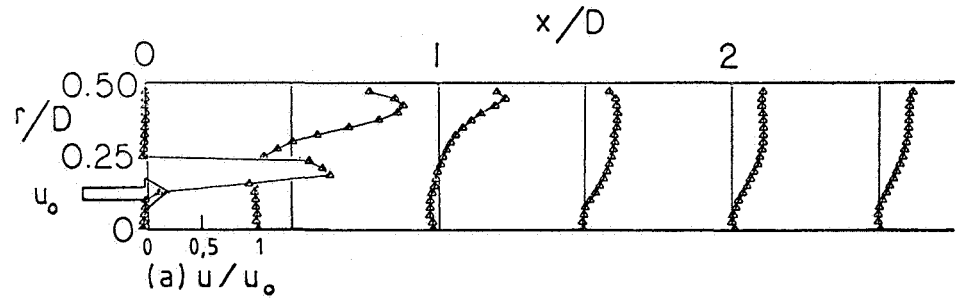
Gradual expansion flows with  $\alpha = 45$  degrees were measured at two axial stations of  $x/D = 0.5$  and 1.0 for swirl vane angles of 0, 38, 45, 60, and 70 degrees. Only the upstream flowfield needed to be thoroughly investigated in these cases, since inlet expansion effects occur in this region the most, and their influence rapidly diminishes in the downstream direction.<sup>2</sup> Measurements were not taken at the inlet in this geometry because the presence of the expansion block interferes with probe positioning.

The corresponding sequence of axial and swirl velocity profiles to a sudden expansion are given in Ref. 1. Velocity profiles for a gradual expansion follow a similar trend to those for a sudden expansion. The major effect of a gradual inlet expansion is to encourage the air to flow along the

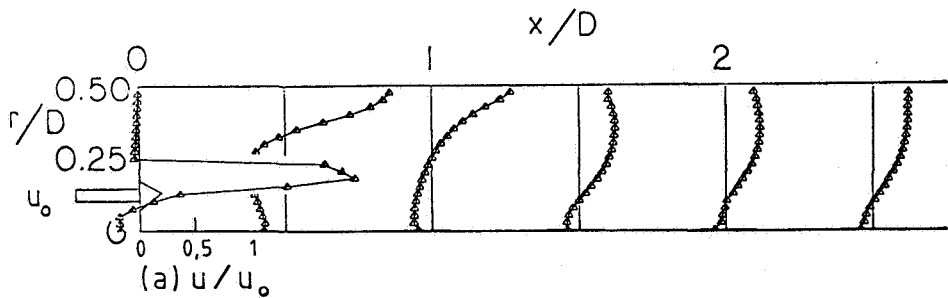




(a) Swirl vane angle  $\phi = 0^\circ$



(b) Swirl vane angle  $\phi = 38^\circ$



(c) Swirl vane angle  $\phi = 45^\circ$

Fig. 5 Velocity profiles for side-wall expansion angle  $\alpha = 90^\circ$  without contraction nozzle

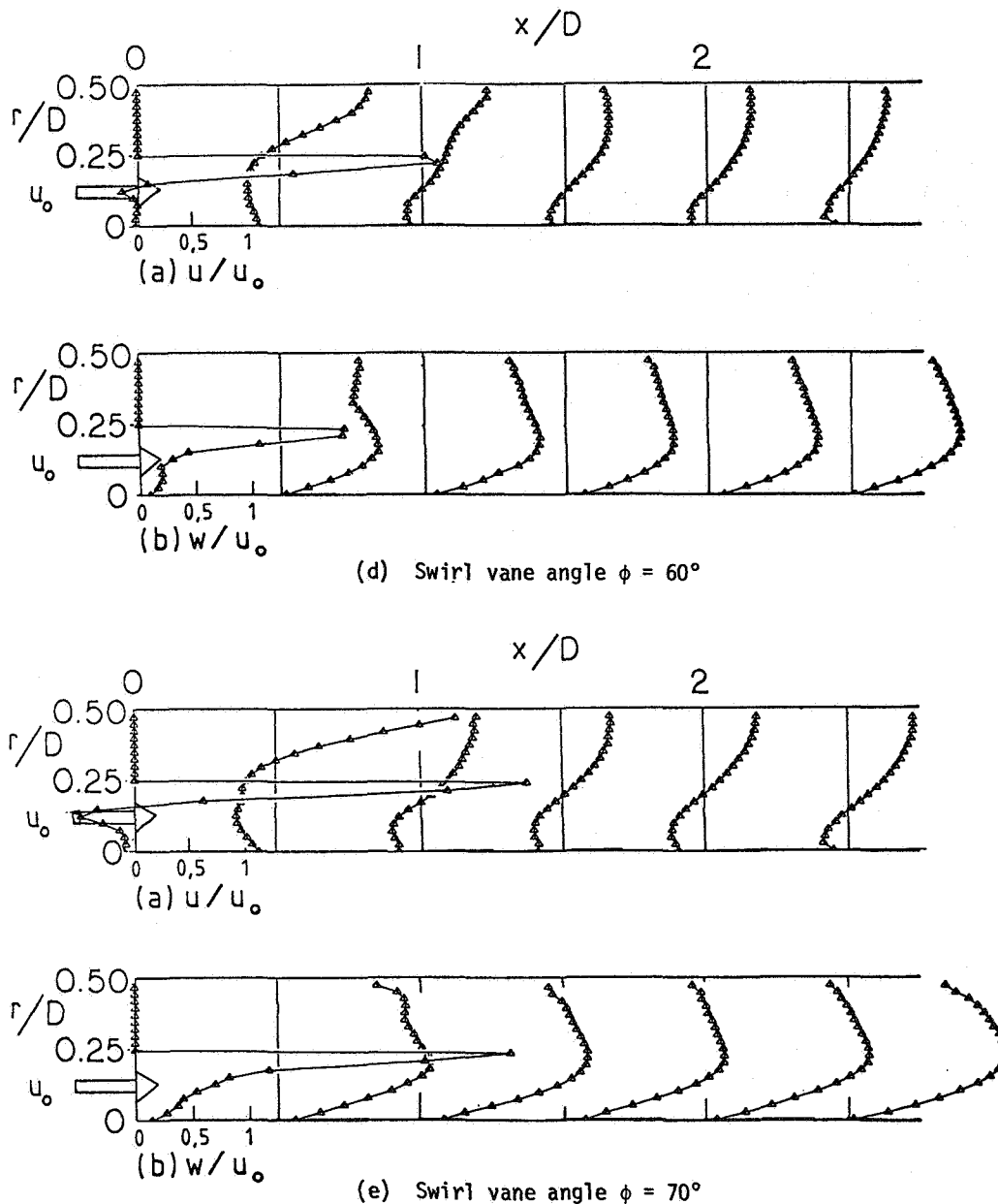


Figure 5 continued

side sloping wall, shorten the corner recirculation zone and accelerate axial velocities close to the top wall. Influence on the central recirculation zone for the swirl flow cases is minimal.

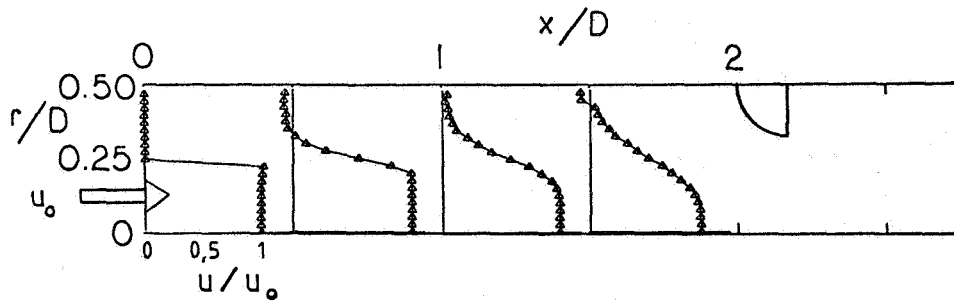
### 3.3 Effects of a Weak Contraction Nozzle

It is best to interpret the data obtained when a contraction nozzle is inserted at different axial stations on the flowfields by comparing them to the data obtained without its presence. The measurements were taken at axial locations ranging from the inlet plane to the axial station just upstream of the station where the contraction block was located. The effect of a weak contraction nozzle with area ratio 2 was investigated with the contraction block located at  $L/D = 1$  and 2 for a range of swirl strengths  $\phi = 0, 45$  and  $70$  deg. with sudden expansion  $\alpha = 90$  deg. only. Figure 6, parts a, b and c

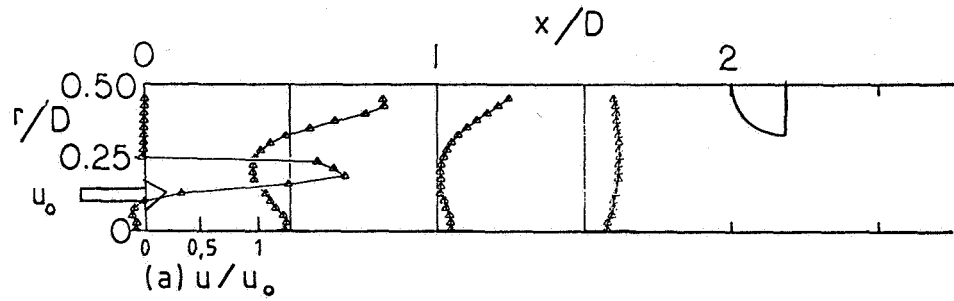
present these velocity profiles with  $L/D = 2$  only; corresponding figures with  $L/D = 1$  appear in Ref. 1.

Figure 6(a) shows that the weak contraction nozzle generally affects the flowfield very little under nonswirling conditions. Furthermore, as the block is moved farther in the downstream direction, its effect on the flowfield decreases. The only effect that can be noticed from the velocity profiles is decreased in length of the corner recirculation region due to the nozzle effect.

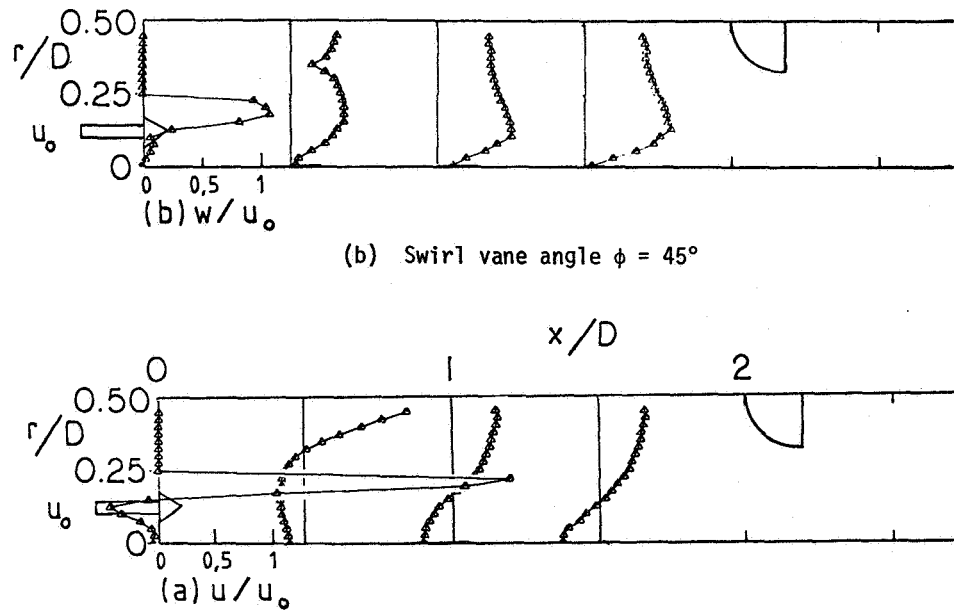
Part b of Fig. 6 shows the axial and swirl velocity profiles for the intermediate swirling flow of  $\phi = 45$  degrees with contraction nozzle at  $L/D = 2$ . Significant positive axial velocities are observed along the centerline, as the nozzle is approached. This situation is in striking contrast to that of the intermediate swirling flow without the contraction block, in which case the



(a) Swirl vane angle  $\phi = 0^\circ$

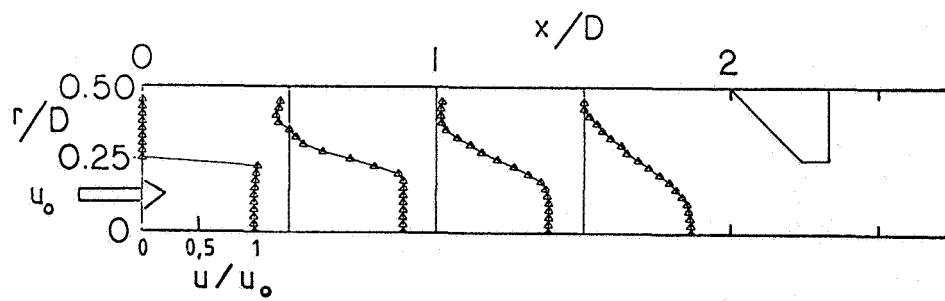


(b) Swirl vane angle  $\phi = 45^\circ$

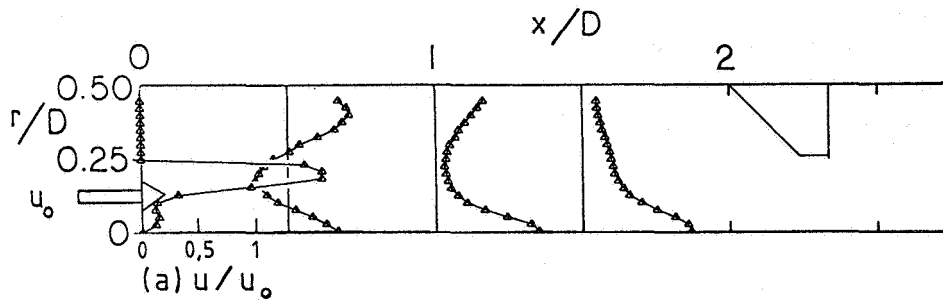


(c) Swirl vane angle  $\phi = 70^\circ$

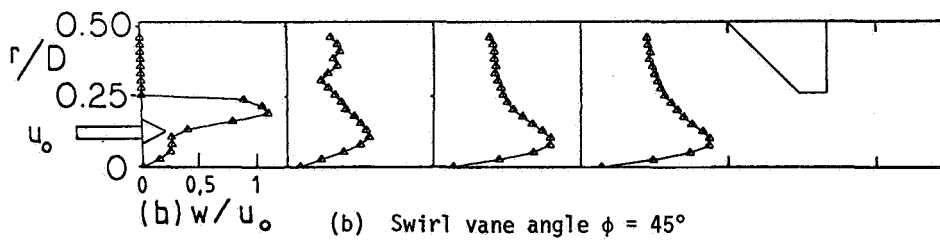
Fig. 6 Velocity profiles with weak contraction nozzle of area ratio 2 located at  $L/D = 2$



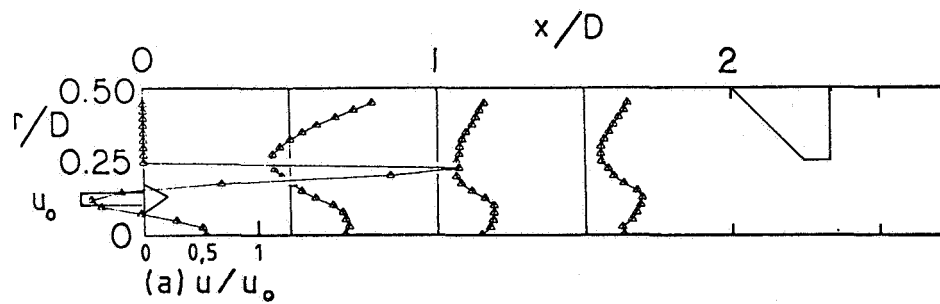
(a) Swirl vane angle  $\phi = 0^\circ$



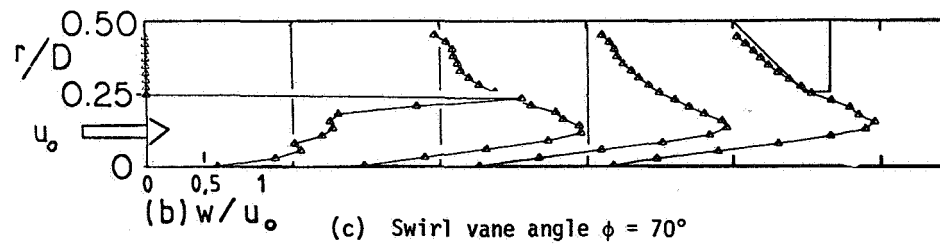
(a)  $u/u_0$



(b)  $w/u_0$  (b) Swirl vane angle  $\phi = 45^\circ$



(a)  $u/u_0$



(b)  $w/u_0$  (c) Swirl vane angle  $\phi = 70^\circ$

Fig. 7 Velocity profiles with strong contraction nozzle of area ratio 4 located at  $L/D = 2$

central recirculation zone spreads extensively along the centerline to  $x/D = 1.5$  with vortex core following it in the test section. Slightly larger swirl velocities are seen in Fig. 6(b) than in Fig. 5(c) without contraction block. This is to be expected as the flow cross-sectional area reduces.<sup>2,3</sup> The axial velocities have quite different profiles at the two axial stations of  $x/D = 1.0$  and  $1.5$ , this region being affected by the proximity of the contraction nozzle. At the axial station of  $x/D = 1.0$ , reverse flow is not observed at all, and considerable positive axial velocities are measured near the axis. A rather uniform velocity profile is obtained at  $x/D = 1.5$ .

For strong swirling flows of  $\phi = 70$  deg., the axial and swirl velocity profiles are shown in Fig. 6(c). The contraction block does not affect the flowfield much except at the axial station immediately upstream of the block. Slightly higher swirl velocities and a slightly narrower core region occur as the blockage is approached as compared with the case without downstream blockage.

In summary, a weak contraction nozzle has most effect on the intermediate swirl case of  $\phi = 45$  deg. Its contraction effect in this case is strong enough to overwhelm the swirling recirculation region. However, a contraction has little effect on weakly swirling and strongly swirling flows, which are dominated by forward flow and centrifugal forces, respectively.

### 3.4 Effects of a Strong Contraction Nozzle

The effect of a stronger contraction nozzle was investigated for a range of swirl strengths  $\phi = 0, 45,$  and  $70$  deg. with side-wall expansion angle  $\alpha = 90$  degrees. The contraction nozzle, of area ratio 4 with 45 degree sloping upstream face, was located at  $L/D = 1$  and  $2$ . Figure 7 parts a, b, and c show these velocity profiles with  $L/D = 2$  only, while results with  $L/D = 1$  appear in Ref. 1.

Figure 7(a) shows that the flowfield with a strong contraction nozzle changes very little as compared to the corresponding flowfield with a weak contraction nozzle shown in Fig. 6(a), or the corresponding flowfield without a contraction nozzle shown in Fig. 5(a).

Figure 7(b) shows the axial and swirl velocity profiles for a swirl vane angle  $\phi = 45$  deg. The presence of a strong contraction nozzle generates a high positive axial velocity near the axis at all axial locations. However, it decelerates the axial velocity close to the top wall. The central recirculation zone is much smaller than previous corresponding cases, and it is located in an annular region. The swirl velocity profiles show narrower core regions with stronger swirl velocity magnitudes and gradients than previously.

For swirl vane angle  $\phi = 70$  degrees, the axial and swirl velocity profiles are given in Fig. 7(c) with the strong contraction blockage located at  $L/D = 2$ . The axial velocity near the axis is highly positive and the central recirculation region is very small, extending in an annular region to less than  $x/D = 1.0$ , much less than its corresponding case with the weak contraction block and considerably less than the no-blockage case of Fig. 5(e). At the axial station  $x/D = 1.0$ , forward flow occurs across the whole test section. This situation is in

sharp contrast to that of a weak contraction nozzle, in which case the contraction block affects the flowfield very little under strong swirling conditions, with centrifugal effects dominating. Swirl velocity profiles given in Fig. 7(c) show the even narrower core than at  $\phi = 45$  deg. with very strong swirl velocity magnitudes and gradients. Summarizing, whereas the effect of a weak contraction nozzle of area ratio 2 is confined to intermediate swirl cases, a strong contraction nozzle of area ratio 4 affects both intermediate and strongly swirling flow cases. Visual impact is enhanced by artistic impressions of the overall flowfield characteristics, which are presented in Figs. 8, 9 and 10 for the cases of no blockage, weak blockage at  $L/D = 2$  and strong blockage at  $L/D = 2$ . In each case a range of swirl strengths is considered, for inlet side-wall angle  $\alpha = 90$  deg. only.

### 4. Conclusions

The nonswirling confined jet possesses a corner recirculation zone extending to just beyond  $x/D = 2$  with no central recirculation zone. The presence of a swirler shortens the corner recirculation zone and generates a central recirculation zone followed by a precessing vortex core. The effect of a gradual inlet expansion is to encourage the flow to remain close to the sidewall and shorten the extent of the corner recirculation zone in all cases investigated. A contraction nozzle of area ratio 2 has little effect on weakly swirling and strongly swirling flows, which are dominated by forward flow and centrifugal forces, respectively. For intermediate swirl cases, it encourages forward movement of otherwise slow-moving air and thereby shortens the central recirculation zone. A strong contraction nozzle of area ratio 4 has a more dramatic effect on the flowfields, particularly affecting both intermediate and strong swirling flow cases. Central recirculation zones are shortened considerably, and axial velocities near the facility axis become highly positive. Core regions become narrower with very strong swirl velocity magnitudes and gradients.

### Acknowledgments

Special thanks are extended to NASA Lewis Research Center and Air Force Wright Aeronautical Laboratories for financial support via NASA Grant No. NAG 3-74, technical monitor Dr. J. D. Holdeman.

### References

1. Yoon, H. K., Five-Hole Pitot Probe Time-Mean Velocity Measurements in Confined Swirling Flows. MS Thesis, Oklahoma State University, July 1982.
2. Rhode, D. L., Lilley, D. G., and McLaughlin, D. K., Mean Flowfields in Axisymmetric Combustor Geometries with Swirl, Paper AIAA 82-0177, Orlando, Florida, Jan. 11-14, 1982. AIAA Journal, 1983 (in press).
3. Lilley, D. G., Turbulent Combustor Flowfield Investigation. Paper in Combustion Fundamentals Research Conference, held at NASA Lewis Research Center, Cleveland, Ohio, Oct. 21-22, 1982, pp. 152-168.
4. Janjua, S. I., McLaughlin, Jackson, T. W., and Lilley, D. G., Turbulence Measurements in

- a Confined Jet Using a Six-Orientation Hot-Wire Probe Technique. Paper AIAA 82-1262, Cleveland, Ohio, June 21-23, 1982.
5. Lilley, D. G., and Rhode, D. L., A Computer Code for Swirling Turbulent Axisymmetric Recirculation Flows in Practical Isothermal Combustor Geometries, NASA CR-3442, Feb. 1982.
  6. Rhode, D. L., Lilley, D. G., and McLaughlin, D. K., On the Prediction of Swirling Flowfields Found in Axisymmetric Combustor Geometries. ASME Journal of Fluids Engng., Vol. 104, 1982, pp. 378-384.
  7. Sander, G. F., and Lilley, D. G., The Performance of an Annular Vane Swirler. Report on Work in Progress, School of Mech. and Aero. Engng., Oklahoma State University, Stillwater, Okla., Oct. 1982.
  8. AbuJelala, M. T., and Lilley, D. G., Confined Swirling Flow Predictions, Paper AIAA-83-0316, Reno, Nevada, Jan. 10-13, 1983.
  9. Rhode, D. L., Predictions and Measurements of Isothermal Flowfields in Axisymmetric Combustor Geometries, Ph.D. Thesis, School of Mech. and Aero. Engng., Oklahoma State University, Stillwater, Okla., Dec. 1981.
  10. Habib, M. A., and Whitelaw, J. H., Velocity Characteristics of Confined Coaxial Jets With and Without Swirl, ASME Paper No. 79-WA/FE-21, New York, Dec. 2-7, 1979.
  11. Srinivasan, R., and Mongia, H. C., Numerical Computations of Swirling Recirculating Flows, Final Report NASA-CR-165196, Sept. 1980.
  12. Vu, B. T., and Gouldin, F. C., Flow Measurement in a Model Swirl Combustor, AIAA Journal, Vol. 20, No. 5, May 1982, pp. 642-651.
  13. Ha Minh, H., and Chassaing, P., Perturbations of Turbulent Pipe Flow, Proc. Symposium on Turbulent Shear Flows, Pennsylvania State University, April 1977, pp. 13.9-13.17.
  14. Moon, L. F., and Rudinger, G., Velocity Distribution in an Abruptly Expanding Circular Duct, ASME Journal of Fluids Engng., March 1977, pp. 226-230.
  15. Phaneuf, J. T., and Netzer, D. W., Flow Characteristics in Solid Fuel Ramjets, Report No. NPS-57Nt-74081, July 1974, Prepared for the Naval Weapons Center by the Naval Postgraduate School.
  16. Back, L. H., and Roschke, E. J., Shear Layer Flow Regimes and Wave Instabilities and Reattachment Lengths Downstream of an Abrupt Circular Channel Expansion, ASME Journal of Applied Mechanics, September 1972, pp. 677-681.
  17. Roschke, E. J., and Back, L. H., The Influence of Upstream Conditions on Flow Reattachment Lengths Downstream of an Abrupt Circular Channel Expansion, J. of Biomech., Vol. 9, 1976, pp. 481-483.
  18. Krahl, K. M., and Sparrow, E. M., Turbulent Heat Transfer in the Separated, Reattached, and Redevelopment Regions of a Circular Tube, ASME Journal of Heat Transfer, February 1966, pp. 131-136.
  19. Chaturvedi, M. C., Flow Characteristics of Axisymmetric Expansions, Proc. Journal Hydraulics Division, ASCE, Vol. 89, No. HY3, 1963, pp. 61-92.
  20. Johnson, B. V., Mass and Momentum Transport Experiments. Paper in Combustion Fundamentals Research Conference, held at NASA Lewis Research Center, Cleveland, Ohio, Oct. 21-22, 1982, pp. 191-198.
  21. Gouldin, F. C., Depskey, J. S., and Lee, S.-L., Velocity Field Characteristics of a Swirling Flow Combustor. Paper AIAA 83-0314, Reno, Nevada, Jan. 10-13, 1983.
  22. Morel, T., Comprehensive Design of Axisymmetric Wind Tunnel Contractions, ASME Paper 75-FE-17, Minneapolis, MN, May 5-7, 1975.
  23. Gupta, A. K., Lilley, D. G., and Syred, N., Swirl Flows, Abacus Press, Tunbridge Wells, England, 1983 (in press).

Table 1 Inlet Velocities and Reynolds numbers

$\phi$	$\alpha = 90^\circ$		$\alpha = 45^\circ$	
	$U_{in}$ (m/s)	$Re_d$	$U_{in}$ (m/s)	$Re_d$
$0^\circ$	15.7	150,000	15.5	154,000
$38^\circ$	10.5	100,000	10.6	105,000
$45^\circ$	12.6	120,000	14.9	148,000
$60^\circ$	8.84	84,000	9.58	95,000
$70^\circ$	5.57	53,000	6.25	62,000

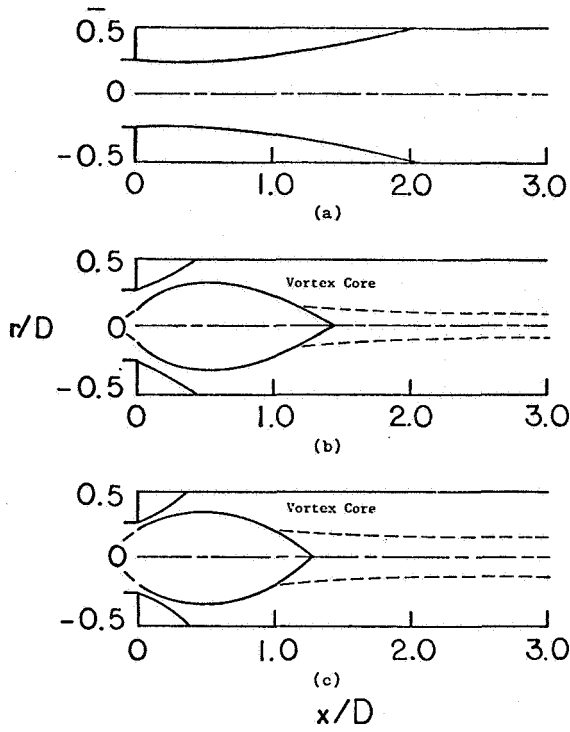


Fig. 8 Artistic impression of dividing streamlines without contraction nozzle for various swirl vane angles: (a)  $\phi = 0^\circ$ , (b)  $\phi = 45^\circ$  and (c)  $\phi = 70^\circ$ .

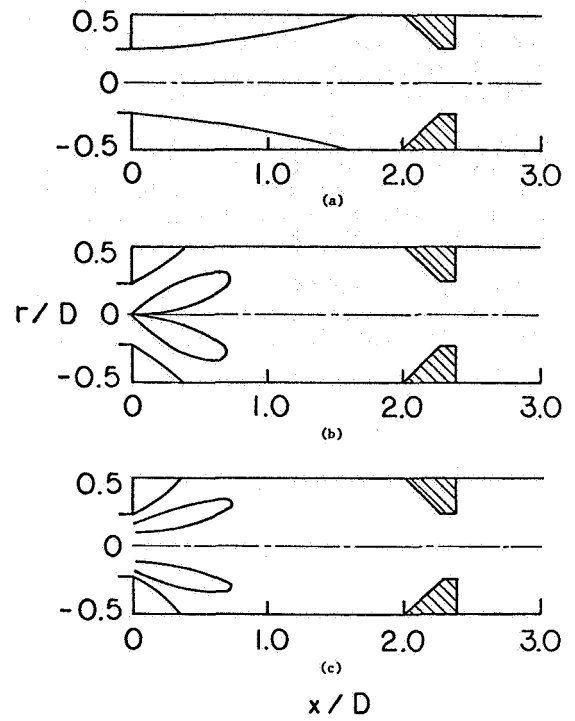


Fig. 10 Artistic impression of dividing streamlines with strong contraction nozzle for various swirl vane angles: (a)  $\phi = 0^\circ$ , (b)  $\phi = 45^\circ$  and (c)  $\phi = 70^\circ$ .

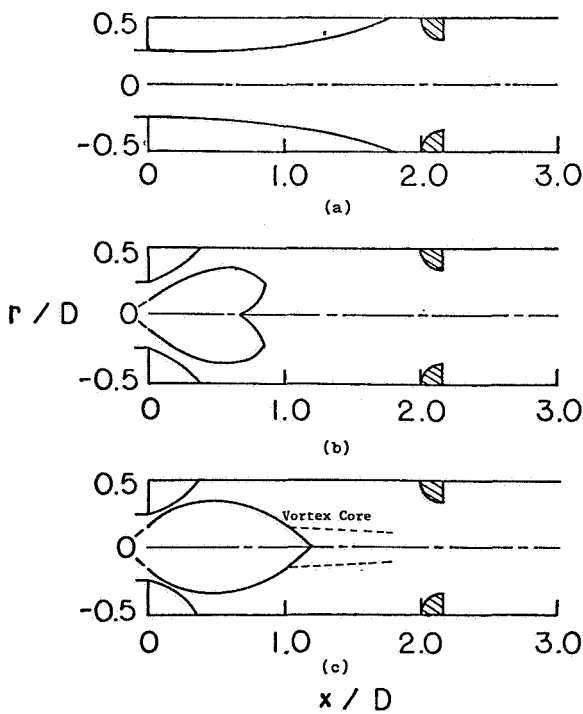


Fig. 9 Artistic impression of dividing streamlines with weak contraction nozzle for various swirl vane angles: (a)  $\phi = 0^\circ$ , (b)  $\phi = 45^\circ$  and (c)  $\phi = 70^\circ$ .

APPENDIX E

CONFINED SWIRLING FLOW PREDICTIONS

(AIAA-83-0316)



# CONFINED SWIRLING FLOW PREDICTIONS

by

M. T. Abujelala\* and D. G. Lilley\*\*  
Oklahoma State University, Stillwater, Okla.

## Abstract

The validity of flowfield predictions resulting from the choice of inlet velocity profiles is assessed. Results demonstrate that realistic predictions are forthcoming only from the inclusion of realistic axial, radial and swirl velocity profiles as inlet conditions. Predictions are then exhibited for a range of swirl strengths  $\phi = 0, 38, 45, 60$  and  $70$  degrees using measured inlet axial, radial and swirl velocity profiles in each case. Downstream nozzle effects (two blockage sizes at two axial locations) are included. The ensuing flowfields are characterized via velocity profiles and streamline patterns, and illustrate the large-scale effects of inlet swirl and outlet nozzles on flowfields.

## Nomenclature

D	test section diameter
d	inlet nozzle diameter
G	$= w_{mo}/u_o$ (without subscript), axial flux of momentum (with subscript)
k	kinetic energy of turbulence
L	contraction nozzle downstream distance
R	inlet nozzle radius = $d/2$
S	swirl number = $G_\theta/(G_x \cdot R)$
$\bar{v} = (u, v, w)$	time-mean velocity (in $x$ -, $r$ -, $\theta$ -directions)
$x, r, \theta$	axial, radial, azimuthal cylindrical polar coordinates
$\alpha$	side-wall expansion angle
$\epsilon$	turbulent energy dissipation rate
$\phi$	swirl vane angle with respect to facility axis

## Subscripts

h	relating to swirler hub
m	station maximum value
o	value at inlet to flowfield
x	relating to axial direction
$\theta$	relating to swirl direction

## Superscripts

( )'	value calculated excluding pressure contribution
------	--

## 1. Introduction

### 1.1 The Problem

Designers of gas turbine and ramjet combustion chambers are aided not only by experiments but also by predictions of their flowfields. Recently, these are being obtained directly via mathematical models incorporating numerical finite difference computer codes. Improvement and use of these tech-

niques will significantly increase understanding and reduce the time and cost of development.<sup>1-5</sup> The present contribution forms part of a project on the investigation of flowfields found in typical combustor geometries; studies are in progress concerned with experimental and theoretical research in 2-D axisymmetric conditions. The general aim is to characterize the time-mean and turbulence flowfield, recommend appropriate turbulence model advances, and implement and exhibit results of flowfield predictions.

In the Oklahoma State University confined jet facility, described at length elsewhere,<sup>6,7</sup> the air flow enters the test section and proceeds into a larger chamber (the expansion ratio  $D/d = 2$ ) via a sudden or gradual expansion (side-wall angle  $\alpha = 90$  and  $45$  degrees). Inlet swirl vanes are adjustable to a variety of vane angles with values of  $\phi = 0, 38, 45, 60$  and  $70$  degrees being emphasized. A downstream flow contraction nozzle of area ratio 2 or 4 may be located at  $L/D = 1$  or  $2$  and its effect studied. The present paper exhibits predictions that illustrate the need to specify realistically the inlet conditions, and presents and discusses predictions for a range of swirl strengths and downstream nozzles using measured inlet conditions in each case.

### 1.2 Previous Studies

The current status of the research program is described with appropriate reference citations in a companion paper.<sup>7</sup> Preliminary efforts at numerical prediction of this flowfield have been documented,<sup>8,9</sup> these using an advanced version<sup>10</sup> (called STARPIC) of the Imperial College TEACH-T computer program.<sup>11</sup> Codes of this type have been applied to other 2-D<sup>12-20</sup> and 3-D<sup>21-24</sup> problems of interest to the combustor designer. Progress in all these areas are extensively reviewed in recent textbooks.<sup>5,25,26</sup> Most application-oriented prediction studies use the familiar two-equation  $k-\epsilon$  turbulence model,<sup>27,28</sup> which has been found to be inadequate for correct simulation of complicated swirling recirculating flows.<sup>25</sup> Success at the turbulence modeling problem is a prerequisite to the prediction of practical turbulent reacting flows, a fact which prompted the present research program on nonreacting flows.

### 1.3 The Present Contribution

The governing differential equations of swirling recirculating flows are elliptic, and solutions depend strongly on the boundary conditions applied around the flow domain. It is important to define adequately the boundary conditions, especially the inlet velocity profiles, yet most of the studies cited earlier<sup>8-24</sup> make gross simplifications regarding inlet conditions, and especially with regard to the inlet radial velocity which is often taken to be zero. Axial and swirl velocity profiles, if not measured, are often assumed to be simple flat profiles, or sometimes a flat axial profile with a solid body rotation swirl profile.

\* Graduate Student, School of Mechanical and Aerospace Engineering, Student Member AIAA

\*\* Professor, School of Mechanical and Aerospace Engineering, Associate Fellow

Numerical predictions of turbulent swirling recirculating confined flows are presented using various inlet velocity starting conditions for the case of swirl vane angles equal to 45 and 70 degrees. The validity of flowfield predictions resulting from the choice of inlet profiles is assessed by comparing the predicted velocity profiles with corresponding experimental velocity profiles.<sup>7</sup> Results demonstrate that realistic predictions are forthcoming only from the inclusion of realistic axial, radial and swirl velocity profiles as inlet conditions, and that considerable errors occur if unrealistic idealized inlet conditions are used.

Predictions are then exhibited for a range of swirl strengths ( $\phi = 0, 38, 45, 60$  and  $70$  degrees) using measured inlet axial, radial and swirl velocity profiles in each case.<sup>29</sup> The ensuing flowfields are characterized via velocity profiles and streamline patterns, and illustrate the large-scale effects of inlet swirl on flowfields. Downstream nozzle effects (two blockage sizes at two axial locations) are included. Results are assessed via comparison with detailed time-mean velocity measurements obtained with a five-hole pitot probe,<sup>7</sup> and appropriate conclusions are deduced.

## 2. Theoretical Approach

### 2.1 The Swirl Number

The degree of swirl usually is characterized by the swirl number  $S$ , which is a nondimensional number representing axial flux of swirl momentum divided by axial flux of axial momentum times equivalent nozzle radius. That is

$$S = \frac{G_\theta}{G_x d/2} \quad (1)$$

where

$$G_\theta = \int_0^\infty (\rho u w + \rho \overline{u'w'}) r^2 dr \quad (2)$$

is the axial flux of swirl momentum, including the  $x$ - $\theta$  direction turbulent shear stress term

$$G_x = \int_0^\infty (\rho u^2 + \rho \overline{u'^2} + (p - p_\infty)) r dr \quad (3)$$

is the axial flux of axial momentum including the  $x$  direction turbulent normal stress term and a pressure term.

One useful deduction is possible when solid body rotation plug flow is assumed at the nozzle, with  $u$  and  $w$  given by the equations of Case 2 in Section 2.2. That is, axial velocity  $u$  is a constant flat profile and swirl velocity  $w$  increases from 0 (at  $r = 0$ ) to  $w_{m0}$  (at  $r = d/2$ , the outer wall of the nozzle). Then local static pressure  $p$  and local swirl velocity  $w$  are related via

$$p - p_\infty = -\frac{1}{2} \rho w^2.$$

where

$$p_\infty = \text{static absolute pressure at } r = d/2 \text{ at the inlet station, } x/D = 0.$$

If the pressure contribution to  $G_x$  is retained in the form of a  $w^2/2$  term, but the turbulent stress terms are omitted, the analysis leads immediately to:

$$G_\theta = \frac{\pi}{2} \rho u_0 w_{m0} (d/2)^3$$

$$G_x = \frac{\pi}{2} \rho u_0^2 (d/2)^2 (1 - (G/2)^2)$$

where  $G = w_{m0}/u_0$  represents the ratio of maximum velocities measured at the exit plane. Thus the swirl strength can be inferred from

$$S = \frac{G/2}{1 - (G/2)^2} \quad (4)$$

if pressure is included in the  $G_x$  definition, and

$$S' = G/2 \quad (5)$$

if pressure is omitted in  $G_x$ . Both  $S$  and  $S'$  are called swirl numbers, but a given velocity distribution gives different  $S$  and  $S'$  values. The theoretical  $S$  vs.  $G$  seems to be valid only for low swirl strengths with  $S \leq 0.2$ , see Refs. 30 and 31. For higher degrees of swirl, however, the axial velocity distribution deviates from plug flow considerably - the major portion of the flow leaves the orifice near the outer edge.<sup>29-32</sup> Then measured  $S$  values (including pressure contribution) are higher<sup>30</sup> than measured  $G$  values would suggest via Eq. (4). In many practical experiments,  $S'$  values are calculated and quoted based on experimental swirler exit velocity profiles only, with the pressure contribution omitted, see for example, Ref. 33. Pressure variations still exist, although quoted  $S'$  values do not make use of these values. Under these circumstances, for a vane swirler with swirl vane angle  $\phi$ , it can be shown<sup>26</sup> approximately that

$$S' = \frac{2}{3} \left[ \frac{1 - (d_h/d)^3}{1 - (d_h/d)^2} \right] \tan \phi \quad (6)$$

with plug flow solid body rotation exit velocity profiles. Table 1 reveals how  $\phi$ ,  $S'$  and  $G$  are related under such conditions for the swirl vane angles of special interest.

Table 1  $\phi$ ,  $S'$  and  $G$  correspondence for plug flow solid body rotation swirlers with  $d_h/d = 0.25$

$\phi$	$S'$	$G$
0	0	0
38	0.547	1.094
45	0.700	1.400
60	1.212	2.425
70	1.923	3.846

Case 2 discussed in Section 2.2 with associated computations given in Section 3 have axial and swirl velocities deduced in this manner [ $\phi \sim S' \sim G$ ], with appropriate radial pressure gradients being automatically set up in the computer program. Notice that

a gross error would be made if Eq. (4) were to be used to set up the inlet velocities [ $\phi \sim S \sim G$ ], since Eq. (6) is valid for  $S'$  values, not  $S$  values. In fact, corresponding  $G$  values would be much lower than those of Table 1, with  $G$  asymptotically approaching 2 as  $\phi$  and  $S$  tend to 90 deg. and  $\infty$ , respectively.

## 2.2 Types of Inlet Boundary Conditions Considered

In all cases considered, the kinetic energy of turbulence  $k$  and its dissipation rate  $\epsilon$  are specified as in general accepted ways.<sup>10,28</sup> The total local time-mean velocity magnitude has been used in specifying  $k$  at any radial position. Four possible specifications of the inlet velocities are considered:

Case 1. Flat inlet axial and swirl velocities with radial velocity zero are assumed. That is, both  $u$  and  $w$  are constant valued:

$$u_0 = \text{constant}$$

$$w_0 = u_0 \tan \phi$$

where  $\phi$  is the swirl vane angle.

Case 2. As Case 1, except that the inlet swirl velocity profile is assumed to be that of solid body rotation:

$$u_0 = \text{constant}$$

$$w_0 = w_{m0} r/R$$

where  $w_{m0}$  is the maximum orifice value of  $w$  which occurs at the outer edge  $r = R$  of the inlet. The value of  $w_{m0}$  is so chosen as to maintain the swirl number  $S'$  the same as in Case 1, as described in Section 2.1.

Case 3. Measured inlet axial and swirl velocities are used<sup>29</sup> with radial velocity assumed to be zero.

Case 4. Measured inlet axial, radial and swirl velocity values are used, taking data from recent five-hole pitot-probe data in close vicinity of the swirler exit.<sup>29</sup>

## 2.3 The Solution Procedure

The prediction procedure starts from partial differential equations of conservation of mass, momentum (in  $x$ ,  $r$  and  $\theta$  directions), turbulent kinetic energy and its dissipation rate, which govern two-dimensional axisymmetric steady flow. The standard two-equation  $k$ - $\epsilon$  turbulence model is employed, which has been used in a wide variety of turbulent flow situations and good predictive capability has been achieved.<sup>5</sup> The equations differ primarily in their final source terms. The corresponding finite difference equations are solved via an advanced version called STARPIC<sup>10</sup> of the TEACH computer code,<sup>11</sup> using a semi-implicit line-by-line method for values at points of a variable size rectangular grid, with variable under-relaxation.

A complete description of the finally developed computer program [with a full description of the equation, source terms, revised cell volumes for axial and radial velocities, constants occurring and techniques for handling turbulent swirling flow near

curved boundaries] is available.<sup>10</sup> Further, previous swirling flow measurements are incorporated as wall functions to avoid the expense of computing within the boundary layer. Zero velocities on all walls are assumed, with symmetry conditions for most variables along the centerline, except swirl velocity which is given a definite zero value.

The code is operated in the manner described in Ref. 10, with sequential swirl vane angles of 0, 38, 45, 60 and 70 deg. being computed to convergence (approximately 400 iterations, each with 5 field updates for pressure, 4 for axial velocity and 3 for other primary variables) with a 23 x 21 nonuniform grid covering a flow domain of length 4D. A typical computer run covering all these swirl strengths requires about 15 min. of IBM 370/168 CPU time for a basic cost of \$200 which is discounted to \$20 after the 90 percent category 4 discount is applied.

It is conceded that the  $k$ - $\epsilon$  turbulence model is in need of improvement for adequate simulation of turbulence swirling recirculating flow. Developments are taking place on differential and algebraic stress models for swirling flows, as exemplified for strongly swirling flow in vortex tubes.<sup>34</sup> However, these models, and others for three-dimensional transient precessing vortex cores and coherent structure development, are not yet ready for use in application-oriented studies. In addition, such approaches will appreciably increase the computer code complexity and time requirements.

## 3. Flowfield Computations

Predictions are discussed first which deal with the flow through the inlet swirler with vane angles set to  $\phi = 45$  and 70 deg. Various types of inlet profile assumptions, Cases 1 through 4 of Section 2.2, are considered and the similarity and differences in the ensuing flowfield predictions are noted. Predictions are then presented for flowfields with a range of swirl strengths using measured inlet flow velocity profiles for axial, radial and swirl velocity in each case.<sup>29</sup> These and the effects of size and location of a downstream nozzle are predicted and compared with available experimental evidence.<sup>7</sup> With the computer code operated in the manner stated in Section 2.3, to aid convergence, the solution for each value of  $\phi$  (0, 38, 45, 60 and 70 deg.) is used for the initial starting values for the next higher value of  $\phi$ . This includes the predictions for the specific cases of  $\phi = 45$  and 70 deg. discussed at length in Section 3.1. The convergence criterion is that all normalized residual source sums have to be less than 0.004 and all results discussed have been obtained in this manner.

### 3.1 Effects of Inlet Velocity Profiles

Swirl Vane Angle  $\phi = 45$  Deg. Consider first the flowfield resulting when the inlet swirl vane angle is 45 deg. Figures 1 through 4 show predicted velocity profiles at various downstream axial stations, obtained when the inlet velocity profiles are specified by:

- Case 1: Flat  $u$  and  $w$  profiles, with  $v$  zero.
- Case 2: Flat  $u$ , profile, with solid body rotation  $w$ , and  $v$  zero.
- Case 3: Measured  $u$  and  $w$  profiles, with  $v$  zero.
- Case 4: Measured  $u$ ,  $v$  and  $w$  profiles.

as discussed in Section 2.2. The flowfield structure

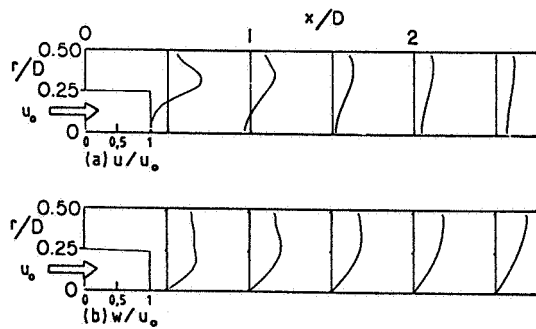


Fig. 1 Predicted velocity profiles for  $\phi = 45$  deg. flowfield using inlet conditions of Case 1

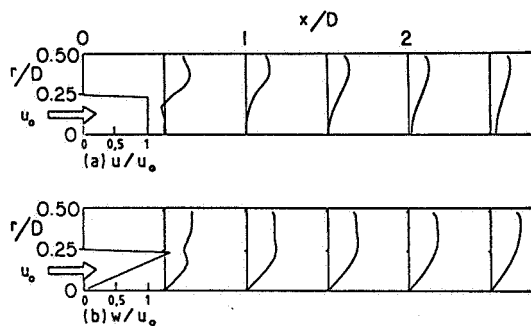


Fig. 2 Predicted velocity profiles for  $\phi = 45$  deg. flowfield using inlet conditions of Case 2

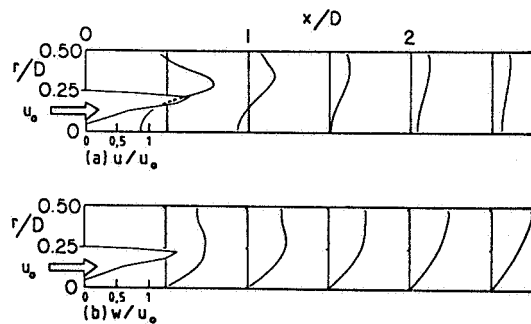


Fig. 3 Predicted velocity profiles for  $\phi = 45$  deg. flowfield using inlet conditions of Case 3

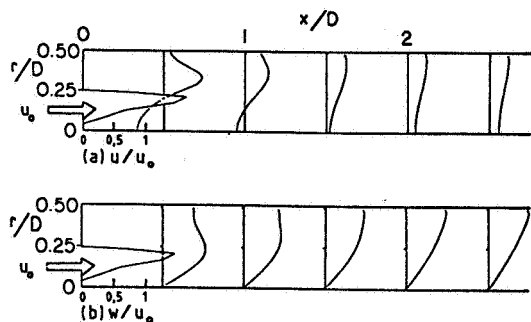
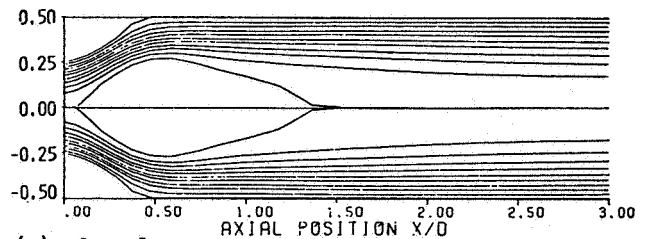
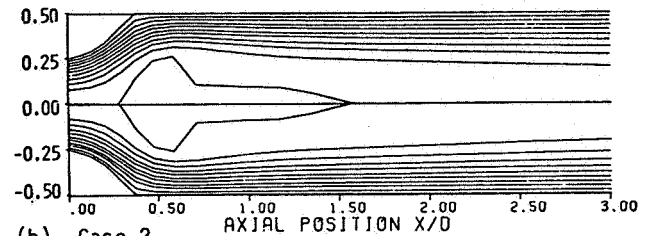


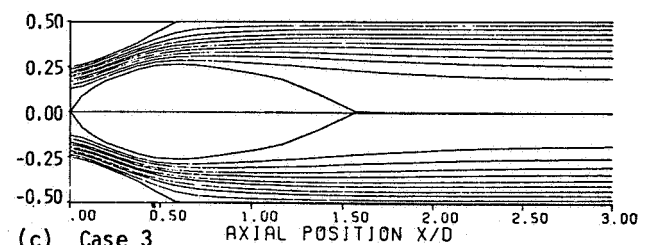
Fig. 4 Predicted velocity profiles for  $\phi = 45$  deg. flowfield using inlet conditions of Case 4



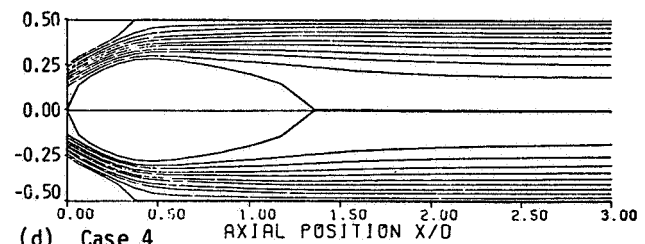
(a) Case 1



(b) Case 2



(c) Case 3



(d) Case 4

Fig. 5 Predicted streamlines for  $\phi = 45$  deg. flowfield using various inlet conditions

for these four cases is further illustrated via streamline plots, which are computer calculated and drawn, in Fig. 5. Inspection of these figures is quite revealing and may be assessed in the light of pitot probe experimental data.<sup>7</sup> Note that in Cases 3 and 4 the appropriate inlet values are plotted at the  $x/D = 0$  location; in fact these are actually the values measured immediately downstream of the swirler,<sup>29</sup> at the location  $x/D = -0.11$ . It is convenient to retain these values on the profile plots in the prediction study, although clearly results at the  $x/D = 0$  location are then not directly comparable with the inlet station data of Ref. 7, which are taken precisely at  $x/D = 0$ . These comments apply also to other plots given in the present paper.

All cases covered in Figs. 1 through 5 give central recirculation zones terminating at about  $x/D = 1.5$ , with Case 4 having a slightly shorter and wider zone. Initial spreading rates vary considerably: only in Cases 3 and 4 does the central

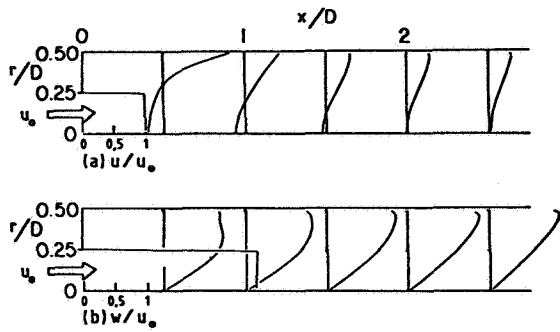


Fig. 6 Predicted velocity profiles for  $\phi = 70$  deg. flowfield using inlet conditions of Case 1

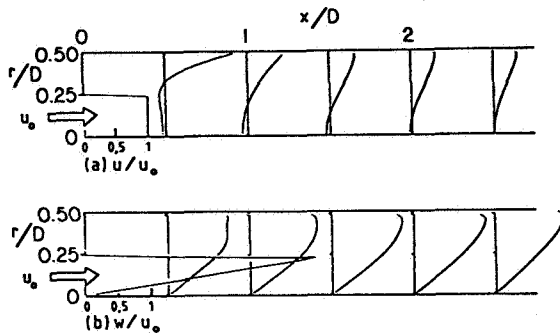


Fig. 7 Predicted velocity profiles for  $\phi = 70$  deg. flowfield using inlet conditions of Case 2

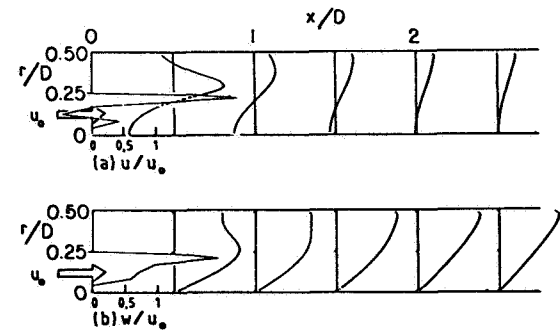


Fig. 8 Predicted velocity profiles for  $\phi = 70$  deg. flowfield using inlet conditions of Case 3

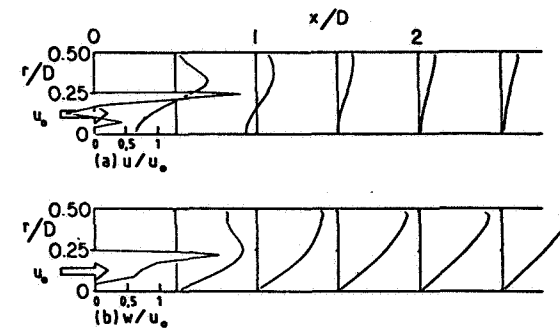
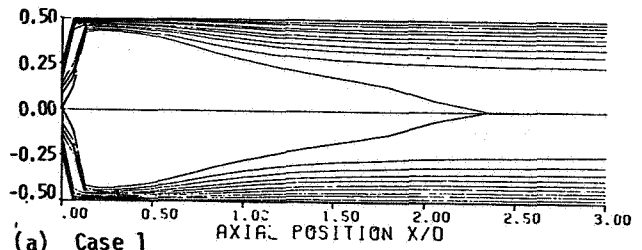
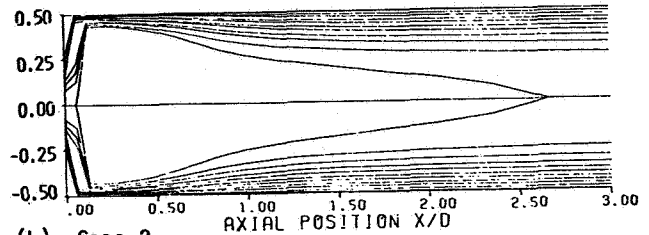


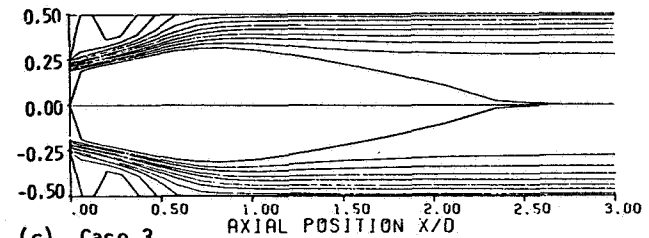
Fig. 9 Predicted velocity profiles for  $\phi = 70$  deg. flowfield using inlet conditions of Case 4



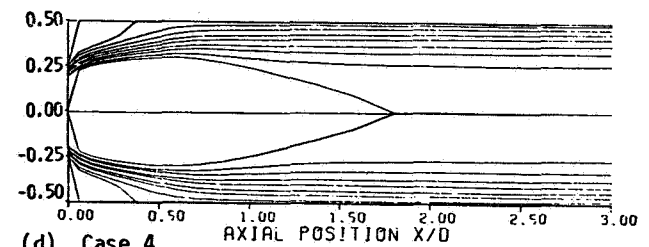
(a) Case 1



(b) Case 2



(c) Case 3



(d) Case 4

Fig. 10 Predicted streamlines for  $\phi = 70$  deg. flowfield using various inlet conditions

recirculation zone begin immediately on entry to the large chamber, with Case 4 spreading most rapidly in the initial region. Cases 1 and 2 do not possess enough centrifugal effect because of their unrealistic inlet swirl velocity profiles. Also, Cases 1 through 3 do not have a radial component of velocity to encourage inlet radial spreading of the streamlines. These inlet flow ideas may be confirmed by observing the size of the corner recirculation zone. Cases 2 and 4 exhibit shorter corner zones, with only Case 4 also possessing the correct central activity near the inlet -- rapid spreading with a central recirculation flow beginning immediately. None of the predictions match the precessing vortex core details found in flow visualization studies<sup>6,35</sup> or the negative axial velocities measured by pitot probe experimentation<sup>7</sup> near the facility axis  $r/D < 0.1$  extending all the way to the test section exit. Nevertheless, comparison of the predictions with the gross features of the corresponding experimental data<sup>7</sup> clearly indicates that the inlet conditions of Case 4 are superior in allowing realistic flowfield prediction.

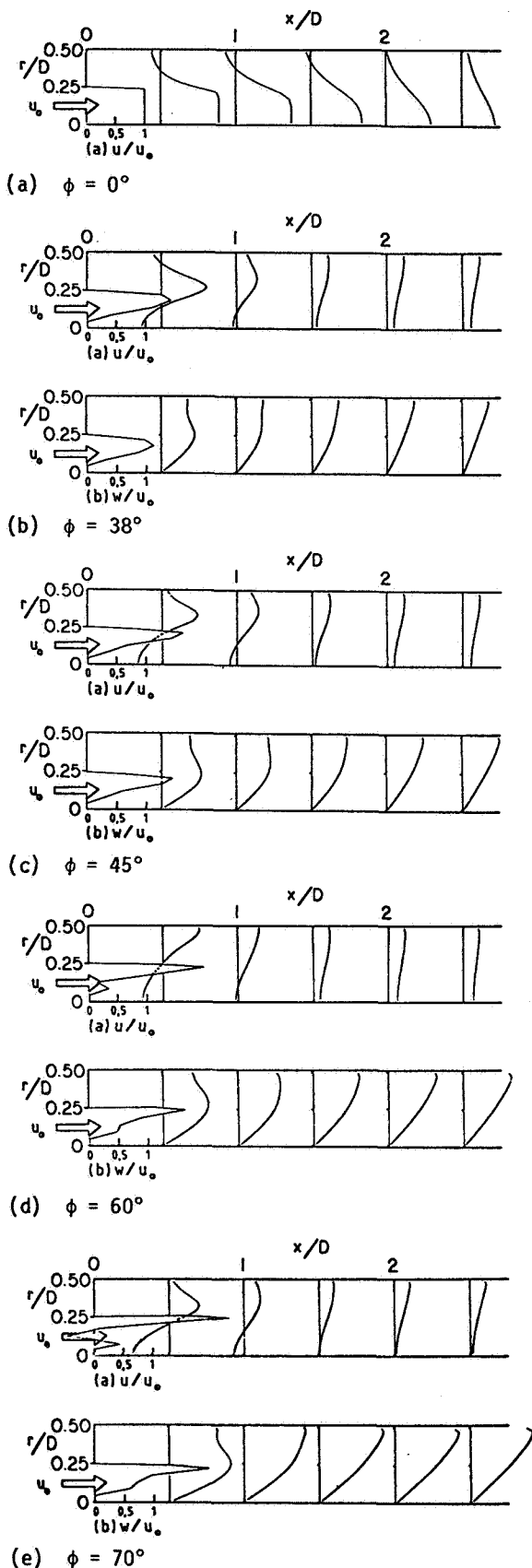


Fig. 11 Predicted velocity profiles using measured inlet  $u$ ,  $v$  and  $w$  profiles

**Swirl Vane Angle  $\phi = 70$  Deg.** Figures 6 through 10 correspond to Figs. 1 through 5 but with the swirl vane angle increased to 70 deg. Now the strong centrifugal forces present in the incoming flow play their part. Initial spreading rates are very high with very small corner recirculation zones in all cases, except that of Case 3 seen in Fig. 8. All central recirculation zones begin immediately at the inlet and are much wider and longer than those with  $\phi = 45$  deg. Those of Cases 1 and 2 are initially very wide: much wider than the measurements<sup>7</sup> indicate. This results from unrealistically large centrifugal forces attributable to unrealistically large swirl velocity magnitudes. Case 3 does not spread rapidly enough at the inlet and a long central recirculation zone extending to  $x/D = 2.5$  is predicted. With the inclusion of the correct inlet radial velocity, a recirculation zone much more like that found experimentally results in Case 4. None of the cases predict swirl velocity profiles very accurately, with  $w$ -profiles more like solid body rotation soon developing in the downstream direction, in contrast to the more free-forced vortex profiles found in the experiments.<sup>7</sup> Fortunately, Cases 1 and 2 seem to do a better job of predicting the long vortex core with negative axial velocity extending a long way downstream, albeit with very poor prediction of initial inlet flow and very wide central recirculation region.

A general deduction may be made from Figs. 1 through 10 when compared with the experimental data.<sup>7</sup> Results demonstrate that realistic predictions are forthcoming only from the inclusion of the most accurate axial, radial and swirl velocity profiles as inlet conditions. Clearly the profiles of Case 4 must be used in future turbulence modeling development studies for improved simulation of this flowfield.

### 3.2 Effects of Swirl

The velocity field predictions for swirl vane angles of 0 (swirler removed), 38, 45, 60 and 70 deg., using measured swirler exit  $u$ ,  $v$  and  $w$  velocity profiles in each case,<sup>29</sup> are displayed in Fig. 11 parts a through e, respectively. Corresponding streamline patterns are plotted as shown in Fig. 12. Three-dimensional axial velocity representations are given in Fig. 13. Here the ordinate of normalized axial velocity is shown impressively as a function of normalized flowfield position. The flow is from right to left, with the sizes and shapes of corner and central recirculation zones being clearly evident, along with axial velocity magnitudes.

The predicted effects of swirl shown in these figures confirm in general the well-known ideas about swirl effects on axisymmetric turbulent confined jet flows.<sup>26</sup> Under nonswirling conditions a large corner recirculation zone exists which extends approximately to  $x/D = 2.3$  for the expansion geometry  $D/d = 2$  and to  $x/D = 1.25$  for  $D/d = 1.43$ , see Refs. 36 and 37. Both these results are consistent with an attachment point about 8 step heights downstream, as found by other researchers.<sup>6,7,14,16</sup> The centerline axial velocity changes gradually from its inlet value as downstream development occurs. However, as the degree of inlet swirl is increased to 38 and 45 deg., axial velocity profiles change dramatically. Near the inlet a central toroidal recirculation zone appears and the corner recirculation zone shortens considerably. Under strong swirl conditions of  $\phi$  equal to 60 and 70 deg., a much wider central recir-

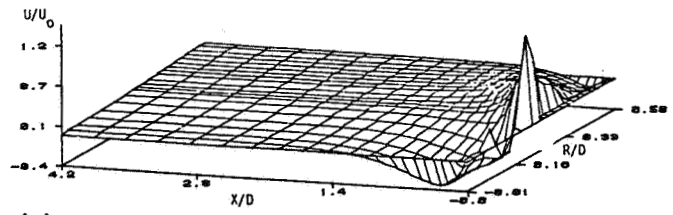
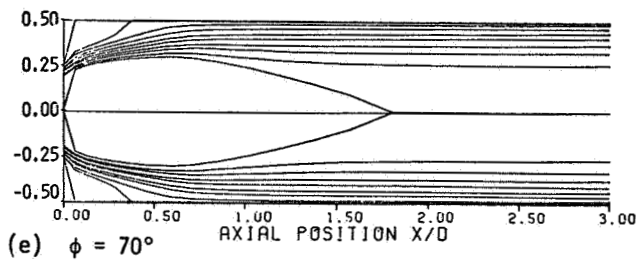
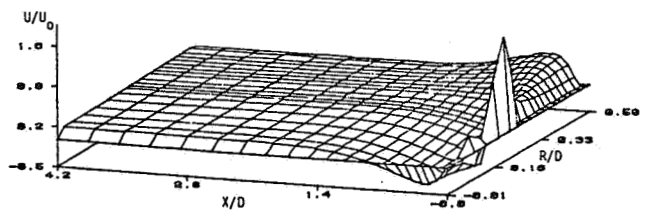
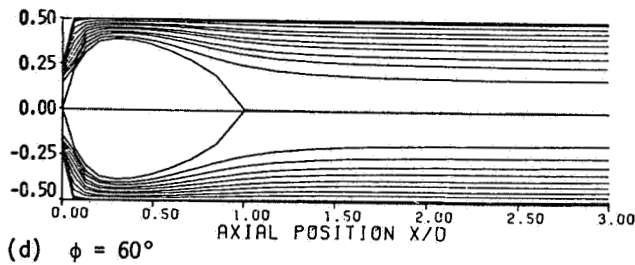
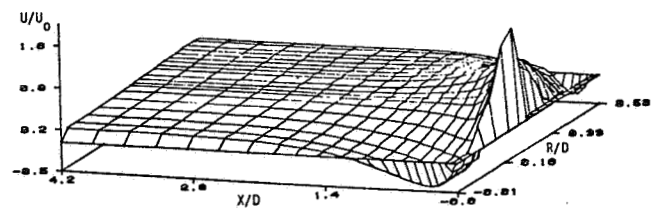
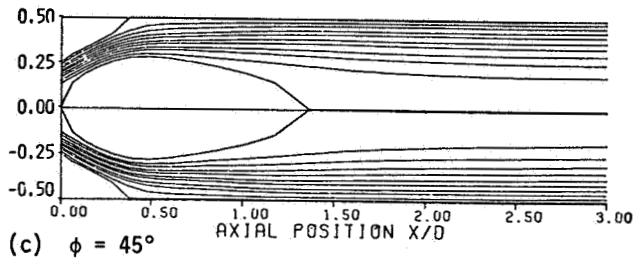
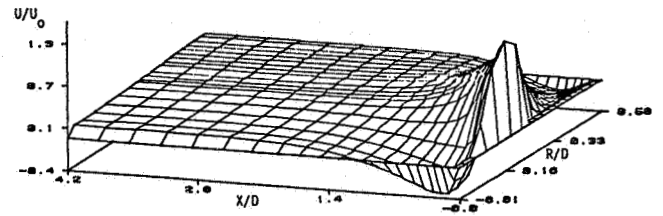
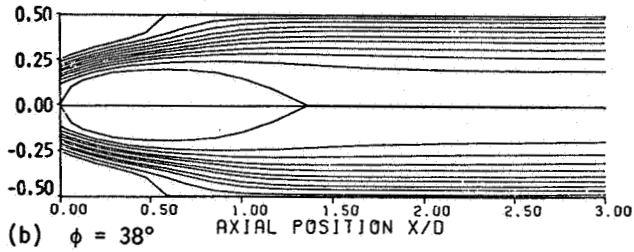
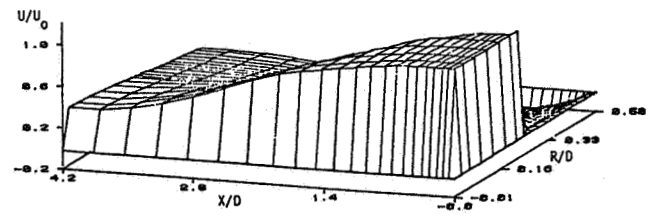
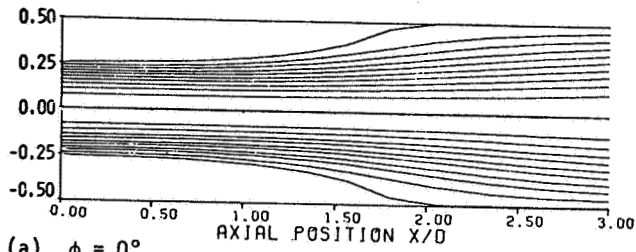


Fig. 12 Predicted streamlines using measured inlet  $u$ ,  $v$  and  $w$  profiles

Fig. 13 Axial velocity representation

ulation region is established. It promotes a very large forward velocity near the confining walls rather than a corner recirculation region.

These predicted effects generally agree with the experimental data,<sup>7</sup> except that precessing vortex core regions of solid body rotation backflow, which occur downstream of central recirculation regions in the swirl flow cases investigated,<sup>26</sup> are not well predicted. Only the 70 deg. case predicts almost zero axial velocity on the centerline extending to  $x/D = 4$ . The central recirculation zone is predicted to be longer than found in practice. Also, swirl velocity profiles do not match well the experimental data -- the radial location of swirl velocity maximum value occurs too close to the confining chamber walls rather than occurring abruptly at the edge of a vortex core region. The observed discrepancies may be because of poor probe sensitivity in turbulent low velocity regions, and/or poor turbulence model performance in these regions. Only further detailed hot-wire and/or laser doppler anemometer measurements and turbulence model development will resolve the inconsistencies.

### 3.3 Effects of a Weak Contraction Nozzle

Sections 3.3 and 3.4 discuss the prediction of flowfields with downstream contraction nozzles located at  $L/D = 1$  and  $2$  for a range of swirl strengths  $\phi = 0, 45$  and  $70$  deg., using swirler exit measured  $u, v$  and  $w$  velocity profiles in each case.<sup>29</sup> Two

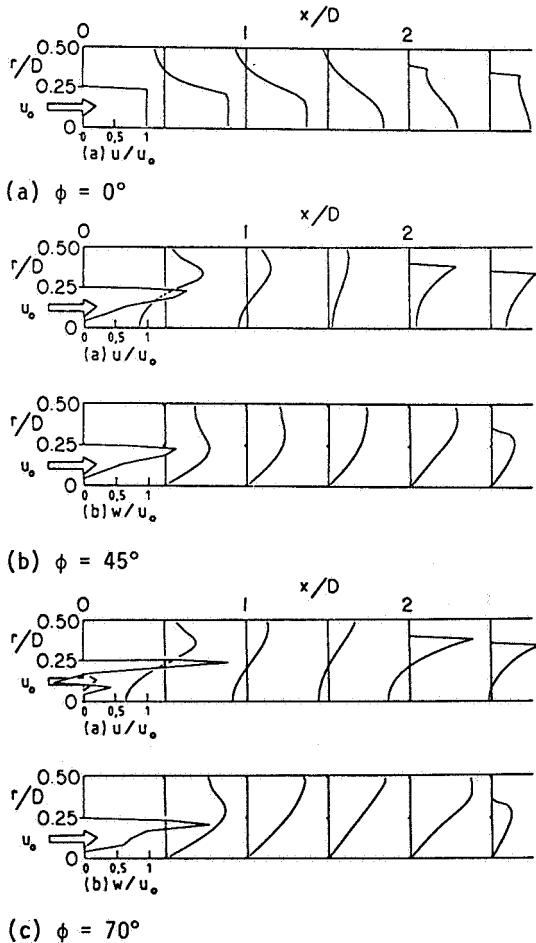


Fig. 14 Predicted velocity profiles with weak contraction nozzle at  $L/D = 2$

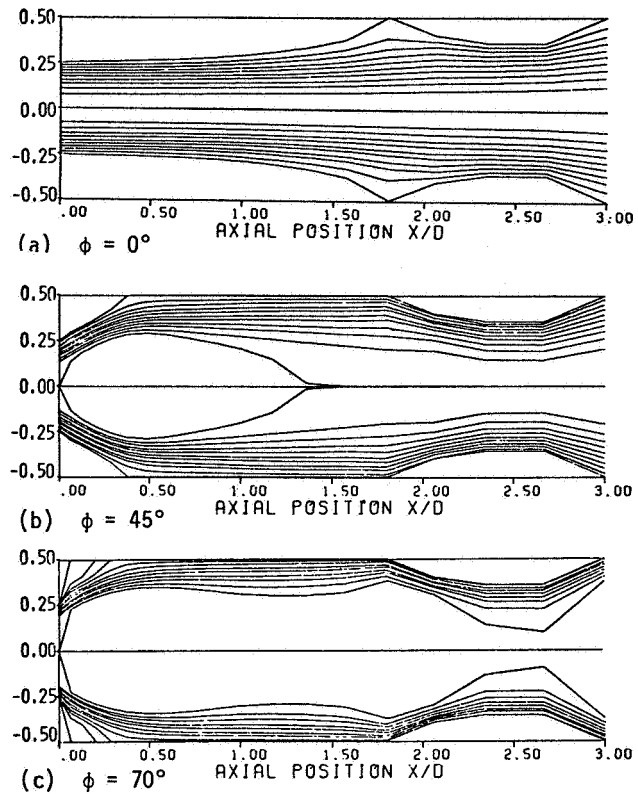


Fig. 15 Predicted streamlines with weak contraction nozzle at  $L/D = 2$

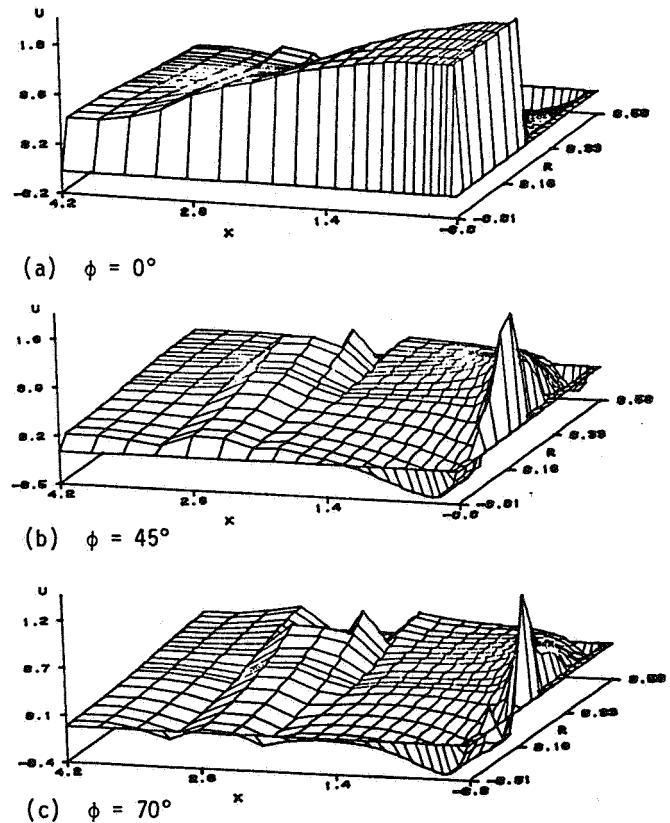


Figure 16 Axial velocity representation with weak contraction nozzle at  $L/D = 2$



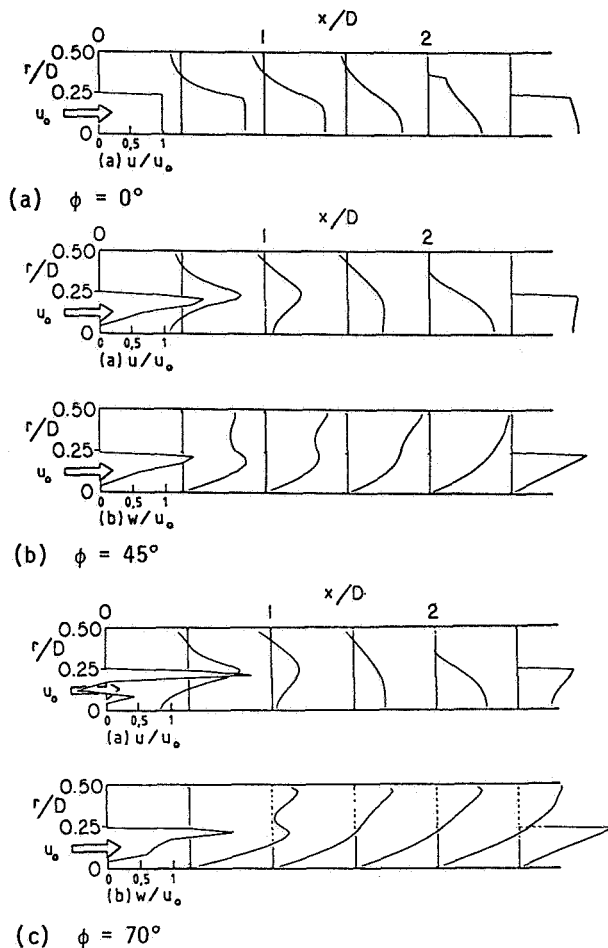


Fig. 17 Predicted velocity profiles with strong contraction nozzle at  $L/D = 2$

nozzles of area ratios 2 (weak nozzle) and 4 (strong nozzle) are being used. The weaker one has its upstream face contoured in a quarter circle; the stronger one has its upstream face in a 45 deg. slope. These are typical of exit nozzles for ramjet and gas turbine combustors, respectively, and are shown schematically in Ref. 7.

When the weak nozzle is located at  $L/D = 1$ , little effect results on the flow as compared with the no blockage case for the nonswirling case. However, at  $\phi = 45$  deg. a larger corner recirculation zone occurs while the lateral constraining effect encourages forward flow movement. It thereby discourages the central recirculation zone whose length is reduced. At  $\phi = 70$  deg. these same effects prevail but with increased intensity. It is as if the constriction effect at  $L/D = 1$  occurs soon enough to affect primary zone features at the heart of their development.

However, with the weak nozzle at  $L/D = 2$ , primary zone features, which depend on inlet conditions, have already established themselves prior to the occurrence of the constriction. Figures 14, 15 and 16 present velocity profiles, streamline patterns and axial velocity development, respectively, when the weak contraction nozzle is at  $L/D = 2$  only; corresponding figures with  $L/D = 1$  are available elsewhere.<sup>38</sup> Little effect of the nozzle

is now observed, especially with the zero and intermediate swirl cases portrayed in parts (a) and (b) of Figs. 14 through 16. But in part (c) of these figures, the weak nozzle is seen to have a strong effect as compared with the corresponding nonconstricted flow shown in part (e) of Figs. 11 through 13. A core region of strongly swirling reverse flow is now established which extends right through the system.

These predictions are somewhat over-dramatic as compared with the experiments.<sup>7</sup> In practice it is found that the weak contraction nozzle has most effect on the intermediate swirl case of  $\phi = 45$  deg. Its contraction effect in this case is strong enough to overwhelm the swirling recirculation region. However, the weak contraction was found to have little effect on weakly swirling and strongly swirling flows, which are dominated by forward flow and centrifugal forces, respectively. The predictions showed a more dramatic nozzle vortex effect with stronger core vortex swirl velocities resulting from the cross-sectional area reduction, as even simple macro-theory would confirm.<sup>26</sup>

### 3.4 Effects of a Strong Contraction Nozzle

Predictions are now discussed for the case of the strong contraction nozzle of area ratio 4 being located at  $L/D = 1$  and 2, with inlet swirl strengths of  $\phi = 0, 45$  and  $70$  deg. Under nonswirling conditions, the blockage effect is minimal at either nozzle location -- the central forward flow is accelerated and the large corner recirculation remains.

Under intermediate and strong swirl conditions, however, the effects of the 4 to 1 area reduction are dramatic at either nozzle location. The corner recirculation zone is encouraged to occur and possess larger negative axial velocities; the central recirculation zone is discouraged as slow moving air is accelerated downstream. The size of central recirculation bubble is considerably reduced as also found experimentally.<sup>7</sup> These effects are seen in Figs. 17, 18 and 19 for the strong contraction nozzle at  $L/D = 2$ ; corresponding figures with  $L/D = 1$  appear in Ref. 38. These figures show velocity profiles, streamline patterns and axial velocity development and may be compared with the earlier Figs. 14, 15 and 16 which have a weak contraction nozzle, and Figs. 11, 12 and 13 which were not constricted.

The strong contraction also results in very large swirl velocity magnitudes and gradients in central core regions, which prevail throughout the flow domain. Axial velocities in the core region are now positive, in contrast to the negative values found in unrestricted and weakly restricted flows. These interesting predictions are confirmed in the associated experiments.<sup>7</sup>

## 4. Conclusions

A numerical prediction using the standard two-equation  $k-\epsilon$  turbulence model and different inlet flow boundary condition assumptions has been applied to a confined swirling flow. Inlet flow boundary conditions have been demonstrated to be extremely important in simulating a flowfield via numerical calculations. Predictions with either flat inlet profiles, solid body rotation or zero radial velocity are inappropriate. Predictions are given for a full range of swirl strengths using measured inlet axial, radial and swirl velocity profiles in each case, and

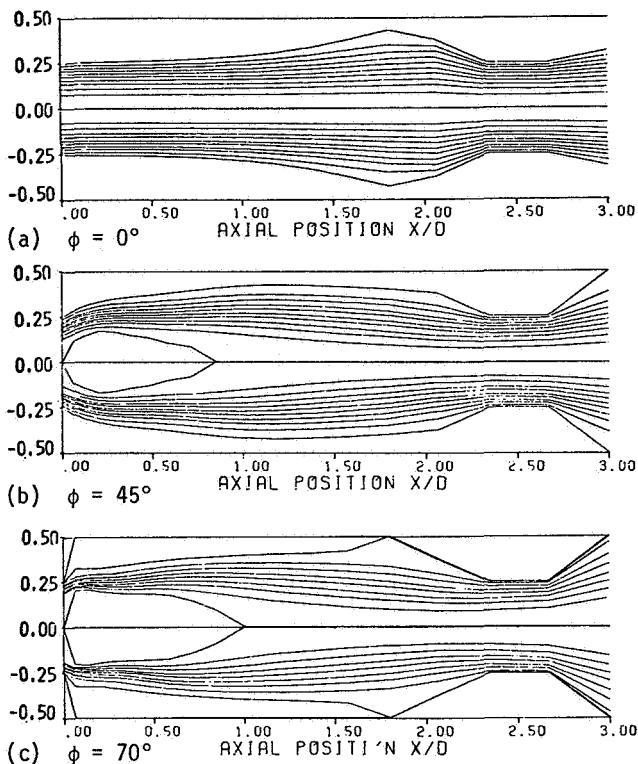


Fig. 18 Predicted streamlines with strong contraction nozzle at  $L/D = 1$

predicted velocity profiles, streamline plots and axial velocity representations illustrate the large-scale effects of inlet swirl on flowfields.

Predictions are included for the effect of weak and strong downstream contraction nozzles on the flow. It appears that a weak nozzle has only a minor effect on the flow. In the swirl flow cases, a weak nozzle leads to the discouragement of central recirculation zones with stronger vortex cores downstream possessing negative axial velocities. A strong nozzle has more pronounced effects on swirl flow cases, with discouragement of central recirculation zones, and forward flow in highly swirled vortex core regions further downstream.

#### Acknowledgments

The authors sincerely express their gratitude to NASA Lewis Research Center and Air Force Wright Aeronautical Laboratories for financial support via NASA Grant No. NAG 3-74, technical monitor Dr. J. D. Holdeman.

#### References

1. Lilley, D. G., Swirl Flows in Combustion: A Review, *AIAA Journal*, Vol. 15, No. 8, August 1977, pp. 1063-1078.
2. Lilley, D. G., Flowfield Modeling in Practical Combustors: A Review, *Journal of Energy*, Vol. 3, July-Aug. 1979, pp. 193-210.
3. Lilley, D. G., Prospects for Computer Modeling in Ramjet Combustors, Paper AIAA 80-1189, Hartford, CT, June 30-July 2, 1980.

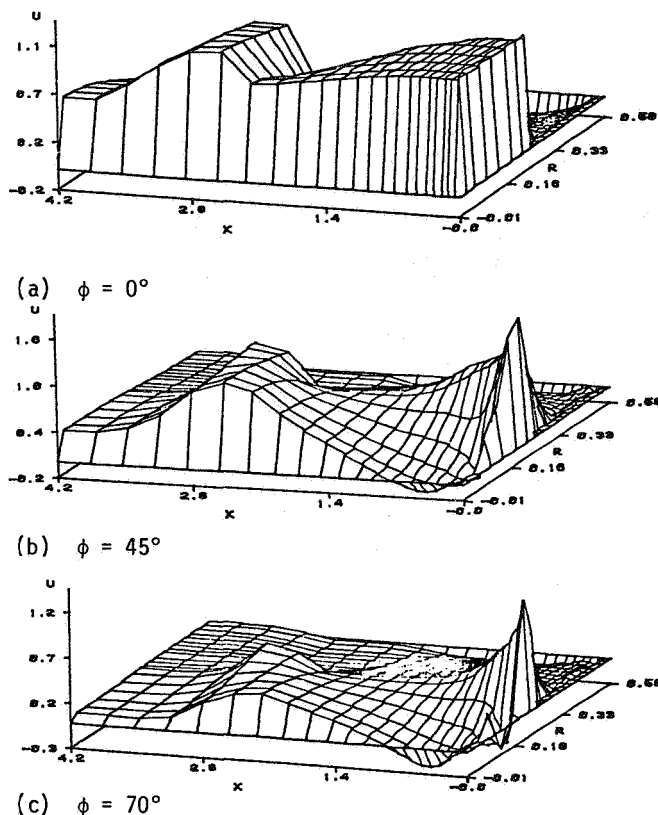


Fig. 19 Axial velocity representation with strong contraction nozzle at  $L/D = 2$

4. Lefebvre, A. H. (ed.), *Gas Turbine Combustor Design Problems*, Hemisphere-McGraw-Hill, New York, 1980.
5. Gupta, A. K., and Lilley, D. G., *Flowfield Modeling and Diagnostics*. Abacus Press, Tunbridge Wells, England, 1983 (in press).
6. Rhode, D. L., Lilley, D. G., and McLaughlin, D. K., Mean Flowfields in Axisymmetric Combustor Geometries with Swirl, Paper AIAA 82-0177, Orlando, Florida, Jan. 11-16, 1982. *AIAA Journal*, 1983 (in press).
7. Yoon, H. K., and Lilley, D. G., Five-Hole Pitot Probe Time-Mean Velocity Measurements in Confined Swirling Flows, Paper AIAA 83-0315, Reno, Nevada, Jan. 10-13, 1983.
8. Rhode, D. L., Predictions and Measurements of Isothermal Flowfields in Axisymmetric Combustor Geometries, Ph.D. Thesis, School of Mech. and Aero. Engng., Oklahoma State University, Stillwater, Okla., Dec. 1981.
9. Rhode, D. L., Lilley, D. G., and McLaughlin, D. K., On the Prediction of Swirling Flowfields Found in Axisymmetric Combustor Geometries, *ASME Journal of Fluids Engng.*, Vol. 104, 1982, pp. 378-384.
10. Lilley, D. G., and Rhode, D. L., A Computer Code for Swirling Turbulent Axisymmetric Recirculating Flows in Practical Isothermal Combustor Geometries, NASA CR-3442, Feb. 1982.

11. Gosman, A. D., and Pun, W. M., Calculation of Recirculating Flows, Rept. No. HTS/74/12, Dept. of Mech. Engng., Imperial College, London, England, 1974.
12. Khalil, E. E., Spalding, D. B., and Whitelaw, J. H., The Calculation of Local Flow Properties in Two-Dimensional Furnaces, *Int. J. Heat Mass Trans.*, Vol. 18, 1975, pp. 775-791.
13. Kubo, I., and Gouldin, F. C., Numerical Calculations of Turbulent Swirling Flow, *Journal of Fluids Engineering*, Vol. 47, Sept. 1975, pp. 310-315.
14. Lilley, D. G., Primitive Pressure-Velocity Code for the Computation of Strongly Swirling Flows, *AIAA Journal*, Vol. 14, June 1976, pp. 749-756.
15. Wuerer, J. E., and Samuelsen, G. S., Predictive Modeling of Backmixed Combustor Flows: Mass and Momentum Transport, *AIAA Paper 79-0215*, New Orleans, Louisiana, Jan. 15-17, 1979.
16. Novick, A. S., Miles, G. A., and Lilley, D. G., Numerical Simulation of Combustor Flowfields: A Primitive Variable Design Capability, *J. of Energy*, Vol. 3, No. 2, March-April, 1979, pp. 95-105.
17. Habib, M. A., and Whitelaw, J. H., Velocity Characteristics of Confined Coaxial Jets With and Without Swirl, *Journal of Fluids Engng.*, Vol. 102, March 1980, pp. 47-53.
18. Srinivasan, R., and Mongia, H. C., Numerical Computations of Swirling Recirculating Flows, Final Report, NASA-CR-165196, Sept. 1980.
19. El-Banhawy, Y., and Whitelaw, J. H., Calculation of the Flow Properties of a Confined Kerosene-Spray Flame, *AIAA J.*, Vol. 18, No. 2, Dec. 1980, pp. 1503-1510.
20. Sturgess, G. J., and Syed, S. A., Widely-Spread Coaxial Jet, Diffusion Flame Combustor: Isothermal Flow Calculation Using the Two-Equation Turbulence Model, Paper No. AIAA 82-0113, Orlando, Florida, January 11-14, 1982.
21. Serag-Eldin, M. A., and Spalding, D. B., Computations of Three-Dimensional Gas-Turbine Combustion Chamber Flows, *Trans. ASME J. of Eng. for Power*, Vol. 101, July 1979, pp. 326-336.
22. Mongia, H. C., and Reynolds, R. S., Combustor Design Criteria Validation Vol. III - User's Manual, Report USARTL-TR-78-55C, U.S. Army Res. and Tech. Lab., Ft. Eustis, VA, Feb. 1979. [See also Vols. I and II].
23. Swithenbank, J., Turan, A., and Felton, P. G., Three-Dimensional Two-Phase Mathematical Modeling of Gas Turbine Combustors, in *Gas Turbine Combustor Design Problems* (Lefebvre, A. H., ed.), Hemisphere-McGraw-Hill, New York, 1980, pp. 249-314.
24. Srivatsa, S. K., Computations of Soot and NO<sub>x</sub> Emissions from Gas Turbine Combustors, NASA CR-167930, May 1982.
25. Khalil, E. E., Modeling of Furnaces and Combustors, Abacus Press, Tunbridge Wells, England, 1982.
26. Gupta, A. K., Lilley, D. G., and Syred, N., Swirl Flows, Abacus Press, Tunbridge Wells, England, 1983 (in press).
27. Launder, B. E., and Spalding, D. B., Mathematical Models of Turbulence, Academic Press, London, England, 1972.
28. Launder, B. E., and Spalding, D. B., The Numerical Computation of Turbulent Flows, *Comp. Methods in Appl. Mech. and Engng.*, Vol. 3, March 1974, pp. 269-289.
29. Sander, G. F., and Lilley, D. G., The Performance of an Annular Vane Swirler. Report on Work in Progress, School of Mech. and Aero. Engng., Oklahoma State University, Stillwater, Okla., Oct. 1982.
30. Chigier, N. A., and Chervinsky, A., Experimental Investigation of Swirling Vortex Motion in Jets, *ASME Journal of Applied Mechanics*, Vol. 89, June 1967, pp. 443-451.
31. Beer, J. M., and Chigier, N. A., Combustion Aerodynamics, Applied Science, London and Wiley, New York, 1972.
32. Chigier, N. A., and Beer, J. M., Velocity and Static Pressure Distributions in Swirling Air Jets Issuing from Annular and Divergent Nozzles, *J. of Basic Engng.*, Dec. 1964, pp. 788-798.
33. Kerr, N. M., and Fraser, D., Swirl, Part I: Effect on Axisymmetrical Turbulent Jets, *J. Inst. Fuel*, Vol. 38, Dec. 1965, pp. 519-526.
34. Boysan, F., Ayers, W. H., and Swithenbank, J., A Fundamental Modeling Approach to Cyclone Design, *Trans. J. Chem. E.*, Vol. 16, No. 4, July 1982, pp. 222-230.
35. Lilley, D. G., Turbulent Combustor Flowfield Investigation, Paper in Combustion Fundamentals Research Conference, held at NASA Lewis Research Center, Cleveland, Ohio, Oct. 21-22, 1982, pp. 152-168.
36. Chaturvedi, M. C., Flow Characteristics of Axisymmetric Expansions, *Proc. Journal Hydraulics Division, ASCE*, Vol. 89, No. HYE, 1963, pp. 61-92.
37. Moon, L. F., and Rudinger, G., Velocity Distribution in an Abruptly Expanding Circular Duct, *ASME Journal of Fluids Engng.*, March 1977, pp. 226-230.
38. Abujelala, M. T., and Lilley, D. G., Confined Swirling Flow Predictions: Effect of Contraction Nozzles on Flowfields. Report on Work in Progress, School of Mech. and Aero. Engng., Oklahoma State University, Stillwater, Okla., Jan. 1983.

APPENDIX F

SINGLE-WIRE SWIRL FLOW TURBULENCE

MEASUREMENTS

(AIAA-83-1202)

# SINGLE-WIRE SWIRL FLOW TURBULENCE MEASUREMENTS

T. W. Jackson\* and D. G. Lilley\*\*  
Oklahoma State University, Stillwater, Okla.

## Abstract

A six-orientation single-wire hot-wire technique is used to investigate nonswirling and swirling nonreacting flow in an axisymmetric test section with expansion ratio  $D/d = 2$ , which may be equipped with a strong contraction nozzle of area ratio 4 at  $L/D = 2$ . The flowfield contains corner and central recirculation zones typical of gas turbine and ramjet combustion chambers. Swirl may be imparted to the in-coming flow by means of a variable-angle vane swirler. The effect of swirl on time-mean velocities and complete Reynolds stress tensor is investigated, and extensive results are given for swirl vane angles of 0 (swirler removed), 38, 45, 60 and 70 deg. The data are being used to aid in the evolution of turbulence models for these complex flow situations. A directional sensitivity analysis is included, which determines the relative accuracy of the measurement technique to approach velocity orientation.

## Nomenclature

A,B,C	calibration constants
D	test section diameter
d	inlet nozzle diameter
E	hot-wire voltage
G	pitch factor
K	yaw factor
L	contraction nozzle downstream distance
p	time-mean pressure
Re	Reynolds number
$\underline{v} = (u,v,w)$	time-mean velocity (in x-, r-, $\theta$ -directions) in facility coordinates
x,r, $\theta$	axial, radial, azimuthal cylindrical polar coordinates
Z	effective cooling velocity acting on a wire
$\phi$	swirl vane angle with respect to facility axis

## Subscripts

o	value at inlet to flowfield
rms	root-mean-squared quantity

## Superscripts

$(\quad)$	time-mean average
$(\quad)'$	fluctuating quantity
$(\quad)^\sim$	relative to probe coordinates

## 1. Introduction

### 1.1 The Problem and its Significance

The present research forms part of a project on the investigation of flowfields found in typical combustor geometries; studies are in progress concerned with experimental and theoretical re-

search in 2-D axisymmetric conditions. The general aim is to characterize the time-mean and turbulence flowfield, recommend appropriate turbulence model advances, and implement and exhibit results of flowfield predictions.<sup>1</sup> Nonreacting flowfields of this type are important, since swirling jets have been found to play a significant role in jet growth, entrainment and decay in nonreacting flows,<sup>2</sup> and in the length, stability and combustion efficiency of flames in combustor chambers.<sup>3-5</sup> Generally, two recirculation zones are observed in confined flows: the corner recirculation zone (CRZ) and the central toroidal recirculation zone (CTRZ). Both of these contain large turbulent eddies which promote mixing between the hot combustion products and the incoming fuel and air flows.

Some recent researchers<sup>6-8</sup> measured time-mean and turbulence properties in the vicinity of these recirculation zones with the presence of chemical reaction. However, more fundamental knowledge about the fluctuating velocities and their cross-correlations for a variety of swirl strengths under isothermal conditions is needed before the complex interactions of chemical reaction and turbulent mixing are fully understood. Chaturvedi<sup>9</sup> measured the time-mean and turbulent properties of a confined jet in the absence of swirl and found high turbulent mixing on the shear layer produced by the sudden expansion. He also found that the CRZ extended to 2 chamber diameters downstream of the expansion station, with an expansion ratio  $D/d$  of 2. Some researchers extended their interest to swirling confined flows, with emphasis on time-mean velocity distributions (see, for example, Refs. 10-13) and turbulence quantities (see, for example, Refs. 14-17). However, only low swirl strengths have been considered in the latter cases.

### 1.2 Objectives

The focus of the present paper is the measurement of time-mean and turbulence data for a full range of swirl strengths. This extends the data base given earlier<sup>16</sup> to higher inlet vane swirl angles and more axial measurement stations. Effects of a strong contraction nozzle of area ratio 4 located at  $L/D = 2$  are included. Results of an accuracy check on sensitivity of results to velocity orientation are also given and assessed.

### 1.3 Outline of the Present Study

The experimental facility being used consists of a sudden expansion (3.2 cm downstream of the downstream face of a variable-angle vane swirler) into a larger chamber of diameter 30 cm and length 150 cm. The expansion ratio  $D/d$  is 2. Figure 1 shows schematically the test section with the associated coordinate system and traversing mechanism. Previous papers describe at length the test facility and general time-mean flow patterns,<sup>11-12</sup> the six-orientation single-wire hot-wire measurement technique,<sup>16</sup> and the performance of the annular vane swirler being used.<sup>18</sup>

\* Graduate Student, School of Mechanical and Aerospace Engineering, Student Member AIAA

\*\* Professor, School of Mechanical and Aerospace Engineering, Associate Fellow AIAA

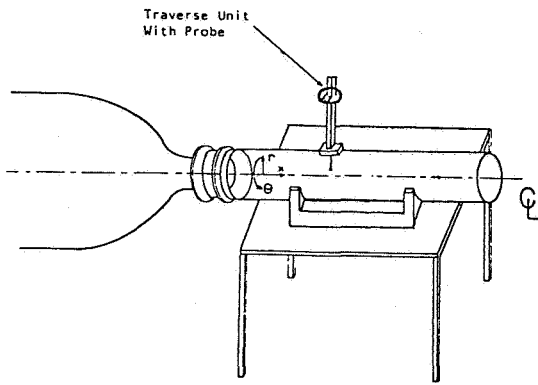


Fig. 1 Hot-wire probe mounted on the test section

The present paper extends the available time-mean and turbulence data base to flows with strong swirl. Time-mean properties and the complete Reynolds stress tensor are presented for a variety of swirl strengths (with swirl vane angle  $\phi$  of 0 (swirler removed), 38, 45, 60 and 70 deg.). Section 2 recalls briefly the measurement technique, and introduces the directional sensitivity study. Results are presented and discussed in Section 3, while Section 4 draws conclusions from the study.

## 2. Measurement Technique

### 2.1 Confined Flowfield Measurements

One of the most widely used instruments to obtain turbulence quantities is the hot-wire anemometer, the most common of which is the single hot-wire. When used on a two-dimensional flow with a predominate flow direction, a single hot-wire used normal to the main flow can be used to measure the streamwise components of the time-mean velocity and the rms velocity fluctuation, in a standard manner.

The anemometer used for the present study is DISA type 55M01, CTA standard bridge. A normal hot-wire probe, DISA type 55P01, is used in the experiments. This probe has two prongs set approximately 3 mm apart which support a 5  $\mu$ m diameter wire which is gold plated near the prongs to reduce end effects and strengthen the wire. The mean voltage is measured with a Hickok Digital Systems, Model DP100, integrating voltmeter and the root-mean-square voltage fluctuation is measured using a Hewlett Packard, Model 400 HR, AC voltmeter.

The hot-wire is supported in the facility by a traversing mechanism, shown schematically in Figure 1. It consists of a base that is modified to mount on the plexiglass tube of the test section at various axial locations. The hot-wire probe is inserted into the tube through a rotary vernier and the base. The rotary vernier is attached to a slide which can traverse across the flow chamber. Thus, it is possible for the probe to be traversed to any radial location at selected downstream locations in the flowfield and to be rotated through 180 degrees.

In a complex swirling flowfield the dominant flow direction is unknown and the standard single-orientation single hot-wire method fails to supply

sufficient information. King<sup>19</sup> developed a technique based on that of Dvorak and Syred<sup>20</sup> using a single hot-wire that can measure the time-mean and turbulence properties in a complex flowfield. The method calls for a normal hot-wire to be orientated through six different positions, each orientation separated by 30 degrees for the adjacent one. Orientation 1 is normal to the facility centerline, orientation 2 is rotated 30° from this, etc. Mean and root-mean-square voltages are measured at each orientation. The data reduction is performed using assumptions that turbulence follows a normal probability distribution having mean voltage as the mean and the squared value of the rms voltage as the variance. It is then possible to obtain the three time-mean velocity components, the three normal Reynolds stresses and the three shear Reynolds stresses, in the manner now described.

The six-orientation hot-wire technique requires a single, straight, hot-wire to be calibrated for three different flow directions in order to determine the directional sensitivity of the probe. In the following relationships, tildes signify components of the instantaneous velocity vector in coordinates on the probe. Each of the three calibration curves is obtained with zero velocity in the other two directions. The calibration curves demonstrate that the hot-wire is most efficiently cooled when the flow is in the direction of the  $\tilde{u}$  component (which is normal to both the wire and the supports). The wire is most inefficiently cooled when the flow is in the direction of the  $\tilde{w}$  component (which is parallel to the wire). Each of the calibration curves follows a second order, least-square fit of the form:

$$E_i^2 = A_i + B_i \tilde{u}_i^{1/2} + C_i \tilde{u}_i \quad (1)$$

which is an extension of the familiar King's law. In this equation,  $A_i$ ,  $B_i$ , and  $C_i$  are calibration constants and  $\tilde{u}_i$  can take on a value of  $\tilde{u}$ ,  $\tilde{v}$ , and  $\tilde{w}$  for the three calibration curves, respectively.

When the wire is placed in a three-dimensional flowfield, the effective cooling velocity experienced by the hot-wire is:

$$Z^2 = \tilde{v}^2 + G^2 \tilde{u}^2 + K^2 \tilde{w}^2 \quad (2)$$

where  $G$  and  $K$  are the pitch and yaw factors, defined by Jorgensen<sup>21</sup> and deduced from the calibration curves. Hence, equations for the effective cooling velocity can now be obtained for each of the six wire orientations. Solving simultaneously any three adjacent equations provides expressions for the instantaneous values of the three velocity components ( $u$ ,  $v$ , and  $w$  in facility  $x$ ,  $r$ , and  $\theta$  coordinates, respectively) in terms of the equivalent cooling velocities. It is then possible to obtain the three time-mean velocity components and the six different components of the Reynolds stress tensor, in the manner described in Ref. 16. Because of lack of directional knowledge, data presented in Section 3 were obtained from an average of the values found in each of the six possible combinations of three adjacent wire-orientations.

### 2.2 Directional Sensitivity Analysis

The directional sensitivity analysis of the technique is performed in a free jet of known flow properties. Measurements were taken on the centerline in the potential core of the jet, correspond-

ing to a laminar flow, and on the shear layer at three nozzle diameters downstream of the jet exit, in a turbulent region. The two regions were chosen to check the directional sensitivity of the technique in laminar and turbulent flows.

The analysis is performed by initially placing the probe in the jet such that the coordinate system of the probe coincides with the coordinate system of the jet. Measurements are then taken by rotating the probe in the manner of the technique described. To simulate the effect of the flow shifting its dominant flow direction, the probe is rotated by  $\theta$  deg. about its  $z$ -axis, as shown in Fig. 2. This rotation causes a misalignment between the probe coordinate system and the facility coordinates. This discrepancy can be accounted for by use of the rotation matrices<sup>22</sup> described in Appendix A. In this configuration, the measured time-mean values, normal and shear stresses are in a coordinate system oblique to the jet coordinate system. However, they can be transformed back to the facility coordinate system.<sup>2,3</sup> Results shown later in Section 3.3 have been obtained in this manner.

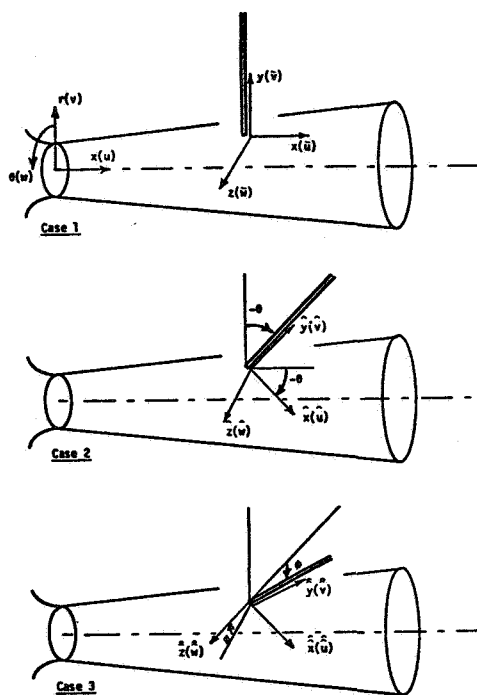


Fig. 2 Cases 1, 2, and 3 of the directional sensitivity study

To examine the directional sensitivity of the wire further, the probe was subsequently rotated about its new  $\hat{x}$ -axis, thereby forming a compound angle between probe and the dominant flow velocity, as also shown in Fig. 2. Again the time-mean velocities and Reynolds stress tensor can be deduced in terms of the jet coordinate system by the method shown in Appendix A, and the results and their accuracy are also discussed in Section 3.3.

### 3. Results and Discussion

Nonswirling and swirling nonreacting flows are investigated in an axisymmetric test section with expansion ratio  $D/d = 2$ , which may be equipped with a strong contraction nozzle of area ratio

4 located at  $L/D = 2$ . This nozzle has a 45 deg. slope facing upstream as described earlier.<sup>12</sup> Measurements are made with the single-wire technique described in Section 2.1 and Ref. 16. The nozzle inlet velocities and Reynolds numbers employed in this study are high enough to ensure that the flowfields are investigated under conditions independent of Reynolds number variation. They correspond approximately to conditions reported in associated studies.<sup>12</sup> Firstly, time-mean and turbulence characteristics for five different swirl strengths are presented and discussed. In each case, radial profiles of interesting properties at six axial locations are presented. Secondly, the effects of the strong contraction nozzle on the time-mean and turbulence properties in the flowfield are clarified for the cases of no swirl, moderate swirl and strong swirl. All properties shown are normalized with respect to the swirler inlet uniform axial velocity  $u_0$  deduced independently from a measurement upstream of the swirler. Finally, a directional sensitivity analysis involving the time-mean and turbulent properties of a round free jet has been performed. Three probe-jet axis orientations have been used to simulate the shifting of the dominant flow direction and consequently the effectiveness of the hot-wire technique to measure the properties of a strongly swirling flow, whose local flow direction is unknown a priori.

#### 3.1 Effects of Swirl

##### Nonswirling Flows ( $\phi = 0$ deg. swirler removed.)

Figure 3 shows time-mean and turbulence data for the nonswirling flow. A nearly-flat axial velocity profile is seen in the entrance region of the test section. As expected, there is no measurable swirl velocity and only a small radial velocity. Although a corner recirculation zone (CRZ) is present, there is no evidence of a central toroidal recirculation zone (CTRZ). Indeed, there is no swirl-induced centrifugal force to encourage its formation. The hot-wire anemometer cannot sense flow direction; however, directional properties of the flow can be inferred from earlier five-hole pitot probe data,<sup>12</sup> and flow visualization photography.<sup>11</sup> Nevertheless, the authors have retained the positive values on all figures wherever possible uncertainties might exist. The time-mean data shows good agreement with that found by Chaturvedi<sup>9</sup> in a similar test section, and with that found by Yoon and Lilley<sup>12</sup> using a five-hole pitot probe in the same test facility with identical flow conditions.

The maximum values of normal stresses appear on the shear layer with the axial fluctuation component dominating. Earlier results<sup>9</sup> indicated that the axial turbulence intensity was larger than the other two components and that the radial turbulence intensity was approximately equal to the tangential turbulence intensity. This is confirmed in the present study.

The six-orientation technique produces positive values of shear stress. However, in certain locations in the vicinity of recirculation zones, the radial gradient of the axial velocity is predominately positive which is associated with negative values of  $u^+v^+$ . Nevertheless, all shear stress values in this document are plotted as positive. Because of the absence of velocity gradients in the  $x$ - and  $\theta$ -directions, only one shear stress (the  $xr$ -component) is significant in the nonswirling case. This shear stress, plotted in Fig. 3, tends

to be lower than the earlier study.<sup>9</sup> It should be noted, however, that the shear stresses are the most difficult turbulent quantities to measure accurately in a complex flowfield. Uncertainties in measurements of time-mean velocities and turbulence intensities are increased in the determination of shear stresses.

Moderate Swirl ( $\phi = 38$  and  $45$  deg.). In confined swirling jet flows the axial and tangential time-mean velocities dominate, as can be seen from Figs. 4 and 5. The corner recirculation zone can be seen clearly at the expansion plane of the test section. The CRZ is not seen at any other axial location, indicating that the swirling flow greatly reduces the length of the CRZ. Swirling flow produces a central toroidal recirculation zone which can also be seen in the figures. The CTRZ appears to have a length of approximately  $1.5 D$ . Downstream of this point on the jet axis, indication is given of a precessing vortex core (PVC) extending to the exit plane of the test section. The PVC is defined as a region of low axial velocity and high almost solid body rotation swirl along the axis and is found to be present in the swirling flows considered. Yoon and Lilley<sup>12</sup> also measured the time-mean swirling flowfield, using a five-hole pitot probe and the present data is found to be in good agreement. The PVC is most clearly observed in flow visualization studies, using still photography<sup>11,24</sup> and videotape recordings.<sup>1</sup>

The three normal turbulent stresses appear to be fairly isotropic at all locations in the test chamber with maximum values occurring in regions of recirculation and regions of high shear. It was found that large-scale turbulence with big eddies occurs in recirculation regions and that small-scale turbulence with small eddies occurs in regions of peak velocities. In the downstream regions of the test chamber, the turbulence levels are low, with a more uniform radial profile, indicating a more developed nature of the flow.

It can also be seen that all three shear stress components are significant in swirling flows, as expected. The maximum values of shear stress occur in the thin shear layer regions but quickly dissipate in the downstream direction as the shear layer broadens. The stresses  $\bar{u}^*v^*/u_0^2$  and  $\bar{u}^*w^*/u_0^2$  are found to have large values close to the wall, because of the steep axial and swirl velocity gradients.

Strong Swirl ( $\phi = 60$  and  $70$  deg.) Time-mean velocity profiles for the strongest swirl cases considered are shown in Figs. 6 and 7. Almost all of the flow leaves the swirler near the outer edge, producing steep velocity gradients in this vicinity. High velocity gradients can also be seen near the wall, especially at  $x/D = 0.5$ . The strong centrifugal forces present in the incoming flow produce rapid outflow to the confining boundary. Both central and corner recirculation zones can be seen clearly from the time-mean plots. However, it appears that the CTRZ is shorter for this strong degree of swirl as compared to the moderate swirl case. In contrast, the PVC gets wider as the swirl strength increases, as also found in five-hole pitot probe data.<sup>12</sup>

The normal turbulent stresses have increased in magnitude, consistent with the increase in swirl strength, and still a good degree of isotropy

is observed throughout the entire flowfield. The highest turbulence levels again occur in regions of recirculation and on the shear layers. It can also be seen that high turbulence levels are found in the PVC.

The most dramatic effect of the increase of swirl swirl is the large increase in all three shear stress values. It can be seen that very high values of shear stress occur in the shear layers and near the walls. The PVC also contains high values of shear stresses and turbulence levels. Overall, the values of shear stresses are higher than in other swirl strengths considered.

### 3.2 Effects of Strong Contraction Nozzle

Nonswirling Flows. Time-mean and turbulence characteristics for the nonswirling flow with a strong contraction nozzle at  $L/D = 2$  are presented in Fig. 8. The plots show that results vary very little from that of the corresponding flowfield without a contraction nozzle, see Fig. 3. The major difference appears to be a slight reduction in the length of the CRZ. The measured time-mean flowfield compares favorably with previous data.<sup>12</sup>

Moderate Swirl. The effects of the contraction nozzle on the moderately swirling flow with  $\phi = 45$  deg. are shown in Fig. 9. The presence of the contraction nozzle accelerates the flow and produces a strong favorable pressure gradient over the entire flowfield of interest. This pressure gradient conflicts with the adverse pressure gradient inherent in swirling flows (associated with recirculation zones). Regions of positive axial velocity occur near the centerline at all axial locations. The central recirculation zone is now located in annular region around the jet axis and is much smaller than in the corresponding open flowfield of Fig. 5. A narrow central core region is observed to extend throughout the length of the test section with strong solid body rotation. Positive axial velocities now occur in this region, as opposed to negative ones in the corresponding open-ended flow case; this and other time-mean data being in excellent agreement with earlier experimental<sup>12</sup> and prediction<sup>24, 25</sup> studies.

The directional turbulence intensities do not show any significant increase in magnitude compared to the open-ended swirling flow. However, the turbulent shear stresses are found to increase near the jet axis as the contraction nozzle exit is approached. This is because of the fairly high turbulence levels in this region and the effect of strong velocity gradients with which these stresses are associated.

Strong Swirl. For swirl vane angle  $\phi = 70$  deg., measurements are given in Fig. 10 with the strong contraction blockage located at  $L/D = 2$ . The axial velocity near the axis is positive, though less so than in the  $45$  deg. case of Fig. 9, since the favorable pressure gradient has now to overcome an even stronger unfavorable pressure gradient. The central recirculation region is now very small, extending in an annular region to less than  $x/D = 1.0$ , considerably less than the no-blockage case of Fig. 7. At the axial station  $x/D = 1.0$ , forward flow occurs across the whole test section. Very strong swirl velocity magnitudes and gradients are seen, which contrasts sharply with the corresponding open-ended flow situation. A wide core region is again noticed



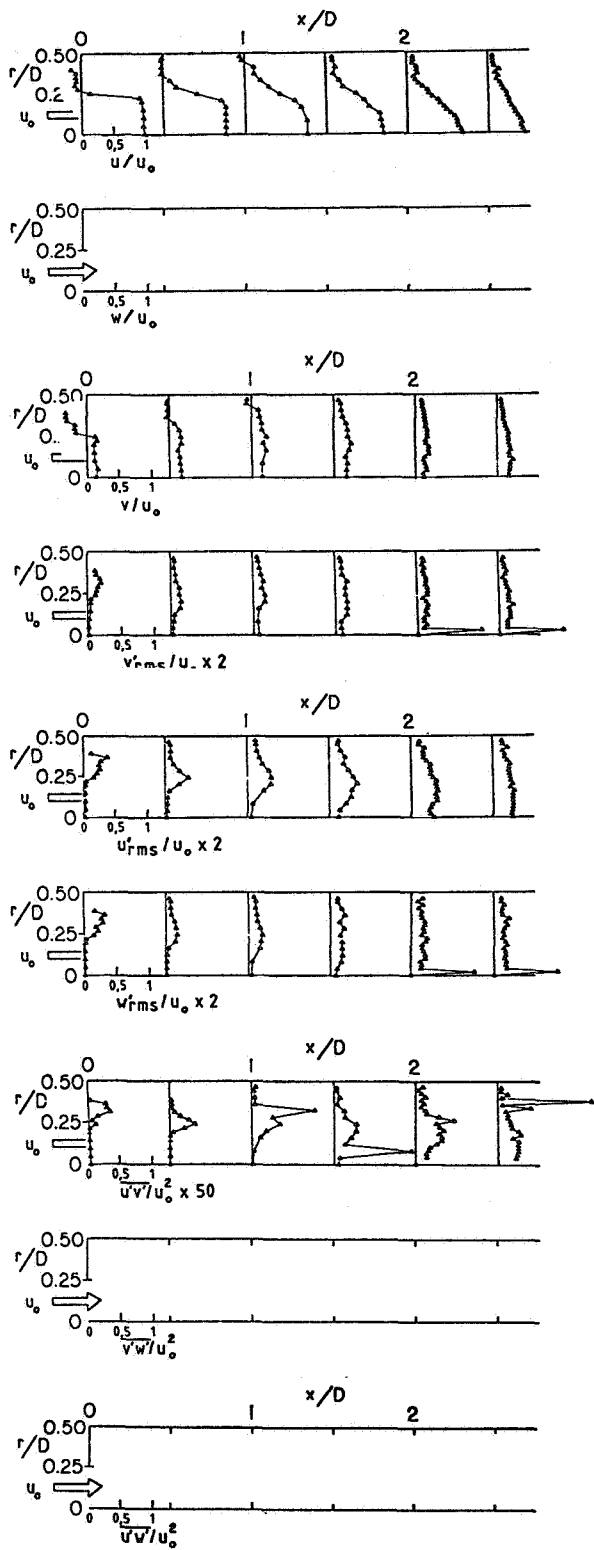


Fig. 3 Time-mean and turbulent flowfield  $\phi = 0$  deg. (no swirler)

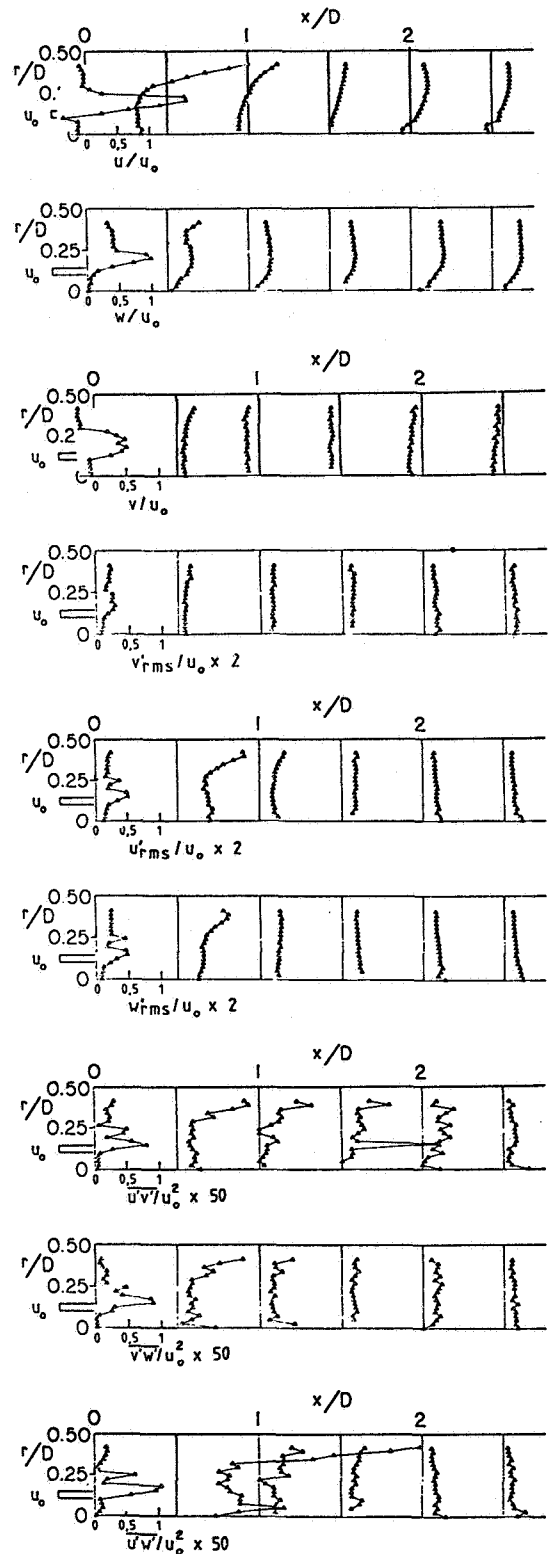


Fig. 4 Time-mean and turbulent flowfield  $\phi = 38$  deg.

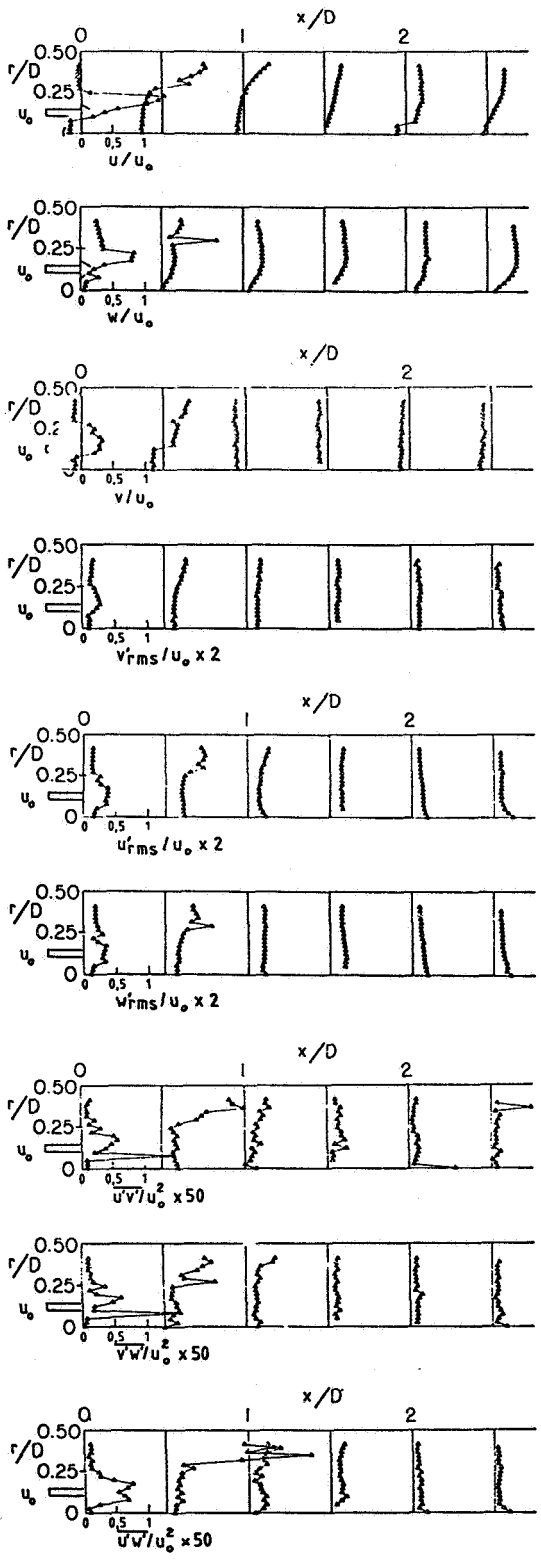


Fig. 5 Time-mean and turbulent flowfield  $\phi = 45$  deg.

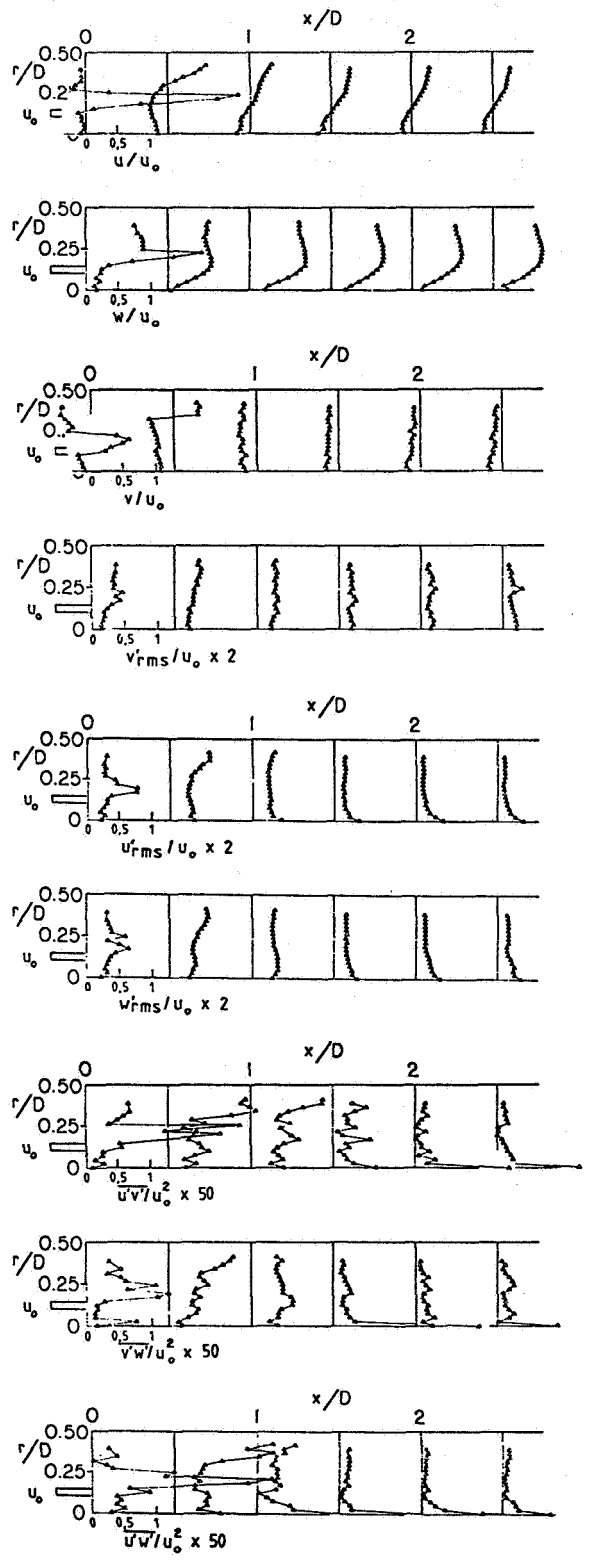


Fig. 6 Time-mean and turbulent flowfield  $\phi = 60$  deg.

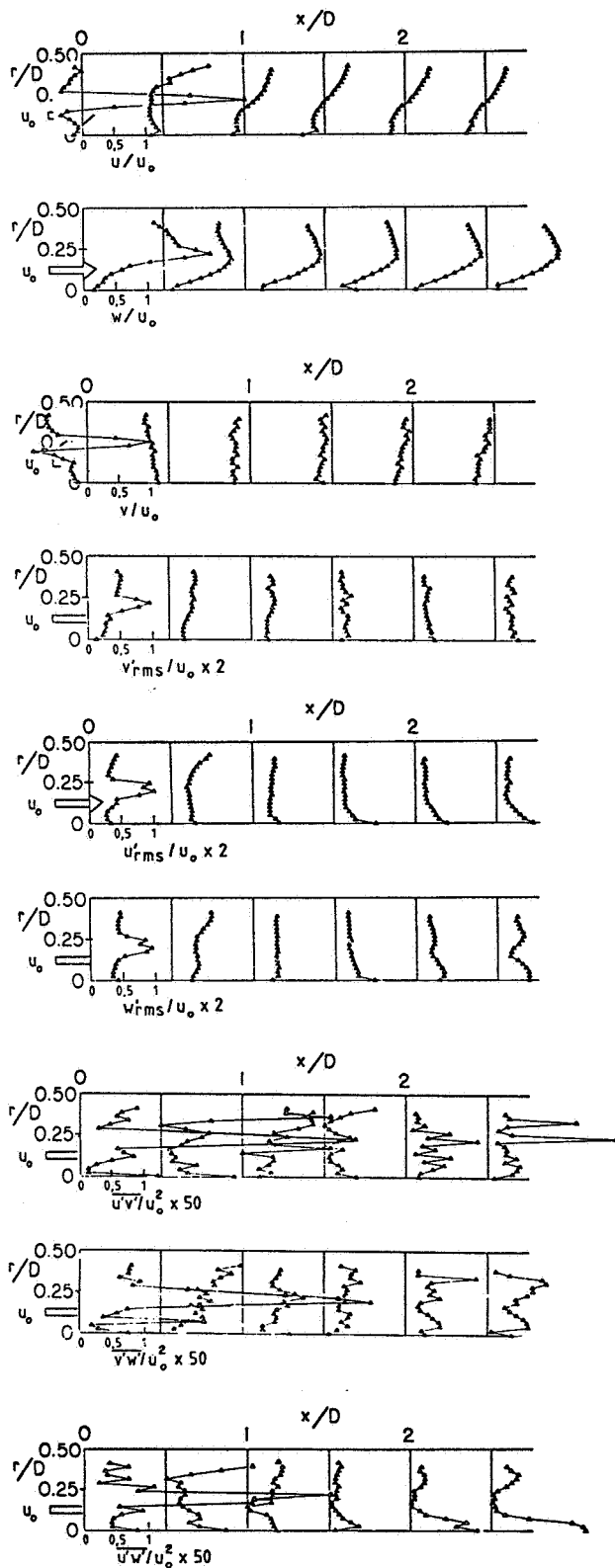


Fig. 7 Time-mean and turbulent flowfield  $\phi = 70$  deg.

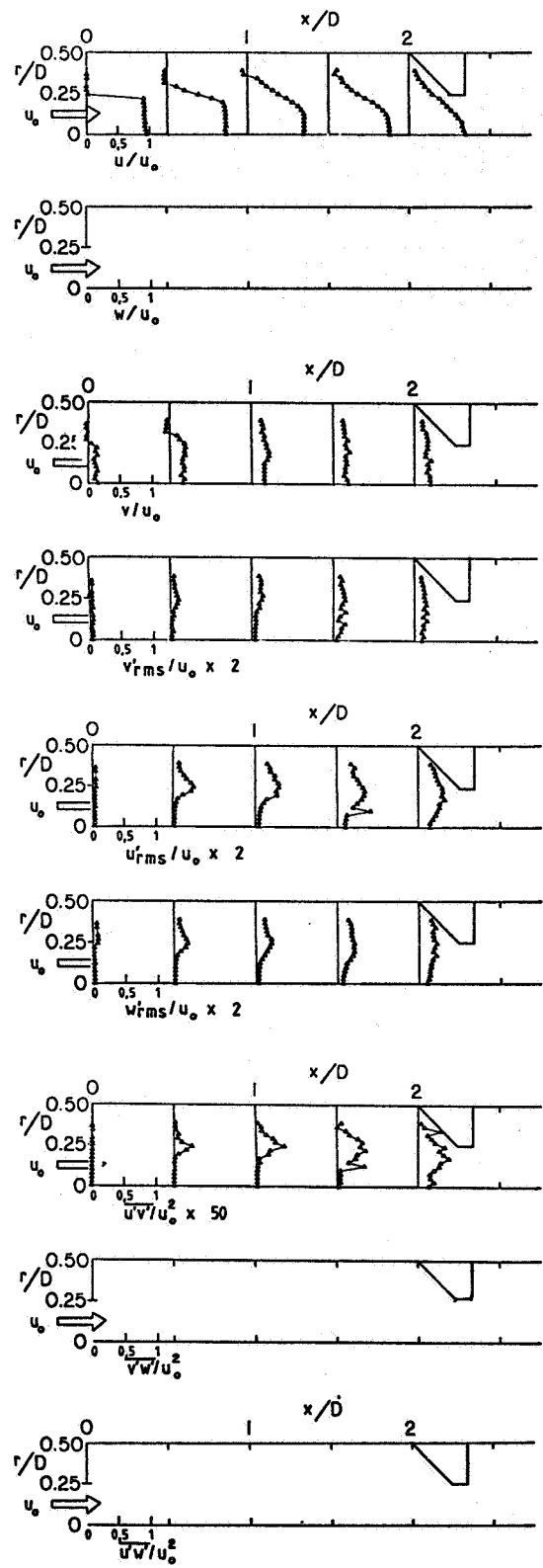


Fig. 8 Time-mean and turbulent flowfield  $\phi = 0$  deg. (no swirler) with strong contraction nozzle at  $L/D = 2$

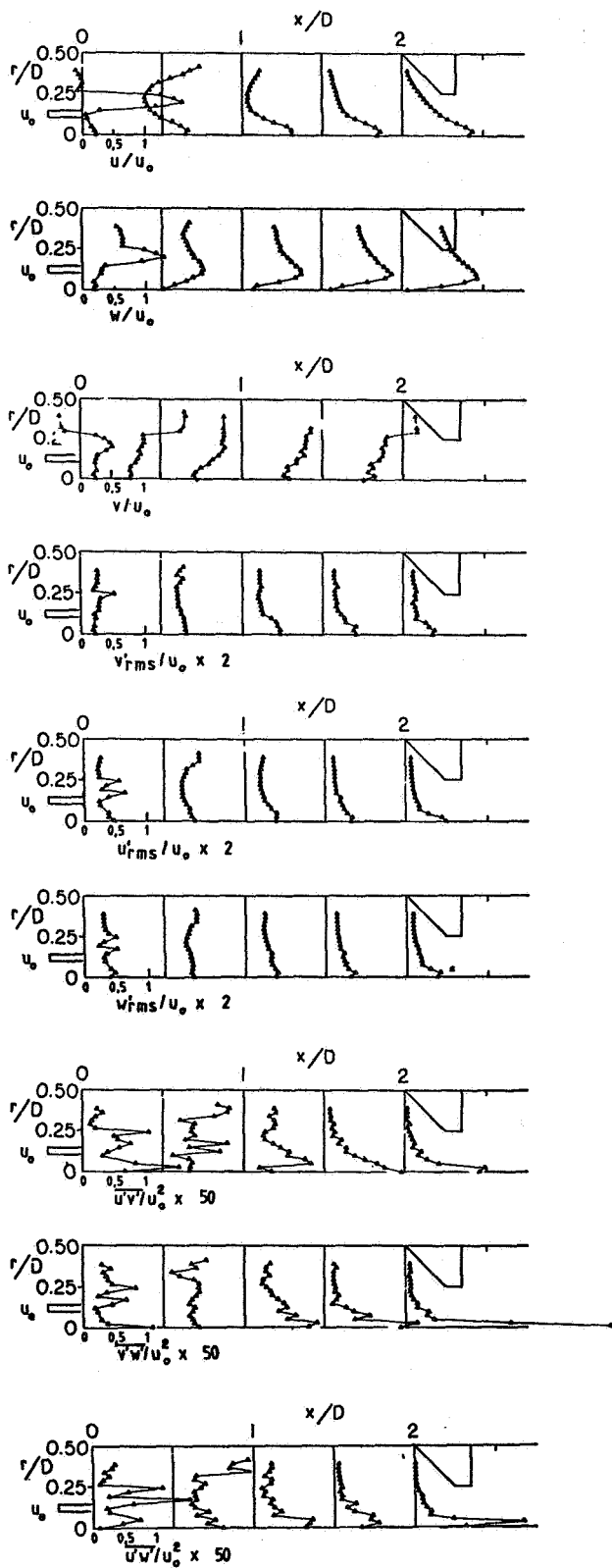


Fig. 9 Time-mean and turbulence flowfield  $\phi = 45$  deg. with strong contraction nozzle at  $L/D = 2$

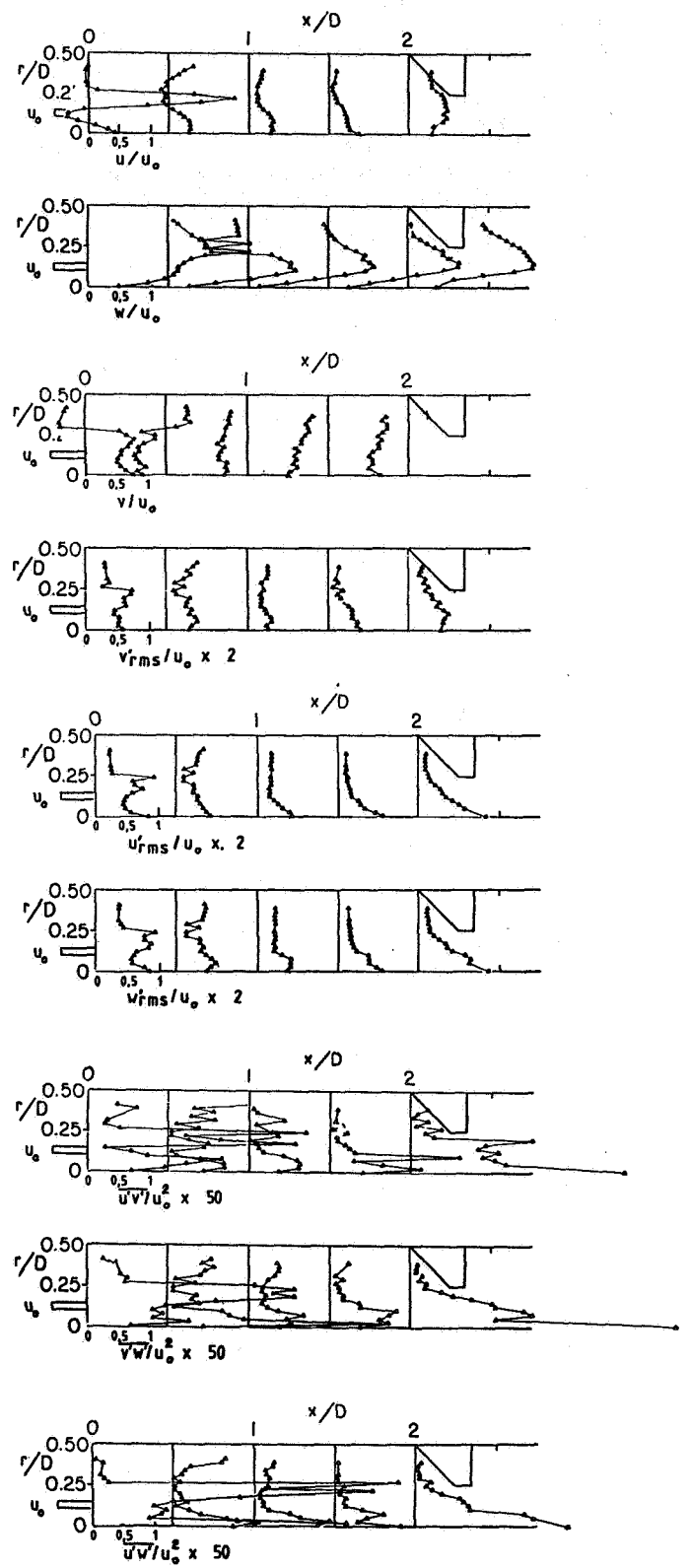


Fig. 10 Time-mean and turbulence flowfield  $\phi = 70$  deg. with strong contraction nozzle at  $L/D = 2$

along the jet axis containing strong solid body rotation; movie photography<sup>1</sup> reveals the precessing nature of this phenomenon. Again, time-mean data compare very well with previous work.<sup>12</sup>

The normal components of the Reynolds stress tensor show an increase in turbulence along the jet axis as the contraction is approached -- more so than in the 45 deg. swirl case of Fig. 9, but similar to those found in the open-ended case of Fig. 7. Now, larger values are found near the axis, associated with the strong vortex core region. Shear stress levels at the entrance to the test section tend to be slightly lower for the blockage case. But the levels are an order of magnitude higher in the core region near the contraction nozzle. Again, this is because of the strong time-mean velocity gradients in this area.

### 3.3 Directional Sensitivity Analysis

The directional sensitivity of the measurement technique is now assessed via its application to a free jet exiting from a contoured nozzle. The laboratory calibration jet was used for this purpose. Results, with the probe in the configuration of Cases 1, 2 and 3 of Fig. 2, are compared with expected values in the laminar potential core region and in the turbulent shear layer region further downstream,<sup>26</sup> see Tables 1 through 3 and 4 through 6, respectively. The ability of the probe to measure time-mean velocities in facility coordinates, using coordinate transformations given in Appendix A, is now assessed.

Laminar Flow. Table 1 gives the results of placing the single hot-wire in the potential core of the free jet at  $x/d = 0$  and  $r/d = 0$ , with the probe coordinates aligned with the facility coordinate systems, as Case 1 in Fig. 2 illustrates. The time-mean velocities, nondimensionalized with the jet exit velocity deduced from an independent measured, are shown with their percentage errors (that is, deviations from expected values). Results using each of the six possible combinations of three adjacent wire-orientations are presented, together with the ensemble average (mean) of these values. As can be seen, the percentage error for the axial and swirl velocities are very low for each combination. The radial velocity error tends to be larger, possibly because of slight probe misalignment with the normal to the jet axis. Ensemble averaging to find the mean of these quantities brings the data to well within acceptable limits.

Results of the probe being rotated by 45 deg. about the z axis (as in Case 2 of Fig. 2 with  $\theta = -45$  deg.) are shown in Table 2. The probe coordinate system is now different from the jet coordinate system but the measured velocities can be related to the facility coordinate by use of the rotational matrices given in Appendix A. The values and percentage errors in Table 2 are given in terms of the facility coordinate system. The results show that this misalignment of the probe with the dominant flow direction still gives excellent values of velocities in the laboratory coordinate system with the use of any of the six possible wire combinations. Consequently, ensemble averaging of the data also gives good results.

Table 3 gives corresponding results with the probe rotated twice (-45 deg. about its z-axis,

followed by -45 deg. about its new  $\hat{x}$ -axis) so as to conform to Case 3 of Fig. 2. Again the laboratory-coordinate deduced values and deviations from expected values are relatively low though not quite as good as in the previous case, however, still well within generally accepted limits. The advantages of ensemble averaging are shown on Table 3, where the under- and/or over-estimation of the velocities for the individual positions are "smoothed" out after averaging.

Turbulent Flow. To examine the directional sensitivity of the technique in a turbulent flowfield, the probe was placed in the shear layer of the free jet at  $x/d = 3$  and  $r/d = 0.5$ . Table 4 shows the results of the test with the probe in the position of Case 1 of Fig. 2. It is seen that the time-mean properties of the free jet are very similar to those of Sami et al.,<sup>26</sup> who reported experimental work on a similar turbulent free jet exiting from a contoured nozzle. They also included measurement stations relatively close to the jet exit. The results compare favorably except for, again the radial velocity. This may infer that the technique may have shortcomings in measuring very low radial velocities (in the direction of the hot-wire supports).

Re-alignment of the probe to that of Case 2 of Fig. 2 generates data in which the error in the radial velocity is greatly reduced. Table 5 exhibits the results. The probe is now more greatly influenced by the radial component (in facility coordinates) of the flow. However, a reduction in the accuracy of the other two components can be seen.

Table 6 shows the results in the turbulent region after two rotations of the probe to the configuration of Case 3 of Fig. 2. The accuracy of the technique for time-mean properties can be seen clearly in these results.

The measuring technique does not appear to have any dependence on dominant flow direction for determination of the time-mean characteristics of the flow.

## 4. Conclusions

The six-orientation single hot-wire technique is a novel cost-effective tool for use in complex turbulent flow situations. The data are being used to aid in the evolution of turbulence models for swirling recirculating flows in combustor geometries. Flowfield surveys of confined jets with increasing amounts of swirl have been performed using the six-orientation single hot-wire technique. These measurements have been used to calculate of the time-mean velocity components and the normal and shear turbulent stresses. The effect of swirl on the time-mean velocity field is found to shorten the corner recirculation zone length and to generate the existence of a central recirculation zone, which is followed by a precessing vortex core region. As the degree of swirl increases, the length of the central recirculation bubble decreases, whereas its width, and also the width of the precessing vortex core, increases. At the jet inlet to the test section, directional turbulence intensities are found to increase significantly with swirl. Throughout the flowfield, the most dramatic effect of swirl is to increase values of the three turbulent shear stress terms.

Introduction of a strong contraction nozzle at  $L/D =$

Table 1. Laminar free jet measurements at  $x/d = 0$  and  $r/d = 0$  using Case 1 probe configuration

Combination Used	Measured			% Deviation		
	$u/u_0$	$v/u_0$	$w/u_0$	$u/u_0$	$v/u_0$	$w/u_0$
612	0.963	0.137	0.020	-3.7	13.7	2.0
123	0.987	0.134	0.030	-1.3	13.4	3.0
234	0.988	0.198	0.060	-1.2	19.8	6.0
345	NR					
456	NR					
561	1.010	0.137	0.010	1.0	13.7	1.0
Mean	0.986	0.152	0.040	-1.4	15.2	4.0

Table 2. Laminar free jet measurements at  $x/d = 0$  and  $r/d = 0$  using Case 2 probe configuration

Combination Used	Measured			% Deviation		
	$u/u_0$	$v/u_0$	$w/u_0$	$u/u_0$	$v/u_0$	$w/u_0$
612	0.978	0.031	0.035	-2.2	3.1	3.5
123	0.972	0.036	0.040	-2.8	3.6	4.0
234	0.990	0.056	0.015	-1.0	5.6	1.5
345	0.982	0.043	0.022	1.8	4.3	2.2
456	0.988	0.024	0.049	-1.2	2.4	4.9
561	0.986	0.022	0.041	-1.4	2.2	4.1
Mean	0.983	0.021	0.033	-1.7	2.1	3.3

Table 3. Laminar free jet measurements at  $x/d = 0$  and  $r/d = 0$  using Case 3 probe configuration

Combination Used	Measured			% Deviation		
	$u/u_0$	$v/u_0$	$w/u_0$	$u/u_0$	$v/u_0$	$w/u_0$
612	0.954	-0.030	-0.008	-4.6	-3.00	-0.8
123	0.954	-0.031	-0.008	-4.6	-3.10	-0.8
234	0.967	-0.039	-0.051	-3.3	-3.90	-5.1
345	0.948	-0.103	0.080	-5.2	-10.30	8.0
456	0.971	0.001	-0.003	-2.9	0.10	-0.3
561	0.951	-0.030	0.006	-4.3	-0.03	-0.6
Mean	0.958	-0.039	0.001	-4.2	-3.90	0.1

Table 4. Turbulent free jet measurements at  $x/d = 3$  and  $r/d = 0.5$  using Case 1 probe configuration

Combination Used	Measured			% Deviation		
	$u/u_0$	$v/u_0$	$w/u_0$	$u/u_0$	$v/u_0$	$w/u_0$
612	0.578	0.190	0.014	-7.18	19.0	1.4
123	0.592	0.184	0.020	-4.53	18.4	2.0
234	0.604	NR	0.002	-2.55	NR	0.2
345	0.570	0.143	0.008	-8.03	14.3	0.8
456	0.596	0.084	0.015	-3.92	8.4	1.5
561	0.585	0.187	NR	-5.69	18.7	NR
Mean	0.587	0.158	0.012	-5.30	15.8	1.2

Table 5. Turbulent free jet measurements at  $x/d = 3$  and  $r/d = 0.5$  using Case 2 probe configuration

Combination Used	Measured			% Deviation		
	$u/u_0$	$v/u_0$	$w/u_0$	$u/u_0$	$v/u_0$	$w/u_0$
612	0.552	0.039	0.043	-10.9	3.9	4.3
123	0.554	0.066	0.033	-10.7	6.6	3.3
234	0.520	-0.055	0.162	-16.2	-5.5	16.2
345	NR	NR	0.124	NR	NR	12.4
456	0.527	-0.033	0.081	-14.9	-3.3	8.1
561	0.576	0.033	0.112	-7.1	3.3	11.2
Mean	0.555	0.019	0.092	-10.5	1.9	9.2

Table 6. Turbulent free jet measurements at  $x/d = 3$  and  $r/d = 0.5$  using Case 3 probe configuration

Combination Used	Measured			% Deviation		
	$u/u_0$	$v/u_0$	$w/u_0$	$u/u_0$	$v/u_0$	$w/u_0$
612	0.548	0.103	-0.035	-11.6	10.3	-3.5
123	0.575	0.076	-0.006	3.4	7.6	-0.6
234	0.559	0.022	-0.024	-9.9	2.2	-2.4
345	0.552	0.037	0.000	-10.9	3.7	0.0
456	0.547	0.025	-0.019	-11.7	2.5	-1.9
561	0.547	0.063	-0.034	-11.7	6.3	3.4
Mean	0.555	0.046	-0.019	-10.5	4.6	-1.9

2 with an area reduction ratio of 4 causes a significant effect on the time-mean swirling flowfield. Central recirculation zones are shortened and axial velocities along the whole jet axis become positive. The core regions become narrow with strong swirl velocities and gradients. Turbulence levels and shear stresses are found to increase along the jet centerline near the exit of the contraction nozzle

A directional sensitivity analysis of the single-wire measurement technique was performed in a free jet of known properties. The analysis reveals that the technique adequately measures the three components of the time-mean flow velocity independent of the dominant flow direction with respect to the probe.

#### Acknowledgments

The authors are indebted to NASA Lewis Research Center and Air Force Wright Aeronautical Laboratories for support under Grant No. NAG 3-74, technical monitor Dr. J. D. Holdeman.

#### References

1. Lilley, D. G., "Turbulent Combustor Flowfield Investigation", Combustion Fundamentals Research Conference, held at NASA Lewis Research Center, Cleveland, Ohio, Oct. 21-22, 1982, pp. 152-168.
2. Chigier, N. A., and Beer, J. M., "Velocity and Static-Pressure Distributions in Swirling Air Jets Issuing from Annular and Divergent Nozzles", ASME Journal of Basic Engineering, Vol. 82, Dec. 1964, pp. 788-796.
3. Beer, J. M., and Chigier, N. A., Combustion Aerodynamics, Applied Science, London and Wiley, New York, 1972. Reprinted by Krieger, Melbourne, Florida, 1983.
4. Gupta, A. K., Lilley, D. G., and Syred, N., Swirl Flows, Abacus Press, Tunbridge Wells, England, 1983 (in press).
5. Lefebvre, A. H., Gas Turbine Combustion, McGraw-Hill, New York, 1983.
6. Owen, F. K., "Laser Velocimeter Measurements of a Confined Turbulent Diffusion Flame Burner", Paper AIAA-76-33, Washington, D.C., Jan. 26-28, 1976.
7. Hutchinson, P., Khalil, E. E., and Whitelaw, J. H., "Measurement and Calculation of Furnace-Flow Properties", Paper AIAA-77-50, Los Angeles, Calif., Jan. 24-26, 1977.
8. Baker, R. J., Hutchinson, P., and Whitelaw, J. H., "Velocity Measurements in the Recirculation Region of an Industrial Flame by Laser Anemometry with Light Frequency Shifting", Combustion and Flame, Vol. 23, 1974, pp. 57-72.
9. Chaturvedi, M. C., "Characteristics of Axisymmetric Expansions", Proceedings, Journal of the Hydraulics Division, ASCE, Vol. 89, No. HY3, 1963, pp. 61-92.
10. Mathur, M. L., and MacCallum, N. R. L., "Swirling Air Jets Issuing from Vane Swirlers, Part 2: Enclosed Jets", Journal of the Inst. of Fuel, Vol. 40, June 1967, pp. 238-245.
11. Rhode, D. L., Lilley, D. G., and McLaughlin, D. K., "Mean Flowfields in Axisymmetric Combustor Geometries with Swirl", Paper AIAA 82-0177, 1982, AIAA Journal (in press).
12. Yoon, H. K., and Lilley, D. G., "Five-Hole Pitot Probe Time-Mean Velocity Measurements in Confined Swirling Flows", Paper AIAA-83-0315, Reno, Nev., Jan. 10-13, 1983.
13. Gouldin, F. C., Depsky, J. S., and Lee, S. L., "Velocity Field Characteristics of a Swirling Flow Combustor", Paper AIAA-83-0314, Reno, Nev., Jan. 10-13, 1983.
14. Habib, M. A., and Whitelaw, J. H., "Velocity Characteristics of Confined Coaxial Jets With and Without Swirl", Paper ASME 79-WA/FE-21, New York, NY, Dec. 2-7, 1979.
15. Vu, B. T., and Gouldin, F. C., "Flow Measurements in a Model Swirl Combustor", AIAA Journal, Vol. 20, No. 5, May 1982, pp. 642-651.
16. Janjua, S. I., McLaughlin, D. K., Jackson, T. W., and Lilley, D. G., "Turbulence Measurements in a Confined Jet Using a Six-Orientation Hot-Wire Probe Technique", Paper AIAA-82-1262, Cleveland, Ohio, June 21-23, 1982. AIAA Journal, 1983 (in press).
17. Sommer, H. T., "Swirling Flow in a Research Combustor", Paper AIAA-83-0313, Reno, Nev., Jan. 10-13, 1983.
18. Sander, G. F., and Lilley, D. G., "The Performance of an Annular Vane Swirler", Paper AIAA-83-1326, Seattle, Wash., June 27-29, 1983.
19. King, C. F., "Some Studies of Vortex Devices - Vortex Amplifier Performance Behaviour", Ph.D. Thesis, University College of Wales, Cardiff, Wales, 1978.
20. Dvorak, K., and Syred, N., "The Statistical Analysis of Hot Wire Anemometer Signals in Complex Flowfields", DISA Conference, University of Leicester, 1972.
21. Jorgensen, F. E., "Directional Sensitivity of Wire and Fiber Film Probes", DISA Information No. 11, Franklin Lakes, NJ, pp. 31-37, May 1971.
22. Paul, R. P., Robot Manipulators, MIT Press, Cambridge, Mass., 1982.
23. Wang, C-T., Applied Elasticity, McGraw-Hill, New York, 1953.
24. Rhode, D. L., Lilley, D. G., and McLaughlin, D. K., "On the Prediction of Swirling Flowfields in Axisymmetric Combustor Geometries", ASME Journal of Fluids Engineering, Vol. 104, Sept. 1982, pp. 378-384.
25. Abujelala, M. T., and Lilley, D. G., "Confined Swirling Flow Predictions", Paper AIAA-83-0316, Reno, Nev., Jan. 10-13, 1983.

26. Sami, S., Carmody, T., and Rouse, H., "Jet Diffusion in the Region of Flow Establishment", Journal of Fluids Mechanics, Vol. 27, Part 2, 1967, pp. 231-252.

#### Appendix A: Coordinate Transformation

In the probe directional sensitivity analysis of Sections 2.2 and 3.3, coordinate rotation relationships are required in order to relate probe-sensed data in Cases 1, 2 or 3 of Fig. 2 back to facility coordinate data. Any (x, y, z)-cartesian coordinate axes may be rotated about the x, y, or z axis, respectively, by an angle  $\theta$ , with corresponding coordinate transformation matrices

$$R_{x\theta} = \begin{bmatrix} 1 & 0 & 0 \\ 0 & \cos\theta & -\sin\theta \\ 0 & \sin\theta & \cos\theta \end{bmatrix}$$

$$R_{y\theta} = \begin{bmatrix} \cos\theta & 0 & \sin\theta \\ 0 & 1 & 0 \\ -\sin\theta & 0 & \cos\theta \end{bmatrix}$$

$$R_{z\theta} = \begin{bmatrix} \cos\theta & -\sin\theta & 0 \\ \sin\theta & \cos\theta & 0 \\ 0 & 0 & 1 \end{bmatrix}$$

For example, a rotation about the z-axis by angle  $\theta$  results in old (x, y, z) coordinates of a point being related to its new (X, Y, Z) coordinates via:

$$[x \ y \ z]^T = R_{z\theta} [X \ Y \ Z]^T$$

Similarly, velocity components (u, v, w) are related to (U, V, W) via

$$[u \ v \ w]^T = R_{z\theta} [U \ V \ W]^T$$

In the notation of Fig 2 with velocity components

u, v, w in x, r,  $\theta$  facility coordinates

$\tilde{u}$ ,  $\tilde{v}$ ,  $\tilde{w}$  in x, y, z probe Case 1 coordinates

$\hat{u}$ ,  $\hat{v}$ ,  $\hat{w}$  in  $\hat{x}$ ,  $\hat{y}$ ,  $\hat{z}$  probe Case 2 coordinates

$\hat{\hat{u}}$ ,  $\hat{\hat{v}}$ ,  $\hat{\hat{w}}$  in  $\hat{\hat{x}}$ ,  $\hat{\hat{y}}$ ,  $\hat{\hat{z}}$  probe Case 3 coordinates

the following relationships prevail:

#### A.1 Case 1

The facility and probe Case 1 coordinates are coincident and

$$[u \ v \ w]^T = [\tilde{u} \ \tilde{v} \ \tilde{w}]^T$$

#### A.2 Case 2

In this case, a rotation of  $\theta = -45$  deg. is applied about the z, axis, resulting in

$$[u \ v \ w]^T = R_{z\theta} [\hat{u} \ \hat{v} \ \hat{w}]^T$$

#### A.3 Case 3

To go from Case 2 to Case 3, a rotation of  $\phi = -45$  deg. is applied about the  $\hat{x}$ -axis, resulting

$$[\hat{u} \ \hat{v} \ \hat{w}]^T = R_{x\phi} [\hat{\hat{u}} \ \hat{\hat{v}} \ \hat{\hat{w}}]^T$$

Clearly, the Case 3 velocity components are simply related to the facility velocity components. Further information on coordinate transformations and their application to velocities, and normal and shear stress terms, is available.<sup>2,2,23</sup>



APPENDIX G

THE PERFORMANCE OF AN ANNULAR VANE SWIRLER

(AIAA-83-1326)

# THE PERFORMANCE OF AN ANNULAR VANE SWIRLER

G. F. Sander\* and D. G. Lilley\*\*  
Oklahoma State University, Stillwater, Okla.

## Abstract

Axial vane swirler performance characteristics are investigated so as to aid in computer modeling of gas turbine combustor flowfields, and in the development and evaluation of turbulence models for swirling confined flow. The swirler studied is annular with a hub-to-swirler diameter ratio of 0.25 and ten adjustable vanes of pitch-to-chord ratio 0.68. Measurements of time-mean axial, radial, and swirl velocities are made at the swirler exit plane using a five-hole pitot probe technique with computer data reduction. Nondimensionalized velocities from both radial and azimuthal traverses are plotted for a range of swirl vane angles  $\phi$  from 0 to 70 degrees. A theoretical study is included of idealized exit-plane velocity profiles relating the swirl numbers  $S$  and  $S'$  to the ratio of maximum swirl and axial velocities for each idealized case.

Measurements of time-mean velocity components at the swirler exit plane show clearly the effects of centrifugal forces, recirculation zones, and blade wakes on the exit-plane velocity profiles. Assumptions of flat axial and swirl profiles are found to be progressively less realistic as the swirl vane angle increases, with axial and swirl velocities peaking strongly at the outer edges of the swirler exit and significant non-zero radial velocities present. A linear idealization of the axial and swirl profiles is appropriate for moderate swirl  $\phi = 45$  deg. but simple idealizations are not applicable to strong swirl cases because of the central recirculation zone extending upstream of the exit plane. Nonaxisymmetry is present in all swirl cases investigated.

## Nomenclature

c	blade chord width
d	swirler exit diameter
D	test section diameter
F	velocity ratio $w_0/u_0$ for case I
G	axial flux of momentum; velocity ratio $w_{mo}/u_0$ for case II
H, I, J	$w_{mo}/u_{mo}$ for cases III - V
p	time-mean pressure
s	blade spacing or pitch
S	swirl number = $G_\theta/(G_x d/2)$
u, v, w	axial, radial and swirl components of velocity
x, r, $\theta$	axial, radial, azimuthal cylindrical polar coordinates
z	hub-to-swirler diameter ratio $d_h/d$
$\beta$	yaw angle of probe = $\tan^{-1}(w/u)$
$\delta$	pitch angle of probe = $\tan^{-1}[v/(u^2 + w^2)^{1/2}]$
$\theta$	azimuth angle
$\rho$	density
$\sigma$	pitch-to-chord ratio = $s/c$
$\phi$	swirl vane angle

\* Graduate Student, School of Mechanical and Aerospace Engineering, Student Member AIAA

\*\* Professor, School of Mechanical and Aerospace Engineering, Associate Fellow AIAA

## Subscripts

atm	ambient atmospheric conditions
C, N, S, E, W	center, north, south, east, west pitot pressure ports
h	hub
in	inlet conditions, upstream of swirler
m	maximum profile value
o	value at swirler outlet
x	axial direction
$\theta$	tangential direction
$\infty$	reference value at edge of swirler exit

## Superscripts

alternate form, neglecting pressure variation; fluctuating quantity  
time-mean quantity

## 1. Introduction

### 1.1 Combustor Flowfield Investigations

The problem of optimizing gas turbine combustion chamber design is complex, because of the many conflicting design requirements. The need for a more complete understanding of the fluid dynamics of the flow in such combustion chambers has been recognized by designers in recent years, and research is continuing on several fronts to alleviate the problem. As part of an on-going project at Oklahoma State University, studies are in progress concerned with experimental and theoretical research in 2-D axisymmetric geometries under low speed, non-reacting, turbulent, swirling flow conditions. The flow enters the test section and proceeds into a larger chamber (the expansion ratio  $D/d = 2$ ) via a sudden or gradual expansion (side-wall angle  $\alpha = 90$  and 45 degrees). Inlet swirl vanes are adjustable to a variety of vane angles with  $\phi = 0, 38, 45, 60$  and 70 degrees being emphasized. The general aim of the entire study is to characterize the time-mean and turbulence flowfield, recommend appropriate turbulence model advances, and implement and exhibit results of flowfield predictions. The present contribution concentrates on the time-mean flow characteristics being generated by the upstream annular swirler, using a five-hole pitot probe technique.

### 1.2 Previous Studies

Research is progressing in several areas related to the flow facility investigation just described. Computer simulation techniques are being used to study the effect of geometry and other parameter changes on the flowfield. An advanced computer code<sup>1</sup> has been developed to predict confined swirling flows corresponding to those studied experimentally. Tentative predictions<sup>2</sup> have now been supplemented by predictions made from realistic inlet conditions<sup>3</sup> for a complete range of swirl strengths with downstream nozzle effects.<sup>4</sup> Accuracy of predictions from a computer model is strongly dependent on the inlet boundary conditions used, which are primarily determined by the swirler and its performance at different vane angle settings. In the earlier predictions, the velocity boundary conditions at the inlet to the model combustor were approxi-

mated by idealized flat profiles for axial and swirl velocity, with radial velocity assumed to be zero. However, recent measurements taken closer to the swirler exit show that the profiles produced are quite nonuniform, with nonzero radial velocity and nonaxisymmetry.

The flowfield in the test section is being characterized experimentally in a variety of ways. Flow visualization has been achieved via still<sup>5</sup> and movie<sup>6</sup> photography of neutrally buoyant helium-filled soap bubbles and smoke produced by an injector and a smoke wire. Time-mean velocities have been measured with a five-hole pitot probe at low<sup>5</sup> and high<sup>7</sup> swirl strengths. To help in turbulence modeling, complete turbulence measurements have been made on weakly<sup>8</sup> and strongly<sup>9</sup> swirling flows, using a six-orientation single-wire hot-wire technique. An alternative three-wire technique has also been shown to be useful in these complex flow situations.<sup>10</sup>

### 1.3 Scope and Objectives

A key element in swirling flow studies is the swirler generator used. Since it lies at the inlet to the combustor model, the swirler can have a strong influence on measurements and/or predictions made further downstream. Better definition of the performance characteristics of the swirler is needed. In the present study, the main objective is to make time-mean velocity measurements as close as possible to the swirler exit, so as to define more accurately the performance characteristics of the swirler. A range of swirl-blade angles  $\phi$  from 0 to 70 deg. is considered. Specific objectives are to:

1. Investigate the flow turning effectiveness of flat blades in annular vane swirlers at various blade angles,  $\phi$ .
2. Investigate the degree of nonaxisymmetry introduced by vane-type swirlers.
3. Establish correlations between the blade angle  $\phi$  and the velocity profiles and degree of swirl actually produced.
4. Evaluate the applicability of idealized velocity profiles used recently in flow-field prediction codes, and specify more realistic idealized profiles for future use.
5. Provide swirler exit data usable as inlet conditions in prediction codes being used to establish, evaluate, and improve turbulence models.

### 1.4 Outline of the Paper

Section 2 describes theoretical analysis of idealized swirler exit velocity profiles, relating the swirl number to the ratio of maximum swirl and axial velocities for several typical cases. Experimental equipment and procedures used for measurement of the swirler exit flowfield are covered in Section 3. It includes descriptions of the swirler, measurement technique, and data reduction procedure. The first two parts of Section 4 discuss experimental results from radial and azimuthal traverses, respectively, noting the presence of nonaxisymmetry, recirculation, and strong velocity gradients at the swirler exit plane. The third part describes the

results of a check on sensitivity of the measurements to calibration errors. Finally, Section 5 presents conclusions drawn from the above results.

## 2. Theoretical Analysis

### 2.1 Idealized Velocity Profiles

All theoretical analyses of swirler performance and most numerical simulations of combustor flowfields have used simple idealized swirler exit velocity profiles. Common assumptions made include flat axial and swirl velocity profiles downstream of the swirler for swirlers with vanes of constant angle<sup>2,5,11,12</sup> and a flat axial profile with a linear swirl profile (solid-body rotation) for swirlers with helicoidal vanes and for tangential-entry swirl generators.<sup>13,14</sup> These, however, have been shown to be quite unrealistic<sup>3,12,15</sup> and to lead to considerable errors in computer predictions of the flowfield.<sup>4</sup> Although the best remedy for numerical simulations is to use experimentally measured swirler exit profiles if they are available, idealized profiles are very useful in theoretical work. If more realistic profile assumptions can be developed which are still mathematically tractable, more useful analytical results may be derived. Better idealized profiles would also be useful as inlet boundary conditions for computer modeling when measured data are not available.

Measurements have shown<sup>3</sup> that linear and parabolic profiles of axial velocity are more appropriate for moderate and high swirl cases, and that the swirl velocity also approaches a parabolic profile at high swirl strengths, with most of the flow leaving near the outer boundary of the swirler. Several combinations of linear and parabolic idealized profiles are shown in Fig. 1, along with the flat, linear and parabolic profile assumptions stated in the form of profile expressions. Parameters associated with these profiles are investigated in Section 2.3.

### 2.2 Definition of Swirl Parameters

The swirl number is a nondimensional parameter used to characterize the degree of swirl generated by a swirler. It is defined as

$$S = \frac{G_{\theta}}{G_x(d/2)} \quad (1)$$

where the axial flux of angular momentum  $G_{\theta}$  is given by

$$G_{\theta} = \int_0^{2\pi} d\theta \int_0^{d/2} [\rho u w + \overline{\rho u' w'}] r^2 dr \quad (2)$$

and the axial flux of axial momentum  $G_x$  is given by

$$G_x = \int_0^{2\pi} d\theta \int_0^{d/2} [\rho u^2 + \overline{\rho u'^2} + (p - p_{\infty})r] dr \quad (3)$$

and  $d/2$  is the swirler exit radius. These equations are obtained from appropriate manipulation of the axial and azimuthal momentum equations, respectively. In free jet flows these two expressions are invariant with respect to downstream location. In the axial momentum expression, the pressure term  $(p - p_{\infty})$  is given from radial integration of the radial momentum equation<sup>16</sup> by

$$S' = \frac{G_\theta}{G'_x(d/2)} \quad (6)$$

If turbulent stress terms are neglected, it is apparent that a knowledge of the distribution of the time-mean  $u$  and  $w$  velocity components across the swirler is sufficient to calculate either swirl number. The idealized exit velocity profiles provide just such knowledge, and expressions relating swirl number to the ratio of maximum exit swirl velocity to maximum or constant axial velocity can now be derived for each of the profile types. As the procedure is similar for each of the five cases, a detailed derivation is shown for the first case only, with results merely stated for the other four cases.

### 2.3 Swirl Numbers for Idealized Profiles

By assuming axisymmetric flow and neglecting turbulent stresses as stated previously, the definitions in Eqs. (2) through (4) reduce to

$$G_\theta = 2\pi \int_0^{d/2} [\rho u w] r^2 dr \quad (7)$$

$$G'_x = 2\pi \int_0^{d/2} [\rho u^2 + (p - p_\infty)] r dr \quad (8)$$

$$(p - p_\infty) = \int_0^r [\rho w^2 \frac{1}{r}] dr \quad (9)$$

When the expressions for axial and swirl velocity for case I (See Fig. 1) are substituted into Eq. (7), one obtains

$$G_\theta = \frac{2}{3} \pi \rho u_0 w_0 (d/2)^3 \quad (10)$$

Substitution of  $w(r) = w_0$  into Eq. (9) and integrating produces

$$(p - p_\infty) = \rho w_0^2 [\ln(r) - \ln(d/2)] \quad (11)$$

After substituting Eq. (11) into Eq. (8) and integrating, the expression becomes

$$G'_x = \pi \rho u_0^2 (d/2)^2 \left[ 1 - \frac{1}{2} \left( \frac{w_0}{u_0} \right)^2 \right] \quad (12)$$

Finally, putting Eqs. (10) and (12) into Eq. (1) and defining the velocity ratio  $F = w_0/u_0$ , the swirl number  $S$  can be expressed thus:

$$S = \frac{2F/3}{1 - F^2/2} \quad (13)$$

The alternate swirl number  $S'$  follows from finding the dynamic axial flux of axial momentum:

$$G'_x = \pi \rho u_0^2 (d/2)^2 \quad (14)$$

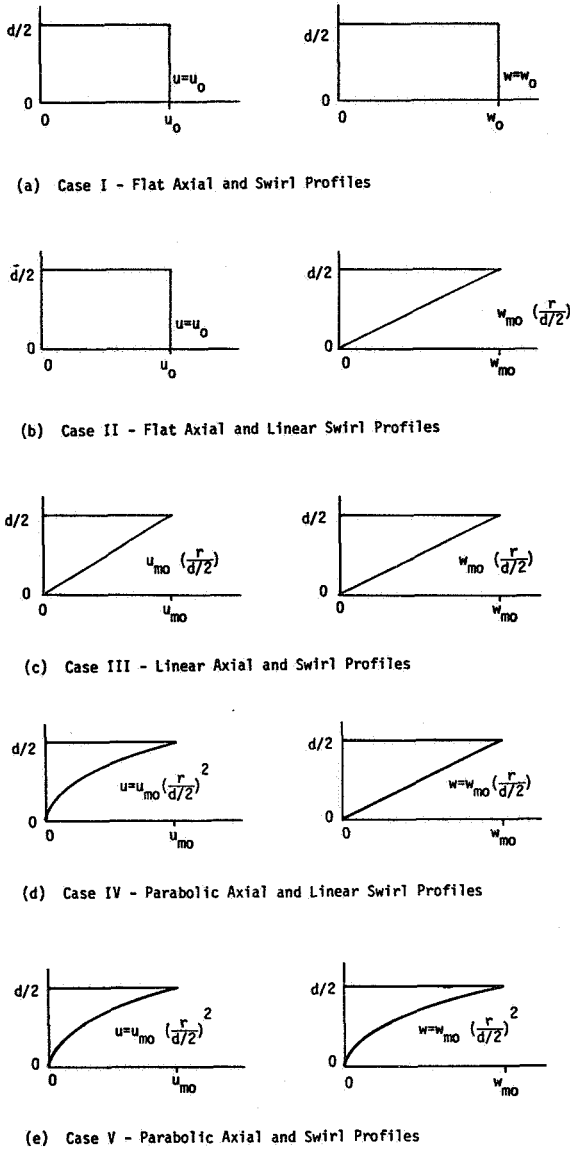


Fig. 1. Idealized axial and swirl velocity profile cases

$$(p - p_\infty) = \int_0^r [\rho w^2 \frac{1}{r}] dr - \overline{\rho v'^2} \quad (4)$$

If the pressure term is omitted from the axial momentum, the dynamic axial momentum flux  $G'_x$  is obtained:

$$G'_x = \int_0^{2\pi} d\theta \int_0^{d/2} [\rho u^2 + \overline{\rho v'^2}] r dr \quad (5)$$

and leads to an alternate definition of swirl number<sup>17</sup>:

Using this in Eq. (6) leads to the simple expression

$$S' = 2F/3 \quad (15)$$

Equations (13) and (15) provide the top row in Table 1, where equations relating  $S$  and  $S'$  to  $F$ ,  $G$ ,  $H$ ,  $I$ , and  $J$  [deduced in a similar manner] are given for the five cases of Fig. 1. Note that the profile equations are given in Fig. 1 and other parameters are defined by:

$$\begin{aligned} F &= w_o / u_o \\ G &= w_{mo} / u_o \\ H &= w_{mo} / u_{mo} \\ I &= w_{mo} / u_{mo} \\ J &= w_{mo} / u_{mo} \end{aligned} \quad (16)$$

It is interesting to see how these parameters vary with  $S$  and  $S'$ , and Fig. 2 portrays the relationships of the equations in Table 1 visually, for a range of commonly encountered swirl numbers.

Table 1. Idealized Swirler Exit Velocity Profiles

Case	$S$	$S'$
I	$S = \frac{2F/3}{1 - F^2/2}$	$S' = 2F/3$
II	$S = \frac{G/2}{1 - G^2/4}$	$S' = G/2$
III	$S = \frac{4H/5}{1 - H^2/2}$	$S = 4H/5$
IV	$S = \frac{I}{1 - 3I^2/4}$	$S' = I$
V	$S = \frac{4J/7}{1 - 2J^2/3}$	$S' = 4J/7$

It is evident from the equations alone that the  $S'$  expressions are all simple linear relations. The parameters  $F$  through  $J$  will increase without bound as  $S'$  is increased in each case. In contrast, the parameter change with  $S$  shows asymptotic behavior; the exit velocity ratios all approach definite values as swirl number increases, or, conversely, the swirl number goes to infinity for a certain value of the velocity ratio in each case.

Although the curves are generally similar in shape, some observations can be made. The curves for cases II and IV are the upper and lower extremes for both the  $S$  and  $S'$  relations, with the curves for cases I, III, and V falling in between. This may be anticipated since the  $w$ -profile is of higher order than the  $u$ -profile for case II (that is, linear versus constant) and the opposite is true for case IV (linear versus parabolic). In the other three cases the  $u$  and  $w$  profiles are of the same order.

In appraising the usefulness of the idealized profiles, comparison may be made with the measured profiles given later in Section 4. As the swirl strength increases from 0 to 70 deg., corresponding

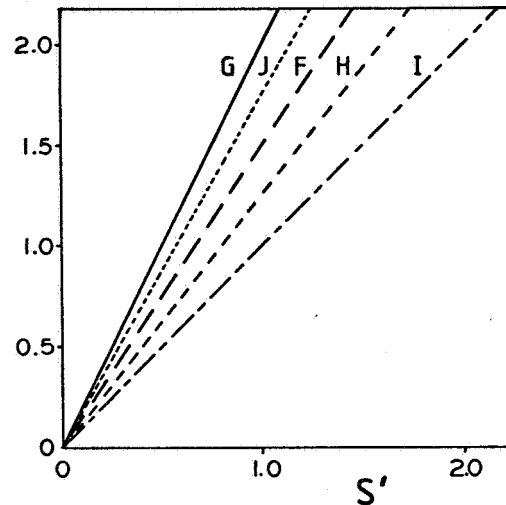
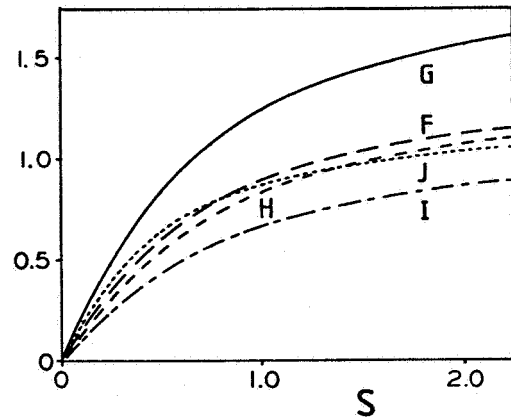


Fig. 2. Variation of velocity ratios  $F$  through  $J$  [Cases I through V, respectively] with  $S$  and  $S'$ .

profiles of cases I to V are roughly appropriate. However, the presence of the hub and central recirculation zone prevent adequate representation via the idealized profiles, except for moderate swirl ( $\phi = 45$  deg.) and its corresponding Case III.

### 3. Experimental Equipment and Procedure

#### 3.1 The Facility

The installation on which all tests were performed is a low-speed wind tunnel designed and built at Oklahoma State University. It produces uniform flow of relatively low turbulence intensity, with continuously adjustable flow rate. The facility consists of a filtered intake, an axial blower, a stilling chamber, a turbulence management section, and a contoured outlet nozzle. It is described at length in several recent documents.<sup>3,5,7</sup> The contoured nozzle is made of molded fiberglass with a steel flange at the outlet for the attachment of the swirler and/or expansion block en route to the test section in associated studies. A 1 cm diameter hole a short distance upstream of the outlet allows for insertion of a standard pitot-static probe to measure the dynamic pressure upstream of the swirler. This measurement, with a small correction for dif-

ference in flow area, is used to calculate the swirler inlet reference velocity,  $u_{in}$ .

### 3.2 The Swirler

The swirler used in this study is annular with hub and housing diameters of 3.75 and 15.0 cm, respectively, giving a hub-to-swirler diameter ratio  $z$  of 0.25. The hub has a streamlined parabolic nose facing upstream and a blunt base (corner radius approximately 2 mm) facing downstream. It is supported by four thin rectangular-sectioned struts or spider arms from the housing wall. The base of the hub protrudes approximately 3 mm downstream of the swirler exit plane. Photographs and schematics of the swirler are shown in Figs. 3 through 5.

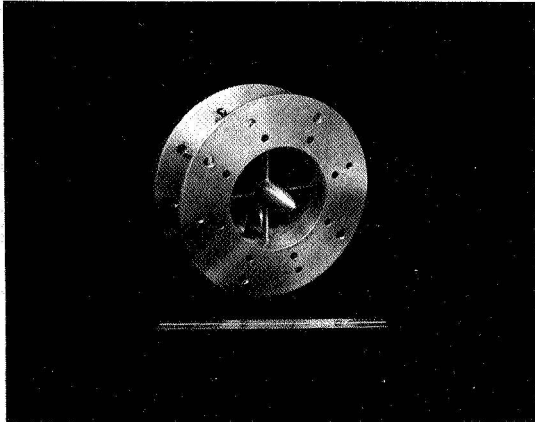


Fig. 3. Photograph of swirler - upstream end

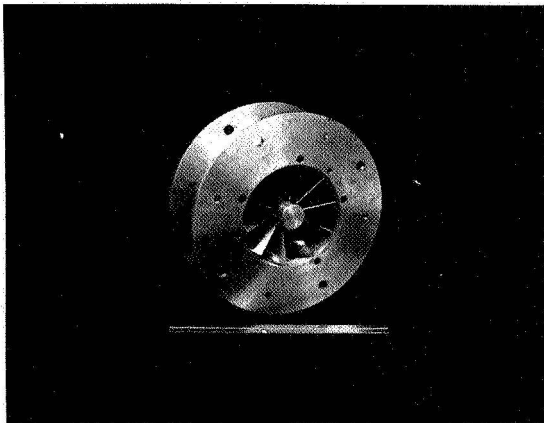


Fig. 4. Photograph of swirler - downstream end

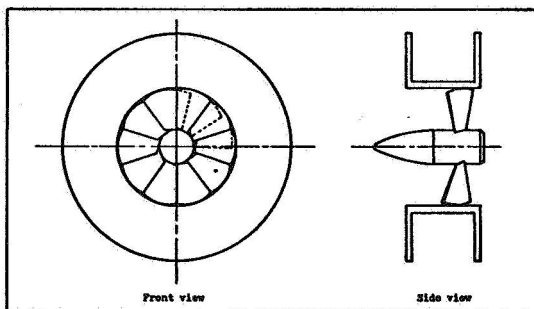


Fig. 5. Diagram of swirler - section and downstream view

The ten vanes or blades are attached to shafts which pass through the housing wall and allow individual adjustment of each blade's angle. The standard vanes are wedge-shaped to give a constant pitch-to-chord ratio  $\sigma$  of 0.68, which according to two-dimensional cascade data, should give reasonably good flow-turning effectiveness. Sets of vane planforms are shown in Fig. 6.

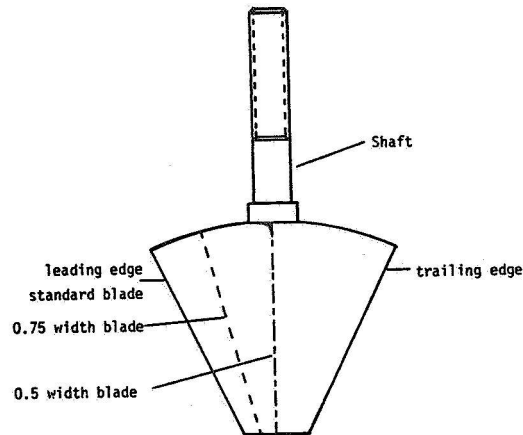


Fig. 6. Swirl vanes

### 3.3 Measurement Procedure

The time-mean velocity components are measured with a five-hole pitot probe which allows determination of the magnitude and direction of the mean velocity vector simultaneously.<sup>5,7</sup> The probe is mounted in a traversing mechanism which allows it to be translated vertically (on a radial line outward from the test section axis) and rotated about the probe's yaw axis. In addition to the motion permitted by the traverse mechanism, the test section tube on which the traverse mechanism is mounted may be rotated about its axis with respect to the swirler, thereby allowing azimuthal traverses to be performed. Tubing from the probe's five pressure taps is routed through selector valves to a differential pressure transducer, and the resulting pressure difference values are read directly from an integrating digital voltmeter. The pressure data are reduced by a computer program to yield nondimensionalized  $u$ ,  $v$ , and  $w$  velocity components, which are then plotted in the form of profiles. Details appear in Refs. 3, 17, 18.

## 4. Experimental Results

Velocity profiles from both radial and azimuthal traverses for each of the flowfields investigated are now presented and discussed. Table 2 gives a summary of the operating conditions used during the studies. With nonswirling conditions, the low fan speed delivers relatively high axial velocity and corresponding Reynolds number. At progressively higher swirl strength conditions, progressively higher fan speeds are used, but even so exit velocities and Reynolds numbers reduce because of increasing flow restriction of the swirler. However, based on a limited study elsewhere,<sup>17</sup> it is expected that all flowfields are in the Reynolds number independent regime.

The radial traverses consist of ten points from the centerline to the swirler exit radius, spaced 7.6 mm apart. Of these ten, only seven stations

Table 2. Summary of Operating Conditions\*

$\phi$ (degrees)	FS (rpm)	$u_{in}$ (m/s)	$Re_d \times 10^{-5}$
0	1950	23.00	2.22
38	2265	13.30	1.30
45	2600	13.00	1.26
60	2800	9.20	0.90
70	2800	5.52	0.53

\* Abbreviations used are:

- $\phi$  Swirl vane angle
- FS Fan speed
- $u_{in}$  Spatial-mean swirler exit axial velocity, deduced from independent upstream measurement, excluding presence of the hub and swirler
- $Re_d$  Swirler-exit Reynolds number based on  $u_{in}$  and swirler diameter

were actually measured since the hub blocked the inner three positions. The azimuthal traverses contain nine points spaced 6 degrees apart at a constant radial distance from the centerline. Azimuth angles  $\phi$  were taken from -24 to +24 degrees, with the  $\theta = 0$  position in line with the shaft of one of the swirl vanes. A diagram showing the traverse patterns on the face of the swirler is given in Fig. 7.

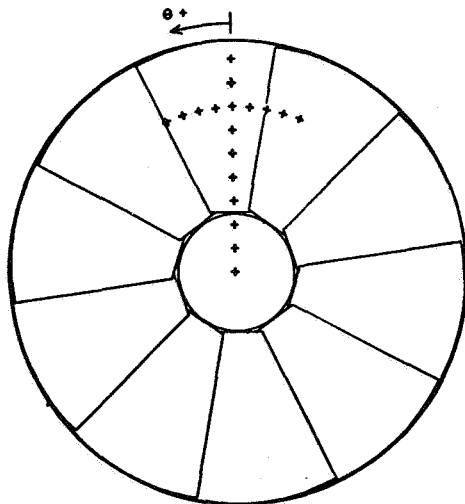


Fig. 7. Measurement locations - radial and azimuthal traverses

All traverses are taken immediately after the swirler exit downstream face with no expansion blocks present. Nominally, this location is  $x/D = -0.109$ , where the position  $x/D = 0.0$  is the expansion station, separated from the swirler in prac-

tice<sup>5-10</sup> with one of the expansion blocks. In Ref. 3, some data are also presented with the expansion block affixed to the downstream face of the swirler and measurements then taken at  $x/D = 0.0$ .

#### 4.1 Velocity Profiles from Radial Traverses

Radial traverses of axial, radial and swirl velocity component data are presented for five values of swirl blade angle: zero (no swirler), zero (with swirler), 38, 45, 60, and 70 deg., in Figs. 8 through 13, respectively, with the profiles extending from the centerline to twice the exit radius ( $r/D = 0.5$  where  $D$  is the test section diameter used in associated studies). All velocities shown are normalized with respect to the swirler inlet uniform axial velocity  $u_{in}$ , deduced independently from the pitot-static measurement upstream of the swirler. The outer ten data points are zero in each profile because the presence of the solid boundary of the swirler flange precluded measurements at these locations.

The nonswirling case shown in Fig. 8 has a nearly-flat axial velocity profile, as expected for the plain nozzle opening without the swirler installed. There is no measurable swirl velocity, and the radial velocity is zero except for points very near the edge of the exit, where the flow begins to anticipate the abrupt expansion to twice the exit diameter. The second nonswirling case, see Fig. 9, has the swirler installed with the blades set to  $\phi = 0$  deg. The traverse was made midway between two blades and away from any of the hub supporting struts. Here again the axial profile is quite flat, with just a slight increase toward the hub. However, the velocity has increased by nearly 25 percent, because of the decrease in flow area with swirler hub and vanes in place. In addition, the hub induces a negative radial velocity across the entire annulus, overriding the tendency to anticipate the expansion corner. The swirl velocity is, as expected, negligible.

The 38-deg. blade-angle case in Fig. 10 shows remnants of the flat inlet profile over a small portion of the radius near the outside edge in both the axial and swirl profiles. The presence of the hub now constrains the three innermost points to zero, and the region between the hub and the flat portion in the axial and swirl profiles is approximately linear. The maximum axial velocity is 1.5 times the inlet axial velocity because the flow area is decreased by the hub and also because centrifugal effects have shifted the profile outward. The radial velocity has an irregular profile with a maximum value of one-half the inlet axial velocity.

In the  $\phi = 45$  deg. case of Fig. 11, the flat segments are no longer present and both axial and swirl profiles vary from zero at the hub to a maximum at or near the rim of the swirler in an almost linear fashion. The similar shape and magnitude of the profiles indicates that the turning angle is fairly uniform and only slightly less than 45 degrees. The radial velocity is again irregular, but shows a step at  $r/D = 0.1$  similar to that in the axial and swirl profiles; this is probably due to the central recirculation zone downstream beginning to slow down the flow upstream of it.

Profiles ensuing from the case of  $\phi = 60$  deg., see Fig. 12, all have a sharply peaked shape, with most of the flow leaving near the outer boundary.

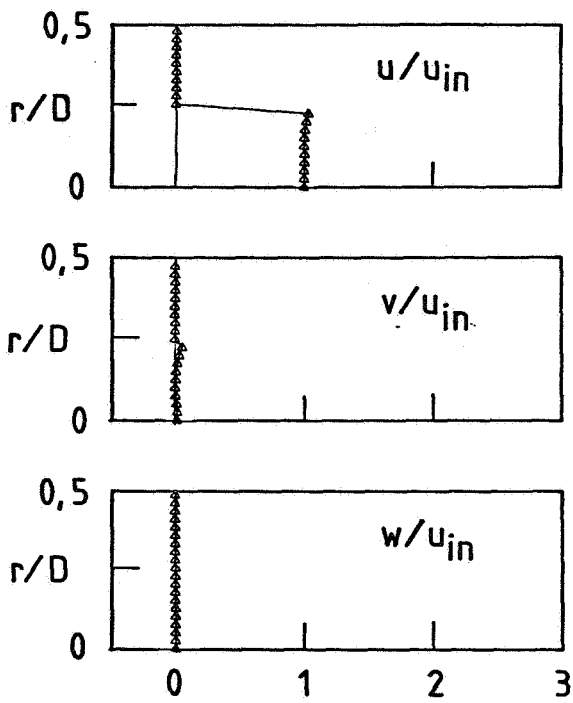


Fig. 8. Normalized velocity profiles from radial traverse,  $\phi = 0$  deg. (No swirler)

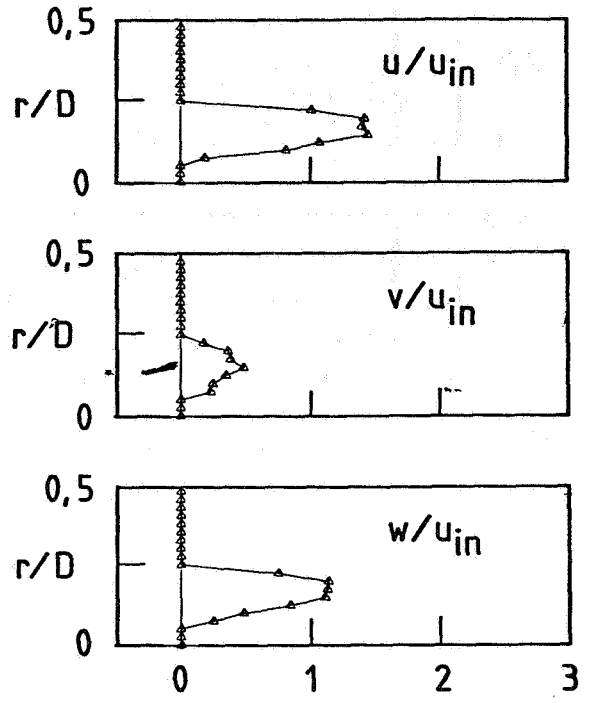


Fig. 10. Normalized velocity profiles from radial traverse,  $\phi = 38$  deg.

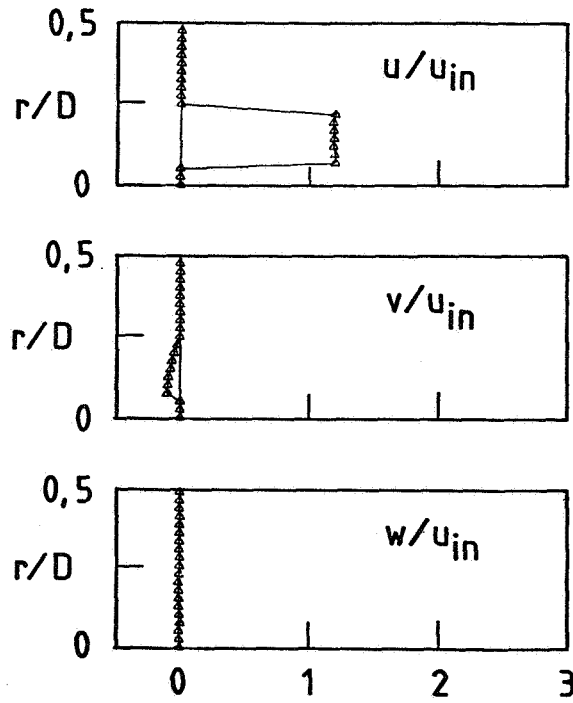


Fig. 9. Normalized velocity profiles from radial traverse,  $\phi = 0$  deg. (Swirler installed)

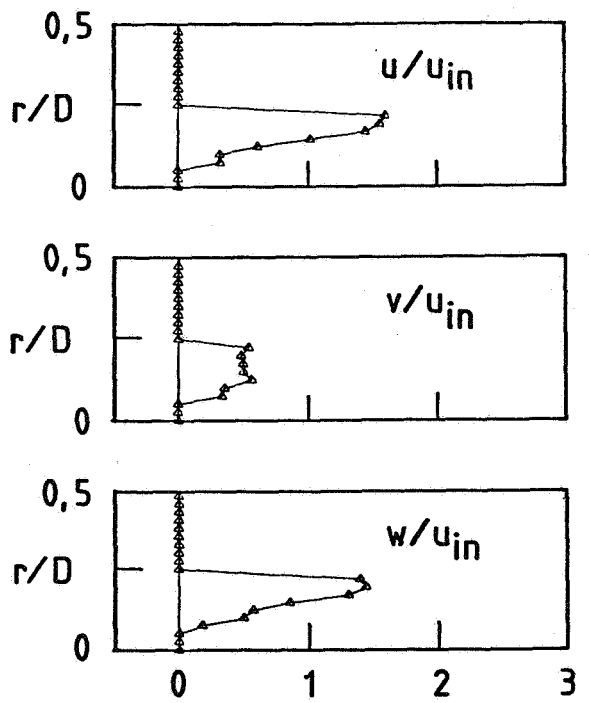


Fig. 11. Normalized velocity profiles from radial traverse,  $\phi = 45$  deg.



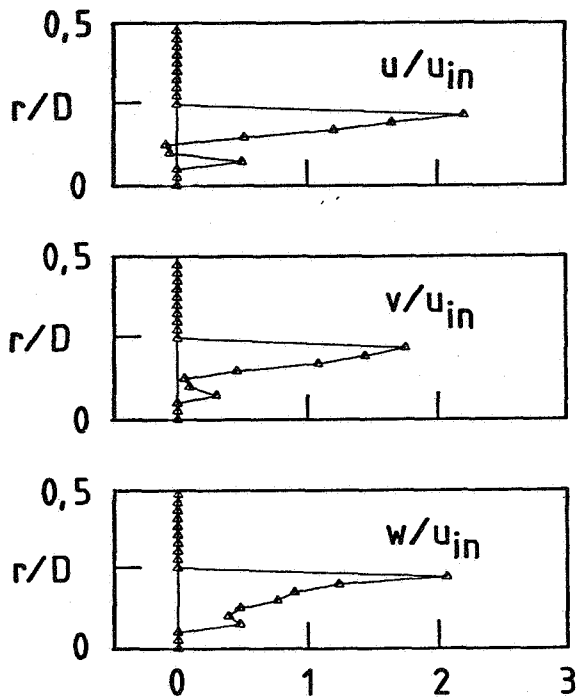


Fig. 12. Normalized velocity profiles from radial traverse,  $\phi = 60$  deg.

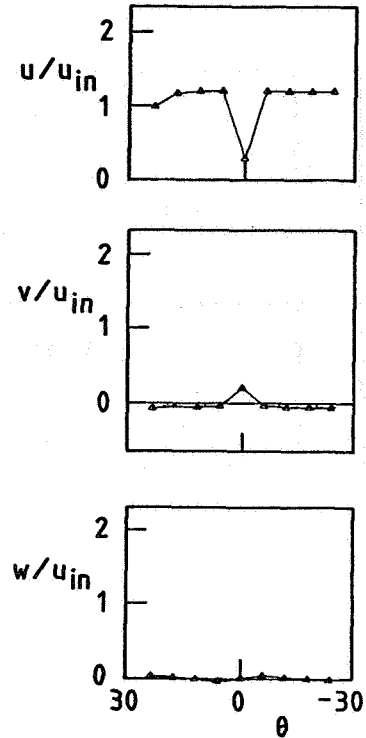


Fig. 14. Normalized velocity profiles from azimuthal traverse,  $\phi = 0$  deg. at  $r/D = 0.179$  (Swirler Installed).

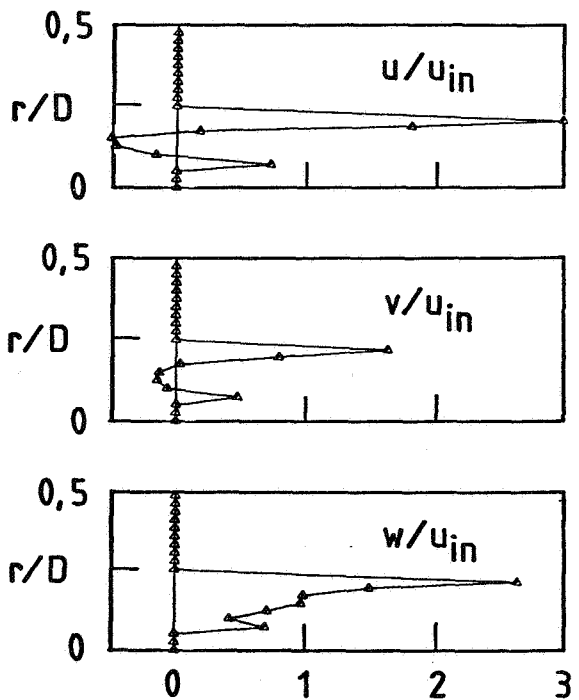


Fig. 13. Normalized velocity profiles from radial traverse,  $\phi = 70$  deg.

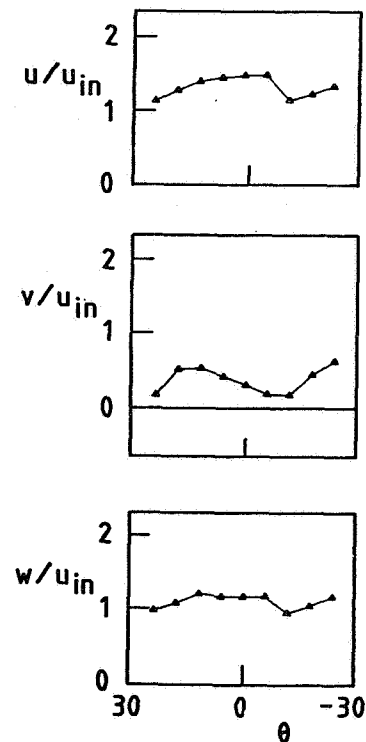


Fig. 15. Normalized velocity profiles from azimuthal traverse,  $\phi = 38$  deg. at  $r/D = 0.179$

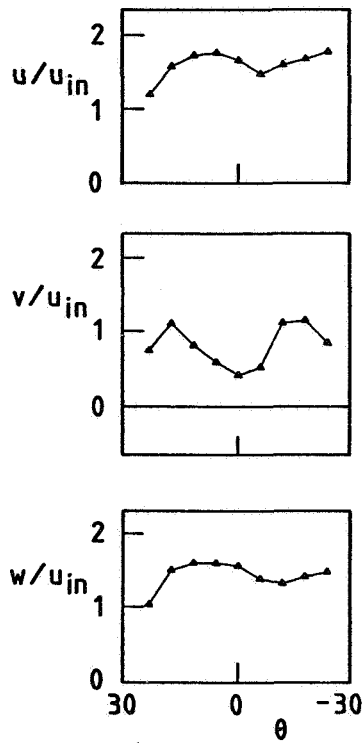


Fig. 16. Normalized velocity profiles from azimuthal traverse,  $\phi = 45$  deg. at  $r/D = 0.179$

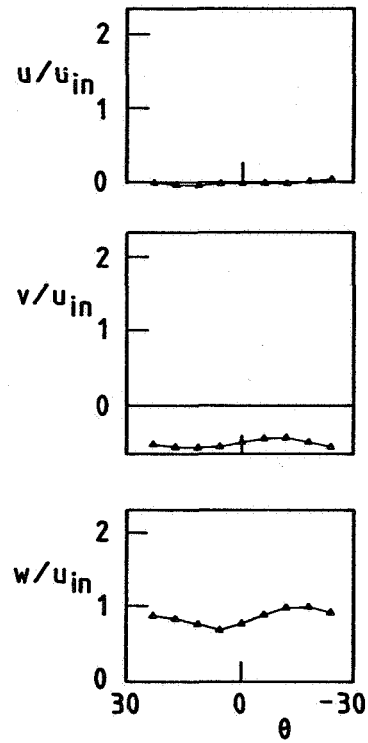


Fig. 18. Normalized velocity profiles from azimuthal traverse,  $\phi = 70$  deg. at  $r/D = 0.179$

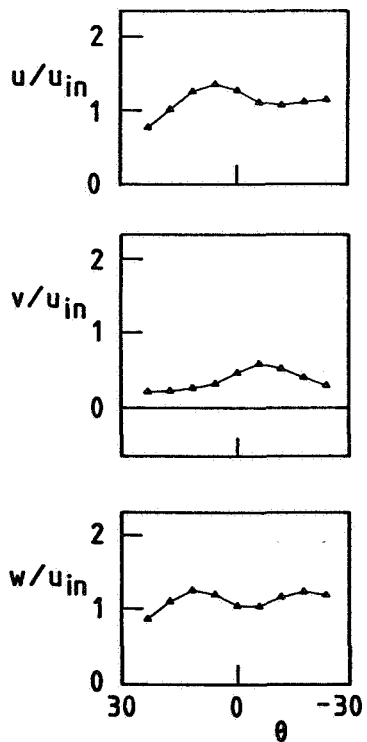


Fig. 17. Normalized velocity profiles from azimuthal traverse,  $\phi = 60$  deg. at  $r/D = 0.179$

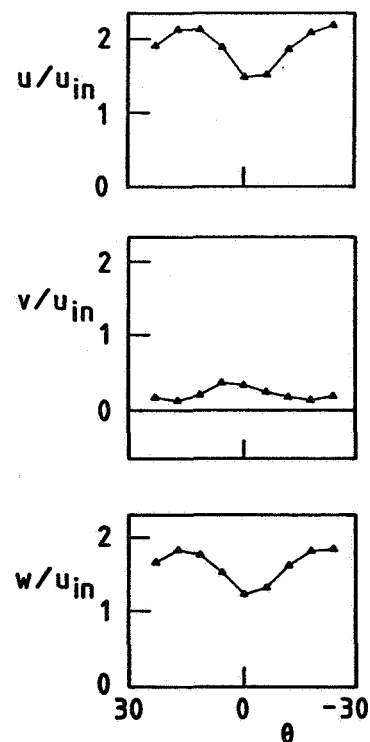


Fig. 19. Normalized velocity profiles from azimuthal traverse,  $\phi = 70$  deg. at  $r/D = 0.204$

The radial component is considerably stronger, with a peak value nearly twice that of the reference velocity upstream of the swirler. The step seen previously in the 45 deg. axial profile, has now developed into reverse flow, indicating that the central recirculation zone now extends upstream past the exit plane. The reverse flow is accompanied by reduced swirl velocity and very low values of radial velocity. The positive axial velocity adjacent to the hub may be the result of a slight clearance between the blades and the hub, allowing air with greater axial momentum to pass through.

Exit velocity profiles obtained for the strongest swirl case considered ( $\phi = 70$  deg.) are shown in Fig. 13. Almost all of the flow leaves the swirler at the outside edge. The maximum axial and swirl velocities are approximately 3 and 2.5 times the upstream reference values, respectively, and the velocity gradients across the profiles are quite large. The reverse flow in the center of the axial profile is stronger than in the 60-deg. case and is now accompanied by negative or inward radial velocity. This suggests the possibility of a vortex ring structure occurring at the exit of the swirler under high-swirl conditions. The swirl velocity profile remains positive but shows a step corresponding to the outer boundary of the recirculation zone.

#### 4.2 Velocity Profiles from Azimuthal Traverses

An indication of the azimuthal or  $\theta$ -variation of axial, radial, and swirl velocities is now given for the same vane angle settings used in the radial traverses. The measurements were taken at a constant radial position of  $r/D = 0.179$ , which in most cases illustrates adequately the azimuthal flow variation. However, measurements at  $r/D = 0.204$  were necessary in the  $\phi = 70$  degree case to get data more representative of the main region of the flow.

In addition, azimuthal traverse measurements were taken  $0.109 D$  downstream (at  $x/D = 0.0$ , the expansion corner with the 90-degree block installed) for  $\phi = 70$  deg. so as to investigate further the upstream extent of the central recirculation zone. These data are reported in Ref. 3, whereas radial profiles at this location, for all degrees of swirl, are already available.<sup>7</sup>

Measurements in each case span an angle of 48 degrees, somewhat more than the 36 degrees between successive blades. Velocity profiles are given in Figs. 14 through 19. The variations in all normalized velocity components,  $u$ ,  $v$ , and  $w$  occur in approximately 36-deg. cycles, coinciding with the blade spacing. The profiles all show significant variation with azimuthal position, except for those in or near recirculation zones where the  $w$ -velocity component is dominant. These variations can be attributed to several causes, among them being blade stall from using flat blades at high angles of attack and wakes from blunt trailing edges.

Figure 14 shows the azimuthal profile with the swirler installed, but with the vanes set to zero angle. The  $\phi = 0$  deg. position is directly downstream of one of the swirl vanes, approximately 3 mm from the trailing edge at the  $r/D = 0.179$  position. The velocity defect in the wake of the blade is clearly seen in the axial velocity profile, although the precise accuracy of these measurements is uncertain because of the velocity gradients

across the width of the probe. The decreased  $u$ -velocity at the left side of the profile is caused by the presence of an upstream strut supporting the hub, located at  $\theta = +24$  deg. The radial velocity is uniformly negative indicating inflow over most of the range, which agrees well with the results of the radial traverse shown earlier in Fig. 9. The radial velocity is positive only in the blade wake region. The swirl velocity, as expected, is effectively zero.

Figure 15 presents the results of an azimuthal traverse for the  $\phi = 38$  deg. low-swirl case. The measurement position at  $r/D = 0.179$  is in the middle of the flat portion of the radial profile, as may be deduced from observation of Fig. 3. The 36 deg. cyclic variation from one blade to the next is apparent in each of the profiles. The  $u$  and  $w$  profiles have a flat portion, apparently between blade wakes, with an average yaw angle of about 39 deg. This confirms the assumption that the blade pitch/chord ratio of one is sufficient to adequately turn the flow. In fact, over the rest of the profile, the turning angle is even higher than the blade angle  $\phi$ . The radial velocity shows no flat region and varies the most of the three components. It is also quite large even at this low degree of swirl.

In the case of  $\phi = 45$  deg., Fig. 16 illustrates that the 36-deg. cycle is not as clear, but nevertheless significant variation exists in all profiles. The radial component is nearly as large as the axial and swirl components in some places, and again exhibits the greatest variation with azimuthal position.

For the 60-deg. swirl case of Fig. 17, variations with azimuthal position are again evident in all profiles. The variation is less than in the cases seen heretofore, possibly because the main flow has shifted further outward under centrifugal effects and the measurement position is in a region of reduced velocity.

This effect is even more notable in the  $\phi = 70$  deg. profiles portrayed in Fig. 18. The measurement position is now no longer in the main exiting flow, but on the edge of the central recirculation zone. The axial velocity here is effectively zero, although considerable swirl and radial velocities are present. The radial velocity, it should be noted, is negative or inward towards the centerline. Azimuthal variations are fairly small here, which is to be expected since the flow is mainly in the azimuthal direction. To get a more representative sample of the exiting flow from the swirler with blades at 70 deg., a traverse was made at the next outward radial station at  $r/D = 0.204$ . When the velocity profiles shown in Fig. 19 are compared with those in the previous figure, the effects of extreme velocity gradients in the radial direction may be perceived. The accuracy of the radial velocity and pitch angle measurements may be suspect in the presence of high radial velocity gradients, but the major features of the flow can still be assessed. In a radial distance of only 7.6 mm, the axial velocity jumps from zero to over 12 m/s. In addition, the swirl velocity increases over 50 percent and the radial velocity changes sign. The 36-deg. cyclic variation with blade spacing is again present in all profiles.

Azimuthal traverses for the flow with swirl vane angle  $\phi = 70$  deg., taken 3.25 cm downstream of the location of measurements just discussed, are reported elsewhere.<sup>3</sup> The results may be compared

with those given in Figs. 18 and 19 of the present paper. It appears from both sets of profiles that the recirculation zone has narrowed somewhat with the additional length before the expansion corner. At the inner radial position ( $r/D = 0.179$ ), the axial velocity is no longer zero. It is now positive, indicating that the main exit flow has moved slightly further inward. The azimuthal variation is still quite small, however, suggesting that the damping influence of the recirculation zone is still in effect. At the outer radial position ( $r/D = 0.204$ ), the axial and radial velocities are larger than at the upstream position, also implying that the outer high-velocity zone has moved further inward. The azimuthal variation is similar to that of the exit-plane position at the same radius.

#### 4.3 Calibration Sensitivity

An indication of sensitivity of the data reduction procedure to variations in probe calibration parameters used was also investigated. The case of swirl vane angle  $\phi = 70$  deg. was used, at  $x/D = -0.109$  and  $r/D = 0.179$ . The most recent calibration provided the baseline values of the pitch and velocity coefficients,<sup>18</sup> which were then varied by increasing the magnitude of each value by ten percent. Three cases were tried: increased pitch coefficient with baseline velocity coefficient, increased velocity coefficient with baseline pitch coefficient, and increased values of both coefficients. The percent difference in the output values of the velocity components is shown in Tables 3 through 5 for each of these three cases respectively.

Referring to Table 3, changing the pitch coefficient value is seen to affect the radial component the most, as expected. The change in output stays below ten percent for all but three of the output values. For the case of increased velocity coefficient only, Table 4 shows a quite uniform increase of less than five percent over all the values. This indicates a relatively predictable, low sensitivity response to changes in the calibration velocity coefficient. The final case, shown in Table 5, indicates that increases in both coefficients tend to cancel each other for the radial velocity measurement, which was the most sensitive to pitch coefficient variation. The axial and swirl components increase somewhat, but all variations remain well below ten percent. This relative insensitivity to calibration errors is encouraging but it should be noted that if the coefficient changes are of opposite sign in the combined case, errors of greater than ten percent in the radial velocity measurements might ensue.

#### 4.4 Swirl Strengths

Swirl numbers  $S$  and  $S'$  were calculated from Eqs. (1) and (6), with the turbulent stress terms omitted. Measured velocities and pressure (with reference pressure  $p_{\infty}$  being at the outer edge of the swirler at  $r/D = 0.25$ ) from the radial traverses of Section 4.1 were used with appropriate numerical integration. Results are shown in Table 6 where the flat blade swirler exhibits asymptotic behavior in its ability to produce strong swirl. Also shown is the measured ratio  $w_{mo}/u_{mo}$  for each swirl vane angle.

Table 3. Calibration Sensitivity Comparison Actual vs. 10% Higher Pitch Coefficient Only

K	$\theta$ (deg.)	Percent Difference		
		$u/u_{in}$	$v/u_{in}$	$w/u_{in}$
1	-24.0	1.91	-8.22	1.91
2	-18.0	0.80	-10.23	0.80
3	-12.0	0.27	-11.43	0.27
4	-6.0	0.92	-10.01	0.92
5	0.0	2.15	-7.89	2.15
6	6.0	1.87	-7.27	2.87
7	12.0	2.55	-7.51	2.55
8	18.0	2.29	-7.73	2.29
9	24.0	1.93	-8.17	1.93

Table 4. Calibration Sensitivity Comparison Actual vs. 10% Higher Velocity Coefficient Only

K	$\theta$ (deg.)	Percent Difference		
		$u/u_{in}$	$v/u_{in}$	$w/u_{in}$
1	-24.0	4.86	4.86	4.86
2	-18.0	4.88	4.88	4.88
3	-12.0	4.88	4.88	4.88
4	-6.0	4.88	4.88	4.88
5	0.0	4.86	4.86	4.86
6	6.0	4.88	4.88	4.88
7	12.0	4.87	4.87	4.87
8	18.0	4.87	4.87	4.87
9	24.0	4.86	4.86	4.86

Table 5. Calibration Sensitivity Comparison Actual vs. 10% Higher, Both Pitch and Velocity Coefficients

K	$\theta$ (deg.)	Percent Difference		
		$u/u_{in}$	$v/u_{in}$	$w/u_{in}$
1	-24.0	6.87	-3.75	6.87
2	-18.0	5.72	-5.85	5.72
3	-12.0	5.15	-7.12	5.15
4	-6.0	5.84	-5.62	5.84
5	0.0	7.12	-3.41	7.12
6	6.0	7.88	-2.75	7.88
7	12.0	7.54	-3.01	7.54
8	18.0	7.27	-3.25	7.27
9	24.0	6.90	-3.70	6.90

Someone unaware of the actual swirler exit velocity and pressure distributions might proceed in the following way. An 'ideal' flat blade swirler operating on a plug flow would produce exit profiles like Case I of Fig. 1 with  $F = w_0/u_0 = \tan \phi$  where  $\phi$  is the swirl vane angle. Corresponding  $S$  and  $S'$  values are then found from the equations of Table 1 which are plotted in Fig. 2. These 'idealized theoretical' values are given in Table 7, where negative values occur when the theoretical pressure contribution dominates in the denominator with negative consequences. It may be noticed immediately that the actual swirler performance is considerably inferior to the idealization, and thus observant theorists must continue to use actual test section inlet data in preference to the most simple idealization of Case I.

Even the other less idealized 'theoretical' cases are also inappropriate. The latter part of Table 7 gives the calculated swirl strengths on the basis of the most appropriate profiles (Cases I through V of Section 2.3) with associated  $F$  through  $J$  values taken from the measurements (values are given in Table 6). These disparities are attributed to the presence of the central hub, the upstream extent of the central recirculation zone, and flat swirl-vane ineffectiveness at high angles of attack, with associated wakes and nonaxisymmetries.

Table 6. Measured Swirl Numbers

$\phi$	$S$	$S'$	$w_{mo}/u_{mo}$
38	0.567	0.559	0.801
45	0.765	0.718	0.876
60	0.850	0.759	0.937
70	0.883	0.750	0.887

Table 7. Theoretical Swirl Numbers

$\phi$	Ideal Case I		Most Appropriate Case	Case $S'$	
	$S$	$S'$		$S$	$S'$
38	0.750	0.521	I	0.786	0.534
45	1.333	0.667	III	1.137	0.584
60	-2.309	1.155	V	1.291	0.625
70	-0.660	1.832	V	1.066	0.591

### 5. Conclusions

Performance characteristics of an axial-flow annular vane swirler have been investigated. A theoretical analysis of swirl numbers associated with several idealized exit velocity profiles was included, and values of the ratio of maximum swirl velocity to maximum axial velocity at different swirl strengths are given for each case. Measurements of actual swirler exit velocity profiles were made for swirl vane angles  $\phi = 0, 38, 45, 60,$  and

70 deg. using a five-hole pitot probe technique. These data form a useful part of a data base for the evaluation of flowfield prediction codes and turbulence models.

Assumptions of flat axial and swirl profiles with radial velocity equal to zero were found to be progressively less realistic as the swirler blade angle increases. At low swirl strengths ( $\phi = 38$  deg.), portions of the  $u$  and  $w$  profiles remain flat while the  $v$ -component is already significant. At moderate swirl  $\phi = 45$  deg., linearly increasing profiles of  $u$  and  $w$  with radius are appropriate with  $v$  nonzero. At stronger swirl  $\phi = 60$  deg., even more spiked profiles are appropriate with most of the flow leaving the swirler near its outer edge, and some reverse flow near the hub. At strong swirl  $\phi = 70$  deg., the profiles are extremely spiked with flow reversal. The central recirculation zone extends upstream of the exit plane, almost to the swirler blades in high-swirl cases. Because of this recirculation, none of the idealizations considered could model strong swirl cases adequately. The flow-turning effectiveness of the flat blades was generally adequate for all vane angles tested. However, the large variations of flow angles and velocities with radius made meaningful comparisons with two-dimensional cascade data impossible. Non-axisymmetry was found in all swirl cases investigated.

### Acknowledgments

Appreciation is expressed to NASA Lewis Research Center and Air Force Wright Aeronautical Laboratories for financial support via NASA Grant No. NAG 3-74, technical monitor Dr. J. D. Holdeman.

### References

- Lilley, D. G., and Rhode, D. L., A Computer Code for Swirling Turbulent Axisymmetric Recirculation Flows in Practical Isothermal Combustor Geometries, NASA CR-3442, Feb. 1982.
- Rhode, D. L., Lilley, D. G., and McLaughlin, D. K., On the Prediction of Swirling Flowfields Found in Axisymmetric Combustor Geometries, ASME Journal of Fluids Engng., Vol. 104, 1982 pp. 378-384.
- Sander, G. F., Axial Vane-Type Swirler Performance Characteristics. M.S. Thesis, School of Mechanical and Aerospace Engineering, Oklahoma State University, Stillwater, Okla., May 1983.
- Abujelala, M. T., and Lilley, D. G., Confined Swirling Flow Predictions, Paper AIAA-83-0316, Reno, Nevada, Jan. 10-13, 1983.
- Rhode, D. L., Lilley, D. G., and McLaughlin, D. K., Mean Flowfields in Axisymmetric Combustor Geometries with Swirl, AIAA Journal, Vol. 21, No. 4, April 1983, pp. 593-600.
- Lilley, D. G., Turbulent Combustor Flowfield Investigation. Paper in Combustion Fundamentals Research Conference, held at NASA Lewis Research Center, Cleveland, Ohio, Oct. 21-22, 1982, pp. 152-168.
- Yoon, H. K., and Lilley, D. G., Five-Hole Pitot Probe Time-Mean Velocity Measurements in Confined Swirling Flows. Paper AIAA-83-0315, Reno, Nevada, January 10-13, 1983.

8. Janjua, S. I., McLaughlin, D. K., Jackson, T. W., and Lilley, D. G., Turbulence Measurements in a Confined Jet Using a Six Orientation Hot-Wire Probe Technique, Paper AIAA-82-1262, Cleveland, Ohio, June 21-23, 1982.
9. Jackson, T. W., and Lilley, D. G., Swirl Flow Turbulence Measurements Using a Single-Wire Technique. Paper AIAA-83-1202, Seattle, Wash., June 27-29, 1983.
10. Janjua, S. I., and McLaughlin, D. K., Turbulence Measurements in a Swirling Confined Jet Flowfield Using a Triple Hot-Wire Probe, Report DT-8178-02, Dynamics Technology, Inc., Torrance, CA, Nov. 1982.
11. Kerr, N. M., and Fraser, D., Swirl. Part I: Effect on Axisymmetrical Turbulent Jets. Journal of the Inst. of Fuel, Vol. 38, Dec. 1965, pp. 519-526.
12. Mathur, M. L., and MacCallum, N. R. L., Swirling Air Jets Issuing from Vane Swirlers. Part I: Free Jets; Part II: Enclosed Jets. Journal of the Inst. of Fuel, Vol. 40, May 1967, pp. 214-245.
13. Chigier, N. A., and Chervinsky, A., Experimental Investigation of Swirling Vortex Motion in Jets. Journal of Applied Mechanics, Vol. 34, June 1967, pp. 443-451.
14. Beer, J. M., and Chigier, N. A., Combustion Aerodynamics. Applied Science Publishers, London, 1972.
15. Beltagui, S. A., and MacCallum, N. R. L., Aerodynamics of Vane-Swirled Flames in Furnaces. Journal of the Inst. of Fuel, Vol. 49, Dec. 1976, pp. 183-193.
16. Gupta, A. K., and Lilley, D. G., Flowfield Modeling and Diagnostics, Abacus Press, Tunbridge Wells, England, 1983 (in press).
17. Rhode, D. L., Predictions and Measurements of Isothermal Flowfields in Axisymmetric Combustor Geometries. Ph.D. Thesis, Oklahoma State University, Stillwater, Okla., Dec. 1981.
18. Yoon, H. K., Five-Hole Pitot Probe Time-Mean Velocity Measurements in Confined Swirling Flows, M.S. Thesis, Oklahoma State Univ., Stillwater, Okla., July 1982.

APPENDIX H

ACCURACY AND DIRECTIONAL SENSITIVITY

OF THE SINGLE-WIRE TECHNIQUE

(AIAA-84-0367)

ACCURACY AND DIRECTIONAL SENSITIVITY

OF THE SINGLE-WIRE TECHNIQUE

T. W. Jackson\* and D. G. Lilley\*\*  
 Oklahoma State University  
 Stillwater, OK 74078

Abstract

Multi-orientation of a single-hot-wire is a novel way to measure the three time-mean velocities, the three turbulent normal stresses, and the three turbulent shear stresses. The present study focuses on the accuracy and directional sensitivity of the technique with respect to mean flow velocity orientation to the probe. Results demonstrate relative insensitivity, indicating that the method is a useful cost-effective tool for turbulent flows of unknown dominant flow direction.

Nomenclature

A,B,C	calibration constants
D	test section diameter
d	inlet nozzle diameter
E	hot-wire voltage
G	pitch factor
K	yaw factor
L	contraction nozzle downstream distance
P,Q,R	selected hot-wire probe positions
$\bar{v} = (u,v,w)$	time-mean velocity (in x-, r- θ-directions) in facility coordinates
x,r,θ	axial, radial, azimuthal cylindrical polar coordinates
Z	effective cooling velocity acting on a wire
$\gamma_{i,j}$	correlation coefficient (estimated) between cooling velocities of adjacent wire orientations
ψ	swirl vane angle with respect to facility axis

Subscripts

o	value at inlet to flowfield
rms	root-mean-squared quantity

Superscripts

( )	time-mean average
{ }	fluctuating quantity
( )	relative to probe coordinates

1. Introduction

1.1 The Single-Wire Technique

As part of a research program aimed at the understanding and modeling of mixing processes in combustion chambers, the six-orientation single normal hot-wire technique is being used in axisymmetric geometries under low speed, nonreacting, swirling flow conditions. The method calls for a normal hot-wire to be oriented through six different positions, each orientation separated by 30 degrees from the adjacent one. Orientation 1 is normal to the facility centerline, orientation 2 is rotated 30 deg. from this, etc. Mean and root-mean-square voltages are measured at each orientation. The data reduction is performed using assumptions that turbulence follows a normal probability distribution having mean voltage as the mean and the squared value of the rms voltage as the variance. It is then possible to obtain the three time-mean velocity components, the three normal Reynolds stresses and the three shear Reynolds stresses.

At Oklahoma State University, Janjua<sup>1</sup> studied the technique, developed a suitable data reduction computer code, and presented results of its application in nonswirling free and confined jet flows. Jackson<sup>2</sup> extended the technique to investigate nonswirling and swirling nonreacting turbulent confined flows in an axisymmetric test section with expansion ratio  $D/d = 2$ , which may be equipped with a strong contraction nozzle of area ratio 4 at  $L/D = 2$ . The flowfield contains corner and central recirculation zones typical of gas turbine and ramjet combustion chambers. Swirl may be imparted to the in-coming flow by means of a variable-angle vane swirler. The technique and its application to nonswirling and weakly-swirling confined flows is described at length in Refs. 3 and 4. A recent paper<sup>5</sup> presents measurements for a full range of swirl strengths in the confined jet facility. This extended the data base given earlier<sup>3</sup> to higher inlet vane swirl angles, more axial measurement stations, and downstream nozzle effects. The data are being used to aid in the evolution of turbulence models for these complex flow situations.

The method is based upon earlier studies on multi-orientation of a single normal hot-wire. Dvorak and Syred<sup>6</sup> presented time-mean and turbulence property measurements in a complex flowfield with 45 deg. between three successive orientations of the wire. A crossed-wire probe was additionally used to measure correlation coefficients. Measurements in swirling recirculating flows at the exit from a swirl generator were obtained with similar techniques, using up to six, separate point measurements, by Syred et al.<sup>7</sup> Later, King<sup>8</sup> developed the six-orientation single normal hot-wire technique and applied it to vortex flows.

\* Graduate Student, School of Mechanical and Aerospace Engineering, Student Member AIAA

\*\* Professor, School of Mechanical and Aerospace Engineering, Associate Fellow AIAA



## 1.2 Objectives

The aim of the present paper is to address questions about accuracy and directional sensitivity of the six-orientation single normal hot-wire technique. An uncertainty analysis is performed on the data reduction procedure by changing individually strategic input parameters, and noting their effect on deduced properties of the flow. A directional sensitivity analysis is presented which assesses the relative values of deduced flow properties (in facility coordinates) to local time-mean velocity orientation relative to the probe.

## 1.3 Outline of the Paper

Essential features of the six-orientation single-wire hot-wire measurement technique are described briefly in Section 2. The directional sensitivity study is discussed in Section 3, while Section 4 presents the mathematical coordinate transformations for velocity vectors, normal and shear stresses. Results are presented and discussed in Section 5, while Section 6 draws conclusions from the study.

## 2. Measurement Technique

One of the most widely used instruments to obtain turbulence quantities is the hot-wire anemometer, the most common of which is the single hot-wire. When used on a two-dimensional flow with a predominate flow direction, a single hot-wire used normal to the main flow can be used to measure the streamwise components of the time-mean velocity and the rms velocity fluctuation, in a standard manner.<sup>9</sup>

The anemometer used for the present study is DISA type 55M01, CTA standard bridge. A normal hot-wire probe, DISA type 55P01, is used in the experiments. This probe has two prongs set approximately 3 mm apart which support a 5  $\mu$ m diameter wire which is gold plated near the prongs to reduce end effects and strengthen the wire. The mean voltage is measured with a Hickok Digital Systems, Model DP100, integrating voltmeter and the root-mean-square voltage fluctuation is measured using a Hewlett Packard, Model 400 HR, AC voltmeter.

In a complex swirling flowfield the dominant flow direction is unknown and the standard single-orientation single hot-wire method fails to supply sufficient information. The six-orientation method calls for a normal hot-wire to be oriented through six different positions, each orientation separated by 30 deg. for the adjacent one. Orientation 1 is normal to the facility centerline, orientation 2 is rotated 30 deg. from this, etc. Mean and root-mean-square voltages are measured at each orientation. The data reduction is performed using assumptions that turbulence follows a normal probability distribution having mean voltage as the mean and the squared value of the rms voltage as the variance. It is then possible to obtain the three time-mean velocity components, the three normal Reynolds stresses and the three shear Reynolds stresses, in the manner now described.

The six-orientation hot-wire technique requires a single, straight, hot-wire to be calibrated for three different flow directions in order to determine the directional sensitivity of the probe. In the following relationships, tildes

signify components of the instantaneous velocity vector in coordinates on the probe. Each of the three calibration curves is obtained with zero velocity in the other two directions. The calibration curves demonstrate that the hot-wire is most efficiently cooled when the flow is in the direction of the  $\tilde{u}$  component (which is normal to both the wire and the supports). The wire is most inefficiently cooled when the flow is in the direction of the  $\tilde{w}$  component (which is parallel to the wire). Each of the calibration curves follows a second order, least-square fit of the form:

$$E_i^2 = A_i + B_i \tilde{u}_i^{1/2} + C_i \tilde{u}_i \quad (1)$$

which is an extension of the familiar King's law. In this equation,  $A_i$ ,  $B_i$ , and  $C_i$  are calibration constants and  $\tilde{u}_i$  can take on a value of  $\tilde{u}$ ,  $\tilde{v}$ , and  $\tilde{w}$  for the three calibration curves, respectively.

When the wire is placed in a three-dimensional flowfield, the effective cooling velocity experienced by the hot-wire is:

$$Z^2 = \tilde{v}^2 + G^2 \tilde{u}^2 + K^2 \tilde{w}^2 \quad (2)$$

where  $G$  and  $K$  are the pitch and yaw factors, defined by Jorgensen<sup>10</sup> and deduced from the calibration curves. Hence, equations for the effective cooling velocity can now be obtained for each of the six wire orientations. Solving simultaneously **any three adjacent equations** provides expressions for the instantaneous values of the three velocity components ( $u$ ,  $v$ , and  $w$  in facility  $x$ ,  $r$  and  $\theta$  coordinates, respectively) in terms of the equivalent cooling velocities. It is then possible to obtain the three time-mean velocity components and the six different components of the Reynolds stress tensor, in the manner described in Refs. 1 and 3.

Dvorak and Syred<sup>6</sup> used a DISA time correlator (55A06) to find the correlation coefficients between the velocity fluctuations in the three directions. One approach is to use the information obtained by all six orientations and devise a mathematical procedure to calculate the covariances. These are calculated using the relationship:

$$K_{Z_i Z_j} = \gamma_{Z_i Z_j} [\sigma_{Z_i}^2 \sigma_{Z_j}^2]^{1/2} \quad (3)$$

where  $\gamma_{Z_i Z_j}$  is the correlation coefficient between the two cooling velocities  $Z_i$  and  $Z_j$ . By definition, the absolute value of the correlation coefficient  $\gamma_{Z_i Z_j}$  is always less than 1.

Certain assumptions are made in order to calculate the covariances. However, King<sup>8</sup> observed that at times the calculated value of the correlation coefficient is greater than one at which instance he assigned previously fixed values to the correlation coefficients. It may be deduced that if two wires are separated by an angle of 30 degrees, the fluctuating signals from the wires at the two locations would be such that their contribution to the cooling of the wire would be related by the cosine of the angle between the wires. This assumption leads to the following three values of

the correlation coefficients

$$\gamma_{Z_P Z_Q} = \cos 30 = 0.866 \quad (4)$$

$$\gamma_{Z_Q Z_R} = \cos 30 = 0.866$$

The correlation coefficients may be related via:<sup>8</sup>

$$\gamma_{Z_P Z_R} = \eta \gamma_{Z_P Z_Q} \gamma_{Z_Q Z_R} \quad (5)$$

where  $\eta$  is given a value of 0.8. Hence:

$$\gamma_{Z_P Z_R} = (0.8)(0.866)(0.866) = 0.6 \quad (6)$$

The three covariances are then obtained by substituting the corresponding values of the correlation coefficients into Eq. (3). King<sup>8</sup> used the above technique. The present study, however, uses Eqs. (4) and (6) during the entire data reduction. This simplification is justified *a posteriori* in Section 5.1, where it is demonstrated that deduced results are relatively insensitive to correlative term inaccuracy.

### 3. Directional Sensitivity Analysis

The analysis is performed at any specific flowfield location by initially placing the probe in a free jet such that the coordinate system of the probe coincides with the coordinate system of the jet, as shown in Part (a) of Fig. 1. Measurements are then taken by rotating the probe in the manner of the technique just described. To simulate the effect of the flow shifting its dominant flow direction, the probe is rotated by  $\theta$  deg. about its z-axis, as shown in Part (b) of the figure. This rotation causes a misalignment between the probe coordinate system and the facility coordinates. This discrepancy can be accounted for by use of the Eulerian matrices described in Section 4. In this configuration, the measured time-mean values, normal and shear stresses are in a coordinate system oblique to the jet coordinate system. However, they can be transformed back to the facility coordinate system.<sup>11</sup> Notice that the correct directional sense of the rotation must be followed so that standard coordinate transformations may be used on the probe data so as to obtain facility coordinate data. Results shown later in Section 5 have been obtained in this manner.

To examine the directional sensitivity of the wire further, the probe was subsequently rotated about its new x-axis, thereby forming a compound angle between probe and the dominant flow velocity, as also shown in Fig. 1, see Part (c). Again the time-mean velocities and Reynolds stress tensor can be deduced in terms of the jet coordinate system by the method shown in Section 4, and the results and their accuracy are also discussed in Section 5.

Specifically, the directional sensitivity of the technique is assessed at **five** flowfield situations for self-consistency using the following **five** configurations:

Case 1	$\theta = 0^\circ$	$\phi = 0^\circ$
Case 2	$\theta = -45^\circ$	$\phi = 0^\circ$
Case 3	$\theta = -45^\circ$	$\phi = -45^\circ$
Case 4	$\theta = -90^\circ$	$\phi = 0^\circ$
Case 5	$\theta = -90^\circ$	$\phi = -90^\circ$

The above **five** probe/flow configurations are used at each of **five** representative situations in a free axisymmetric nonswirling jet at  $x/d = 0$  (laminar in potential core region), 3 and 10 (turbulent in shear layer region); and in a free axisymmetric swirling jet at a location in a region of strong shear just downstream of the exit from a variable-angle vane swirler with swirl vane angles of 45 and 70 deg., representing moderate and strong swirl cases. In these swirling jet cases, the probe was located just downstream of the swirler exit, outside of any regions of recirculation: This part of the flow was chosen as it is in an area of rapid acceleration and is unlikely to contain any instantaneous flow reversals which might cause erroneous readings. Specifically, the following five situations are used:

Situation A	$x/d = 0$	nonswirling laminar region
Situation B	$x/d = 3$	nonswirling turbulent region
Situation C	$x/d = 10$	nonswirling turbulent region
Situation D	$x/d = 0$	swirling turbulent region with swirl vane angle 45 deg.
Situation E	$x/d = 0$	swirling turbulent region with swirl vane angle 70 deg.

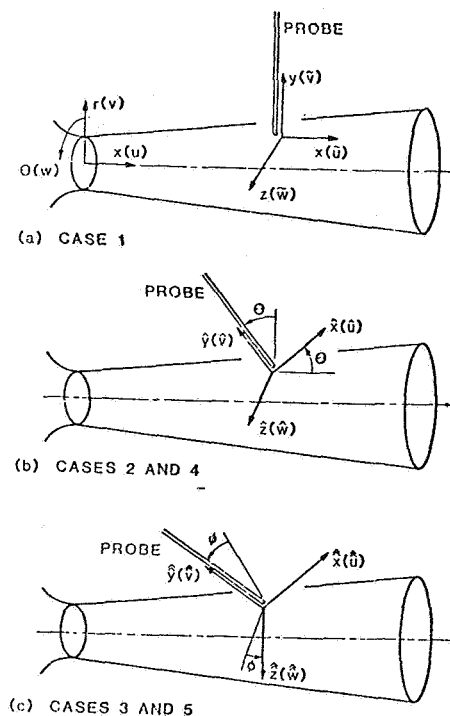


Fig. 1. Configurations Used in the Directional Sensitivity Study

These locations are illustrated in Figs. 2 and 3. It will be seen later that the sensitivity analysis assures users that knowledge of local configuration of probe vs flow direction is not required **a priori**, and useful results are forthcoming and relatively insensitive to specific configurations.

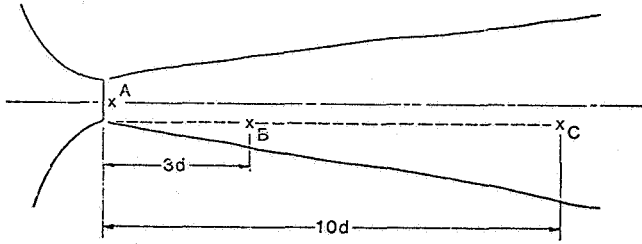


Fig. 2. Free Nonswirling Jet Measurement Locations for Situations A, B, and C

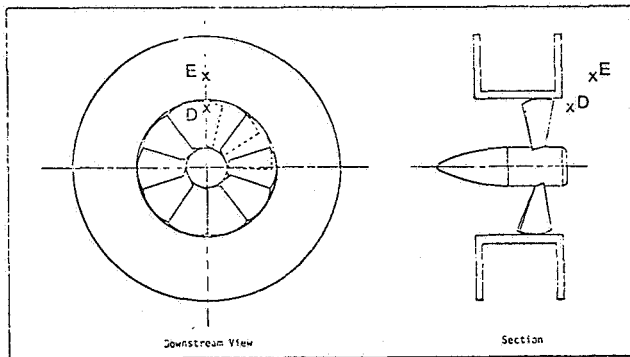


Fig. 3. Free Swirling Jet Measurement Locations for Situations D and E

#### 4. Coordinate Transformation

##### 4.1 Rotational Matrices

To investigate the shifting of the dominant flow direction, the probe holder vs local time-mean flow vector configuration is varied through **five** different cases of interest. To relate probe coordinate data back to the facility coordinate system, use is made of Eulerian rotational matrices. These make it possible to relate all time-mean velocities and the full Reynolds stress tensor back to the facility coordinate system after any axis rotation.

Any (x,y,z)-cartesian coordinate axes may be rotated about the x, y, or z axis, respectively, by an angle  $\theta$ , with corresponding coordinate transformation matrices

$$R_{x\theta} = \begin{bmatrix} 1 & 0 & 0 \\ 0 & \cos\theta & -\sin\theta \\ 0 & \sin\theta & \cos\theta \end{bmatrix}$$

$$R_{y\theta} = \begin{bmatrix} \cos\theta & 0 & \sin\theta \\ 0 & 1 & 0 \\ -\sin\theta & 0 & \cos\theta \end{bmatrix}$$

$$R_{z\theta} = \begin{bmatrix} \cos\theta & -\sin\theta & 0 \\ \sin\theta & \cos\theta & 0 \\ 0 & 0 & 1 \end{bmatrix}$$

For example, a rotation about the z-axis by angle  $\theta$  results in old (x, y, z) coordinates of a point being related to its new (X, Y, Z) coordinates via:

$$[x \ y \ z]^T = R_{z\theta} [X \ Y \ Z]^T$$

Similarly, velocity components (u, v, w) are related to (U, V, W) via

$$[u \ v \ w]^T = R_{z\theta} [U \ V \ W]^T$$

In the notation of Fig. 1 with velocity components

u, v, w in x, r,  $\theta$  facility coordinates

$\tilde{u}$ ,  $\tilde{v}$ ,  $\tilde{w}$  in x, y, z probe Case 1 coordinates

$\hat{u}$ ,  $\hat{v}$ ,  $\hat{w}$  in  $\hat{x}$ ,  $\hat{y}$ ,  $\hat{z}$  probe Case 2 and 4 coordinates

$\hat{\hat{u}}$ ,  $\hat{\hat{v}}$ ,  $\hat{\hat{w}}$  in  $\hat{\hat{x}}$ ,  $\hat{\hat{y}}$ ,  $\hat{\hat{z}}$  probe Case 3 and 5 coordinates

the following relationships prevail:

##### 4.2 Case 1

The facility and probe Case 1 coordinates are coincident and

$$[u \ v \ w]^T = [\tilde{u} \ \tilde{v} \ \tilde{w}]^T$$

##### 4.3 Cases 2 and 4

In this case, a rotation of  $\theta$  degrees is applied about the z-axis, resulting in

$$[u \ v \ w]^T = R_{z\theta} [\hat{u} \ \hat{v} \ \hat{w}]^T$$

which leads to

$$\begin{bmatrix} u \\ v \\ w \end{bmatrix} = \begin{bmatrix} \hat{u} \cos\theta - \hat{v} \sin\theta \\ \hat{u} \sin\theta + \hat{v} \cos\theta \\ \hat{w} \end{bmatrix}$$

From this the directional time-mean velocities in facility coordinates can easily be inferred. The angle terms in the relationship are, in fact, the directional cosines,<sup>11</sup> which can be used to determine the stress transformations in terms of facility coordinates. The directional cosines between any new coordinate axes, for example,  $\hat{x}$ ,  $\hat{y}$ , and  $\hat{z}$ , and the original coordinate axes  $x$ ,  $y$  and  $z$  can be conveniently tabulated as follows:

	$x$	$y$	$z$
$\hat{x}$	$l_1$	$m_1$	$n_1$
$\hat{y}$	$l_2$	$m_2$	$n_2$
$\hat{z}$	$l_3$	$m_3$	$n_3$

These directional cosines ( $l_i, m_i, n_i$  for  $i = 1, 2$  and 3) can be used in the general three-dimensional stress equations<sup>11</sup> governing the transformation of coordinates via

$$\tau_{xx} = l_1^2 \tau_{xx}^{\hat{\hat{}}} + m_1^2 \tau_{yy}^{\hat{\hat{}}} + n_1^2 \tau_{zz}^{\hat{\hat{}}} + 2l_1 m_1 \tau_{xy}^{\hat{\hat{}}} + 2m_1 n_1 \tau_{yz}^{\hat{\hat{}}} + 2n_1 l_1 \tau_{zx}^{\hat{\hat{}}}$$

$\tau_{yy}$  = as above with subscript 1 replaced by 2

$\tau_{zz}$  = as above with subscript 1 replaced by 3

$$\tau_{xy} = l_1 l_2 \tau_{xx}^{\hat{\hat{}}} + m_1 m_2 \tau_{yy}^{\hat{\hat{}}} + n_1 n_2 \tau_{zz}^{\hat{\hat{}}} + (l_1 m_2 + l_2 m_1) \tau_{xy}^{\hat{\hat{}}} + (m_1 n_2 + m_2 n_1) \tau_{yz}^{\hat{\hat{}}} + (n_1 l_2 + n_2 l_1) \tau_{zx}^{\hat{\hat{}}}$$

$\tau_{yz}$  = as above with subscripts (1, 2) replaced by (2, 3)

$\tau_{zx}$  = as above with subscripts (1, 2) replaced by (3, 1)

These relationships lead to evaluation of all the stress components in facility coordinates, from corresponding data originally reduced in probe coordinates.

#### 4.4 Cases 3 and 5

To go from Cases 2 and 4, to Cases 3 and 5, a rotation of  $\phi$  degrees is applied about the new  $x$ -axis, resulting in

$$[\hat{u} \hat{v} \hat{w}]^T = R_{x\phi} [\hat{u} \hat{v} \hat{w}]^T$$

and

$$[u \ v \ w]^T = R_{z\theta} R_{x\phi} [\hat{u} \ \hat{v} \ \hat{w}]^T$$

which is

$$\begin{bmatrix} u \\ v \\ w \end{bmatrix} = \begin{bmatrix} \cos \theta & -\sin \theta \cos \phi & +\sin \theta \sin \phi \\ \sin \theta & +\cos \theta \cos \phi & -\cos \theta \sin \phi \\ 0 & \sin \phi & \cos \phi \end{bmatrix} \begin{bmatrix} \hat{u} \\ \hat{v} \\ \hat{w} \end{bmatrix}$$

Again, this relationship permits time-mean velocity components to be converted back into facility coordinates. The coefficient matrix defines the directional cosines relating the two coordinate systems; these can be used for normal and shear stress transformations in the manner described in Section 4.3.

## 5. Results

### 5.1 Uncertainty Analysis

The uncertainty analysis includes a determination of the sensitivity of the six-orientation hot-wire data reduction to various input parameters which have major contributions in the response equations. Pitch and yaw factors (G and K) are used in the response equations described in Section 2 in order to account for the directional sensitivity of the single hot-wire probe. Figure 4 shows the pitch and the yaw factors plotted against the hot-wire mean effective voltage. Both the pitch and yaw factors are functions of the hot-wire mean effective voltage, but the yaw factor is far more sensitive. A one percent increase in the hot-wire voltage reduces the pitch factor by 1.3 percent and the yaw factor by 56 percent. For the present study, the values of these factors are chosen at an average hot-wire voltage experienced in the flowfield. This was appropriate since the output quantities ( $u$ ,  $u'_{rms}$ ,  $u'v'$ , etc) are only weakly dependent on the value of K. This can be seen in the data of Table 1 which summarizes an analysis performed on the data reduction program at a representative position in the flowfield.

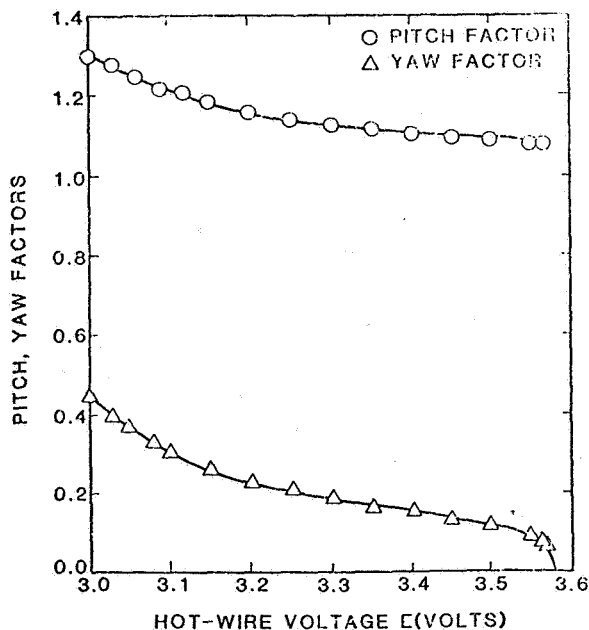


Fig. 4. Pitch and Yaw Factors G and K

Table 1 demonstrates the percent change in the output quantities for a 1 percent change in most of the important input quantities. For the data presented in this table only quantities calculated from the probe orientation combination 5, 6 and 1 are used, for simplicity. The situation is that of a moderately swirling confined flowfield from a swirl generator with vane angle of 38 degrees. In this swirling flow orientation 6 was the minimum of the 6 mean effective cooling velocities. King<sup>6</sup> has

argued that the probe orientation combination approximately centered around the minimum effective cooling velocity produces more accurate estimates of calculated turbulence quantities, than do the other orientation combinations. However, all previously reported data has been obtained by averaging all the six possible combinations.

It is not unusual in hot-wire anemometry to have the mean velocity components and turbulence quantities that are measured, be quite sensitive to changes in mean hot-wire voltage. For interpretive purposes, the mean hot-wire voltage variations can be thought of as being either errors in measuring the mean voltage, or shifts in the individual wire calibrations due to contamination or strain 'aging' of the wire. The data of Table 1 demonstrate that the most serious inaccuracies in the measurement and data reduction technique will be in the estimates of turbulent shear stresses, the most inaccurate output term being  $u'w'$ .

Table 1. Effect of Input Parameters on Turbulence Quantities in a Confined Swirling Flow with Swirl Angle of 38 deg. at a Representative Flowfield Position ( $x/D = 1$ ,  $r/D = 0.25$ ).

PARAMETER	VARIATION	CHANGE IN TIME-MEAN AND TURBULENCE QUANTITIES								
		$\bar{u}$	$\bar{v}$	$\bar{w}$	$\overline{u'u'}$	$\overline{v'v'}$	$\overline{w'w'}$	$\overline{u'v'}$	$\overline{u'w'}$	$\overline{v'w'}$
$E_u$	+1	+16.10	+0.86	+4.93	+15.75	-2.06	-2.75	+6.0	+51.43	+11.94
$E_v$	+1	+2.19	-2.21	+11.49	-6.50	+2.42	+12.88	+4.0	+14.29	+7.46
$E_w$	+1	-13.59	+0.26	-8.50	-1.80	+1.07	-9.54	-5.0	-34.29	-11.94
$E_{u'rms}$	+1	+0.27	-0.06	+0.14	+1.63	+0.13	+0.39	+2.0	+2.86	-1.49
$E_{v'rms}$	+1	+0.05	0.0	+0.14	0.0	-0.13	+1.57	0.0	0.0	+1.49
$E_{w'rms}$	+1	-0.16	+0.18	-0.14	-0.63	+1.03	-1.08	-2.0	-5.71	0.0
G	+1	-1.02	0.0	-1.01	-1.0	0.0	-0.98	-2.0	-2.85	-1.49
K	+1	+0.01	-0.04	+0.01	+0.01	0.0	+0.01	0.0	0.0	0.0
$\gamma_{z_p z_0}$	+1	+0.05	0.0	+0.14	-0.13	-0.13	-1.77	0.0	-2.86	-1.49
$\gamma_{z_0 z_p}$	+1	-0.21	+0.01	+0.05	-1.63	+0.13	-0.79	0.0	-5.71	-1.49
$\gamma_{z_p z_2}$	+1	-0.15	+0.18	-0.03	+0.13	0.0	+0.69	-2.0	-2.86	0.0

As already discussed in Section 2, an *ad hoc* assumption is made regarding the numerical values of the correlation coefficients used in the deduction of time-mean and turbulence quantities. The results of the uncertainty analysis (Table 1) show the time-mean and turbulence quantities to be relatively insensitive to variations in the correlation coefficients. Therefore, the major *ad hoc* assumption made in the technique does not seem to have a great effect on the output quantities compared to the effect of other input quantities.

## 5.2 Laminar Jet

The directional sensitivity of the technique is assessed at the five locations A through E, see Figs. 2 and 3, corresponding to five different flow situations. The first of these is in the laminar potential core region, at  $x/d = 0$  and  $r/d = 0$ . Table 2 gives the results with the probe coordinates aligned with facility coordinates, as Case 1 of Fig. 1 illustrates. This is referred to as Situation A Case 1 with analogous statements later. The time-mean velocities, nondimensionalized with the jet exit velocity deduced from an independent measurement, are shown. In this one-dimensional

flowfield the axial velocity is expected to be unity with the other two components of the velocity vector to be equal to zero. Results using each of the six possible combinations of three adjacent wire-orientations are presented, together with the mean of the values. The standard deviation and its ratio with the mean are also presented to show the amount of scatter in the readings. As can be seen, the error for the axial and swirl velocities are very low for each combination. The radial velocity error tends to be larger, possibly because of slight probe misalignment with the normal to the jet axis. The mean of these quantities brings the data to well within acceptable limits.

Results of the probe being rotated by 45 deg. about the z-axis (as in Case 2 with  $\theta = -45$  deg.) are shown in Table 3. This is Situation A Case 2. The probe coordinate system is now different from the jet coordinate system but the measured velocities can be related to the facility coordinates by use of the rotational matrices given in Section 4. The values given in Table 3 and indeed all the Tables are presented in terms of the facility coordinate system. The results show that this misalignment of the probe with the dominant flow direction still gives excellent values of velocities in the laboratory coordinate system with the use of any of the six possible wire combinations. Consequently, averaging of the data also gives good results.

Rotation about the z-axis by -90 deg. to obtain Case 4 results in no data being generated by the technique. This is because in a steady one-dimensional flowfield all the instantaneous cooling velocities acting on the hot-wire are equal for all of the 6 rotations. As the data analysis requires that their cooling velocities be subtracted from each other (see Ref. 3) all the output terms are deduced as zero.

To further investigate the shifting of the dominant flow direction, the probe was rotated twice (-45 deg. about its z-axis, followed by -45 deg. about its new x-axis) so as to conform to Case 3. The results of these axis rotations can be seen in Table 4. Again the laboratory coordinate deduced values and deviations from expected values are relatively low, although not quite as good as in the previous case. The advantages of averaging can be seen in Table 4, where the under- and/or over-estimation of the velocities for the individual positions are smoothed out after averaging.

Rotations of  $\theta = -90$  deg. and  $\phi = -90$  deg. were also carried out at the same flow location, so obtaining Case 5. Table 5 shows the results of these rotations. Good axial and tangential velocity values can be seen but with a decrease in the accuracy of the radial velocity.

## 5.3 Turbulent Nonswirling Jet

Similar rotations of the probe about its axes have been performed on the shear layer of a free nonswirling axisymmetric jet at two axial locations,  $x/d = 3$  and 10, referred to as Situations B and C. At these points in the flow the axial velocity dominates with a small contribution from the radial velocity. In axisymmetric jets it is well-known that the axial directional turbulence intensity is larger than its other two components.<sup>12</sup> The only significant shear stress in this flowfield is the

rx-shear. Tables 6 and 7, obtained with Case 1 probe configuration in Situations B and C, confirm this. Incidentally, all the data presented in this paper are a consequence of a typical set of readings obtained from the hot-wire technique. If a large amount of scatter is found in deduced results at a particular location, the problem is further investigated and/or remeasured before being accepted as valid. Data reported elsewhere<sup>3,4</sup> has been thoroughly analyzed and checked for repeatability.

Tables 6 and 7 are used as a standard for nonswirling flowfield values at locations B and C, so as to be able to compare the results obtained from other probe configuration cases. However, the radial time-mean velocity appears to be very large for this particular flowfield and could possibly be in error. The coefficient of variation ( $\sigma/\bar{x}$ ) is seen to be acceptable for most of the flow properties except for the shear stresses. These large variations are caused by the shear stresses being two orders of magnitudes lower than the time-mean velocities. Sometimes the data reduction will not resolve a particular parameter. This is usually the consequence of subtracting two almost equal effective cooling velocities as described earlier. If a large proportion of the data is not resolved from the different combinations of cooling velocities used, the parameter deduced is taken to be zero.

Results for probe configurations of Cases 2 and 4 for location B are given in Tables 8 and 9, corresponding data for location C are given in Tables 10 and 11. It can be seen, from Tables 9 and 11, that the Case 4 results give poor estimates of the time-mean radial and swirl velocities and underestimates of the axial components of the velocity vector. This is expected because the time-mean velocity vector is almost parallel to the hot-wire support axis, and rotating the probe through its six orientations yields little effect on the sensed data. This also decreases values of the axial turbulence intensity but significantly increases the other two normal stress components. Acceptable values of the axial normal stress are obtained via  $\theta = -45$  deg. (Case 2 probe configuration) but again the tangential and radial turbulence intensities are increased; however, not as significantly as in the previous Case 4. Shear stress values for both Case 2 and 4 are found to be very poor with large coefficients of variation. Also, many of the turbulence quantities are not resolved.

It would appear from these results that the six-orientation hot-wire technique is a poor tool to use if the flow is dominantly in the direction of the probe support, for reasons just described. If this occurs, simply reconfiguring the probe holder vs flow direction can overcome the problem.

Tables 12 through 15 correspond to the last four tables, but now probe configurations of Cases 3 and 5 are used at locations B (Tables 12 and 13) and C (Tables 14 and 15). Now the time-mean velocity components are seen to be in excellent agreement with the values determined from the standard configuration of Case 1. The axial normal stress tends to be underestimated at  $x/d = 3$  and overestimated at  $x/d = 10$ , relative to the Case 1 calculations. The radial turbulence intensity is consistently overestimated for both compound configurations and both axial locations. This could

infer a failing of the hot-wire technique. The tangential turbulence intensity measurements are found to provide acceptable results. The dominant shear stress (the rx-component) in this flow is found measured very well in the configurations of Cases 3 and 5, relative to Case 1 values. The coefficient of variation is not too large considering the magnitude of the numbers involved. The final components of the Reynolds stress tensor, although appearing to be measurable, exhibit a great deal of scatter, perhaps indicating that these values are close to zero.

#### 5.4 Turbulent Swirling Jet

Two free swirling jets were considered for further assessment of the hot-wire technique. The air flow exiting from an axisymmetric nozzle of a wind tunnel passes through a vane swirler with 10 adjustable flat blades. The test facility and time-mean performance of the swirler are described at length elsewhere.<sup>13</sup> For the present study, the subsequent large chamber confinement was removed and the free jet flow alone was studied, with swirl vane angles of 45 and 70 deg. being used. Figure 3 gives the specific measurement locations D and E used for measuring the 45 and 70 deg. swirl situations, respectively. These locations are in the high shear region of the flow close to the swirler exit. They were chosen since it was expected that all six components of the stress tensor would be significant, thereby providing a good test of the technique for their measurement. The hot-wire was also placed well away from the edge of the recirculation zone, so as to avoid any instantaneous flow reversal on the wire. Rotations of the probe axes have been performed conforming to Cases 4 and 5 only, for both of the swirl strengths.

The standard six-orientation technique in the configuration of Case 1 produces the properties of both swirling jets as given in Tables 16 and 17. As can be seen all components of the time-mean flow and the Reynolds stress tensor are evaluated. The two sets of results are not quite at the same flowfield location because of the change in size and shape of the recirculation zone as swirl strength increases. However, the increase in the turbulent properties of the flow are clearly evident.

Rotation about the z-axis by -90 deg. to Case 4 probe configuration causes a deterioration in the accuracy of the results obtained from the technique, as inspection of Tables 18 and 19 for 45 and 70 deg., respectively, shows. The axial and swirl time-mean velocities are still fairly accurate for both flows but the radial velocity has suffered a large increase (or decrease), relative to its measurement with Case 1. The normal stresses deduced after the rotation appear to be reasonable except for the radial and swirl components in the strong swirl flow of Situation E. These two components are greatly overestimated with a great deal of scatter in the results. It is again felt that these poor results are because of the technique's inability to measure accurately flow properties when the dominant flow direction is in the direction of the probe holder. That is, when a large velocity is approximately normal to the wire in each of the six measuring orientations, insensitivity results as already discussed earlier. Correspondingly, the shear stresses also show a reduction in accuracy, with all three components either over- or under-predicting the Case

1 values.

The results of the compound angle of Case 5 are presented in Tables 20 and 21, respectively, for the 45 and 70 deg. swirl cases. The axial time-mean velocity is seen to be good when compared to the standard case, but the other two components show a reduction in accuracy in these highly turbulent flowfields. The inaccuracy of the radial velocity has been discussed earlier. The three components of the turbulence intensity appear to be fairly good with reasonable values deduced compared to the standard Case 1 values. Again however, the radial and tangential component are less than desirable for the strongly swirling flowfield. The shear stresses for the 45 deg. swirl situation D are considered good except for the  $u'w'$  term. This component is subject to great inaccuracies for only slight errors in this input data, as described earlier in Section 5.1. For the strongly swirling flow (Situation E) the measured stresses are not so good when compared with the standard Case 1 measurements. As these tables indicate, the time-mean velocities and normal stresses are subject to error which is magnified in the determination of the shear stresses.

### 5.5 Assessment of the Technique

General results of the present and previous studies are now assessed in connection with the applicability, accuracy and directional sensitivity of the six-orientation single normal hot-wire technique.

Previously, in his measurements of strongly swirling vortex flows, King<sup>8</sup> compared his time-mean velocity and normal stress measurements with corresponding measurements obtained using a Laser Doppler Velocimeter. He found excellent agreement indicating the validity of the method. He was not able to compare shear stress measurements in his swirl flow, however, because he was unable to use his LDV for this purpose. In fact, despite the existence of advanced multicolor LDV systems, and their use for shear stress measurement, no one has yet reported them in highly swirling flow situations: certainly not over a range of swirl strengths as reported in Ref. 5.

The present authors have already compared their six-orientation measurements with previously-available data whenever possible. In the nonswirling confined jet case, results for time-mean velocities  $u$  and  $v$ , normal stresses  $u'_{rms}$  and  $v'_{rms}$  and shear stress  $u'v'$  compare very favorable (see Ref. 3, Figs. 7 and 8) with those of Chaturvedi.<sup>14</sup> He used a crossed-wire probe for the shear stress measurements. So also did McKillop<sup>15</sup> for nonswirling confined flow in the same facility as the present authors.<sup>5</sup> Results, with and without exit nozzles, are in good agreement for the above quantities, also, see Ref. 15, Figs. 21 through 28.

In the swirling confined jet case, comparison with Janjua and McLaughlin<sup>16</sup> for a moderate swirl strength in an identical facility has been possible. They made triple-wire hot-wire measurements in a flow with an inlet swirl vane angle  $\phi = 38$  deg., using analog-to-digital signal conversion and computer data reduction. For this purpose, it was necessary to know in advance the local time-mean velocity vector direction; the data of Yoon and Lilley<sup>16</sup> was used for this purpose. Their measurements<sup>16</sup> of time-mean velocity compare

very well with those of Ref. 17 and hence of Refs. 3 through 5; their measurements<sup>16</sup> of the three normal

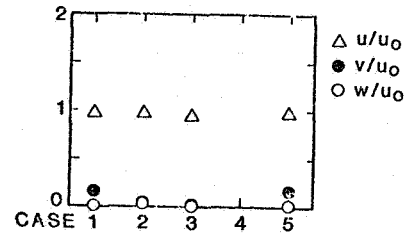


Fig. 5. Measurement for Situation A with Different Probe Configuration Cases

Reynolds stresses and the three shear Reynolds stresses are compared at  $x/D = 0.5, 1.0$  and  $1.5$  with the six-orientation single-wire measurements of Ref. 5. There is excellent agreement (see Ref. 16, Figs. 10 through 18), indicating again the validity of the present measurement technique. It appears to be an extremely viable, cost-effective technique for turbulent flows of unknown dominant direction. Probe interference appears not to be a major problem. Results are useful in recent prediction studies for confined swirling flows.<sup>18-20</sup>

For the present study, Figs. 5 through 9 summarize measured values for the five situations A through E, respectively. Each figure presents facility coordinate time-mean velocity, normal and shear stress values obtained with each of the five probe holder vs facility configuration possibilities of Cases 1 through 5. A remarkable observation is that, in general, the configuration is of little importance, results appearing quite constant across the five cases.

On the other hand, production run results<sup>1-5</sup> have used the Case 1 configuration exclusively. In those results, generally, ensemble average of deduced results from each of the six possible combinations of three adjacent wire orientations has been used. This was because of lack of local flow directional knowledge - if this knowledge is available it is expected<sup>8</sup> that the combination with minimum cooling velocity in the central of the three wire orientations used will produce more accurate estimates of deduced flow quantities. From results of the present study for Situations A through E, Table 22 confirms this, especially for time-mean values. In any case, the appropriate choice of wire orientation for minimum cooling velocity is not known a priori. The values given in the table could only be determined after the measurement. However, for turbulence quantities and in the 45 and 70 deg. situations, more confidence may be placed in the average of all possible wire combinations. This smoothing has been used exclusively in recent studies.<sup>1-5</sup>

## 6. Conclusions

The accuracy and directional sensitivity of the six-orientation hot-wire technique has been performed in axisymmetric and swirling free jets. Variation of input parameters and their effect on the output data has shown that the least accurate output quantities are the shear stresses, in particular the  $x_0$ -component.

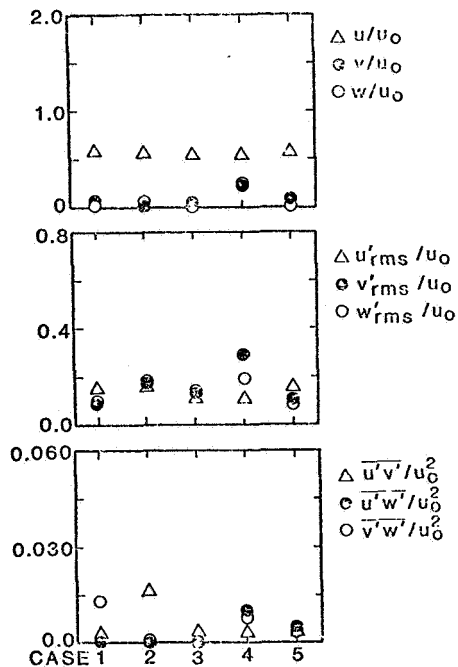


Fig. 6. Measurements for Situation B with Different Probe Configuration Cases

The directional sensitivity analysis has shown that the technique adequately measures the properties of a flowfield independent of the dominant flow direction except when the flow is predominately in the direction of the probe holder, with the six-orientations of the probe creating insignificant changes in hot-wire response. The analysis shows that this component of time-mean velocity is inadequately deduced. Only re-configuring of the probe can overcome this problem *a posteriori*.

#### Acknowledgments

The authors wish to extend their gratitude to NASA Lewis Research Center and the Air Force Wright Aeronautical Laboratories for their support under Grant No. NAG 3-74, technical monitor Dr. J. D. Holdeman. Thanks are also given to Lawrence H. Ong for assistance with the experiments.

#### References

1. Janjua, S. I., "Turbulence Measurements in a Complex Flowfield Using a Six-Orientation Hot-Wire Probe Technique." M.S. Thesis, Oklahoma State University, Stillwater, OK., Dec. 1981.
2. Jackson, T. W., "Turbulence Characteristics of Swirling Flowfields." Ph.D. Thesis, Oklahoma State University, Stillwater, OK., Dec. 1983.
3. Janjua, S. I., McLaughlin, D. K., Jackson, T. W., and Lilley, D. G., "Turbulence Measurements in a Confined Jet Using a Six-Orientation Hot-Wire Probe Technique", Paper AIAA-82-1262, Cleveland, Ohio, June 21-23, 1982.
4. Janjua, S. I., McLaughlin, D. K., Jackson, T. W. and Lilley, D. G., "Turbulence Measurements in Confined Jets Using a Rotating Single-Wire Probe Technique." AIAA Journal, 1984 (in press).

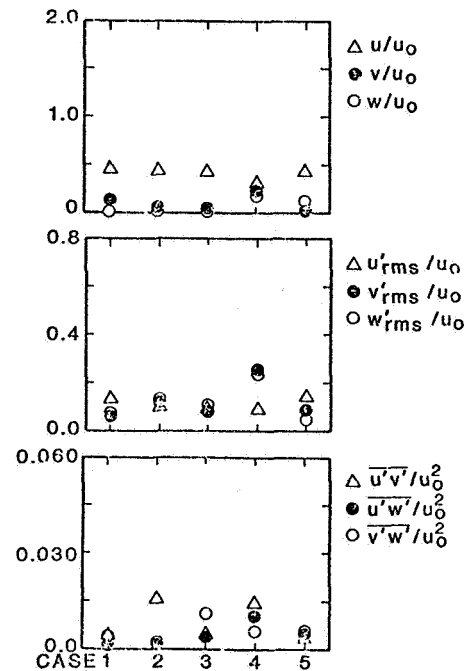


Fig. 7. Measurements for Situation C with Different Probe Configuration Cases

5. Jackson, T. W., and Lilley, D. G., "Single-Wire Swirl Flow Turbulence Measurements," Paper AIAA-83-1202, Seattle, Washington, June 27-29, 1983.
6. Dvorak, K., and Syred, N., "The Statistical Analysis of Hot Wire Anemometer Signals in Complex Flowfields", DISA Conference, University of Leicester, 1972.
7. Syred, N., Beer, J. M. and Chigier, N. A., "Turbulence Measurements in Swirling Recirculating Flows." Proc. Salford Symp. on Internal Flows, Inst. of Mech. Engineers, London, 1971, pp. B27-B36.
8. King, C. F., "Some Studies of Vortex Devices - Vortex Amplifier Performance Behaviour", Ph.D. Thesis, University College of Wales, Cardiff, Wales, 1978.
9. Perry, A. E., "Hot-Wire Anemometry", Clarendon, Oxford, England, 1982.
10. Jorgensen, F. E., "Directional Sensitivity of Wire and Fiber Film Probes", DISA Information No. 11, Franklin Lakes, NJ, May 1971, pp. 31-37.
11. Yuan, S. W., "Foundations of Fluid Mechanics", Prentice-Hall, Englewood Cliffs, NJ, 1967.
12. Corrsin, S. and Uberoi, M. S., "Spectrums and Diffusion in a Round Turbulent Jet", NACA Report No. 1040, 1949.
13. Sander, G. F., and Lilley, D. G., "The Performance of an Annular Vane Swirler", Paper AIAA-83-1326, Seattle, Wash., June 27-29, 1983.
14. Chaturvedi, M. C., "Characteristics of Axisymmetric Expansions", Proceedings, Journal of the Hydraulics Division, ASCE, Vol. 89, No. HY3, 1963, pp. 61-92.



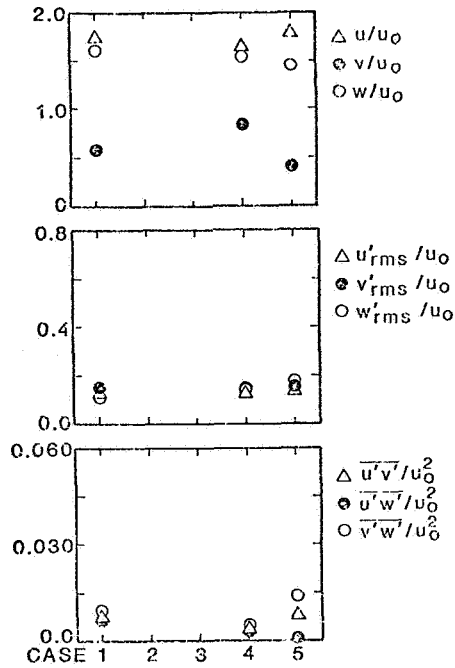


Fig. 8. Measurements for Situation D with Different Probe Configuration Cases

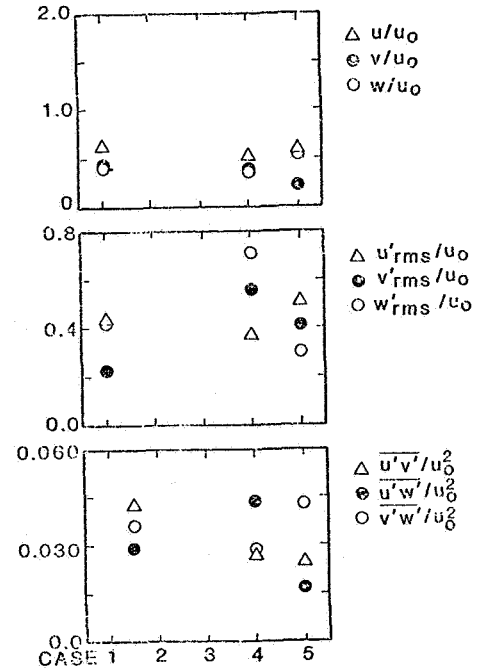


Fig. 9. Measurements for Situation E with Different Probe Configuration Cases

15. McKillop, B. E., "Turbulence Measurements in a Complex Flowfield Using a Crossed Hot-Wire", M.S. Thesis, Oklahoma State University, Stillwater, OK., July 1983.
16. Janjua, S. I., and McLaughlin, D. K., "Turbulence Measurements in a Swirling Confined Jet Flowfield Using a Triple Hot-Wire Probe", Report DT-8178-02 from Dynamics Technology to NASA Lewis Research Center, Nov. 1982.
17. Yoon, H. K., and Lilley, D. G., "Five-Hole Pitot Probe Time-Mean Velocity Measurements in Confined Swirling Flows", Paper AIAA-83-0315, Reno, Nev., Jan. 10-13, 1983.
18. Abujelala, M. T., and Lilley, D. G., "Confined Swirling Flow Predictions," Paper AIAA-83-0316, Reno, Nevada, Jan. 10-13, 1983.
19. Abujelala, M. T., and Lilley, D. G., "Limitations and Empirical Extensions of the  $k-\epsilon$  Model as Applied to Turbulent Swirling Flows." Paper AIAA-84-0441, Reno, Nevada, Jan. 9-12, 1984.
20. Abujelala, M. T., Jackson, T. W., and Lilley, D. G., "Turbulence Parameter Variation in Confined Swirling Flows," Paper for 29th Int. Gas Turbine Conference, Amsterdam, June 4-7, 1984.

Table 2. Measurements for Situation A Case 1

Combination Used	$u/u_0$	Measured $v/u_0$	$w/u_0$
612	0.978	0.203	0.009
123	0.961	0.199	NR
234	0.970	0.126	0.020
345	0.968	NR*	0.013
456	0.976	0.011	0.008
561	0.967	0.197	0.017
Mean $\bar{x}$	0.970	0.147	0.013
S.D. $\sigma$	0.006	0.074	0.005
$\sigma/\bar{x}$	0.006	0.503	0.353

\* Not Resolved

Table 3. Measurements for Situation A Case 2

Combination Used	$u/u_0$	Measured $v/u_0$	$w/u_0$
612	0.978	0.031	0.035
123	0.972	0.036	0.040
234	0.990	0.056	0.015
345	0.982	0.043	0.022
456	0.989	0.024	0.049
561	0.986	0.022	0.041
Mean $\bar{x}$	0.983	0.021	0.033
S.D. $\sigma$	0.006	0.012	0.012
$\sigma/\bar{x}$	0.006	0.553	0.353

Table 4. Measurements for Situation A Case 3

Combination Used	$u/u_0$	Measured $v/u_0$	$w/u_0$
612	0.954	-0.030	-0.008
123	0.954	-0.031	-0.008
234	0.967	-0.039	-0.051
345	0.948	-0.103	0.080
456	0.971	0.001	-0.003
561	0.951	-0.030	0.006
Mean $\bar{x}$	0.958	-0.039	0.001
S.D. $\sigma$	0.008	0.031	0.039
$\sigma/\bar{x}$	0.009	0.805	38.986

Table 5. Measurements for Situation A Case 5

Combination Used	$u/u_0$	Measured $v/u_0$	$w/u_0$
612	0.976	0.203	0.010
123	0.960	0.200	NR
234	0.971	0.126	0.019
345	0.968	NR	0.013
456	0.976	0.010	0.008
561	0.968	0.198	0.017
Mean $\bar{x}$	0.969	0.147	0.013
S.D. $\sigma$	0.005	0.074	0.004
$\sigma/\bar{x}$	0.006	0.503	0.317

Table 6. Measurements for Situation B Case 1

Combination Used	$u/u_0$	$v/u_0$	$w/u_0$	$u'_{rms}/u_0$	Measured $v'_{rms}/u_0$	$w'_{rms}/u_0$	$\overline{u'v'}/u_0^2$	$\overline{u'w'}/u_0^2$	$\overline{v'w'}/u_0^2$
612	0.593	0.211	0.036	0.171	0.062	0.066	0.0101	0.0019	NR
123	0.577	0.195	0.056	0.142	0.035	0.099	0.0020	0.0010	0.0037
234	0.582	0.220	0.012	0.142	0.091	0.136	0.0001	0.0029	NR
345	0.587	0.110	0.019	0.125	0.209	0.126	0.0001	0.0000	NR
456	0.616	NR	0.014	0.156	0.027	0.148	NR	NR	0.0221
561	0.602	0.207	0.042	0.157	0.079	0.056	0.0031	0.0000	NR
Mean $\bar{x}$	0.593	0.189	0.030	0.149	0.084	0.105	0.0031	0.0012	0.0129
S.D. $\sigma$	0.013	0.040	0.016	0.014	0.060	0.035	0.0037	0.0011	0.0092
$\sigma/\bar{x}$	0.022	0.212	0.537	0.098	0.718	0.330	1.1910	0.9350	0.7130

Table 7. Measurements for Situation C Case 1

Combination Used	$u/u_0$	$v/u_0$	$w/u_0$	$u'_{rms}/u_0$	Measured $v'_{rms}/u_0$	$w'_{rms}/u_0$	$\overline{u'v'}/u_0^2$	$\overline{u'w'}/u_0^2$	$\overline{v'w'}/u_0^2$
612	0.433	0.158	0.009	0.147	0.052	0.059	0.0077	0.0011	NR
123	0.464	0.153	0.026	0.128	0.067	0.051	0.0022	NR	NR
234	0.477	0.093	0.026	0.127	0.066	0.119	NR	NR	0.0057
345	NR								
456	0.460	0.167	0.034	0.123	0.070	0.118	0.0032	NR	0.0015
561	0.449	0.151	NR	0.124	0.056	0.070	0.0016	NR	NR
Mean $\bar{x}$	0.456	0.144	0.023	0.130	0.052	0.083	0.0038	0.0011	0.0037
S.D. $\sigma$	0.015	0.026	0.009	0.009	0.007	0.029	0.0024	0	0.0021
$\sigma/\bar{x}$	0.032	0.182	0.396	0.068	0.112	0.353	0.6468	0	0.5833

Table 8. Measurements for Situation B Case 2

Combination Used	$u/u_0$	$v/u_0$	$w/u_0$	$u'_{rms}/u_0$	Measured $v'_{rms}/u_0$	$w'_{rms}/u_0$	$\overline{u'v'}/u_0^2$	$\overline{u'w'}/u_0^2$	$\overline{v'w'}/u_0^2$
612	0.552	0.039	0.043	0.133	0.133	0.174	-0.0215	-0.0039	0.0039
123	0.554	0.066	0.033	0.168	0.168	0.125	0.0126	0.0011	-0.0011
234	0.520	-0.055	0.162	0.147	0.149	0.156	-0.0053	NR	NR
345	NR	NR	0.124	0.217	0.217	0.300	0.0922	NR	NR
456	0.527	-0.033	0.091	0.137	0.142	0.164	0.0205	NR	NR
561	0.576	0.033	0.112	0.155	0.155	0.103	-0.0001	NR	NR
Mean $\bar{x}$	0.546	0.010	0.092	0.159	0.161	0.170	0.0163	-0.0014	0.0014
S.D. $\sigma$	0.020	0.046	0.045	0.028	0.027	0.063	0.0365	0.0025	0.0025
$\sigma/\bar{x}$	0.037	4.600	0.493	0.177	0.170	0.369	2.2371	1.7875	1.7375

Table 9. Measurements for Situation B Case 4

Combination Used	$u/u_0$	$v/u_0$	$w/u_0$	$u'_{rms}/u_0$	Measured $v'_{rms}/u_0$	$w'_{rms}/u_0$	$\overline{u'v'}/u_0^2$	$\overline{u'w'}/u_0^2$	$\overline{v'w'}/u_0^2$
612	0.537	0.342	0.197	0.097	0.179	0.289	0.0032	0.0003	NR
123	0.607	0.157	0.236	0.140	0.270	0.123	NR	0.0031	0.0234
234	0.501	0.379	0.023	0.071	0.245	0.198	NR	0.0031	NR
345	0.594	0.119	0.326	0.129	0.314	0.079	NR	0.0053	0.0008
456	0.484	0.065	0.408	NR	0.422	0.126	NR	0.0428	NR
561	0.568	NR	NR	0.117	0.281	0.289	NR	NR	0.0007
Mean $\bar{x}$	0.549	0.212	0.238	0.111	0.285	0.184	0.0032	0.0109	0.0083
S.D. $\sigma$	0.045	0.125	0.130	0.024	0.074	0.082	0	0.0160	0.0107
$\sigma/\bar{x}$	0.083	0.589	0.546	0.221	0.259	0.446	0	1.4700	1.2864

Table 10. Measurements for Situation C Case 2

Combination Used	$u/u_0$	$v/u_0$	$w/u_0$	$u'_{rms}/u_0$	Measured $v'_{rms}/u_0$	$w'_{rms}/u_0$	$\overline{u'v'}/u_0^2$	$\overline{u'w'}/u_0^2$	$\overline{v'w'}/u_0^2$
612	0.446	0.052	0.007	0.099	0.099	0.153	0.0050	0.0012	0.0000
123	0.447	0.076	0.050	0.123	0.123	0.096	NR	0.0030	NR
234	0.450	0.084	0.016	0.124	0.124	0.111	0.0110	NR	NR
345	0.458	-0.009	0.004	0.105	0.105	0.133	0.0230	0.0023	NR
456	0.443	0.095	0.017	0.130	0.130	0.132	0.0240	NR	NR
561	0.428	0.100	NR	0.136	0.136	0.099	0.0140	0.0016	0.0025
Mean $\bar{x}$	0.445	0.066	0.019	0.119	0.119	0.121	0.0160	0.0013	0.0012
S.D. $\sigma$	0.009	0.037	0.016	0.013	0.013	0.020	0.0062	0.0008	0.0012
$\sigma/\bar{x}$	0.020	0.561	0.862	0.111	0.111	0.169	0.3861	0.6421	1.0000

Table 11. Measurements for Situation C Case 4

Combination Used	$u/u_0$	$v/u_0$	$w/u_0$	$u'_{rms}/u_0$	Measured $v'_{rms}/u_0$	$w'_{rms}/u_0$	$\overline{u'v'}/u_0^2$	$\overline{u'w'}/u_0^2$	$\overline{v'w'}/u_0^2$
612	0.300	0.471	0.085	NR	NR	0.347	0.0262	NR	0.0779
123	0.360	0.073	0.191	0.099	0.285	0.210	NR	NR	NR
234	0.382	0.124	NR	0.109	0.237	0.225	NR	NR	0.0236
345	0.354	0.244	0.135	0.080	0.185	0.214	0.0036	0.0053	NR
456	0.380	0.227	0.191	0.105	0.216	0.181	NR	0.0161	NR
561	0.289	NR	0.279	NR	0.337	0.248	NR	NR	NR
Mean $\bar{x}$	0.343	0.228	0.176	0.098	0.252	0.237	0.0149	0.0107	0.0507
S.D. $\sigma$	0.037	0.137	0.065	0.011	0.053	0.053	0.0113	0.0054	0.0271
$\sigma/\bar{x}$	0.107	0.602	0.368	0.113	0.210	0.223	0.7584	0.5047	0.5355

Table 12. Measurements for Situation B Case 3

Combination Used	$u/u_0$	$v/u_0$	$w'/u_0$	$u'_{rms}/u_0$	Measured $v'_{rms}/u_0$	$w'_{rms}/u_0$	$\overline{u'v'}/u_0^2$	$\overline{u'w'}/u_0^2$	$\overline{v'w'}/u_0^2$
612	0.548	0.053	-0.022	0.069	0.112	0.118	-0.0015	-0.0261	-0.0272
123	0.575	0.076	-0.006	0.120	0.084	0.088	-0.0064	0.0342	-0.0073
234	0.559	0.022	-0.024	0.099	0.118	0.121	-0.0024	-0.0163	-0.0058
345	0.559	0.037	0.000	0.142	0.139	0.146	-0.0033	-0.0060	-0.0033
456	0.547	0.025	-0.019	0.118	0.159	0.162	0.0181	-0.0428	0.0181
561	0.547	0.063	-0.034	0.135	0.125	0.136	0.0112	0.0044	0.0112
Mean $\bar{x}$	0.556	0.046	-0.017	0.117	0.123	0.128	0.0031	-0.0028	-0.0024
S.D. $\sigma$	0.010	0.020	0.011	0.0186	0.023	0.023	0.0100	0.0243	0.0145
$\sigma/\bar{x}$	0.018	0.429	0.669	0.159	0.188	0.183	2.9016	2.7612	6.0300

Table 13. Measurements for Situation B Case 5

Combination Used	$u/u_0$	$v/u_0$	$w/u_0$	$u'_{rms}/u_0$	Measured $v'_{rms}/u_0$	$w'_{rms}/u_0$	$\overline{u'v'}/u_0^2$	$\overline{u'w'}/u_0^2$	$\overline{v'w'}/u_0^2$
612	0.656	0.211	0.015	0.170	0.069	0.060	NR	0.0103	NR
123	0.579	0.188	0.043	0.161	0.114	0.031	0.0017	0.0021	0.0051
234	0.587	0.141	0.021	0.163	0.157	0.101	0.0080	NR	NR
345	0.504	0.354	0.012	0.164	0.154	0.133	NR	NR	NR
456	0.590	0.130	0.053	0.148	0.137	0.120	0.0008	NR	NR
561	0.580	0.205	0.065	0.147	0.066	0.047	NR	0.0040	0.0019
Mean $\bar{x}$	0.583	0.205	0.035	0.159	0.116	0.082	0.0035	0.0054	0.0035
S.D. $\sigma$	0.044	0.073	0.020	0.008	0.037	0.038	0.0032	0.0035	0.0016
$\sigma/\bar{x}$	0.076	0.357	0.573	0.053	0.320	0.465	0.9143	0.6490	0.4571

Table 14. Measurements for Situation C Case 3

Combination Used	$u/u_0$	$v/u_0$	$w/u_0$	Measured			$\overline{u'v'}/u_0^2$	$\overline{u'w'}/u_0^2$	$\overline{v'w'}/u_0^2$
				$u'_{rms}/u_0$	$v'_{rms}/u_0$	$w'_{rms}/u_0$			
612	0.467	0.043	-0.057	0.073	0.090	0.092	-0.0130	-0.0146	-0.0008
123	0.451	0.066	-0.063	0.100	0.074	0.075	0.0010	0.0256	-0.0002
234	0.456	0.055	-0.063	0.085	0.106	0.108	-0.0011	0.0199	-0.0029
345	0.448	-0.017	0.002	0.111	0.080	0.114	0.0095	-0.0023	0.0068
456	0.434	0.046	-0.141	0.118	0.115	0.119	0.0188	0.0013	0.0211
561	0.418	0.097	-0.141	0.100	0.101	0.105	0.0143	-0.0032	0.0120
Mean $\bar{x}$	0.445	0.048	-0.060	0.098	0.094	0.102	0.0049	0.0044	0.0063
S.D. $\sigma$	0.158	0.034	0.042	0.015	0.014	0.015	0.0106	0.0139	0.0085
$\sigma/\bar{x}$	0.035	0.713	0.707	0.154	0.153	0.145	2.1632	3.1641	1.3516

Table 15. Measurements for Situation C Case 5

Combination Used	$u/u_0$	$v/u_0$	$w/u_0$	Measured			$\overline{u'v'}/u_0^2$	$\overline{u'w'}/u_0^2$	$\overline{v'w'}/u_0^2$
				$u'_{rms}/u_0$	$v'_{rms}/u_0$	$w'_{rms}/u_0$			
612	0.417	NR	0.162	0.142	0.062	0.047	0.0044	0.0068	0.0011
123	0.454	0.013	0.152	0.156	0.069	0.061	NR	0.0025	NR
234	0.473	0.024	0.075	0.154	0.147	0.032	NR	NR	0.0083
345	NR								
456	0.453	0.064	0.176	0.141	0.131	0.041	0.0041	0.0038	0.0039
561	0.431	0.014	0.168	0.141	0.038	0.054	0.0023	0.0024	NR
Mean $\bar{x}$	0.446	0.029	0.147	0.147	0.089	0.047	0.0036	0.0038	0.0044
S.D. $\sigma$	0.019	0.021	0.037	0.007	0.042	0.010	0.0009	0.0018	0.0030
$\sigma/\bar{x}$	0.044	0.717	0.249	0.046	0.473	0.214	0.2608	0.4676	0.6735

Table 15. Measurements for Situation D Case 1

Combination Used	$u/u_0$	$v/u_0$	$w/u_0$	Measured			$\overline{u'v'}/u_0^2$	$\overline{u'w'}/u_0^2$	$\overline{v'w'}/u_0^2$
				$u'_{rms}/u_0$	$v'_{rms}/u_0$	$w'_{rms}/u_0$			
612	1.661	0.633	1.616	0.077	0.142	0.106	0.0073	0.0074	0.0056
123	1.763	0.577	1.724	0.127	0.148	0.092	0.0065	0.0120	0.0079
234	1.808	0.355	1.590	0.149	0.138	0.142	NR	0.0018	0.0127
345	1.773	0.457	1.597	0.170	0.196	0.135	NR	0.0063	NR
456	1.726	0.223	1.540	0.142	0.181	0.143	0.0075	0.0020	NR
561	1.702	0.665	1.609	0.133	0.091	0.103	0.0043	0.0045	0.0056
Mean $\bar{x}$	1.739	0.565	1.613	0.134	0.149	0.123	0.0064	0.0057	0.0082
S.D. $\sigma$	0.048	0.022	0.055	0.028	0.004	0.019	0.0013	0.0035	0.0027
$\sigma/\bar{x}$	0.029	0.038	0.034	0.213	0.225	0.158	0.1983	0.6131	0.3321

Table 17. Measurements for Situation E Case 1

Combination Used	$u/u_0$	$v/u_0$	$w/u_0$	$u'_{rms}/u_0$	Measured $v'_{rms}/u_0$	$w'_{rms}/u_0$	$\overline{u'v'}/u_0^2$	$\overline{u'w'}/u_0^2$	$\overline{v'w'}/u_0^2$
612	0.708	0.522	0.424	0.218	0.303	0.341	0.0623	0.0057	0.0422
123	0.562	0.590	0.419	0.420	0.322	0.252	0.0298	0.0108	0.0091
234	0.752	0.269	0.338	0.487	0.129	0.433	NR	0.0020	0.3600
345	0.563	0.482	0.373	0.591	0.121	0.649	0.3900	NR	0.0475
456	0.628	0.323	0.478	0.463	0.135	0.525	0.0384	0.0411	NR
561	0.533	0.563	0.383	0.443	0.304	0.332	NR	0.0881	0.0462
Mean $\bar{x}$	0.624	0.458	0.403	0.437	0.219	0.422	0.0424	0.0295	0.0362
S.D. $\sigma$	0.081	0.120	0.044	0.112	0.091	0.133	0.01207	0.0324	0.0141
$\sigma/\bar{x}$	0.130	0.263	0.110	0.256	0.451	0.315	0.2846	1.0975	0.3903

Table 18. Measurements for Situation D Case 4

Combination Used	$u/u_0$	$v/u_0$	$w/u_0$	$u'_{rms}/u_0$	Measured $v'_{rms}/u_0$	$w'_{rms}/u_0$	$\overline{u'v'}/u_0^2$	$\overline{u'w'}/u_0^2$	$\overline{v'w'}/u_0^2$
612	1.640	0.806	1.556	0.126	0.112	0.100	0.0054	0.0067	NR
123	1.641	0.747	1.523	0.122	0.098	0.134	NR	0.0002	0.0033
234	1.680	0.806	1.489	0.141	0.171	0.096	0.0024	0.0028	0.0043
345	1.774	0.809	1.394	0.107	0.179	0.183	0.0045	NR	0.0023
456	1.472	1.026	1.532	0.097	0.167	0.155	0.0018	NR	0.0015
561	1.639	0.806	1.654	0.130	0.114	0.132	0.0044	NR	0.0108
Mean $\bar{x}$	1.641	0.833	1.525	0.121	0.140	0.133	0.0037	0.0032	0.0044
S.D. $\sigma$	0.089	0.051	0.078	0.015	0.033	0.030	0.0014	0.0027	0.0033
$\sigma/\bar{x}$	0.089	0.107	0.051	0.120	0.234	0.226	0.3690	0.8348	0.7578

Table 19. Measurements for Situation E Case 4

Combination Used	$u/u_0$	$v/u_0$	$w/u_0$	$u'_{rms}/u_0$	Measured $v'_{rms}/u_0$	$w'_{rms}/u_0$	$\overline{u'v'}/u_0^2$	$\overline{u'w'}/u_0^2$	$\overline{v'w'}/u_0^2$
612	0.320	0.347	NR	NR	0.856	NR	NR	0.0802	NR
123	0.688	0.556	0.157	0.370	0.196	0.363	0.0080	0.0192	0.0060
234	0.442	0.156	0.647	NR	0.642	0.637	0.0421	0.0309	NR
345	NR	NR	NR	NR	NR	0.914	NR	NR	NR
456	0.430	0.476	0.435	NR	0.694	0.694	0.0313	NR	0.0458
561	0.723	NR	0.289	0.375	0.418	0.613	NR	NR	0.0346
Mean $\bar{x}$	0.521	0.394	0.362	0.373	0.561	0.704	0.0271	0.0440	0.0288
S.D. $\sigma$	0.157	0.163	0.182	0.002	0.230	0.108	0.0142	0.0273	0.0167
$\sigma/\bar{x}$	0.302	0.414	0.476	0.007	0.410	0.154	0.5251	0.6197	0.0582

Table 20. Measurements for Situation D Case 5

Combination Used	$u/u_0$	$v/u_0$	$w/u_0$	$u'_{rms}/u_0$	Measured $v'_{rms}/u_0$	$w'_{rms}/u_0$	$\overline{u'v'}/u_0^2$	$\overline{u'w'}/u_0^2$	$\overline{v'w'}/u_0^2$
612	1.777	0.452	1.445	0.128	0.155	0.198	0.0133	NR	0.0133
123	1.744	0.491	1.428	0.186	0.183	0.174	0.0004	NR	0.0186
234	1.703	0.310	1.603	0.196	0.202	0.178	0.0031	NR	0.0179
345	1.852	0.362	1.388	0.126	0.183	0.184	NR	0.0004	0.0215
456	1.853	0.350	1.387	0.124	0.113	0.184	0.0103	0.0009	0.0014
561	1.886	0.491	1.433	0.090	0.110	0.198	NR	NR	0.0124
Mean $\bar{x}$	1.802	0.409	1.447	0.142	0.158	0.186	0.0068	0.0007	0.0142
S.D. $\sigma$	0.066	0.072	0.073	0.037	0.035	0.009	0.0052	0.0003	0.0065
$\sigma/\bar{x}$	0.036	0.175	0.050	0.026	0.224	0.492	0.7682	0.3571	0.4571

Table 21. Measurements for Situation E Case 5

Combination Used	$u/u_0$	$v/u_0$	$w/u_0$	$u'_{rms}/u_0$	Measured $v'_{rms}/u_0$	$w'_{rms}/u_0$	$\overline{u'v'}/u_0^2$	$\overline{u'w'}/u_0^2$	$\overline{v'w'}/u_0^2$
612	0.797	NR	0.547	0.318	0.447	0.316	0.0195	0.0103	0.0275
123	0.552	NR	0.613	0.624	0.338	0.356	0.0342	NR	0.0831
234	0.740	0.103	0.246	0.645	0.610	NR	0.0148	0.0086	NR
345	0.734	0.251	0.336	0.573	0.564	0.165	0.0460	NR	0.0170
456	0.435	0.225	0.695	0.546	0.363	0.319	0.0147	0.0300	NR
561	0.424	0.301	0.613	0.496	0.177	0.346	0.0175	NR	0.0284
Mean $\bar{x}$	0.599	0.220	0.508	0.534	0.416	0.300	0.0245	0.0163	0.0425
S.D. $\sigma$	0.135	0.073	0.162	0.108	0.145	0.059	0.0117	0.0097	0.0290
$\sigma/\bar{x}$	0.225	0.331	0.318	0.202	0.349	0.231	0.4773	0.5958	0.6824

Table 22. Comparison of averaged results from six possible wire combinations with optimal combination

Situation	$u/u_0$	$v/u_0$	$w/u_0$	$u'_{rms}/u_0$	Measured $v'_{rms}/u_0$	$w'_{rms}/u_0$	$\overline{u'v'}/u_0^2$	$\overline{u'w'}/u_0^2$	$\overline{v'w'}/u_0^2$	
A	345	0.568	NR	0.013						
	$\bar{x}$	0.970	0.147	0.013						
B	345	0.587	0.110	0.019	0.125	0.209	0.126	0.0001	0.0000	NR
	$\bar{x}$	0.593	0.189	0.030	0.157	0.084	0.105	0.0031	0.0012	0.0129
C	345	NR								
	$\bar{x}$	0.456	0.144	0.023	0.130	0.062	0.083	0.0037	0.0011	0.0036
D	561	1.702	0.665	1.609	0.138	0.091	0.169	0.0043	0.0045	0.0066
	$\bar{x}$	1.739	0.585	1.613	0.134	0.149	0.123	0.0064	0.0057	0.0082
E	561	0.628	0.323	0.478	0.463	0.135	0.525	0.0384	0.0411	NR
	$\bar{x}$	0.624	0.456	0.403	0.437	0.219	0.422	0.0424	0.0295	0.0362

APPENDIX I

LIMITATIONS AND EMPIRICAL EXTENSIONS OF THE

$k-\epsilon$  MODEL AS APPLIED TO TURBULENT CONFINED

SWIRLING FLOWS

(AIAA-84-0441)



LIMITATIONS AND EMPIRICAL EXTENSIONS OF THE k-ε MODEL

AS APPLIED TO TURBULENT CONFINED SWIRLING FLOWS

M. T. Abujelala\* and D. G. Lilley\*\*  
 Oklahoma State University  
 Stillwater, OK 74078

Abstract

Shortcomings and recommended corrections to the standard two-equation k-ε turbulence model suggested by previous investigators are presented. They are assessed regarding their applicability to turbulent swirling recirculating flow. Recent experimental data on swirling confined flows, obtained with a five-hole pitot probe and a six-orientation hot-wire probe, are used to obtain optimum values of the turbulence parameters C<sub>1</sub>, C<sub>2</sub>, and σ<sub>ε</sub> for swirling flows. General predictions of moderately and strongly swirling flows with these values are more accurate than predictions with the standard or previous simple extensions of the k-ε turbulence model.

1. Introduction

1.1 The Need for Turbulence Modeling

Turbulent swirling recirculating flows are used in many practical situations. They provide the fundamentals of physical processes occurring in aircraft combustors and in industrial furnaces. These types of flow are characterized by strong streamline curvature, complex eddy structures and high turbulence intensities. The practical need for computation of this category of flows has encouraged many workers to develop turbulence models that can provide accurate information about such flows. These models consist of a set of equations which, when solved with the mean flow equation, allow calculation of the relevant correlations and simulate the behavior of real fluids in many respects. These models may conveniently be distinguished by the number of turbulence characterizing properties which appear as the dependent variable of the differential equations. The most widely used model is the k-ε turbulence model. A brief description of this model and its limitations are presented next.

1.2 The k-ε Turbulence Model

The k-ε model has been used by many workers<sup>1-6</sup> to provide realistic predictions of the velocity fields and the turbulence parameters. This model involves two transport equations for turbulence characteristics. One of these equations governs the distribution throughout the field of the turbulence energy k, which measures the local kinetic energy of the fluctuating motion; the other governs the turbulence energy dissipation rate ε. The k equation can be obtained from the exact

transport equation of the Reynolds stresses  $\overline{u_i u_j}$  by summation over the three equations for the normal stresses. The resulting equations in the axisymmetric cylindrical system are:

$$\rho u \frac{\partial k}{\partial x} + \rho v \frac{\partial k}{\partial r} = \frac{1}{r} \frac{\partial}{\partial r} \left[ r \frac{\mu_e}{\sigma_k} \frac{\partial k}{\partial r} \right] + \frac{\partial}{\partial x} \left[ \frac{\mu_e}{\sigma_k} \frac{\partial k}{\partial x} \right] + G - \rho \epsilon$$

$$\rho u \frac{\partial \epsilon}{\partial x} + \rho v \frac{\partial \epsilon}{\partial r} = \frac{1}{r} \frac{\partial}{\partial r} \left[ r \frac{\mu_e}{\sigma_\epsilon} \frac{\partial \epsilon}{\partial r} \right] + \frac{\partial}{\partial x} \left[ \frac{\mu_e}{\sigma_\epsilon} \frac{\partial \epsilon}{\partial x} \right] + C_1 G \epsilon / k - C_2 \rho \epsilon^2 / k$$

The values usually adopted for the empirical constants C<sub>μ</sub>, C<sub>1</sub>, C<sub>2</sub>, σ<sub>k</sub> and σ<sub>ε</sub> are those quoted in Ref. 1; <sup>μ</sup> they are listed in Table 1. The generation term is

$$G = \mu_e \left[ 2 \left\{ \left( \frac{\partial u}{\partial x} \right)^2 + \left( \frac{\partial v}{\partial r} \right)^2 + \left( \frac{v}{r} \right)^2 \right\} + \left( \frac{\partial u}{\partial r} + \frac{\partial v}{\partial x} \right)^2 + \left\{ r \frac{\partial}{\partial r} \left( \frac{w}{r} \right) \right\}^2 + \left( \frac{\partial w}{\partial x} \right)^2 \right]$$

TABLE 1. THE k-ε EMPIRICAL CONSTANTS

C <sub>μ</sub>	C <sub>1</sub>	C <sub>2</sub>	σ <sub>k</sub>	σ <sub>ε</sub>
0.09	1.44	1.92	1.00	1.30

where μ<sub>e</sub> is the sum of turbulent and laminar viscosities. Knowledge of k and ε allows the length scale ℓ and turbulent viscosity μ<sub>t</sub> to be determined from which the turbulent shear stresses can be evaluated via

$$\mu_t = C_\mu \rho k^2 / \epsilon$$

$$-\rho u'_i u'_j = \mu_t \left[ \frac{\partial \bar{u}_i}{\partial x_j} + \frac{\partial \bar{u}_j}{\partial x_i} \right] - \frac{2}{3} \rho k \delta_{ij}$$

To account for the wall effect in the near-wall regions, equations are introduced to link velocities, k and ε on the wall to those in the near-wall region. These equations, called "wall functions", are introduced and used in finite difference calculations at near-wall points. They occur in the momentum equations and k-generation terms, and their implementation is discussed elsewhere<sup>1</sup> together with appropriate near-wall

\* Graduate Student, School of Mechanical and Aerospace Engineering, Student Member AIAA  
 \*\* Professor, School of Mechanical and Aerospace Engineering, Associate Fellow AIAA

$\epsilon$  specification. The main assumptions considered in these formulations are:

1. Convection and diffusion of turbulence kinetic energy are nearly negligible.
2. Eddy viscosity is isotropic.
3. The sublayer extends up to a value of wall function parameter  $y^+$  equal to 11.63.
4. The length scale is proportional to the normal distance from the wall.

### 1.3 The k- $\epsilon$ Empirical Constants

Reference 7 discussed in some detail the basis for choosing the k- $\epsilon$  constants. Therefore, it may suffice to mention here that  $C_\mu$  is fixed by the requirement that in a constant stress layer production and dissipation of  $\epsilon$  are balanced

$[\tau_w/(\rho k) = C_\mu^{1/2}]$ ,  $C_2$  is determined by reference to the decay of grid turbulence, and  $C_1$  is chosen so that the von Karman constant equals 0.42. The 'Schmidt' numbers  $\sigma_k$  and  $\sigma_\epsilon$  are fixed by computer optimization in Ref. 8. The main assumptions considered in determining the constants are: the flow is not far from equilibrium so that the convection and diffusion are small compared to production and dissipation terms; and the turbulent Reynolds number is high. These assumptions have led to the nonuniversality of the model constants; even in certain fairly simple flows, some constants require different values. Usually, the extension of the model applicability is achieved by algebraic formulation of  $C_2$  and  $C_\mu$  to account for a specified flow case. These formulations will be discussed later.

### 1.4 The Present Contribution

The basic objectives of this study are to evaluate the standard k- $\epsilon$  model and its previously-proposed available extensions as applied to turbulent recirculating swirling flows, and to highlight the current problems with this model. Section 2 presents the shortcomings and previously-proposed extensions. Regarding their applicability to turbulent swirling recirculating flows, Section 3 exhibits their predictive capability, and then goes on to optimize three particular parameters for swirling flows. Predictions are given using the model with these optimum values, starting from good quality measured inlet conditions. Conclusions drawn from the study are given in Section 4.

## 2. Current Status of the Turbulence Model

### 2.1 Shortcomings of the Standard Model

The width of applicability of the standard model was tested in Ref. 9, where nine substantially different kinds of turbulent flow were considered. The model demonstrated the capability of prediction of both near-wall and free shear flow phenomena without adjustments to constants or functions. However, in some flow cases, this model has some shortcomings, a brief summary of which is now given.

Habib and Whitelaw<sup>10</sup> found that the velocity maxima and minima on the centerline for confined swirling flows with coaxial jets are not correctly predicted. However, the measured values of the two components of the rms value of the velocity fluctuation and the kinetic energy are in excellent

agreement with the predicted values. This led to their support of Gibson's assumption<sup>11</sup> that a constant value of  $C_\mu$  is inappropriate in flows with curved streamlines: empirical adjustments to constants may produce better results.

Syed and Sturgess<sup>12</sup> predicted the rms value of axial velocity fluctuation, turbulence parameters, velocity profiles and turbulence shear stresses for coaxial jets in confined sudden expansion flows. A maximum error of about 27 percent was obtained in the rms values. The maximum discrepancy in the predicted velocity profiles was found at the centerline. The maximum level of turbulent shear stress was predicted as occurring closer to the centerline than was measured. This led to the conclusion that the dissipation rate is not represented correctly and/or the convection of shear stress is not negligible and its value is not based solely on the local properties.

Measured and predicted streamline contours, velocity and turbulence intensity profiles for isothermal flow in axisymmetric models of combustor geometries have been compared.<sup>13</sup> It was seen that the turbulence modeling errors are prevalent in regions of recirculation, flow development, and in the near-wall region.

In widely spaced coaxial isothermal jets in combustors, it was found<sup>14</sup> that the transport of turbulent stress is involved in producing the local centerline axial velocity peak. This peak cannot be predicted by the eddy viscosity model because the turbulence characteristics are derived from the velocity profiles and eddy viscosity, and they are incapable of calculating the correct flow characteristics at positions of negligible velocity gradient. A recommendation is made to take into account the transport of turbulent shear stress.

### 2.2 Previous Proposed Extensions

The above mentioned problems have commanded considerable attention from many investigators. Most of the investigators have agreed that some of the model shortcomings can be eliminated by algebraic formulation of variations of the parameters  $C_2$  and  $C_\mu$ . These corrections were expected either to account for low Reynolds number or streamline curvature effects, or both.

A new term

$$2 \mu \left( \frac{\partial k}{\partial y} \right)^{1/2}{}^2$$

was added<sup>8</sup> to the k-equation to represent the energy dissipation rate at the wall. Also, another term

$$2 \mu \mu_t \left( \frac{\partial^2 u}{\partial y^2} \right)$$

was added to the  $\epsilon$ -equation in order for the peak level of the turbulent kinetic energy to agree with experimental data. Both  $C_2$  and  $C_\mu$  were modeled to account for low Reynolds number effect via:

$$\begin{aligned} C_\mu &= 0.09 \exp [-2.5/(1 + R_t/50)] \\ C_2 &= 2.0 [1.0 - 0.3 \exp (-R_t^2)] \end{aligned} \quad (1)$$

where  $R_t = \rho k^2 / (\epsilon \mu)$ .

This model was tested<sup>15</sup> by application to isothermal low Reynolds number pipe flow, and wall boundary layers with streamwise pressure gradient and wall injection. The model predictions were not completely in accord with the experimental data.

Lauder et al<sup>16</sup> incorporates streamline curvature effects on the turbulence structure in the k- $\epsilon$  model. The direct effect of curvature in the model is limited to a single empirical coefficient whose magnitude is directly proportional to a Richardson number based on a time scale of the energy-containing eddies. For boundary layer flow types, the proposed  $C_2$  formulation is

$$C_2 = C_2^i (1 - 0.2 Ri) \quad (2)$$

where  $C_2^i$  is the  $C_2$  value before the correction, and  $Ri$  is a Richardson number defined as:

$$Ri = \frac{k^2}{\epsilon^2} \frac{w}{r} \frac{\partial}{\partial r} (rw) \quad (3)$$

where  $w$  is the swirl velocity. The model was applied to a variety of boundary layer flows developing over curved and spinning surfaces; satisfactory agreement with experiments was obtained. On the other hand, Durst and Rostogi<sup>17</sup> solved Reynolds equations using the k- $\epsilon$  model in the separated flow region, and both the k- $\epsilon$  model and the k- $\epsilon$ - $u^i v^j$  models in the region downstream of the separation. They concluded that in the redevelopment region the three-equation turbulence model does not offer worthwhile advantages over the two equation k- $\epsilon$  model.

Ljuboja and Rodi<sup>18</sup> replaced the empirical constant  $C_\mu$  by a function which was derived by reducing a model from the Reynolds stress transport equations to an algebraic expression by introducing simplifying assumptions about the convection and diffusion terms. Good results were obtained when this model was applied to a wall jet in stagnant surroundings, and in a moving stream.

Hanjalic and Launder<sup>19</sup> introduced into the  $\epsilon$ -equation a term proportional to

$$k \frac{\partial \bar{u}_i}{\partial x_j} \frac{\partial \bar{u}_j}{\partial x_m} \epsilon_{ijk} \epsilon_{lmk}$$

where  $\epsilon_{ijk}$  stands for the third-order alternating tensor. For thin shear flows this term reduced to  $k(\frac{\partial \bar{u}}{\partial y})^2$ . This correction was expected to promote a higher rate of dissipation for irrotational strains as opposed to rotational strains. Indeed, they found that this minor modification brought substantial improvement to the prediction of boundary layers in adverse pressure gradient conditions.

A streamline curvature correction was proposed by Leschziner and Rodi<sup>20</sup>, derived from the Reynolds-stress equations, following a method described in Ref. 11. Also, they adapted a modification which accounts for the preferential influence of normal stresses and the dissipation of

turbulent energy; this modification was originally proposed for strongly accelerated flows.<sup>21</sup> This correction has led to greatly improved agreement with experimental data when applied to the recirculating flow in an annulus, and a plane twin-parallel jet in still air.

Finally, good agreement with experimental data was obtained<sup>22</sup> when a modified k- $\epsilon$  model was applied to fully developed pipe flow. The modified version can be used without introducing the empirical wall function formulas.

### 3. Confined Swirling Flow Predictions

#### 3.1 Predictive Capability with the Standard and Modified Model

None of the studies presented in the previous sections extended the k- $\epsilon$  turbulence model for application to confined turbulent recirculating swirling flows. However, the practical needs for accurate predictions of the characteristics of these flows are considerable. An earlier study by the authors<sup>6</sup> reveals that inaccurate predictions for the size and strength of the recirculation zone were obtained by using the standard k- $\epsilon$  model. These predictions and all other predictions given in the present paper have been made starting from measured time-mean velocities  $u$ ,  $v$ , and  $w$ , and best-estimate  $k$  and  $\epsilon$  values, at the swirler exit.<sup>30</sup> The inaccuracy of the standard model can easily be seen by comparing the measurements of Yoon and Lilley<sup>23</sup> for swirl vane angles of 45 and 70 deg. against the corresponding predicted velocity profiles using the STARPIC computer code<sup>24</sup> shown in Figs. 1 and 2, respectively. Inspection of these figures reveals that the turbulence model over-predicts the dissipation of the kinetic energy of the flow; and the centrifugal force produces a shorter central recirculation core than the measurements show. Thus, in order to extend the k- $\epsilon$  turbulence model to perform satisfactorily for confined swirling flows, some corrections concerning the  $\epsilon$ -equation have to be made. The general approach, as shown in the previous sections, is to consider the streamline curvature effects through the modeling of the constant  $C_2$ .

A Richardson number for swirling flows may be defined by<sup>25</sup>

$$Ri = \frac{2 \frac{w}{r} \frac{\partial}{\partial r} (rw)}{(\frac{\partial u}{\partial r})^2 + [r \frac{\partial}{\partial r} (\frac{w}{r})]^2} \quad (4)$$

An extensive preliminary study was conducted to evaluate this equation and Eq. (3) as applied to turbulent swirling recirculating flows. The distribution of  $C_2$  values over the flowfield obtained by these two expressions were compared, along with time-mean velocity predictions, with the conclusion that the Eq. (4) Richardson number is superior to the Eq. (3) Richardson number when used with Eq. (2) for the prediction of this flow.

Equation (2) with the Richardson number as defined by Eq. (4) was added to the  $\epsilon$ -equation of the k- $\epsilon$  model, and the flowfields for swirl vane angles of 45 and 70 deg. were predicted. The value of  $C_2$  was not allowed to be less than 0.1 nor greater than 2.4, with  $C_\mu$  and the other model

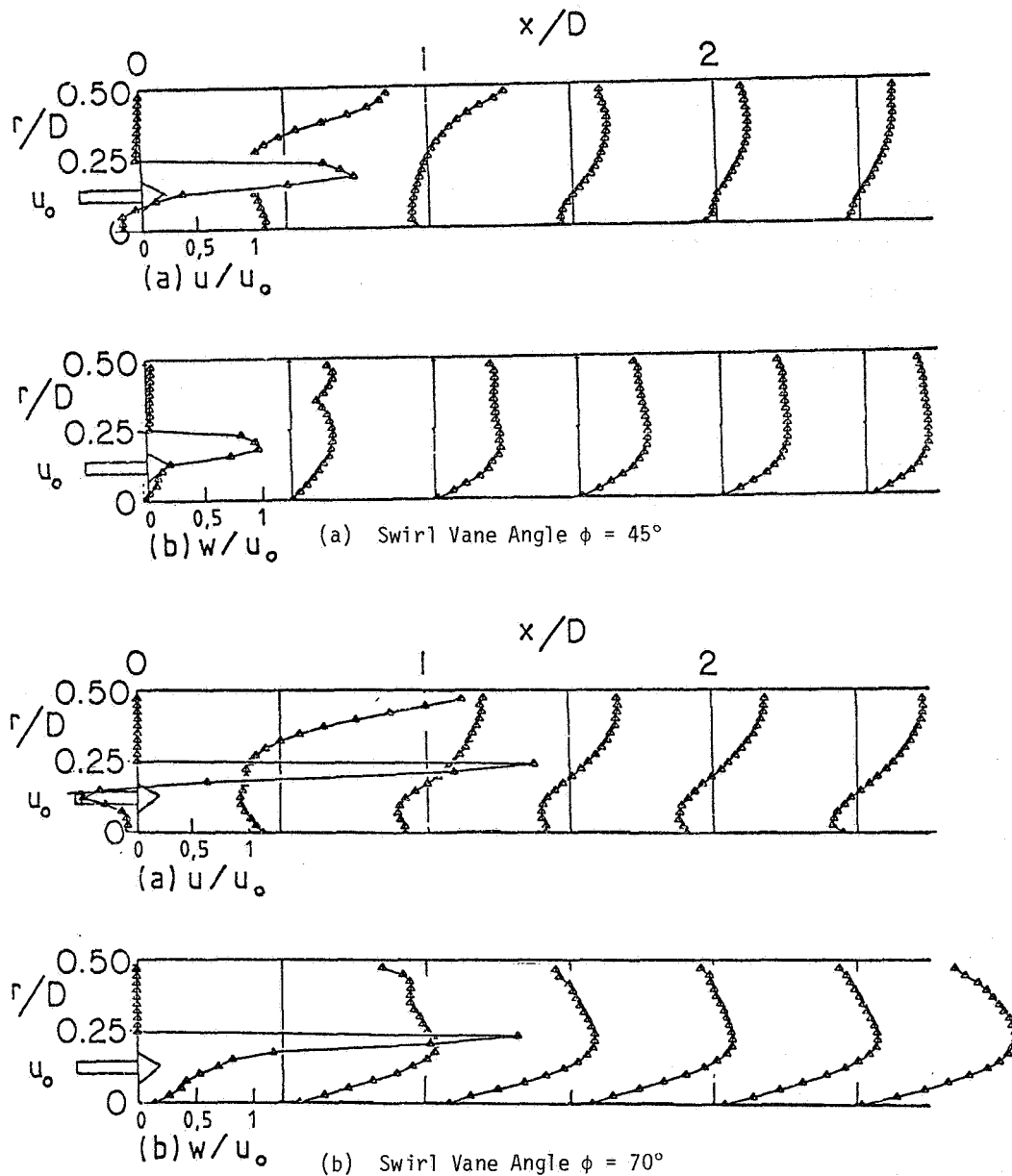


Fig. 1 Measured Velocity Profiles<sup>23</sup>

constants assigned the conventional values. The distribution of  $C_2$  values over the flowfield is portrayed in Tables 2 and 3. Table 2 displays a moderate swirl strength flowfield ( $\phi = 45$  deg.), and Table 3, exhibits the flowfield for a stronger swirl strength ( $\phi = 70$  deg.); the  $C_2$  values not included in the above mentioned range have been replaced by a negative sign [-]. The corresponding velocity profiles for  $\phi = 45$  and  $70$  deg. are displayed in Fig. 3, Parts (a) and (b), respectively. Inspection of the predicted data associated with these figures reveals that the corrected  $\epsilon$ -equation under-predicts the dissipation of the turbulent kinetic energy. The dominant centrifugal forces drive the flow off the centerline.

### 3.2 Optimization of the Model Parameters

It is clear from the previous section that the variation of the  $C_2$  parameter given in Eq. (2) does

not enhance the predictions of turbulent swirling recirculating flows, and it was decided to optimize the  $k$ - $\epsilon$  model constants for the flow under consideration. It was mentioned in Section 1 that only  $\sigma_k$  and  $\sigma_\epsilon$  were fixed earlier by computer optimization.<sup>5</sup> However, because of lack of the necessary experimental data,  $C_1$  and  $C_2$  were also optimized in this study. The constant  $\sigma_k$  was dropped from the optimization because of the feeling that the  $k$ -equation produces sufficient accuracy in determining the  $k$ -values. An effective optimization code is the Hill Algorithm. Reference 26 describes this method at length, in terms of its mathematical formulation and practical applications, and it need be described only briefly here. It is based on the direct search method proposed by Refs. 27 and 28. This method has proven effective in solving some problems where the variables are constrained. The procedure requires a starting point that satisfies the constraints and does not lie in the boundary zones. The effect of

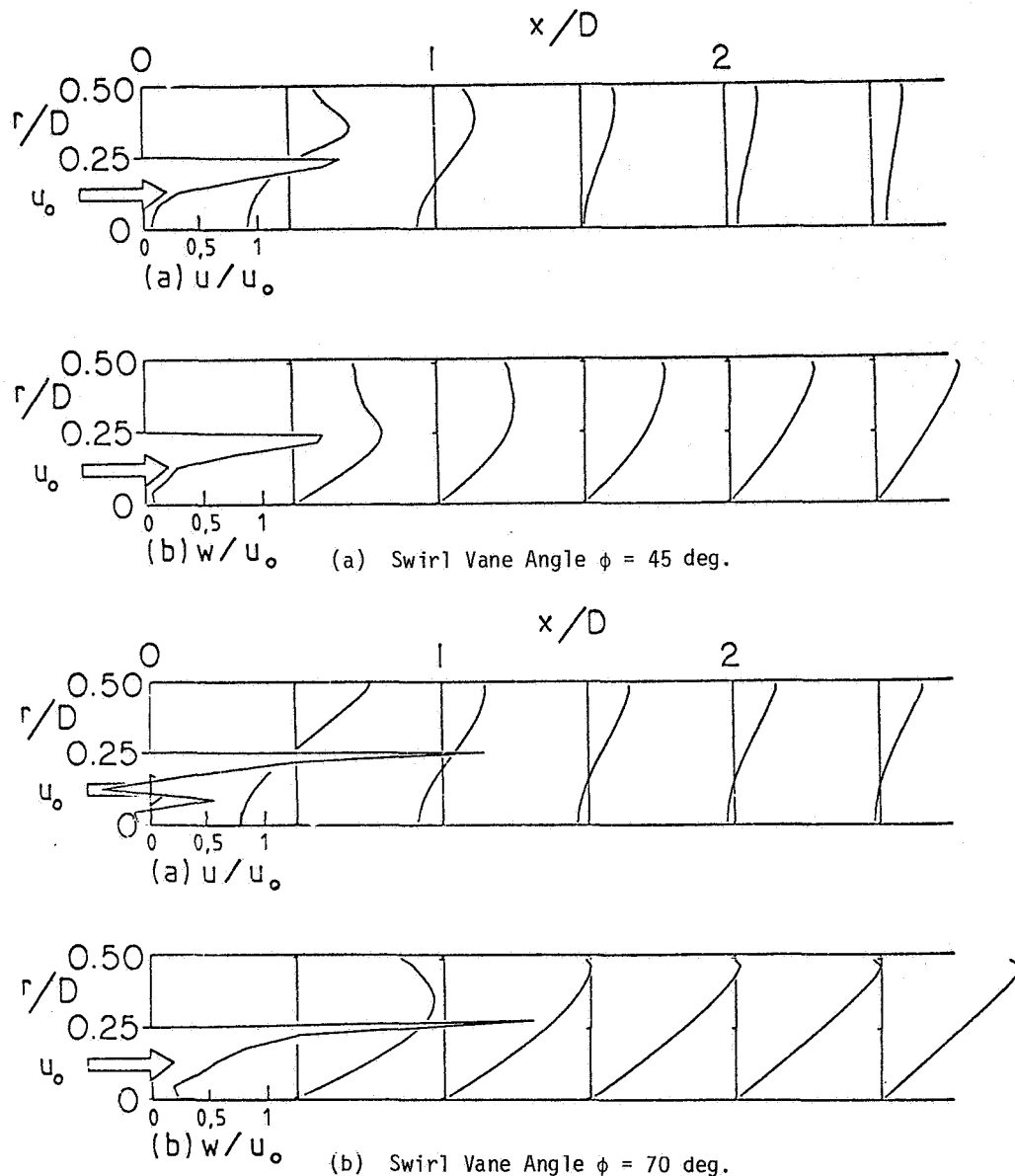


Fig. 2 Predicted Velocity Profiles Using the  $k-\epsilon$  Constants of Table 1

a small stepping in the first variable on the objective function is evaluated. If an improvement in the objective function were obtained without violating the boundary zones or constraints, the step size is reduced, and the direction of movement is reversed. The next variable is in turn stepped by a small distance parallel to the axis. The same acceleration or deceleration and reversal procedure is followed for all variables in consecutive repetitive sequences until the convergence criterion is satisfied.

The parameters  $C_1$ ,  $C_2$  and  $\sigma$  were optimized by minimizing the maximum absolute discrepancy between predicted axial and swirl velocity and the corresponding experimental values throughout the flowfield. The experimental data used are from recent five-hole pitot probe surveys of the flowfield.<sup>23</sup> The optimum constants were obtained by an iterative computer procedure; the velocity fields, after the iteration limit was exceeded,

were compared with the experiments. Because of the rather large computing time that would have been required if the iteration was continued until the convergence criterion was fully achieved, only 80 iterations were performed during each optimization cycle, with current flowfield values taken as initial values for the next optimization cycle in each case. The  $k-\epsilon$  constants optimum values obtained after 20 optimization cycles were found to be only marginally dependent on swirl strength. The values obtained for this wide range of swirl strengths ( $\phi = 45$  to  $70$  deg.) are displayed in Table 4. It should be noted that these values are not as good as the Table 1 values in the prediction of nonswirling flows.

### 3.3 Predictions Using Optimized Parameters

The predicted velocity profiles for swirl vane angles of  $45$  and  $70$  degs. using Table 4 values of the optimized but constant values of the parameters

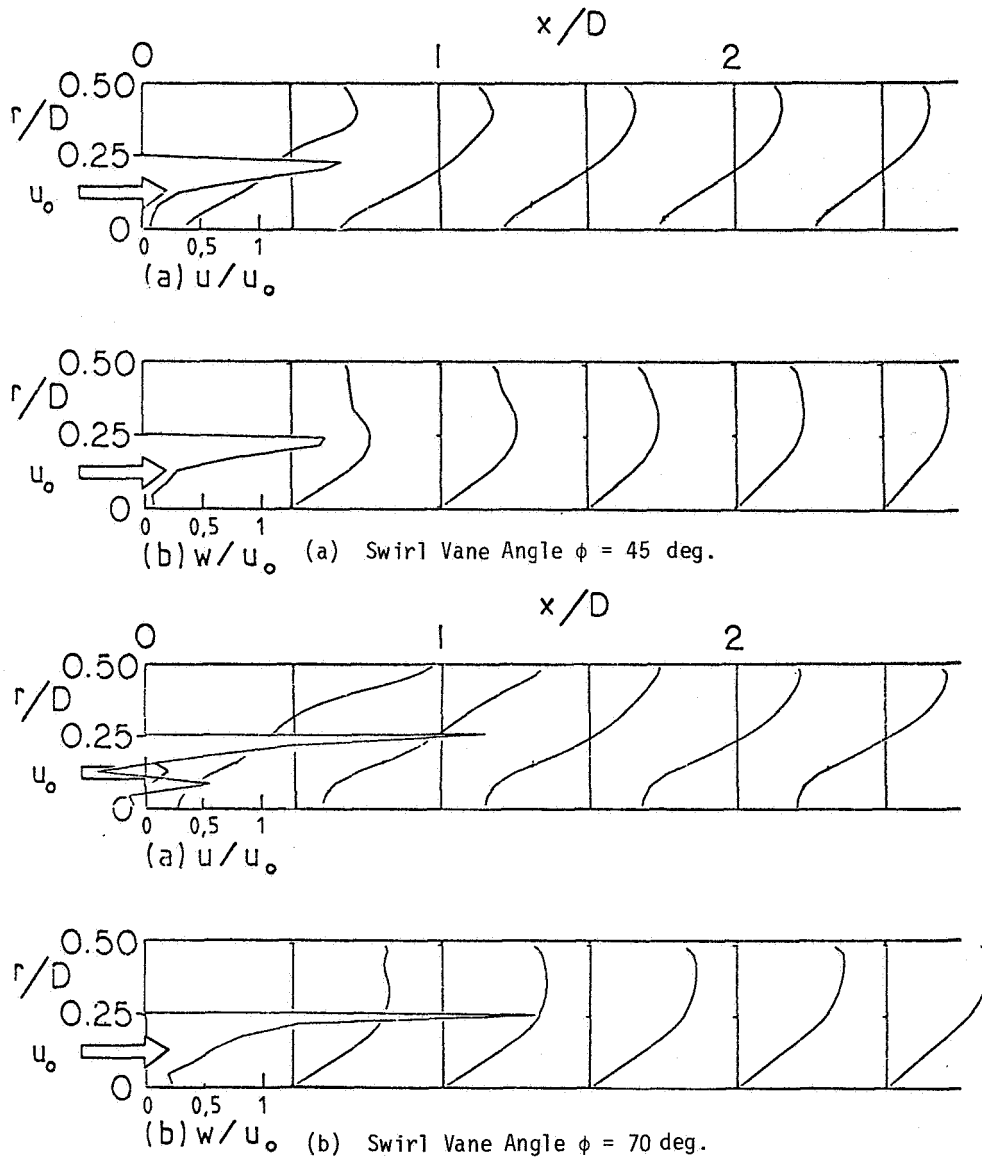


Fig. 3 Predicted Velocity Profiles Including Effect of Streamline Curvature via Eqs. (2) and (4)

$C_1$ ,  $C_2$  and  $\sigma_\epsilon$  are displayed in Figs. 4a and 4b, respectively. Comparisons with the corresponding Figs. 1a and 1b reveals very good agreement between the predicted results and the experimental data.

Figure 5 shows a comparison of the predicted central recirculation zone boundary using Table 1 (original  $k-\epsilon$  parameter values) and Table 4 (optimized parameter values) with corresponding data of Yoon and Lilley<sup>23</sup> and Jackson and Lilley.<sup>29</sup> The predicted central recirculation zone envelope using the Table 4 values is in very good agreement with the data, with a small discrepancy near the peak of the recirculation zone core. However, using Table 1 values produces a less realistic shorter central recirculation zone.

Figure 6 shows predicted centerline axial velocity longitudinal variation using the standard and modified  $k-\epsilon$  parameters, and compares them with measurements of Refs. 23 and 29. Notice that the

negative values are over-predicted in absolute magnitude -- a trend which was also found by others (Habib and Whitelaw<sup>10</sup> and Syed and Sturgess<sup>12</sup>) as reported in Section 2. Clearly the Table 4 values of the parameters provide a more satisfactory prediction than those of Table 1.

#### 4. Conclusions

An evaluation for the standard  $k-\epsilon$  model and its previously-available extensions as applied to different flow types has been presented. Neither the standard model nor its extensions show effective capability for predicting turbulent recirculating swirling flows. Recent experimental data on swirling confined flows, obtained with a five-hole pitot probe and a six-orientation hot-wire probe, are used to obtain optimum values of the turbulence parameters  $C_1$ ,  $C_2$ , and  $\sigma_\epsilon$  for swirling flows. General predictions of moderately and strongly swirling flows with these values are

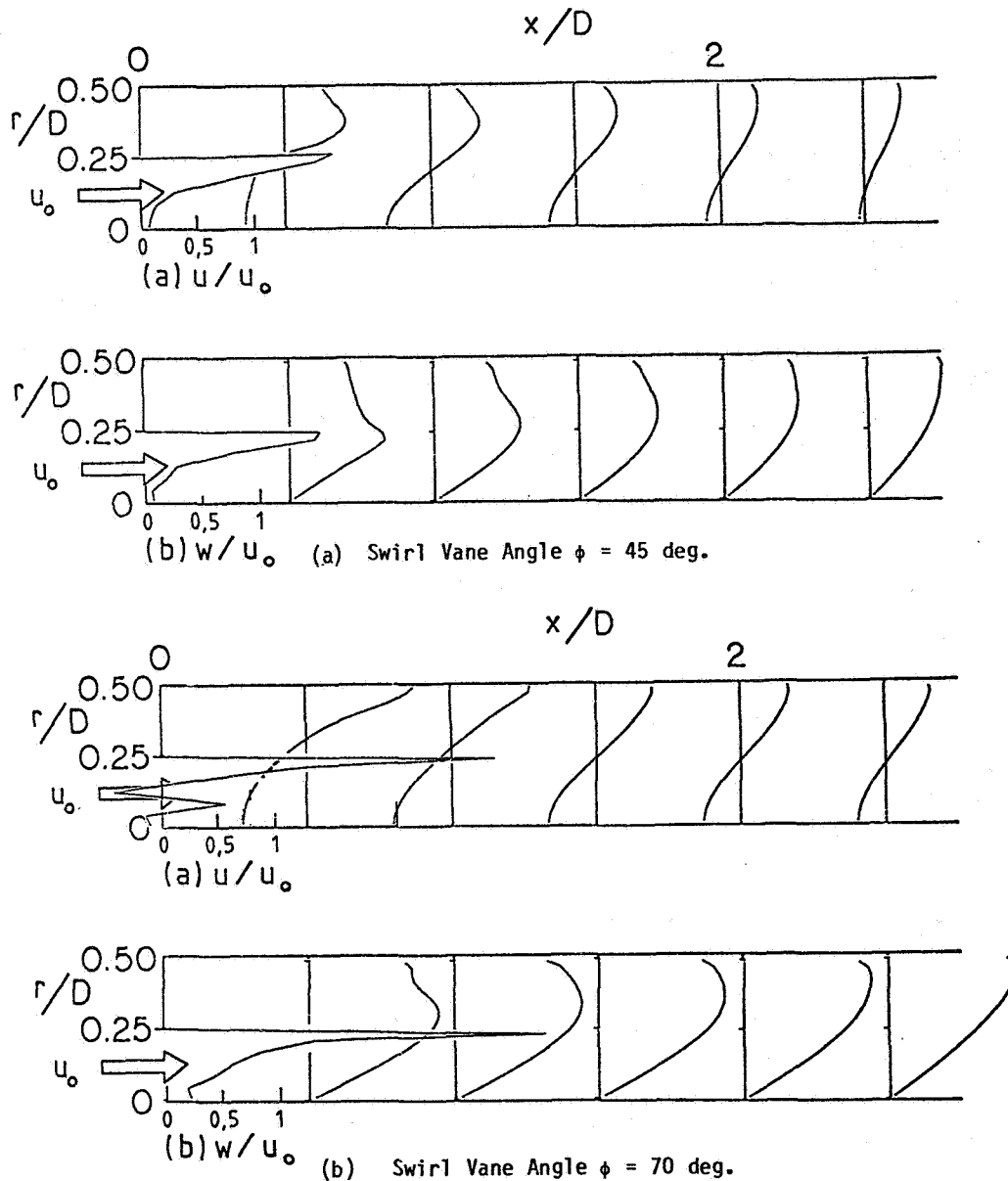


Fig. 4 Predicted Velocity Profiles Using the  $k-\epsilon$  Constants of Table 4

more accurate than predictions with the standard or previous simple extensions of the  $k-\epsilon$  turbulence model.

#### Acknowledgments

Special thanks are offered to NASA Lewis Research Center and Air Force Wright Aeronautical Laboratories for support via Grant No. NAG 3-74, technical monitor Dr. J. D. Holdeman.

#### References

1. Launder, B. E., and Spalding, D. B., "Mathematical Models of Turbulence", Academic Press, London and New York, 1972.
2. Moon, L. E., and Rudinger, G., "Velocity Distribution in the Abruptly Expanding Circular Duct", ASME J. of Fluids Engineering, Vol. 99, March 1977, pp. 226-230.
3. Ideriah, F. J. R., "Numerical Procedure for Calculating Partly Elliptic Flows", J. Mech. Engineering Sci., Vol. 21, 1978, pp. 372-380.
4. Green, A., and Whitelaw, J. H., "Measurements and Calculations of the Isothermal Flow in Axisymmetric Models of Combustor Geometries", J. Mech. Engineering Sci., Vol. 22, 1980, pp. 119-124.
5. Syed, S. A., and Sturgess, G. J., "Validation Studies of Turbulence and Combustion Models for Aircraft Gas Turbine Combustors", Momentum and Heat Transfer Processes in Recirculating Flows, HTD-Vol. 13, edited by Launder, B. E., and Humphrey, J. A. C., ASME, New York, 1980, pp. 71-89.
6. Abujelala, M. T., and Lilley, D. G., "Confined Swirling Flow Predictions", Paper AIAA-83-0316, Reno, Nevada, Jan. 10-13, 1983.

TABLE 2. DISTRIBUTION OF  $C_2$  VALUES OVER THE FLOW-FIELD OF  $\phi = 45$  DEG. USING EQS. (2) AND (4)

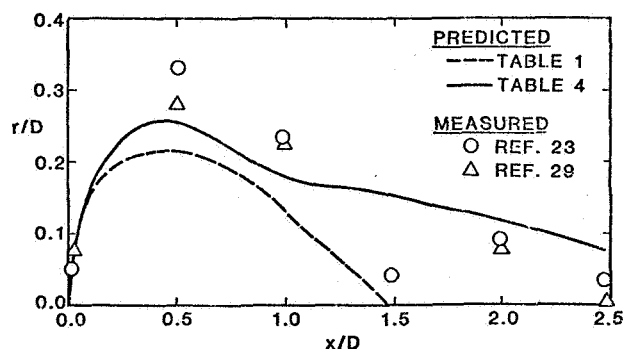
$r/D \backslash x/D$	0.03	0.33	0.53	1.08	1.93	2.50
0.495	1.60	1.91	1.91	1.91	1.91	1.90
0.448	1.92	1.82	1.71	1.78	1.89	1.63
0.406	1.92	1.56	1.56	1.92	1.85	1.38
0.365	1.96	1.56	1.81	1.88	1.72	1.34
0.328	1.99	1.84	1.95	1.78	1.56	1.10
0.275	1.87	1.91	1.83	1.59	1.54	1.51
0.243	1.80	1.68	1.39	1.07	0.98	0.86
0.175	1.81	0.10	0.51	1.16	1.19	1.25
0.085	1.62	1.07	1.11	1.24	1.28	1.35
0.013	1.69	1.86	1.86	1.86	1.86	1.87

TABLE 3. DISTRIBUTION OF  $C_2$  VALUES OVER THE FLOW-FIELD OF  $\phi = 70$  DEG. USING EQS. (2) AND (4)

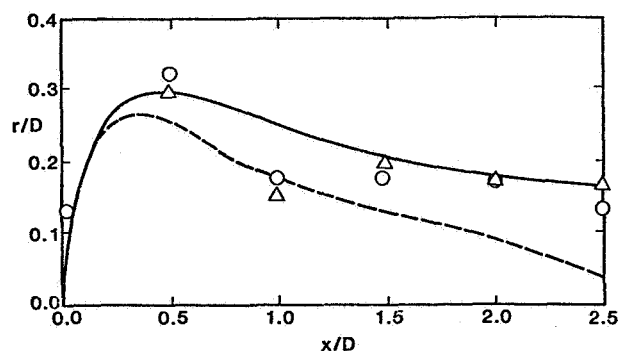
$r/D \backslash x/D$	0.03	0.33	0.53	1.08	1.93	2.50
0.495	1.84	1.91	1.91	1.91	1.90	1.90
0.448	1.90	1.88	1.88	1.86	1.74	1.44
0.406	1.91	1.90	1.89	1.78	1.58	1.08
0.365	1.90	1.88	1.86	1.68	1.48	1.19
0.328	1.94	1.57	1.59	1.31	1.01	0.74
0.275	1.89	1.33	1.44	1.46	1.45	1.54
0.243	1.49	0.34	0.30	0.57	0.72	0.94
0.175	1.81	0.83	0.88	1.16	1.26	1.29
0.085	--	--	--	0.29	0.15	--
0.013	1.87	1.88	1.87	1.87	1.87	1.88

7. Hanjalic, K., and Launder, B. E., "A Reynolds Stress Model of Turbulence and Its Application to Thin Shear Flows", J. Fluid Mech., Vol. 52, 1972, pp. 609-638.
8. Jones, W. P., and Launder, B. E., "The Prediction of Laminarization with a Two-Equation Model of Turbulence", Int. J. Heat Mass Transfer, Vol. 15, 1972, pp. 301-314.
9. Launder, B. E., and Spalding, D. B., "The Numerical Computation of Turbulent Flows", Computer Methods in Applied Mechanics and Engineering, Vol. 3, 1974, pp. 269-289.
10. Habib, M. A., and Whitelaw, J. H., "Velocity Characteristics of Confined Coaxial Jets With and Without Swirl", Transaction of the ASME, Journal of Fluids Engineering, Vol. 102, March 1980, pp. 47-53.
11. Gibson, M. M., "An Algebraic Stress and Heat-Flux Model Turbulent Shear Flow with Streamline Curvature", Int. J. Heat Mass Transfer, Vol. 21, 1978, pp. 1609-1617.

12. Syed, S. A., and Sturgess, G. J., "Velocity and Concentration Characteristics and Their Gross Correlations for Coaxial Jets in Confined Sudden Expansion. Part II: Predictions", Proceedings, ASME Symposium on Fluid Mechanics of Combustion Stress, Boulder, Colorado, June 22-23, 1981, pp. 145-160.
13. Whitelaw, H. J., and Green, A., "Measurements and Calculations of the Isothermal Flow in Axisymmetric Models of Combustor Geometries", J. Mech. Engineering Science, Vol. 22, 1980, pp. 117-124.
14. Sturgess, G. J., and Syed, S. A., "Widely-Spaced Co-axial Jet, Diffusion-Flame Combustor: Isothermal Flow Calculations Using the Two-Equation Turbulence Model", AIAA Paper No. 82-0113, Orlando, Florida, January 11-19, 1982.
15. Jones, W. P., and Launder, B. E., "The Calculation of Low Reynolds Number Phenomena with a Two-Equation Model of Turbulence", Int. Journal of Heat and Mass Transfer, Vol. 16, 1973, pp. 1119-1129.
16. Launder, B. E., Priddin, C. H., and Sharma, B. I., "The Calculation of Turbulence Boundary Layers on Spining and Curved Surfaces", Transactions of the ASME, J. of Fluids Engineering, Vol. 99, March 1977, pp. 231-238.



(a) Swirl Vane Angle  $\phi = 45$  deg.



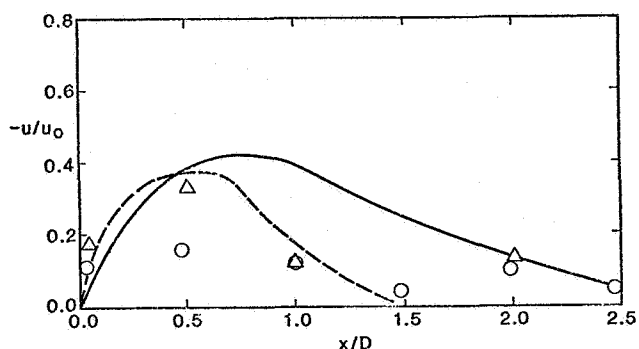
(b) Swirl Vane Angle  $\phi = 70$  deg.

Fig. 5 Central Recirculation Zone Envelope

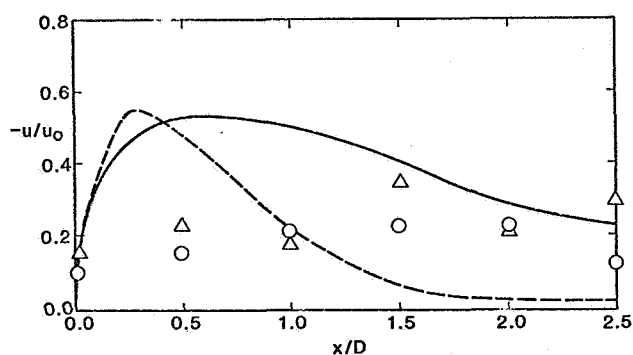


TABLE 4. THE OPTIMUM  $k$ - $\epsilon$  CONSTANTS FOR SWIRLING FLOWS

$c_\mu$	$c_1$	$c_2$	$\sigma_k$	$\sigma_\epsilon$
0.125	1.44	1.5942	1.0	1.1949



(a) Swirl Vane Angle  $\phi = 45$  deg.



(b) Swirl Vane Angle  $\phi = 70$  deg.

Fig. 6 Centerline Velocity Longitudinal Variation  
[Notation as in Fig. 5]

17. Durst, F., and Rostogi, A. R., "Theoretical and Experimental Investigations of Turbulent Flows with Separation", Turbulent Shear Flows (Durst, F., Launder, B. E., Schmidt, F. W., and Whitelaw, J. H., eds.), Springer-Verlag, Berlin Heidelberg, Germany, Vol. 1, 1973, pp. 205-219.
18. Ljuboja, M., and Rodi, W., "Calculation of Turbulent Wall Jets with an Algebraic Reynolds Stress Model", Transactions of the ASME, J. of Fluids Engineering, Vol. 102, Sept. 1980, pp. 351-356.
19. Hanjalic, K., and Launder, B. E., "Sensitizing the Dissipation Equation to Irrotational Strains", Transactions of the ASME, J. of Fluids Engineering, Vol. 102, March 1980, pp. 34-40.
20. Leschziner, M. A., and Rodi, W., "Calculation of Annular and Twin Parallel Jets Using Various Discretization Schemes and Turbulence

Model Variations", Transactions of the ASME, J. of Fluids Engineering, Vol. 103, June 1981, pp. 352-360.

21. Hanjalic, K., and Launder, B. E., "Preferential Spectral Transport by Irrotational Staining", Turbulent Boundary Layers, (Weber, H. E., ed.), ASME, New York, 1979, pp. 101-109.
22. Lam, C. K. G., and Bremhost, K., "A Modified Form of the  $k$ - $\epsilon$  Model for Predicting Wall Turbulence", Transactions of the ASME, J. of Fluids Engineering, Vol. 103, Sept. 1981, pp. 456-460.
23. Yoon, H. K., and Lilley, D. G., "Five-Hole Pitot Probe Time-Mean Velocity Measurements in Confined Swirling Flows", Paper AIAA 83-0315, Reno, Nevada, Jan. 10-13, 1983.
24. Lilley, D. G., and Rhode, D. L., "A Computer Code for Swirling Turbulent Axisymmetric Recirculating Flows in Practical Isothermal Combustor Geometries", NASA CR-3442, Feb. 1982.
25. Reynolds, M. C. So, "Turbulence Velocity Scales for Swirling Flows", Turbulence in Internal Flows (Murthy, S. N. B., ed.), Hemisphere Corp., Washington, 1976, pp. 347-369.
26. Kuester, J. L., and Mize, J. H., "Optimization Techniques with FORTRAN", McGraw-Hill Book Company, New York, 1973.
27. Rosenbrock, H. H., "An Automatic Method for Finding the Greatest or Least Value of a Function", Computer Journal, Vol. 3, 1980, pp. 175-184.
28. Rosenbrock, H. H., and Storcy, C., "Computational Technique for Chemical Engineers", Pergamon Press, New York, 1960.
29. Jackson, T. W., and Lilley, D. G., "Swirl Flow Turbulence Measurements Using a Single-Wire Technique", Paper AIAA-83-1202, Seattle, WA, June 27-29, 1983.
30. Sander, G. F., and Lilley, D. G., "The Performance of an Annular Vane Swirler", Paper AIAA-83-1326, Seattle, WA, June 27-29, 1983.

APPENDIX J

SWIRL FLOW TURBULENCE MODELING

(AIAA-84-1376)

## SWIRL FLOW TURBULENCE MODELING

M. T. Abujelala\*, T. W. Jackson\*, and D. G. Lilley\*\*  
Oklahoma State University  
Stillwater, Oklahoma 74078

### SUMMARY

Confined turbulent swirling flow data obtained from a single hot-wire using a six-orientation technique are analyzed numerically. The effects of swirl strength and the presence of a strong contraction nozzle further downstream on deduced parameters is also presented and discussed for the case of chamber-to-inlet diameter ratio  $D/d = 2$ . Three swirl strengths are considered with inlet swirl vane angles of 0, 45 and 70 deg. A strong contraction nozzle with an area ratio of 4 is located when needed two chamber-diameters downstream of the inlet to the flowfield. It is found that both the swirl strength and the contraction have strong effects on the turbulence parameters. Generally, the most dramatic effect of increase of swirl strength is the considerable increase in values of all the parameters considered - that is, increase in  $\rho x$ -viscosity, kinetic energy of turbulence, length scales, and degree of nonisotropy. The presence of a strong contraction nozzle tends to increase the turbulence parameter values in regions of acceleration and to reduce them in deceleration regions. Based on similarity of viscosity and length scale profiles, a  $C_v$ -formulation is deduced which is shown to improve the predictive capability of the standard  $k-\epsilon$  turbulence model in swirling recirculating flows.

### 1. INTRODUCTION

#### 1.1 Characteristics of Turbulent Swirling Flow

Turbulent swirling flows are of considerable practical importance. The degree of swirl is usually characterized by the ratio of axial fluxes of swirl momentum and axial momentum, as described at length in Refs. 1 through 3. Experimental and numerical studies<sup>2-6</sup> show that swirl has large-scale effects on turbulent flows: jet growth, entrainment, and decay and flame size, shape, stability, and combustion intensity are affected by the degree of swirl imparted to the flow. It is found that swirling jets spread more quickly and mean velocities decay more rapidly than in nonswirling jets. In duct flows, at high swirl strength, backflow can occur in the central region of the flow. This plays an important role in flame stabilization by providing a hot flow of recirculated combustion products and a reduced velocity region where flame speed and flow velocity can be matched.<sup>6</sup> It should be mentioned here that time-mean and turbulence characteristics of the swirling flow generated are generally affected by the way of imparting the swirl. The data to be given and discussed in this paper is appropriate to the particular facility<sup>2-5</sup> with variable-angle flat

blade swirler<sup>3</sup> at the inlet, although it may be expected that general trends in other situations will exhibit similar features.

#### 1.2 The Present Study

Multi-orientation of a single hot-wire is a novel way to measure the three time-mean velocities, the three turbulent normal stresses and the three turbulent shear stresses.<sup>5</sup> As part of a research program directed toward an understanding of the aerodynamics of the flow occurring in combustion chambers, the present study analyzes the data of Ref. 5, so as to provide details which assist in the development of advanced turbulence models for these complex flow situations. The data are for nonswirling and swirling flows (with inlet swirl vane angles of 0 (swirler removed), 45 and 70 deg.) in an axisymmetric test section with expansion ratio  $D/d = 2$ , which may be equipped with a contraction nozzle of area ratio  $A/a = 4$  located at  $L/D = 2$ .

## 2. MATHEMATICAL BACKGROUND

### 2.1 Turbulence Modeling

In solving the Reynolds equations for time-mean velocities, specification is required of the turbulent stresses, usually via the turbulent viscosity  $\mu_t$ . Although simple models are available for the specification of  $\mu_t$ , especially in boundary layer flows, for example, their validity is in doubt for swirling recirculating flows. Currently, two-equation models are popular in these circumstances. The present work emphasizes them in the context of swirling recirculating flows.

The two-equation turbulence model solves differential equations for the turbulence energy  $k$  and either the turbulence dissipation  $\epsilon = k^{3/2}/\lambda$  or the length scale  $\lambda$ . From these, the turbulent viscosity can be specified. First, auxiliary relations must be introduced to relate the double velocity correlations  $\overline{u_i u_j}$  to other known quantities. Usually, the Boussinesq eddy viscosity concept is used, which relates the Reynolds stresses to time-mean velocity gradients via (in Cartesian tensor notation)

$$-\rho \overline{u_i u_j} = \mu_t \left( \frac{\partial u_j}{\partial x_i} + \frac{\partial u_i}{\partial x_j} \right) - \frac{2}{3} \rho k \delta_{ij} \quad (1)$$

where  $\delta_{ij}$  is the Kronecker delta,  $\rho$  is the fluid density and  $\mu_t$  is the turbulent eddy viscosity which can be obtained from a two-equation turbulence model as:<sup>7</sup>

$$\mu_t = C_\mu \rho k^{1/2} \lambda \quad (2)$$

where  $C_\mu$  is a constant of value 0.09.

\* Graduate Student, School of Mechanical and Aerospace Engineering, Student Member AIAA

\*\* Professor, School of Mechanical and Aerospace Engineering, Associate Fellow AIAA

In cylindrical polar coordinates, assuming the flow is axisymmetric but allowing nonisotropy of the turbulent viscosity, Eq. (1) reduces to

$$\begin{aligned} -\rho \overline{u^2} &= 2 \mu_{xx} \frac{\partial u}{\partial x} - \frac{2}{3} \rho k \\ -\rho \overline{v^2} &= 2 \mu_{rr} \frac{\partial v}{\partial r} - \frac{2}{3} \rho k \\ -\rho \overline{w^2} &= 2 \mu_{\theta\theta} \frac{v}{r} - \frac{2}{3} \rho k \\ -\rho \overline{u v} &= \mu_{rx} \left( \frac{\partial u}{\partial r} + \frac{\partial v}{\partial x} \right) \\ -\rho \overline{u w} &= \mu_{x\theta} \frac{\partial w}{\partial x} \\ -\rho \overline{v w} &= \mu_{r\theta} r \frac{\partial}{\partial r} \left( \frac{w}{r} \right) \end{aligned} \quad (3)$$

## 2.2 Analytic Inverse Methods

Evaluation of the accuracy of a turbulence model may be obtained by comparing the predicted time-mean and turbulence values with experimental data. Alternatively, Eq. (3) may be used to make deductions directly from experimental data. Velocity gradients are calculated from experimental time-mean velocities using a suitable finite difference technique and relating these to appropriate measurements of Reynolds stresses via Eq. (3) allows the turbulent viscosity components to be deduced. Then Eq. (2) with measured  $k$ ,  $C = 0.09$  and  $\mu_t$  replaced by  $\mu_{rx}$  permits the turbulence length scale  $\lambda$  to be deduced. Values of  $\lambda_m$  are not presented in the present paper, but they are deduced and discussed in Ref. 11 (where  $\lambda_m$  is the Prandtl mixing length):

$$\begin{aligned} \mu_{rx} &= \rho \lambda_m^2 \left[ 2 \left( \frac{\partial u}{\partial x} \right)^2 + 2 \left( \frac{\partial v}{\partial r} \right)^2 + 2 \left( \frac{v}{r} \right)^2 + \left( \frac{\partial u}{\partial r} + \frac{\partial v}{\partial x} \right)^2 \right. \\ &\quad \left. + \left\{ r \frac{\partial}{\partial r} \left( \frac{w}{r} \right) \right\}^2 + \left( \frac{\partial w}{\partial x} \right)^2 \right]^{1/2} \end{aligned} \quad (4)$$

where Eq. (3) provides the value of  $\mu_{rx}$ .

In using Eqs. (3) and (4), lack of detailed time-mean velocity data in the axial direction has led to the axial derivative terms being dropped. In nonswirling and moderately swirling flows, they are usually small, except near recirculation zones. At high swirl, the central recirculation zone develops and this simplification cannot be faithfully invoked.<sup>9</sup> However, it will be only in quite small regions of the flow that errors of any significant magnitude might occur. In all swirl cases, the presence of the exit nozzle creates large radial vs. axial velocity gradients.

## 3. RESULTS AND DISCUSSION

### 3.1 Assumptions and Parameter Normalizations

Based on the available data, curves are usually fitted to the spatial distribution of measured time-mean values before further analytical manipulation, as effected in Ref. 11. However, in this study, the velocity gradients are calculated directly from the measured data. In any case, very similar trends and deductions emerge. The radial velocity gradients were determined analytically from the experimental data. The axial velocity

gradients were ignored because their values are considerably less than the radial gradient values in most flow situations studied here.

The turbulent viscosity was normalized with respect to the swirler inlet uniform axial velocity  $u_0$  (deduced independently from a measurement upstream of the swirler), fluid density and combustor diameter. The turbulence kinetic energy was normalized with respect to  $u_0^2$ . The length scale and mixing length were nondimensionalized with respect to the combustor diameter. The normalized values of the viscosity in the  $r$ - $x$  plane  $\mu_{rx}$ , the length scale and the kinetic energy are displayed in tables in Ref. 11. Also, the other viscosity components are tabulated as a fraction of  $\mu_{rx}$  values

$$\sigma_{ij} = \mu_{rx} / \mu_{ij}$$

and displayed among these tables. In the present paper, only the most important  $r\theta$  viscosity ratio  $\sigma_{r\theta}$  is presented in Tables 1 through 6. The turbulent viscosity  $\mu_{rx}$  and length scale  $\lambda$  are computer plotted and are shown in Figs. 1 through 6.

### 3.2 Effects of Swirl on Turbulence Parameters

The swirl vane angles  $\phi$  considered in this study are 0 (swirler removed), 45, and 70 deg. Part (a) of Figs. 1 through 3 displays the nondimensionalized turbulent viscosity  $\mu_{rx}$  and part (b) shows the normalized length scale  $\lambda$  as deduced from Eq. (2) with constant  $C = 0.09$  for  $\phi = 0, 45,$  and  $70$  deg., respectively, for the open-ended flow. It should be noted that the allowed maximum range of the values plotted in Figs. 1 through 3 was 2, and data beyond this range was assigned the range maximum values. The actual values of the affected points can be found in the tables.<sup>11</sup>

The  $\mu_{rx}$  profiles shown in part (a) of Figs 1 through 3 reveal that the  $\mu_{rx}$  values marginally increase as the swirl strength increases from zero to a moderate value and sharply increase beyond this range. Comparison of these figures with the mean velocity plots presented in Ref. 5 indicates that the peak of  $\mu_{rx}$  may or may not coincide with the peak of the velocity gradients. Inspection of part (b) of Figs. 1 through 3 shows that the normalized length scale profiles are almost similar to the corresponding  $\mu_{rx}$  profiles for each swirl case. This fact is exploited in Section 3.4 in turbulence model formulations.

Tables in Ref. 11 display the mixing length values obtained from Eq. (4), with the axial velocity gradients ignored, using the scattered data of Ref. 5. Comparison between these tables reveals that the mixing length values are slightly higher for swirl vane angle  $\phi$  of 45 deg. than for  $\phi = 0$  or 70 deg. However, the presented values for  $\phi = 0$  deg. are smaller than the corresponding ones for 70 deg. It is expected that these findings are due to the effect of swirling motion of the flow on the eddy size distribution. Other tables contrast the kinetic energy of turbulence distributions as the swirl strength increases. The tables show that results for moderate swirl are slightly higher than the corresponding ones for nonswirling flow. The most dramatic effect of swirl is seen at high swirl

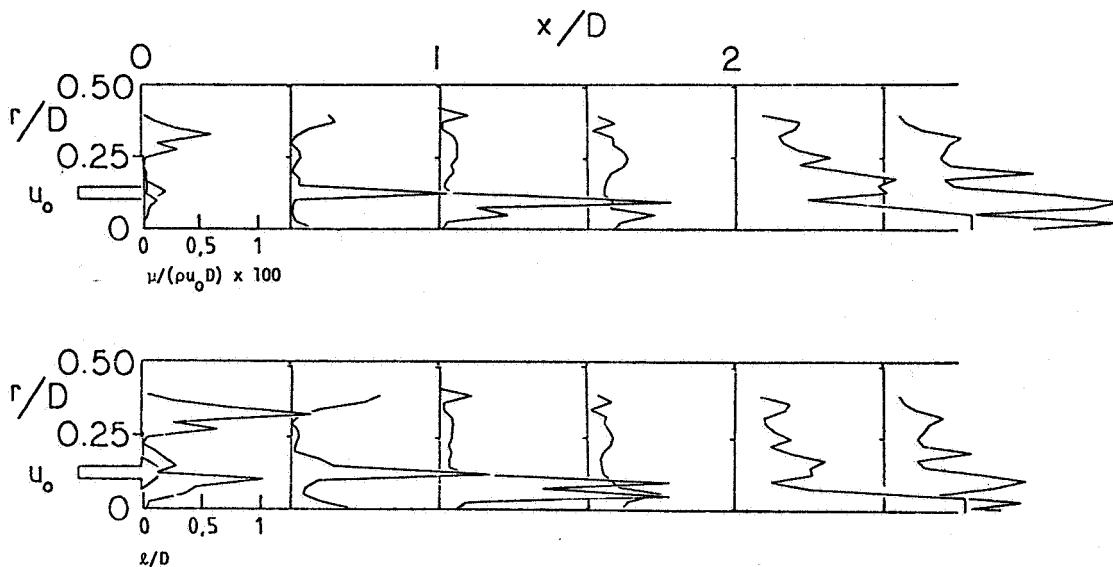


Fig. 1 Normalized  $u_{rx}$  and  $\lambda$  for Swirl Vane Angle  $\phi = 0$  deg.

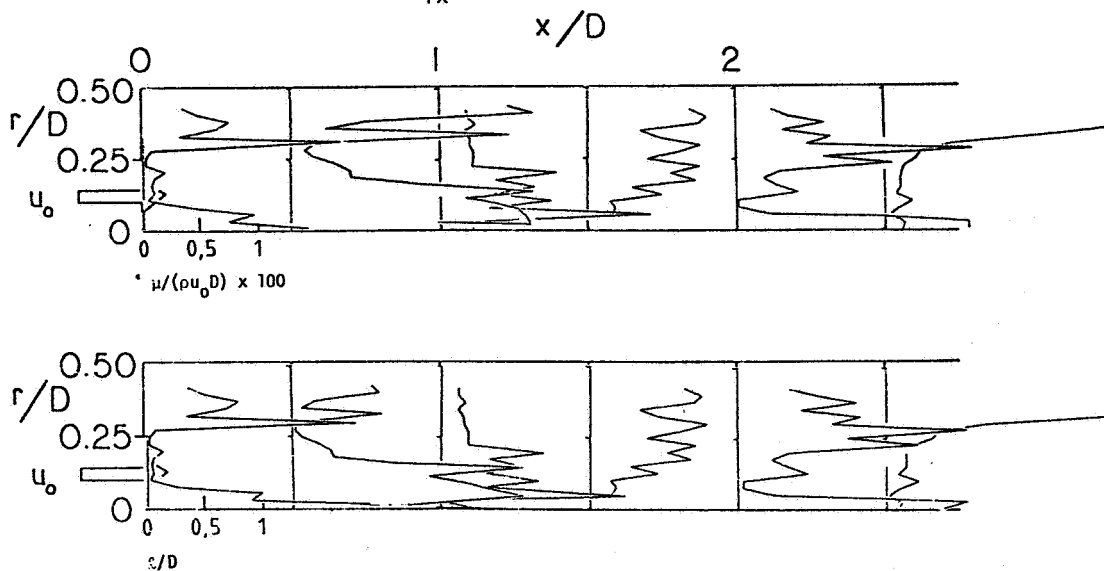


Fig. 2 Normalized  $u_{rx}$  and  $\lambda$  for Swirl Vane Angle  $\phi = 45$  deg.

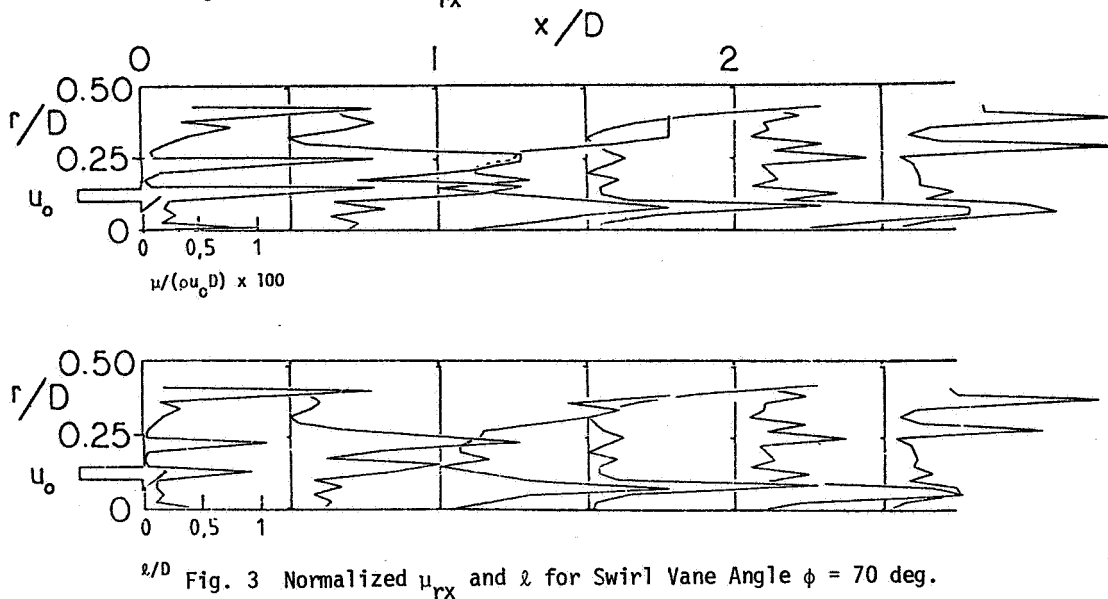


Fig. 3 Normalized  $u_{rx}$  and  $\lambda$  for Swirl Vane Angle  $\phi = 70$  deg.

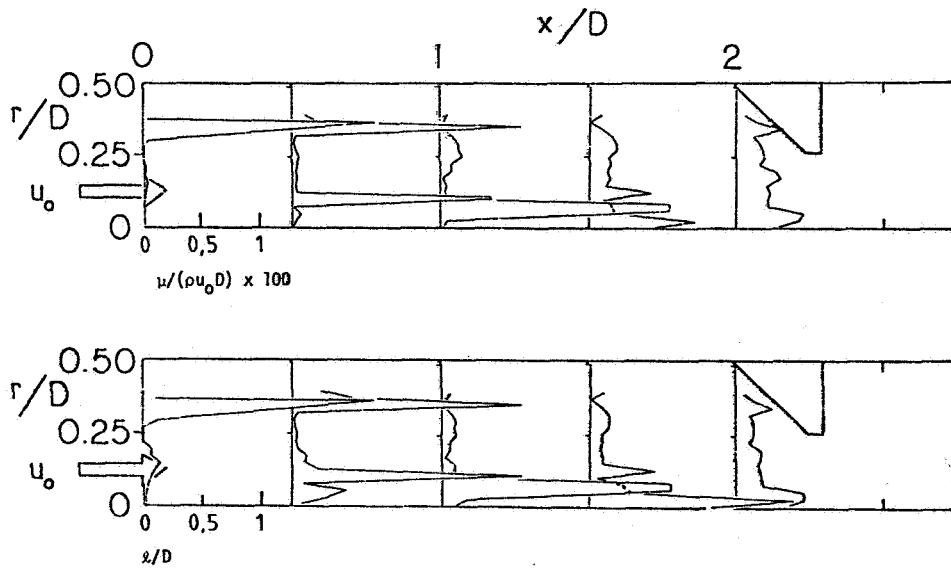


Fig. 4 Normalized  $u_{rx}$  and  $u_{\theta}$  for Swirl Vane Angle  $\phi = 0$  deg. with Strong Contraction Nozzle at  $L/D = 2$ .

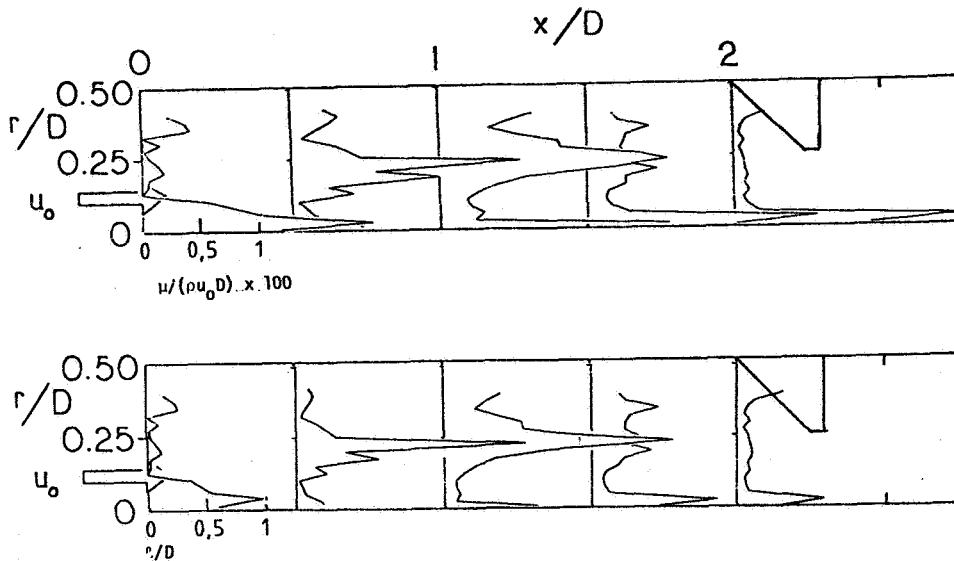


Fig. 5 Normalized  $u_{rx}$  and  $u_{\theta}$  for Swirl Vane Angle  $\phi = 45$  deg. with Strong Contraction Nozzle at  $L/D = 2$ .

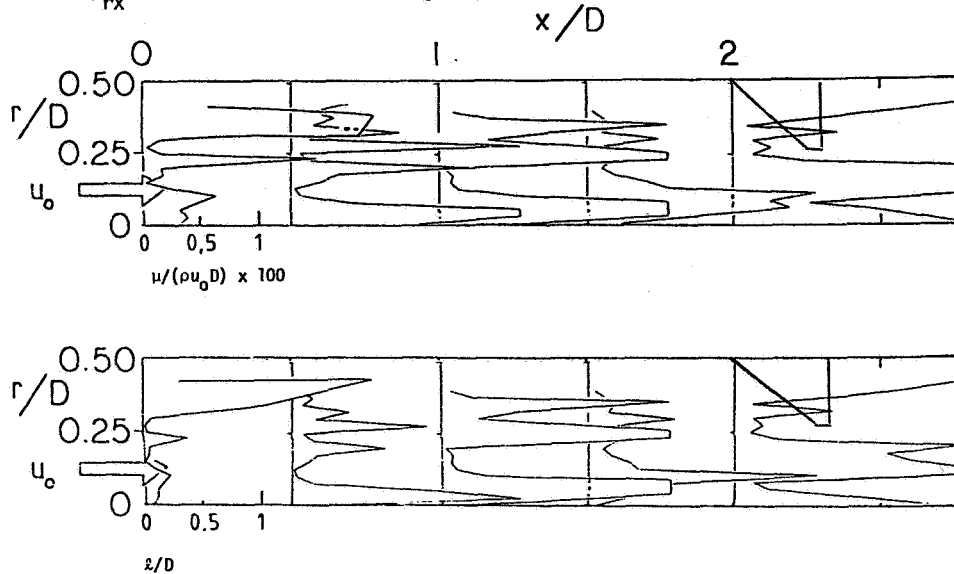


Fig. 6 Normalized  $u_{rx}$  and  $u_{\theta}$  for Swirl Vane Angle  $\phi = 70$  deg. with Strong Contraction Nozzle at  $L/D = 2$ .

values. The turbulence energy maximum values occur in regions of recirculation and regions of high stress.

The degree of nonisotropy has increased in magnitude, consistent with the increase in swirl strength throughout the entire flowfield, as can be seen in Tables 1 through 3 for the  $r\theta$  component, and elsewhere<sup>11</sup> for the other components. Also, it can be noticed that the  $rx$ -component of turbulent viscosity may be higher or lower than its corresponding value in the other planes depending on the location of the point in the flowfield.

Generally, the effect of increase of swirl strength is the considerable increase in all the turbulence parameters considered - that is, increase in  $rx$ -viscosity, kinetic energy of turbulence, length scales, and degrees of nonisotropy. The peak location of these parameters depends on the parameter under consideration. Overall, the swirl produces large-scale effects on turbulence parameters and, therefore, its effects should be considered in turbulence modeling.

### 3.3 Effects of Strong Contraction Nozzle on Turbulence Parameters

The normalized turbulent viscosity in the  $rx$ -plane and the length scale for swirl vane angles of 0, 45 and 70 deg., and with a strong contraction nozzle of area ratio 4 located at  $L/D = 2$  are presented in parts (a) and (b) of Figs. 4 through 6, respectively. The nozzle diameter is half the combustor diameter. Some of the plotted points were assigned the maximum values allowed if the normalized values were larger than 2. Actual values are included in the corresponding tables in Ref. 11, where the effect of the contraction nozzle on turbulence parameters is presented in tables. In the present paper, only the more important  $r\theta$  viscosity ratio  $\sigma_{r\theta}$  is exhibited. It is displayed in Tables 4 through 6.

Comparison between Figs. 4 through 6 and Figs. 1 through 3 reveals that the presence of the nozzle tends to increase the  $\mu_{rx}$  and  $\lambda$  values in the shear layers and to decrease them elsewhere. It is suggested that this is because of the high velocity gradients which are generated by accelerating the flow near the centerline as the exit is approached. The similarity between the profiles shown in parts (a) and (b) of Figs. 4 through 6 is also evident, as it was also in Figs. 1 through 3. Thus the presence of the nozzle does not affect the  $\mu_t$  vs  $\lambda$  relationship.

Tables elsewhere<sup>11</sup> show that the contraction nozzle generally changes the turbulence characteristics. This effect increases as the swirl strength increases. The nozzle tends to increase the mixing length and the kinetic energy in the region of recirculation, and to reduce their values near the wall. This is because the presence of a contraction nozzle accelerates the flow near the centerline and decelerates it close to a wall. A high degree of nonisotropy is seen with the presence of the nozzle and associated streamline curvature effects.

### 3.4 Proposed $C_\mu$ Formulation

An earlier study<sup>2</sup> made predictions of swirling confined flowfields using as inlet conditions time-

mean velocity data measured at the swirler exit.<sup>3</sup> A full range of swirler vane angles  $\phi$  from 0 to 70 deg. was considered. Results showed clearly that the effect of swirl and downstream contraction nozzles could be generally simulated, and justified the need to specify inlet boundary conditions very clearly. The STARPIC computer program<sup>10</sup> was used, with turbulence simulated via the standard  $k-\epsilon$  turbulence model.<sup>7</sup>

Later, the constants  $C_\mu$ ,  $C_2$  and  $\sigma_\epsilon$  were optimized via comparison of  $\mu$  predicted time-mean axial and swirl velocities with measured data.<sup>4</sup> Reference 12 describes the optimization procedure and presents the revised flowfield computations. Predictions using the same measured inlet data as before but with the new optimized constants yield superior results in terms of the time-mean quantities. This is especially evident in the predictions of general flow patterns and recirculation zone characterization.

In the present study, use can be made of the more detailed turbulence measurements which have been obtained using a six-orientation single-wire hot-wire technique.<sup>5</sup> The basic data include time-mean velocities, normal and shear Reynolds stresses in the same confined flow facility, for a full range of swirl strengths (with  $\phi$  from 0 to 70 deg.) and strong downstream contraction nozzle effects. Deduced data from the measurements have been presented partially in Figs. 1 through 6 of the present paper, with full details in Ref. 11.

Inspection of the nondimensionalized  $rx$ -viscosity  $\mu_{rx}$  and length scale  $\lambda$ , shown in Figs. 1 through 6 of the present paper, reveals a strong similarity between the radial profiles. That is

$$\mu_t / (\rho u_0 D)$$

is almost proportional to  $\lambda/D$ . Since

$$\mu_t = C_\mu \rho k^{1/2} \lambda$$

or equivalently

$$\mu_t / (\rho u_0 D) = (C_\mu k^{1/2} / u_0) (\lambda/D)$$

it follows that

$$C_\mu k^{1/2} / u_0$$

is approximately constant throughout the flowfield. That is:

$$C_\mu = A u_0 / k^{1/2} \quad (5)$$

where  $A$  is a constant independent of spatial position in the flow. Using an optimization procedure similar to that described in Ref. 12, optimal values of  $A$ ,  $C_2$  and  $\sigma_\epsilon$  have been deduced for the present situation. It was found that

$$\begin{aligned}
 A &= 0.0083 \\
 C_2 &= 1.804 \\
 \sigma_\epsilon &= 1.455
 \end{aligned}
 \tag{6}$$

The flowfields for inlet swirl vane angles of  $\phi = 45$  and  $70$  deg. have been predicted using the  $C_\mu$  variation as given by Eq. (5), with the optimized values of Eq. (6) used in this and other equations occurring in the simulation.

Tables 7 and 8 exhibit the values of predicted  $k$  and  $C_\mu$  obtained in this manner for corresponding inlet swirl vane angles of  $\phi = 45$  and  $70$  deg., respectively. Values vary throughout the flow domain. Flowfield predictions with this formulation are given in the next section.

### 3.5 Predictions and Assessment

The predicted velocity profiles for inlet swirl vane angles of  $0$ ,  $45$  and  $70$  deg. using the  $C_\mu$  formulation of Eq. (5) are given and compared with five-hole pitot probe experimental data<sup>4</sup> in Fig. 7. Inspection of this figure reveals that very good agreement between the predicted results and the experimental data has been achieved. Note that the measured inlet profiles are plotted at the  $x/D = 0$  location; in fact, these are actually the values measured immediately downstream of the swirler, at the location  $x/D = -0.11$ . It is convenient to retain these values on the profile plots in the prediction study, although clearly results at the  $x/D = 0$  location are then not directly comparable with the inlet station data of Ref. 4, which are taken precisely at  $x/D = 0$ . The discrepancies in the centerline velocity values at the peak of the central recirculation core are expected due to the assumption of axisymmetry at that location in the predictions.

For comparison purposes, Fig. 8 shows predictions using the standard  $k-\epsilon$  model for the same cases as in Fig. 7. The results in Fig. 8 indicate inaccurate predictions for the size and strength of the recirculation zone, when using the standard  $k-\epsilon$  model. However, predicted results using the  $C_\mu$  formulation exhibit very good agreement with experimental data, as seen in Fig. 7. Thus, it is clear that the proposed  $C_\mu$  formulation has provided superior results over the standard  $k-\epsilon$  model.

The predicted kinetic energy of turbulence,  $k$ , and its dissipation rate,  $\epsilon$ , using the standard  $k-\epsilon$  model of Eq. (2) with  $C_\mu = 0.09$  and the modified version of Eq. (5) are compared with the corresponding hot-wire data<sup>13</sup> for swirl vane angles  $45$  and  $70$  deg. as shown in Fig. 9. Both versions of the  $k-\epsilon$  model have provided qualitatively good predictions. The modified model shows closer predicted values of  $k$  and  $\epsilon$  to the experimental data (especially within the recirculation zone and far downstream of the inlet domain) than the standard model.

In summary, the  $C_\mu$  formulation of Eq. (5) provides better predictions of the time-mean and turbulence parameters than the standard model of Eq. (2) with  $C_\mu = 0.09$ . Also, the size of the

recirculation zone and the centerline velocity are quantitatively very well predicted by using this  $C_\mu$  formulation model as described in Section 3.4. Further predictions using this model for different flow geometries than considered here (with  $D/d = 1$  and  $1.5$  and exit contraction nozzle of area ratio  $A/a = 4$  located at  $L/D = 2$  for a range of swirl numbers) are given in a companion paper.<sup>14</sup>

## 4. CONCLUSIONS

The data of confined swirling flow obtained from a hot-wire using the six-orientation technique were numerically analyzed. The effects of swirl strength and a strong contraction nozzle on the turbulence parameters were found to have strong effects on the turbulence parameters. Generally, the most dramatic effect of the increase of swirl is the considerable increase in all the parameters considered - that is, in particular, increase of turbulent viscosity and kinetic energy. The presence of a strong contraction nozzle tends to increase the parameter values in regions of acceleration where large radial velocity gradients occur, and to reduce them in the deceleration region near the outer boundary.

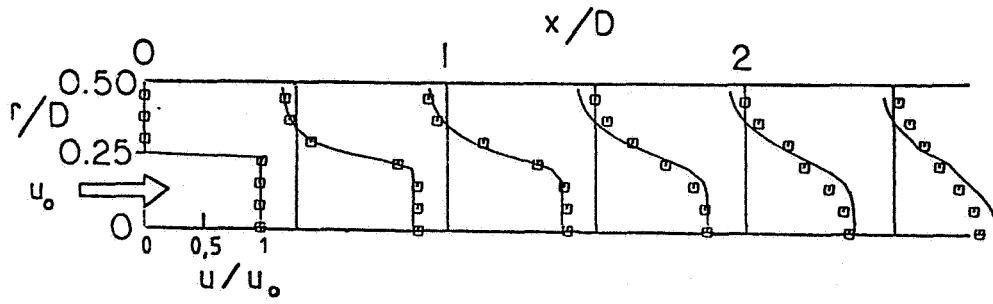
### ACKNOWLEDGMENT

The authors sincerely would like to thank NASA Lewis Research Center and Air Force Wright Aeronautical Laboratories for support via Grant No. NAG 3-74, technical monitor Dr. J. D. Holdeman.

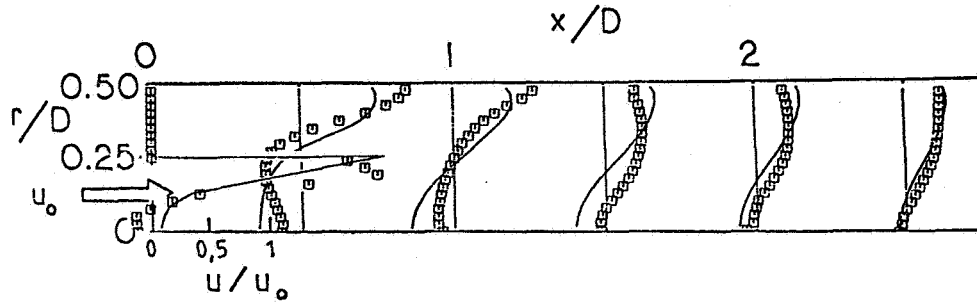
### REFERENCES

1. Beer, J. M., and Chigier, N. A., "Combustion Aerodynamics", Wiley, New York, 1972.
2. Abujelala, M. T., and Lilley, D. G., "Confined Swirling Flow Predictions", Paper AIAA 83-0316, Reno, Nevada, Jan. 10-13, 1983.
3. Sander, G. F., and Lilley, D. G., "The Performance of an Annular Vane Swirler", Paper AIAA 83-1326, Seattle, Wash., June 27-29, 1983.
4. Yoon, H. K., and Lilley, D. G., "Five-Hole Pitot Probe Time-Mean Velocity Measurements in Confined Swirling Flows", Paper AIAA 83-0315, Reno, Nevada, Jan. 10-13, 1983.
5. Jackson, T. W., and Lilley, D. G., "Single-Wire Swirl Flow Turbulence Measurements", Paper AIAA 83-1202, Seattle, Wash., June 27-29, 1983.
6. Lilley, D. G., "Swirl Flows in Combustion: A Review", AIAA Journal, Vol. 15, No. 8, August 1977, pp. 1063-1078.
7. Launder, B. E., and Spalding, D. B., "The Numerical Computation of Turbulent Flows", Comp. Method in Appl. Mech. and Engng., Vol. 3, March 1974, pp. 269-289.
8. Lilley, D. G., "Numerical Solution of Turbulent Swirling Flows", Computational Methods and Problems in Aeronautical Fluid Dynamics (B. L. Hewitt, et al., eds.), Academic Press, London, 1976, pp. 492-525.

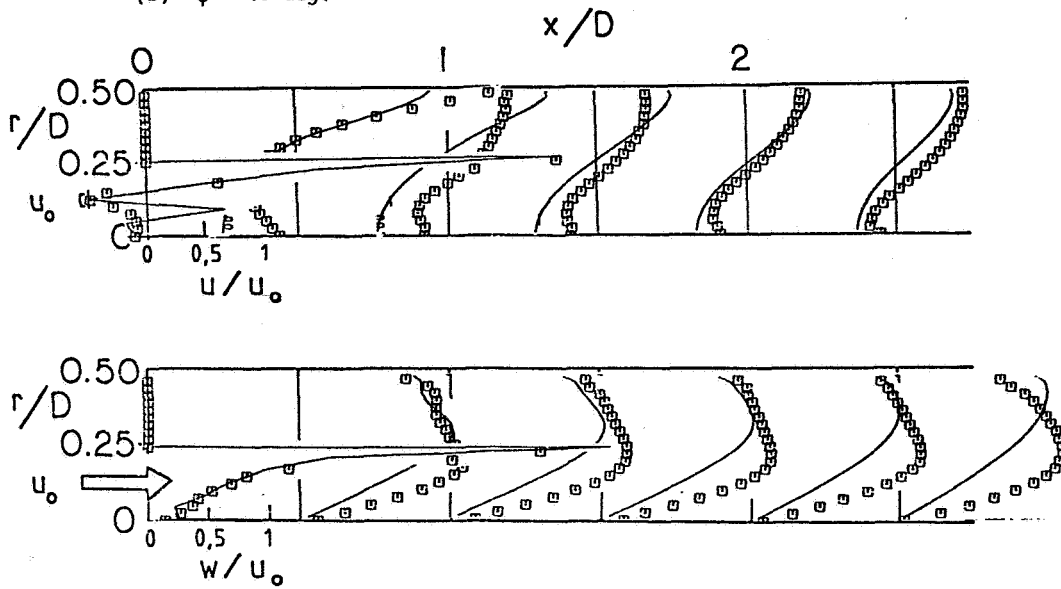




(a)  $\phi = 0$  deg.

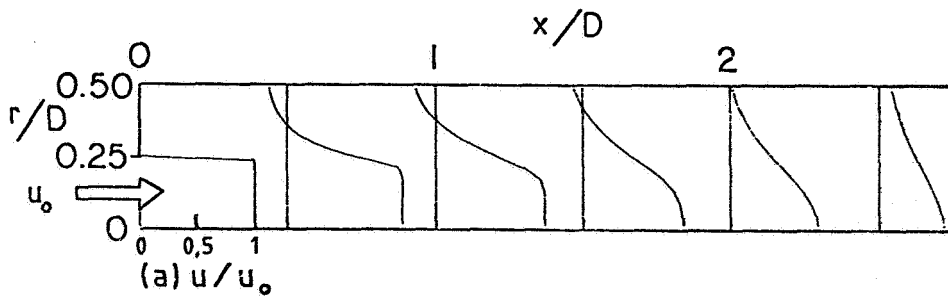


(b)  $\phi = 45$  deg.

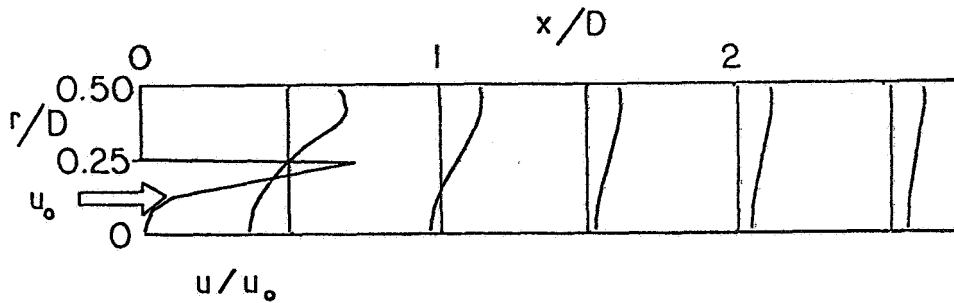


(c)  $\phi = 70$  deg.

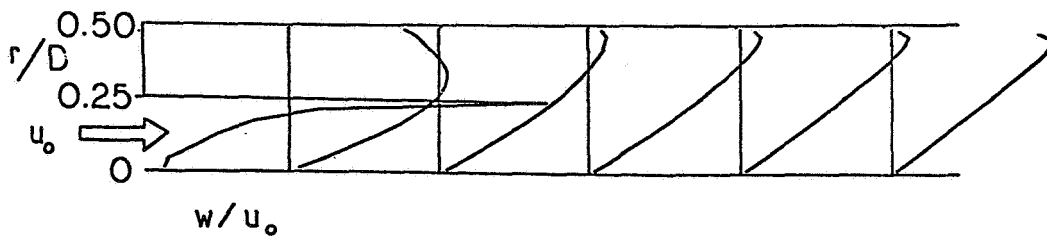
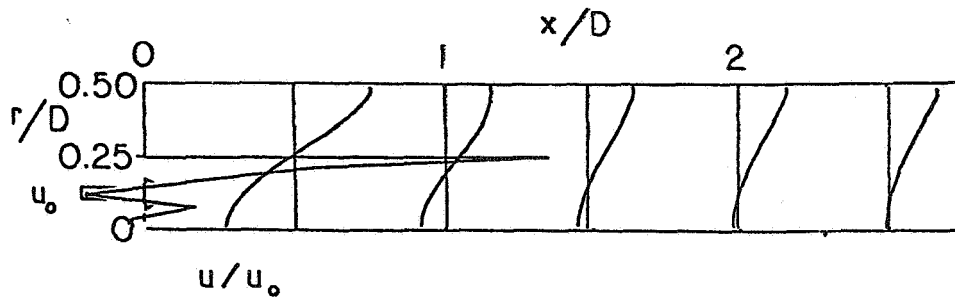
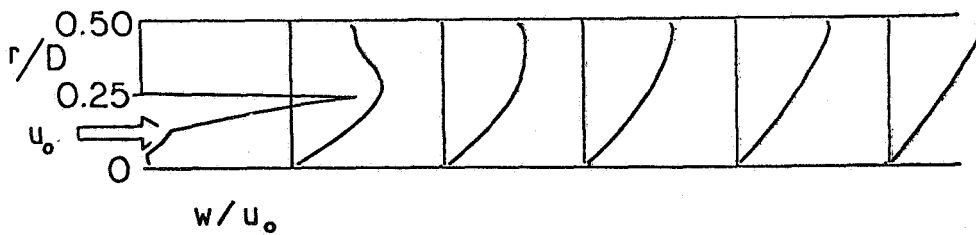
Fig. 7 Measured and Predicted Velocity Profiles Using Empirical Relation of Eq. (5) for  $C_u$   
 [□ Measured<sup>†</sup>, \_\_\_\_\_ Predicted]



(a)  $\phi = 0$  deg.

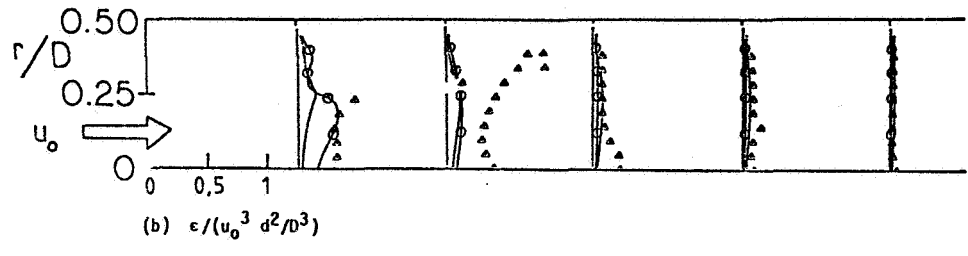
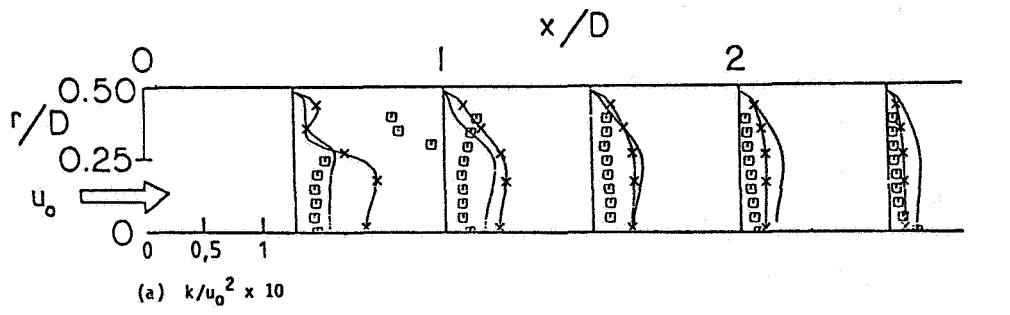


(b)  $\phi = 45$  deg.

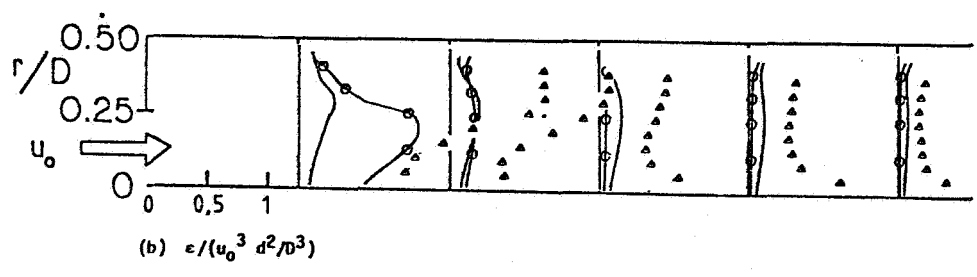
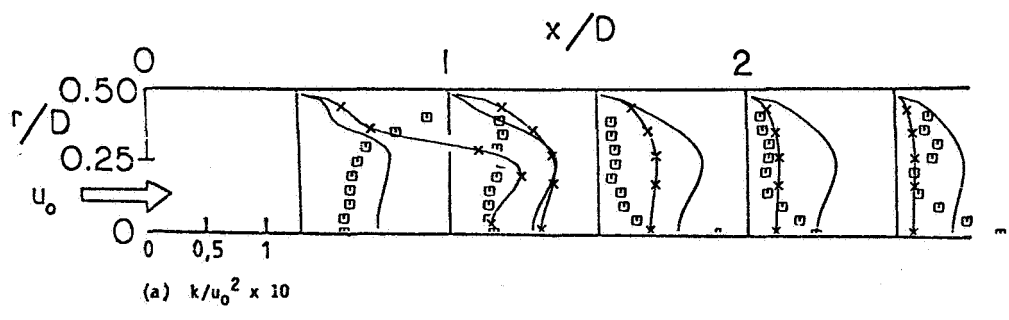


(c)  $\phi = 70$  deg.

Fig. 8 Predicted Velocity Profiles using Standard  $k-\epsilon$  Model of Eq. (2) with  $C_\mu = 0.09$



(a)  $\phi = 45 \text{ deg.}$



(b)  $\phi = 70 \text{ deg.}$

Fig. 9 Measured and Predicted Turbulence Parameters  
 [  $\square$  ,  $\Delta$  Ref. 5;  $\times$  o Eq. (2); \_\_\_\_\_ Eq. (5) ]

9. Lilley, D. G., "Analytical Inverse of the Turbulent Swirl Flow Boundary Layer Equations", Paper AIAA 75-856, Hartford, Conn., June 16-18, 1975.
10. Lilley, D. G., and Rhode, D. L., "A Computer Code for Swirling Turbulent Axisymmetric Recirculating Flows in Practical Isothermal Combustor Geometries", NASA CR-3442, Feb. 1982.
11. Abujelala, M. T., "Confined Turbulent Swirling Recirculating Flow Predictions", Ph.D. Thesis, Oklahoma State University, Stillwater, Okla., June 1984.
12. Abujelala, M. T., and Lilley, D. G., "Limitations and Empirical Extensions of the k-ε Model as Applied to Turbulent Confined Swirling Flows", Paper AIAA 84-0441, Reno, Nevada, Jan. 9-12, 1984.
13. Jackson, T. W., "Turbulence Characteristics of Swirling Flowfields", Ph.D. Thesis, Oklahoma State University, Stillwater, Okla., Dec. 1983.
14. Abujelala, M. T., and Lilley, D. G., "Swirl, Confinement and Nozzle Effects on Confined Turbulent Flow", Paper AIAA 84-1377, Cleveland, OH, June 11-13, 1984.

Table 1. Viscosity Ratio  $\sigma_{r\theta}$  for Swirl Vane Angle  $\phi = 0$  deg.

R/D	X/D					
	0.1	0.5	1.0	1.5	2.0	2.5
0.425	9.999	9.999	0.000	9.999	9.999	9.999
0.400	0.374	1.301	0.732	1.745	1.372	0.132
0.375	1.829	0.156	0.047	0.807	0.096	0.036
0.350	0.241	2.127	0.044	0.010	0.915	0.158
0.325	1.732	0.966	0.143	0.235	1.114	0.674
0.300	2.601	0.000	0.311	0.011	0.092	0.057
0.275	6.971	0.137	0.303	0.487	0.053	0.151
0.250	0.421	0.007	0.548	0.051	0.363	0.098
0.225	0.071	0.154	0.182	0.580	0.102	0.400
0.200	0.320	0.003	0.298	0.314	4.144	1.029
0.175	0.332	0.305	0.036	0.019	1.110	0.164
0.150	1.415	4.181	0.074	0.233	0.550	0.148
0.125	0.126	0.788	0.411	0.097	0.000	0.471
0.100	7.974	2.552	37.574	0.101	0.000	2.158
0.075	2.663	5.135	12.443	1.743	12.723	1.341
0.050	1.763	6.841	23.628	0.625	10.694	0.306
0.025	0.387	16.916	7.191	0.811	4.036	2.847
0.000	0.000	0.000	0.000	0.000	0.000	0.000

Table 2. Viscosity Ratio  $\sigma_{r\theta}$  for Swirl Vane Angle  $\phi = 45$  deg.

R/D	X/D					
	0.0	0.5	1.0	1.5	2.0	2.5
0.425	0.135	0.364	0.113	0.406	0.768	9.999
0.400	3.070	0.552	0.253	4.912	1.633	9.132
0.375	4.609	0.312	0.934	4.314	2.569	271.534
0.350	4.075	0.484	0.596	1.541	2.245	26.218
0.325	1.781	40.617	0.631	2.074	3.967	13.070
0.300	9.909	0.843	0.667	3.880	2.895	4.547
0.275	0.279	0.351	0.938	4.009	28.132	3.571
0.250	0.351	0.421	1.155	3.211	4.247	2.750
0.225	0.775	1.458	1.206	6.432	15.089	1.632
0.200	1.313	2.032	4.281	3.565	1.614	1.747
0.175	0.316	1.779	2.015	3.646	0.489	2.621
0.150	0.690	2.028	2.581	1.376	2.382	1.602
0.125	0.835	5.333	1.876	2.600	4.706	0.958
0.100	0.270	2.708	4.033	0.591	0.430	1.982
0.075	0.353	1.360	1.088	0.931	0.346	0.769
0.050	18.517	5.681	7.430	1.193	2.941	0.292
0.025	9.488	5.386	0.000	9.999	419.055	5.768
0.000	0.000	0.000	0.000	9.999	0.000	0.000

Table 3. Viscosity Ratio  $\sigma_{r\theta}$  for Swirl Vane Angle  $\phi = 70$  deg.

R/D	X/D					
	0.0	0.5	1.0	1.5	2.0	2.5
0.425	0.350	0.319	9.999	5.674	0.757	0.588
0.400	222.302	0.583	6.205	3.545	5.393	5.303
0.375	1.463	0.820	7.277	1.924	0.474	7.046
0.350	3.637	0.912	13.912	0.743	1.656	0.968
0.325	1.440	0.000	11.311	0.023	1.026	0.713
0.300	0.950	0.400	7.192	0.479	3.878	1.758
0.275	0.299	4.297	3.159	1.172	2.210	7.896
0.250	0.282	8.776	2.212	2.409	5.576	0.665
0.225	3.334	69.720	0.936	1.359	1.302	0.932
0.200	0.215	5.208	1.288	0.000	9.999	9.999
0.175	0.094	2.411	2.340	1.871	3.632	1.967
0.150	0.233	6.558	0.000	0.650	0.872	1.331
0.125	2.091	4.013	1.890	0.294	2.511	1.662
0.100	0.265	0.539	4.054	0.805	1.004	0.411
0.075	0.082	1.601	81.309	70.103	4.832	1.140
0.050	2.432	0.709	2.630	2.059	4.302	0.485
0.025	1.395	5.848	9.543	3.031	7.175	9.935
0.000	0.000	0.000	0.000	0.000	0.000	0.000

9.999 DATA POINT MEANS NO AVAILABLE DATA

Table 4. Viscosity Ratio  $\sigma_{r0}$  for Swirl Vane Angle  $\phi = 0$  deg.  
With Strong Contraction Nozzle at L/D = 2

R/D	x/D				
	0.0	0.5	1.0	1.5	2.0
0.400	9.999	2.131	0.247	0.629	0.016
0.375	0.125	0.215	0.126	0.008	0.331
0.350	46.231	48.069	0.000	0.037	2.426
0.325	9.999	0.069	0.433	0.001	0.082
0.300	0.394	0.117	3.815	0.159	0.032
0.275	0.000	0.081	0.065	0.217	0.022
0.250	0.016	0.105	0.273	0.071	0.084
0.225	0.005	0.018	0.048	0.100	0.040
0.200	0.256	0.026	0.094	0.011	0.017
0.175	0.157	0.049	0.185	0.076	0.001
0.150	0.152	0.283	0.329	0.006	0.373
0.125	0.260	3.254	0.479	0.000	0.251
0.100	0.290	330.426	0.583	0.004	0.120
0.075	0.105	0.068	21.971	0.110	0.119
0.050	1.240	3.058	69.654	0.375	2.087
0.025	0.080	4.901	1.136	5.176	1.582
0.000	0.000	0.000	0.000	0.000	0.000

Table 5. Viscosity Ratio  $\sigma_{r0}$  for Swirl Vane Angle  $\phi = 45$  deg.  
With Strong Contraction Nozzle at L/D = 2

R/D	x/D				
	0.0	0.5	1.0	1.5	2.0
0.425	9.999	0.613	9.999	9.999	9.999
0.400	0.397	0.248	0.052	0.961	1.419
0.375	1.322	0.066	2.017	1.536	2.145
0.350	1.638	0.525	1.184	5.052	1.198
0.325	0.000	0.400	1.937	3.695	1.376
0.300	0.412	0.929	5.672	3.866	2.546
0.275	0.165	1.112	5.840	3.735	1.177
0.250	0.612	1.796	8.877	6.015	2.268
0.225	2.227	14.873	50.120	5.041	3.612
0.200	0.768	3.287	10.551	8.585	3.702
0.175	0.570	7.811	5.295	6.749	4.206
0.150	0.611	2.050	3.645	13.067	2.533
0.125	0.000	2.708	2.296	2.909	4.141
0.100	1.444	0.195	1.755	1.842	1.462
0.075	9.999	0.296	0.735	0.838	2.196
0.050	4.498	0.407	0.106	0.386	2.071
0.025	22.104	0.465	0.151	1.478	4.600
0.000	0.000	0.000	0.000	0.000	0.000

Table 6. Viscosity Ratio  $\sigma_{r0}$  for Swirl Vane Angle  $\phi = 70$  deg.  
With Strong Contraction Nozzle at L/D = 2

R/D	x/D				
	0.0	0.5	1.0	1.5	2.0
0.425	0.136	0.640	9.999	9.999	5.416
0.400	36.696	0.578	0.173	0.032	35.588
0.375	9.999	0.899	2.221	3.843	23.618
0.350	9.999	0.600	89.058	1.782	5.635
0.325	14.824	6.956	7.446	5.300	22.153
0.300	1.159	3.203	5.184	13.683	5.863
0.275	0.198	13.998	9.999	6.725	6.568
0.250	0.629	3.869	245.115	23.098	3.924
0.225	2.663	19.628	951.871	7.210	6.639
0.200	0.228	49.839	0.968	3.192	57.832
0.175	0.070	8.606	2.837	8.631	21.741
0.150	0.039	4.295	4.013	9.512	20.289
0.125	1.008	2.725	4.183	8.784	71.770
0.100	3.907	0.798	6.883	16.116	5.235
0.075	2.765	2.194	28.953	2.076	0.586
0.050	2.481	10.205	17.453	5.924	2.039
0.025	2.820	8.428	27.849	5.731	9.999
0.000	0.000	0.000	0.000	0.000	0.000

9.999 DATA POINT MEANS NO AVAILABLE DATA

Table 7. Predicted Dimensionless Turbulence Energy and  $C_\mu$   
Distributions for Swirl Vane Angle  $\phi = 45$  deg.

(a)  $k/u_0^2$

R/D	x/D					
	-0	0.5	1.1	1.5	1.9	2.5
0.495	0.000	0.001	0.001	0.001	0.001	0.002
0.447	0.000	0.011	0.006	0.010	0.015	0.016
0.406	0.000	0.011	0.011	0.018	0.024	0.023
0.365	0.000	0.012	0.022	0.030	0.032	0.029
0.327	0.000	0.024	0.035	0.040	0.039	0.033
0.275	0.000	0.040	0.048	0.049	0.046	0.037
0.243	0.278	0.039	0.051	0.052	0.047	0.038
0.175	0.069	0.035	0.050	0.051	0.046	0.037
0.085	0.003	0.033	0.043	0.044	0.040	0.033
0.012	0.001	0.033	0.041	0.041	0.038	0.031

(b)  $C_\mu$

R/D	x/D					
	-0	0.5	1.1	1.5	1.9	2.5
0.495	0.000	0.217	0.268	0.262	0.224	0.209
0.447	0.000	0.079	0.106	0.085	0.067	0.065
0.406	0.000	0.079	0.078	0.062	0.054	0.055
0.365	0.000	0.072	0.056	0.048	0.046	0.049
0.327	0.000	0.053	0.044	0.042	0.042	0.046
0.275	0.000	0.042	0.038	0.038	0.039	0.043
0.243	0.016	0.042	0.037	0.037	0.038	0.043
0.175	0.032	0.044	0.037	0.037	0.039	0.043
0.085	0.146	0.046	0.040	0.040	0.042	0.046
0.012	0.365	0.046	0.041	0.041	0.043	0.047

Table 8. Predicted Dimensionless Turbulence Energy and  $C_\mu$   
Distributions for Swirl Vane Angle  $\phi = 70$  deg.

(a)  $k/u_0^2$

R/D	x/D					
	-0	0.5	1.1	1.5	1.9	2.5
0.495	0.000	0.006	0.004	0.005	0.006	0.006
0.447	0.000	0.036	0.034	0.048	0.055	0.049
0.406	0.000	0.043	0.063	0.076	0.078	0.065
0.365	0.000	0.066	0.096	0.102	0.097	0.079
0.327	0.000	0.096	0.118	0.120	0.110	0.088
0.275	0.000	0.115	0.134	0.134	0.121	0.095
0.243	0.893	0.114	0.136	0.135	0.122	0.097
0.175	0.044	0.109	0.128	0.128	0.116	0.093
0.085	0.017	0.100	0.112	0.110	0.100	0.082
0.012	0.003	0.098	0.105	0.103	0.094	0.077

(b)  $C_\mu$

R/D	x/D					
	-0	0.5	1.1	1.5	1.9	2.5
0.495	0.000	0.106	0.125	0.117	0.106	0.104
0.447	0.000	0.044	0.045	0.038	0.035	0.038
0.406	0.000	0.040	0.033	0.030	0.030	0.033
0.365	0.000	0.032	0.027	0.026	0.027	0.030
0.327	0.000	0.027	0.024	0.024	0.025	0.028
0.275	0.000	0.025	0.023	0.023	0.024	0.027
0.243	0.009	0.025	0.023	0.023	0.024	0.027
0.175	0.040	0.025	0.023	0.023	0.024	0.027
0.085	0.064	0.026	0.025	0.025	0.026	0.029
0.012	0.154	0.027	0.026	0.026	0.027	0.030

APPENDIX K

SWIRL, CONFINEMENT AND NOZZLE EFFECTS ON  
CONFINED TURBULENT FLOW

(AIAA-84-1377)

# SWIRL, CONFINEMENT AND NOZZLE EFFECTS ON CONFINED TURBULENT FLOW

M. T. Abujelala\* and D. G. Lilley\*\*  
Oklahoma State University  
Stillwater, Oklahoma 74078

## Abstract

Predictions of swirl, confinement and nozzle effects on confined turbulent flow are exhibited and compared with five-hole pitot-probe time-mean velocity measurements. Two sets of computations are given, one using the standard  $k-\epsilon$  turbulence model and the other using a  $C_u$  formulation model deduced from recent six-orientation single-wire hot-wire measurements. Results confirm that the accuracy of the latter model is superior. To highlight the effects of confinement and exit nozzle area on this flow, three expansion ratios and two contraction ratios are used. Predictions are given for a full range of swirl strengths using measured inlet conditions for axial, radial and swirl velocity profiles. The predicted velocity profiles illustrate the large-scale effects of inlet swirl on flowfields. It appears that a strong contraction nozzle has a pronounced effect, on swirl flow cases, with discouragement of central recirculation zones, and forward flow in highly swirled vortex core regions. The expansion ratio value has large-scale effects on the size and location of the recirculation zones.

## Nomenclature

A	Combustion chamber cross-sectional area
a	Downstream nozzle area
D	Combustion chamber diameter
d	Inlet nozzle diameter
k	Kinetic energy of turbulence
L	Location of contraction nozzle downstream of inlet domain
x	Downstream distance from domain inlet
$\epsilon$	Kinetic energy dissipation rate
$\phi$	Swirl vane angle

## 1. Introduction

### 1.1 Confinement Turbulent Swirling Flows

Confined turbulent swirling flows are of considerable practical importance. In heat generators, swirl is used to assist in the stabilization of the flame and to promote rapid mixing in combustion chambers and industrial furnaces. In heat transfer devices, the swirling motion increases the rate of heat transfer. These types of flow are characterized by strong streamline curvature, complex eddy structures and high turbulence intensities, particularly at high swirl strength. The practicality of this category of flows has commanded the need for the understanding of their characteristics.

The efforts of many researchers have provided accurate information about confined swirling flows. Some of the earlier studies were reviewed by Lilley.<sup>1</sup> Recently, Yoon and Lilley<sup>2</sup> and Jackson and Lilley<sup>3</sup> have provided experimental data for confined swirling flows resulting from the application of an upstream annular vane swirler with ten flat blades with constant pitch to chord ratio 0.68. A corresponding numerical study was conducted by Abujelala and Lilley.<sup>4</sup> These studies and others (see, for example, Refs. 5 through 9) show that swirl has large-scale effects on turbulent flows: jet growth, entrainment, and decay; and flame size, shape, stability, and combustion intensity being affected by the degree of swirl imparted to the flow. It is found that swirling jets spread more quickly and the mean velocities decay more rapidly than nonswirling jets. In duct flows, at high swirl strength, backflow can occur in the central region of the flow, and this plays an important role in flame stabilization. It produces a hot flow of recirculated combustion products and a low velocity region which can be matched with the flame speed.

### 1.2 Scope of the Present Study

The effects of inlet swirl strength (with inlet swirl vane angles  $\phi = 0$  (swirler removed), 45 and 70 deg.), confinement (with expansion ratios  $D/d = 1, 1.5$  and 2), and downstream nozzle (with area contraction ratios  $A/a = 2$  and 4) are investigated. The contraction nozzle is located at  $L/D = 2$  or  $L/D = 1$ , where  $L$  is the distance downstream of the inlet to the flow domain. In each case results are presented with the  $C_u$  formulation turbulence model in the main text; results with the standard  $k-\epsilon$  model are appended for completeness.

## 2. The Prediction Procedure

### 2.1. The Computer Code

The prediction procedure starts from partial differential equations of conservation of mass, momentum (in  $x, r$  and  $\theta$  directions), turbulent kinetic energy and its dissipation rate, which govern two-dimensional axisymmetric steady flow. The  $k-\epsilon$  model, with a  $C_u$  formulation obtained from relevant experimental<sup>10</sup> data as described by Abujelala et al,<sup>10</sup> is employed. The equations differ primarily in their final source terms. The corresponding finite difference equations are solved via an advanced version STARPIC<sup>11</sup> of the TEACH computer code,<sup>12</sup> using a semi-implicit line-by-line method for updating values at points of a variable size rectangular grid, with variable under-relaxation.

A complete description of the finally-developed computer program [with a full description of the equations, source terms, revised cell volumes for axial and radial velocities, constants occurring and techniques for handling turbulent

\* Graduate Student, School of Mechanical and Aerospace Engineering, Student Member AIAA

\*\* Professor, School of Mechanical and Aerospace Engineering, Associate Fellow AIAA



swirling flow near curved boundaries] is available.<sup>11</sup> Further, previous swirling flow measurements are incorporated as wall functions to avoid the expense of detailed computations within the boundary layer. The solution is obtained via an iterative procedure, with the desired variables being computed to convergence for sequential swirl vane angles of 0, 45 and 70 degrees. The convergence criterion in each case is that all normalized residual source sums are to be less than 0.009.

## 2.2 The Physical Domain

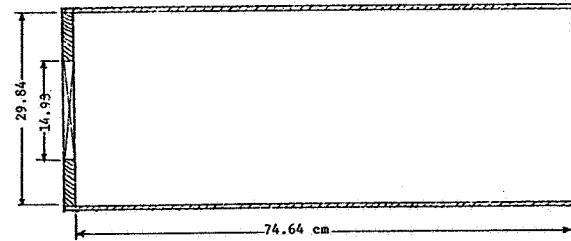
The physical domain is an axisymmetric test section with variable expansion ratio. This domain is selected to simulate combustion chambers of expansion ratios 2, 1.5 and 1 which may be equipped with a contraction nozzle of area ratio 2 or 4 located at  $L/D = 1$  or 2. A schematic of the physical domain, weak and strong nozzles, and typical grid system are shown in Fig. 1. The flow domain is covered with a  $23 \times 21$  nonuniform grid, which extends downstream up to a length of 4 times the combustion chamber diameter, as shown in Fig. 1 (d). The open ended flowfield with expansion ratios of 1.5 and 1 are covered by  $23 \times 15$  and  $23 \times 9$  nonuniform grid systems, respectively. It should be noted that the refinement of the grid was necessary only for highly and moderately expanding flow. The downstream contraction nozzle was simulated by the way of a stairstep approach that represents a 45 deg. slope; it is accommodated at  $L/D = 2$  by way of two steps, six cells each, in the radial direction. Even this relatively coarse subdivision enables useful predictions to be obtained.

## 2.3 Boundary Conditions

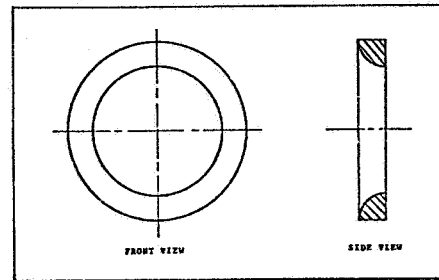
The inlet axial, radial and swirl velocity values were measured using the six-orientation, single hot-wire technique and used as inlet conditions for the computations. The data are very similar to corresponding five-hole pitot probe measurements.<sup>2</sup> The kinetic energy of turbulence  $k$  and its dissipation rate  $\epsilon$  are specified as in general accepted ways.<sup>11,13</sup> The total local time-mean velocity magnitude has been used in specifying  $k$  at any radial location of the domain inlet. The boundary conditions at the solid wall and centerline are as described by Lilley and Rhode.<sup>11</sup>

## 3. Results

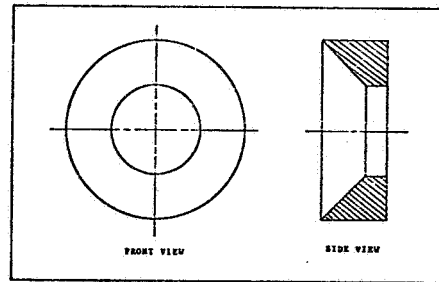
The effects of swirl strength, downstream contraction nozzle area and the degree of confinement on turbulent flows are presented in this section. In discussing the effects of swirl strength, the velocity field predictions for swirl vane angles of 0, 45 and 70 deg. are considered. Two area ratios are employed in the investigation of the influence of downstream contraction nozzle. Confinement effects are explored through inspection of the predicted flowfields for expansion ratios of 2, 1.5 and 1. As mentioned earlier, the predictions are obtained via the STARPIC computer code along with the modified C formulation version of the  $k-\epsilon$  model. Results are compared with corresponding experimental data of Refs. 2 and 14. The agreement is generally very good and better than would be seen were the standard  $k-\epsilon$  model used instead. For completeness, predictions with the standard model are appended.



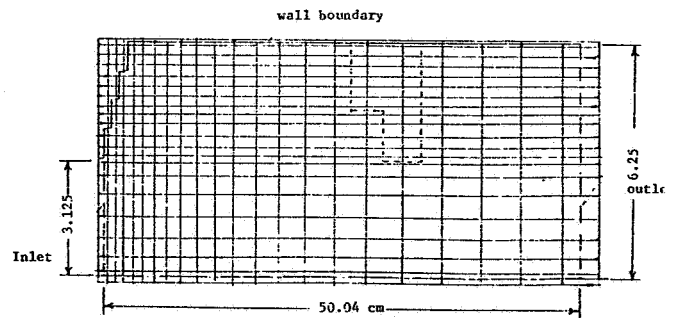
(a) Experimental Model



(b) The Weak Contraction Nozzle with Area Ratio 2



(c) The Strong Contraction Nozzle with Area Ratio 4

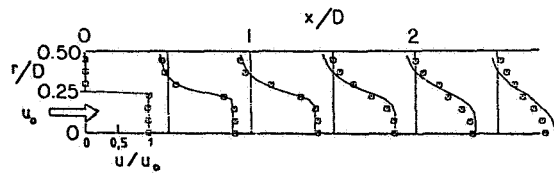


(d) Computer Model [--- Possible Nozzle Boundary]

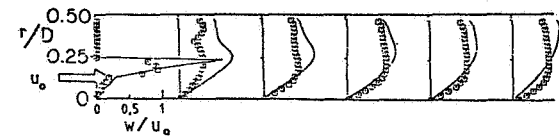
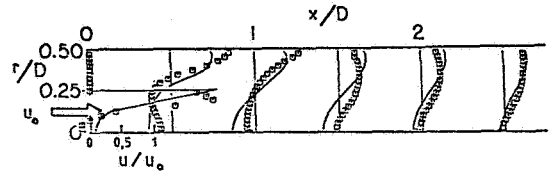
Fig. 1. Combustor Flowfield Simulation

### 3.1 Flowfield with $D/d = 2$

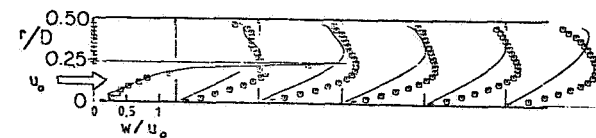
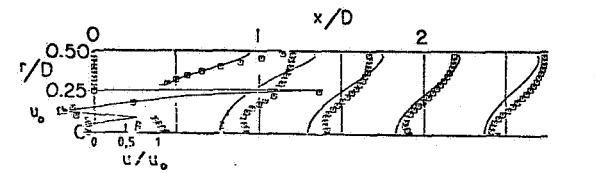
**Effects of Swirl Strength.** The effects of swirl strength on the flow pattern were investigated via a flow visualization technique, which uses neutrally-buoyant helium-filled soap bubbles, as shown in Ref. 14. To obtain



(a)  $\phi = 0$  deg.



(b)  $\phi = 45$  deg.



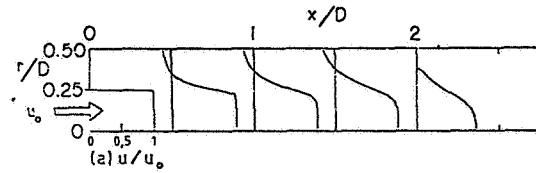
(c)  $\phi = 70$  deg.

[□ experimental data<sup>2</sup>]

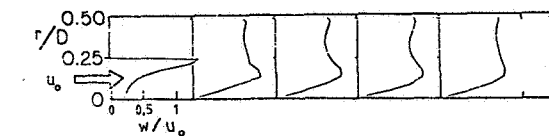
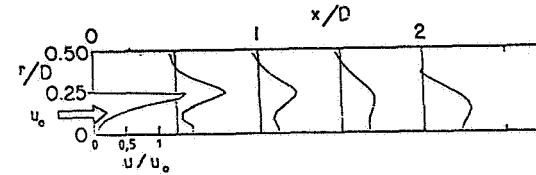
Fig. 2 Measured and Predicted Velocity Profiles for Flowfield with  $D/d = 2$

quantitative values, predictions were made for different swirl strengths. The velocity field predictions for swirl vane angles 0, 45, and 70 deg. are displayed in Parts (a) through (c) of Fig. 2, respectively, and compared with the experiental data.

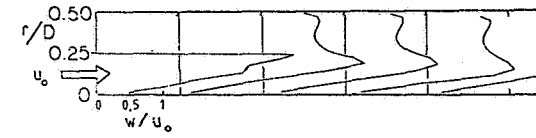
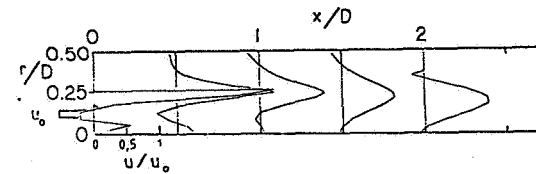
The predicted effects of swirl shown in this figure confirm in general the well-known ideas about swirl effects on axisymmetric turbulent confined jet flows. Under nonswirling conditions a large corner recirculation zone exists which extends approximately to  $x/D = 2.3$  for the expansion geometry  $D/d = 2$  and to  $x/D = 1.25$  for  $D/d = 1.43$ , see Refs. 15 and 16. Both these results are consistent with an attachment point about 8 step heights downstream of the expansion plane, as found by other researchers.<sup>2,17,18</sup> The centerline axial velocity changes gradually from its inlet value as downstream development occurs. However, as the degree of inlet swirl is increased to 45 deg., axial velocity profiles change dramatically. Near the inlet a central toroidal recirculation zone appears and the corner recirculation zone shortens considerably. Under strong swirl condition of  $\phi$  equal to 70 deg., a



(a)  $\phi = 0$  deg.



(b)  $\phi = 45$  deg.



(c)  $\phi = 70$  deg.

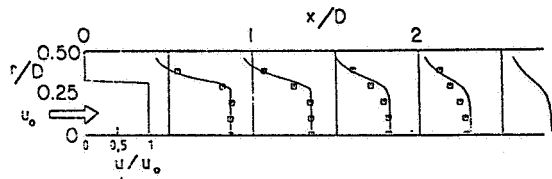
Fig. 3 Nozzle Velocity Profiles for Flowfield with  $D/d = 2$  and Strong Nozzle at  $L/D = 2$

much wider central recirculation region is established. It promotes a very large forward velocity near the confining walls rather than a corner recirculation region.

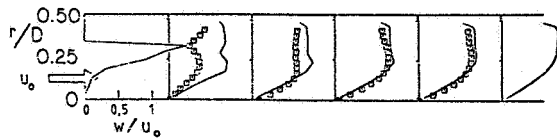
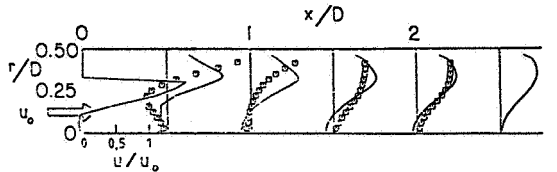
Generally, the following results can be drawn from Fig. 2:

1. The higher the swirl strength, the higher the centrifugal force, hence the larger the central recirculation zone core diameter;
2. The stronger the swirl strength, the longer the central zone extends downstream;
3. The corner recirculation zone size reduces sharply as swirl strength increases.

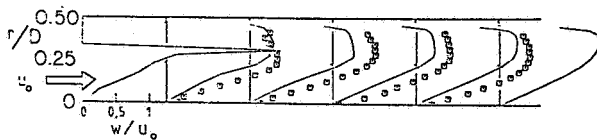
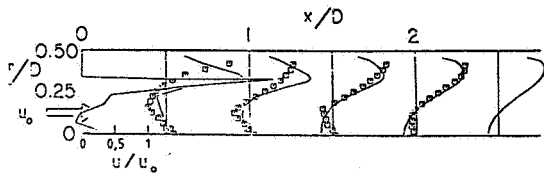
**Effect of Downstream Contraction Nozzle.** This section discusses the prediction of flowfields with a downstream contraction nozzle located at  $L/D = 1$  and 2 for nonswirling, moderate and strong swirl strengths, which correspond to swirl vane angles  $\phi = 0, 45$  and  $70$  deg., respectively. Two nozzles of area ratio 2 (weak) and 4 (strong) are being used. The weaker one has its upstream face contoured in a quarter circle; the stronger one has its upstream face in a 45 deg. slope. These are



(a)  $\phi = 0$  deg.



(b)  $\phi = 45$  deg.



(c)  $\phi = 70$  deg.

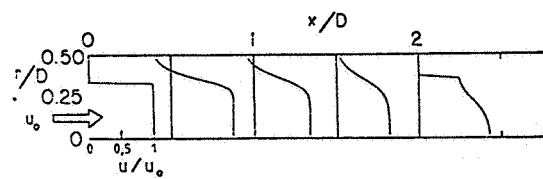
[  $\square$  experimental data<sup>21</sup> ]

Fig. 4 Measured and Predicted Velocity Profiles for Flowfield with  $D/d = 1.5$

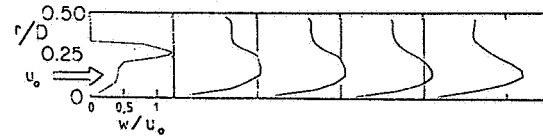
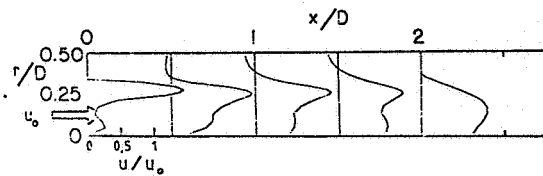
typical of exit nozzle for ramjet and gas turbine combustors, respectively, and shown schematically in Fig. 1.

The nozzle area ratio and location effects on the predicted flowfield, using the STARPIC computer code with the standard  $k-\epsilon$  model, were discussed at length by Abujelala and Lilley.<sup>4</sup> They reported that the weak nozzle produces minor effects on the predicted flowfield, especially at low swirl strengths and at high  $L/D$  value. In the present study, only the strong nozzle effects are explored numerically, with the nozzle located at the axial station 2 chamber diameters downstream of the inlet to the test section.

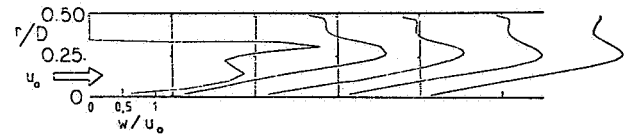
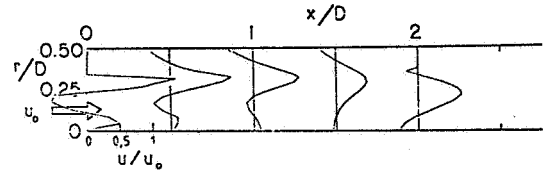
Under nonswirling conditions, the blockage effects are minimal at either nozzle location -- the central forward flow is accelerated and the large corner recirculation remains. Under intermediate and strong swirl conditions, however, the effects of the 4 to 1 area reduction are dramatic at either nozzle location. The corner recirculation zone is encouraged to occur. This is expected due to the grid size near the nozzle wall; the nozzle should accelerate the flow. The central



(a)  $\phi = 0$  deg.



(b)  $\phi = 45$  deg.

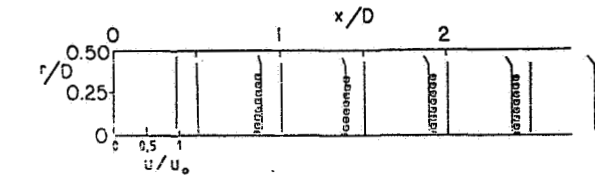


(c)  $\phi = 70$  deg.

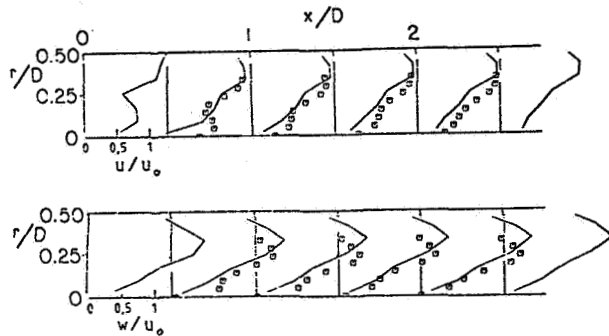
Fig. 5 Predicted Velocity Profiles for Flowfield with  $D/d = 1.5$  and Strong Nozzle at  $L/D = 2$

recirculation zone is removed, particularly for the moderate swirl strength, and a small annular recirculation zone is formed for the strong swirl flowfield, as also found experimentally,<sup>2,3</sup> and numerically.<sup>19</sup> These effects are seen in Parts (a) through (c) of Fig. 3 (with  $L/D = 2$ ) for swirl vane angles  $\phi = 0, 45$  and  $70$  deg. This figure shows axial and swirl velocity profiles and may be compared with the earlier Fig. 2 which was for the open-ended flowfield. The strong contractions also result in very large swirl velocity magnitudes and gradients in central core regions, which prevail throughout the flow domain for both moderate and strong swirl strengths.

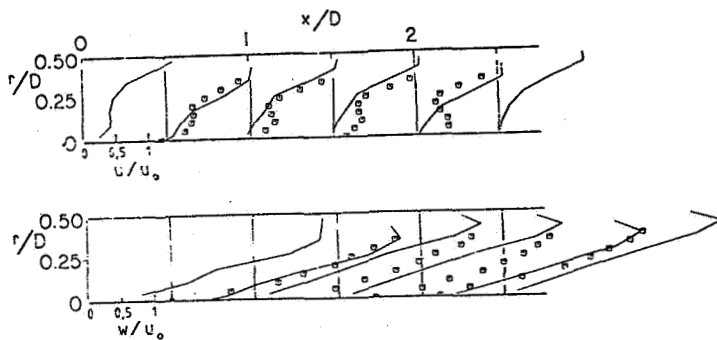
Generally, the predicted nozzle effects on the flowfield characteristics are in good agreement with the experimental data,<sup>2,3</sup> except the values just upstream of the nozzle obstacle; the predictions show a small corner recirculation zone. However, the experimental data display an accelerated flow near the wall. It is expected that better predictions will be obtained if the grid size is further refined, especially near the nozzle location.



(a)  $\phi = 0$  deg.



(b)  $\phi = 45$  deg.



(c)  $\phi = 70$  deg.

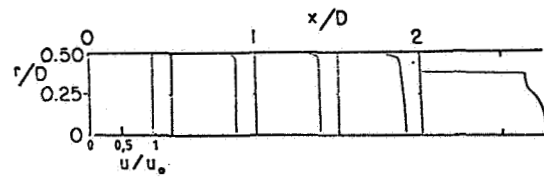
[  $\square$  experimental data<sup>21</sup> ]

Fig. 6 Measured and Predicted Velocity Profiles for Flowfield with  $D/d = 1$

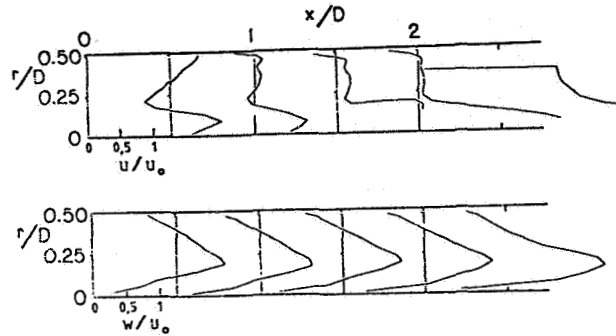
### 3.2 Flowfield with $D/d = 1.5$

**Effects of Swirl Strength.** The time-mean axial and swirl velocity profiles were predicted for nonswirling, moderate and strong swirl flows which corresponding to swirl vane angles of 0, 45 and 70 deg., respectively, as shown in Parts (a), (b) and (c) of Fig. 4. Inspection of this figure reveals that the size of the corner recirculation zone reduces and the central recirculation zone builds up as swirl strength increases. These observations are in accord with the results in Section 3.1, and compare well with the experimental data. The predicted axial and swirl velocity values are higher than the corresponding ones for the flowfield with  $D/d = 2$  as a result of the flow area reduction.

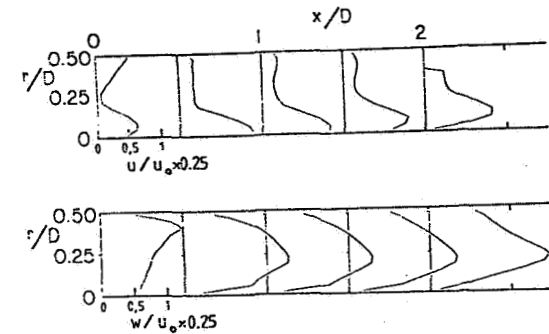
**Effects of Downstream Contraction Nozzle.** In these particular predictions, a contraction nozzle of area ratio 4 is located only at  $L/D = 2$  downstream of the inlet domain, since it is known<sup>2</sup> that the nozzle produces comparable effects at either one or two diameters downstream of the inlet. The predicted axial and swirl velocity profiles for swirl vane angles of 0, 45 and 70 deg.



(a)  $\phi = 0$  deg.



(b)  $\phi = 45$  deg.



(c)  $\phi = 70$  deg.

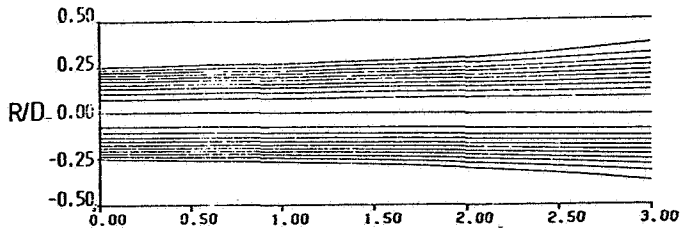
Fig. 7 Predicted Velocity Profiles for Flowfield with  $D/d = 1$  and Strong Nozzle at  $L/D = 2$

are displayed in Parts (a), (b) and (c) of Fig. 5, respectively.

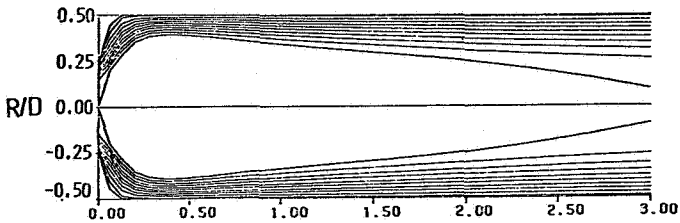
Comparison of the predicted velocity profiles displayed in Fig. 5 and the corresponding ones of Fig. 3 reveals that the presence of the nozzle produces effects similar to those reported in Section 3.1. However, the absolute velocity magnitudes are higher. The small central recirculation zone which appears in Fig. 3 (c) is not seen in Part (c) of Fig. 5, for the case of  $\phi = 70$  deg.

### 3.3 Flowfield with $D/d = 1$

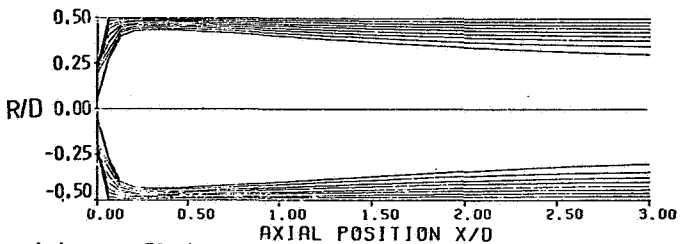
**Effects of Swirl Strength.** The previous sections describe a flowfield with an abrupt expansion. That flowfield has been found to be characterized by a complex flow with recirculation zones. This section discusses a flowfield that is found in a circular cross-sectioned duct flow without inlet expansion. The predicted results are computer plotted and displayed in Fig. 6, along with the experimental data. The agreement is satisfactory. Three swirl strengths vary from zero to strong swirl as described in Section 3.1 are shown in Parts (a), (b) and (c) of this figure. It shows no corner recirculation zone for nonswirling



(a)  $\phi = 0$  deg.

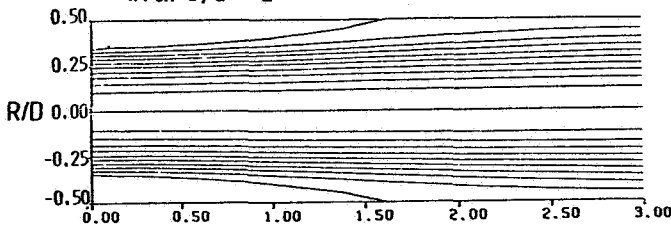


(b)  $\phi = 45$  deg.

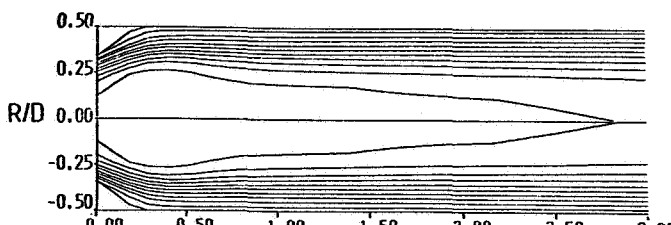


(c)  $\phi = 70$  deg.

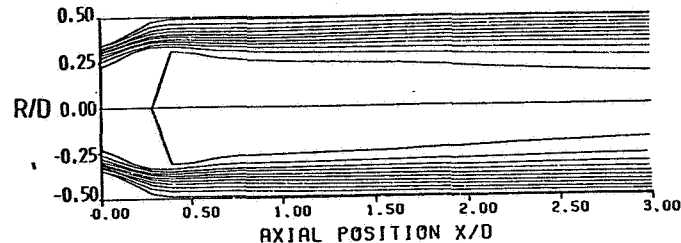
Fig. 8 Predicted Streamline Pattern for Flowfield with  $D/d = 2$



(a)  $\phi = 0$  deg.

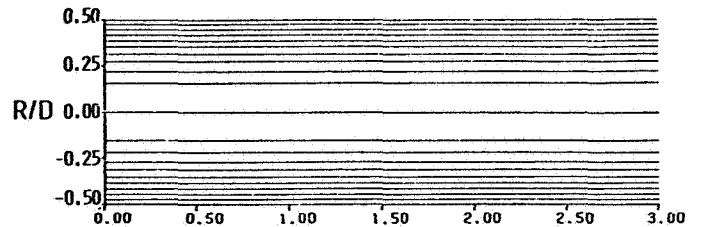


(b)  $\phi = 45$  deg.

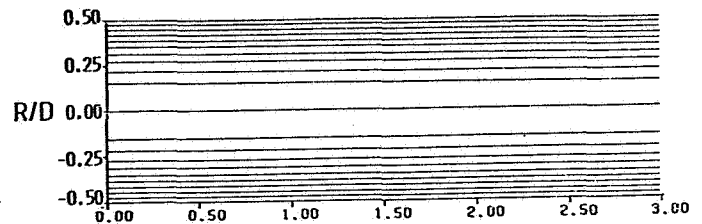


(c)  $\phi = 70$  deg.

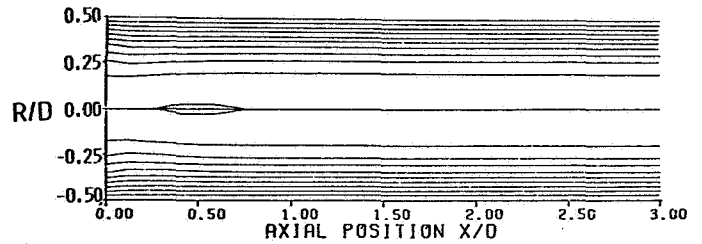
Fig. 9 Predicted Streamline Pattern for Flowfield with  $D/d = 1.5$



(a)  $\phi = 0$  deg.



(b)  $\phi = 45$  deg.



(c)  $\phi = 70$  deg.

Fig. 10 Predicted Streamline Pattern for Flowfield with  $D/d = 1$

and moderately swirling flows. However, the strongly swirling flow ( $\phi = 70$  deg.) shows a very small central recirculation zone close to the domain inlet. The aforementioned observations, extracted from the figure, are in accord with expectations, and information about the vortex breakdown phenomenon.<sup>20</sup>

**Effects of Downstream Contraction Nozzle.** The predictions presented in this section are similar to the ones of Sections 3.1 and 3.2, except that there is no flow expansion in the present case, and more uniform flow approaches the nozzle. The predicted profiles for time-mean axial and swirl velocity for swirl vane angles of 0, 45 and 70 deg. are displayed in Fig. 7. Inspection of this figure reveals that the general effects of the presence of the nozzle are again expected. The flow accelerates as the nozzle is approached. The central recirculation zone disappears, even at the highest swirl strength considered.

#### 3.4 Predictions with Standard $k-\epsilon$ Model

Previous predictions shown so far have been obtained with the C<sub>μ</sub> formulation model and general flow trends exhibited. How do these predictions compare with standard  $k-\epsilon$  model predictions? For the  $D/d = 2$  case, predictions were given in Ref. 4 for the open-ended flow and the flow with a strong nozzle at  $L/D = 2$ . These may be compared with Figs. 2 and 3, respectively, of the present paper. For completeness of the present paper, predictions with the standard  $k-\epsilon$  model for the open-ended and strong nozzle at  $L/D = 2$  are given

for the cases discussed in Sections 3.2 and 3.3, for different chamber diameters. The figures are appended. Results for  $D/d = 1.5$  are given in Figs. A1 and A2, and these may be compared with Figs. 4 and 5. Similar results for  $D/d = 1$  are given in Figs. A3 and A4, and these may be compared with Figs. 6 and 7.

#### 4. Summary and Discussion

##### 4.1. Effects of Expansion Ratio and Swirl Strength

Sections 3.1 through 3.4 have shown that the expansion ratio can considerably affect the aerodynamics (with corresponding effects on flame shape, heat transfer and stability limits), especially at high expansion ratio and high swirl strength. Both the corner and central recirculation zones are dramatically affected. The location of the top corner dividing streamline reattachment point is of particular interest.<sup>21-23</sup>

In this study three expansion ratios are considered: 2, 1.5, and 1. Computer plots of predicted streamline patterns using the C<sub>μ</sub> formulation model for each expansion ratio for 0, 45 and 70 deg. of swirl respectively, are displayed in Figs. 8, 9, and 10. Part (a) of these figures represent flowfield patterns for nonswirling flow, and Parts (b) and (c) show the streamline plot for  $\phi = 45$  and 70 deg., respectively.

Comparison between Part (a) of Figs. 8 through 10 reveals that the length of the corner recirculation zone (CRZ) increases almost linearly with expansion ratio. These figures show that the CRZ extends to about 3, 2 and 0 times the combustion chamber diameter for  $D/d = 2, 1.5$  and 1, respectively. These results are in accord with the finding of Back and Roschke,<sup>21</sup> who reported that the reattachment length should increase linearly with both Reynolds number and the dimensionless geometric ratio of step height and inlet nozzle diameter. In addition, the maximum reattachment length and the Reynolds number at which this occurs, depends on the type of inlet velocity profiles and on the flow geometry.<sup>23</sup>

Parts (b) and (c) of Figs. 8 through 10 show effects of the expansion ratio and swirl strengths on the width and length of the central recirculation zone. It is clear from inspection of these figures that the expansion ratio alters the streamline patterns of the flowfield. In the case of 45 deg. swirl, it seems that as the expansion ratio decreases, the beginning of the central recirculation zone moves further downstream of the inlet to the flow domain; as the expansion ratio approaches one, no recirculation zone occurs in the flow domain. However, the effects of reducing the expansion ratio on a  $\phi = 70$  deg. flowfield are seen to be that the central recirculation zone sharply reduces in size, becoming very small as the expansion ratio reduces to the nonexpanded case.

##### 4.2. Superiority of the C<sub>μ</sub> Formulation Model

Comparison of general time-mean velocity experimental data of Refs. 2 (for  $D/d = 2$ ) and 14 (for  $D/d = 1.5$  and 1), obtained using a five-hole pitot probe, indicate that the predictions using the proposed C<sub>μ</sub> formulation in Figs. 2 through 7 are superior to those using the standard  $k-\epsilon$  model, as shown in the Appendix and given in Ref. 4. This is especially true regarding the central

recirculation core diameter and length, and magnitudes of axial and swirl velocities.

#### 5. Closure

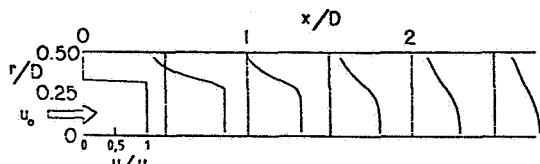
A numerical prediction using the  $k-\epsilon$  model, with a C<sub>μ</sub> formulation obtained from relevant experimental data, has been applied to a confined swirling flow. Predictions are given for a full range of swirl strengths using measured inlet axial, radial and swirl velocity profiles. The predicted velocity profiles illustrate the large-scale effects of inlet swirl on flowfields. Predictions are included for the effects of the presence of a strong downstream contraction nozzle and the expansion ratio on the flowfield. It appears that a strong nozzle has pronounced effects on swirl flow cases, with discouragement of central recirculation zones, and forward flow in highly swirled vortex core regions further downstream. The expansion ratio value has large-scale effects on the size and location of the recirculation zones.

#### Acknowledgments

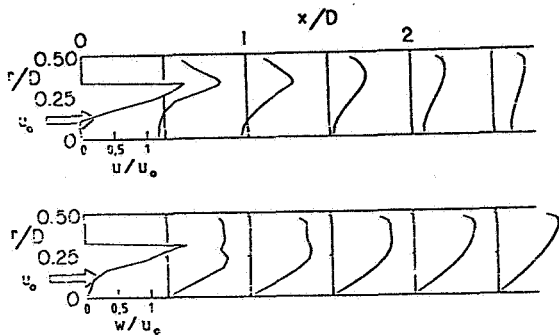
NASA Lewis Research Center and Air Force Wright Aeronautical Laboratories are to be thanked for their support under Grant No. NAG 3-74, technical monitor Dr. J. D. Holdeman.

#### References

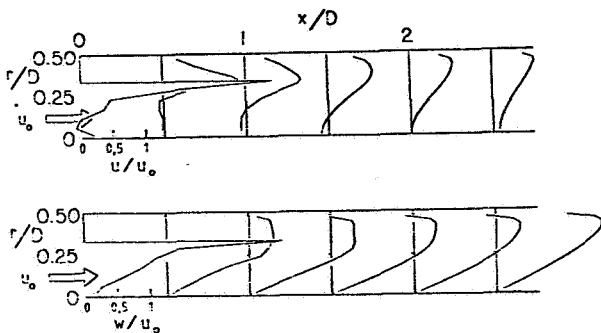
1. Lilley, D. G., "Swirl Flows in Combustion: A Review", AIAA Journal, Vol. 15, No. 8, Aug. 1977, pp. 1063-1078.
2. Yoon, H. K., and Lilley, D. G., "Five-Hole Pitot-Probe Time-Mean Velocity Measurements in Confined Swirling Flows", Paper AIAA-83-0315, Reno, Nevada, January 10-13, 1983. AIAA Journal (in press), 1984.
3. Jackson, T. W., and Lilley, D. G., "Single-Wire Swirl Flow Turbulence Measurements", Paper AIAA-83-1202, Seattle, Wash., June 27-29, 1983.
4. Abujelala, M. T., and Lilley, D. G., "Confined Swirling Flow Predictions", Paper AIAA-83-0316, Reno, Nevada, January 10-13, 1983.
5. Scott, C. J., and Rask, D. R., "Turbulent Viscosities for Swirling Flow in a Stationary Annulus", Transactions of the ASME, J. Fluids Engineering, 1973, pp. 557-566.
6. Weske, D. R., and Sturov, G. Y., "Experimental Study of Turbulent Swirled Flows in a Cylindrical Tube", Fluid Mechanics - Soviet Research, Vol. 3, No. 1, 1974, pp. 77-82.
7. Murakami, M., Kito, O., Katayama, Y., and Iida, Y., "An Experimental Study of Swirling Flows in Pipes", Bulletin of the ASME, Vol. 19, No. 128, 1976, pp. 118-126.
8. Scott, C. J., and Bartelt, K. W., "Decaying Annular Swirl Flow with Inlet Solid Body Rotation", Transaction of the ASME, J. Fluids Engineering, 1976, pp. 33-40.



(a)  $\phi = 0$  deg.



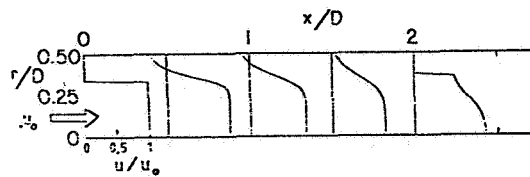
(b)  $\phi = 45$  deg.



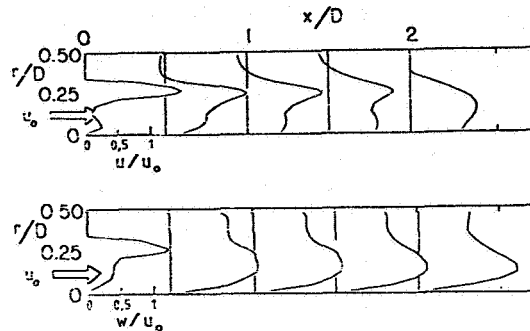
(c)  $\phi = 70$  deg.

Fig. A1 Predicted Velocity Profiles for Flowfield with  $D/d = 1.5$  Using Standard  $k-\epsilon$  Model

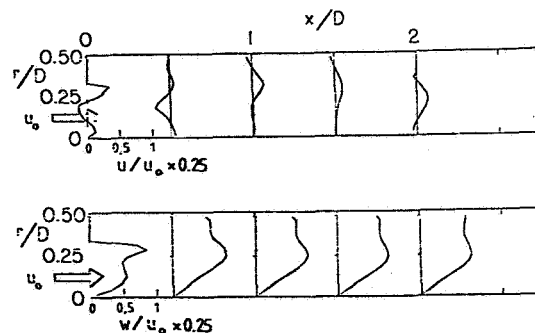
9. Sukhovich, Y. P., "Experimental Investigation of Local Properties of Swirled Turbulent Flow in Cylindrical Channels", Fluid Mechanics - Soviet Research, Vol. 7, No. 3, 1978, pp. 74-84.
10. Abujelala, M. T., Jackson, T. W., and Lilley, D. G., "Swirl Flow Turbulence Modeling", Paper AIAA-84-1376, Cincinnati, OH, June 11-13, 1984.
11. Lilley, D. G., and Rhode, D. L., "A Computer Code for Swirling Turbulent Axisymmetric Recirculating Flows in Practical Isothermal Combustor Geometries", NASA CR-3442, Feb. 1982.
12. Gosman, A. D., and Pun, W. M., "Calculation of Recirculating Flows", Rept. No. HTS-74/12, Dept. of Mech. Engng., Imperial College, London, England, 1974.
13. Launder, B. E., and Spalding, D. B., "The Numerical Computation of Turbulent Flows", Comp. Methods in Appl. Mech. and Engng., Vol. 3, March 1974, pp. 269-289.



(a)  $\phi = 0$  deg.



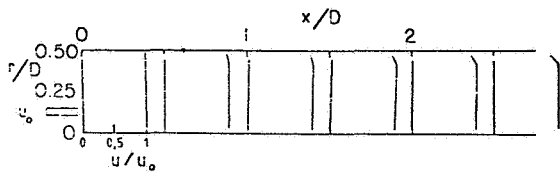
(b)  $\phi = 45$  deg.



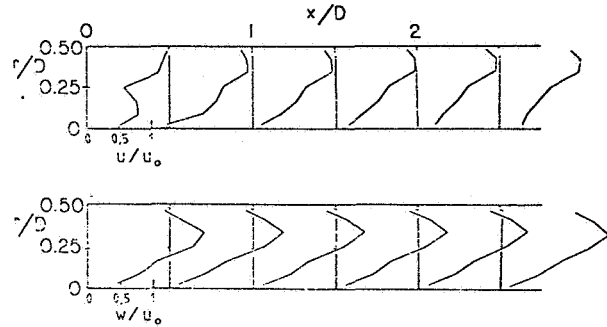
(c)  $\phi = 70$  deg.

Fig. A2 Predicted Velocity Profiles for Flowfield with  $D/d = 1.5$  and Strong Nozzle at  $L/D = 2$  Using Standard  $k-\epsilon$  Model

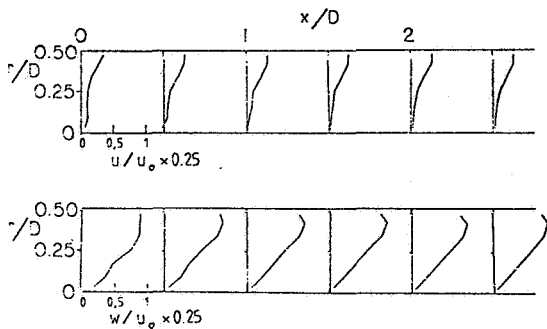
14. Scharrer, G. L., and Lilley, D. G., "Five-Hole Pitot Probe Measurements of Swirl, Confinement and Nozzle Effects on Confined Turbulent Flows", Paper AIAA-84-1605, Snowmass, CO, June 24-28, 1984.
15. Chaturvedi, M. C., "Flow Characteristics of Axisymmetric Expansions", Proc. Journal Hydraulics Division, ASCE, Vol. 89, No. HYE, 1963, pp. 61-92.
16. Moon, L. F., and Rudinger, G., "Velocity Distribution in an Abruptly Expanding Circular Duct", ASME Journal of Fluids Engng., March 1977, pp. 226-230.
17. Lilley, D. G., "Primitive Pressure-Velocity Code for the Computation of Strongly Swirling Flows", AIAA Journal, Vol. 14, June 1976, pp. 749-756.
18. Novick, A. S., Miles, G. A., and Lilley, D. G., "Numerical Simulation of Combustor Flowfields: A Primitive Variable Design Capability", J. of Energy, Vol. 3, No. 2, March-April 1979, pp. 95-105.



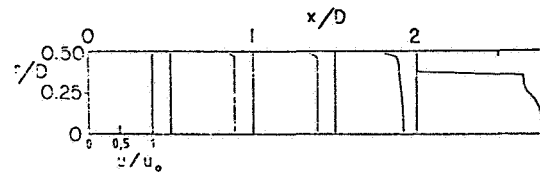
(a)  $\phi = 0$  deg.



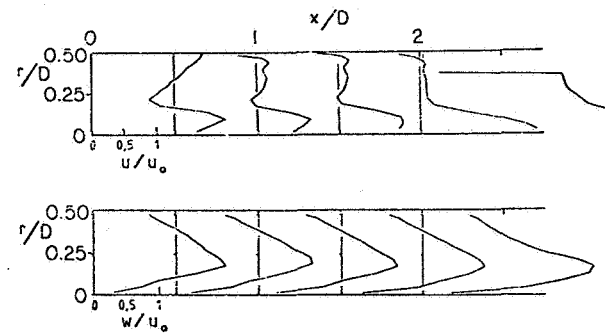
(b)  $\phi = 45$  deg.



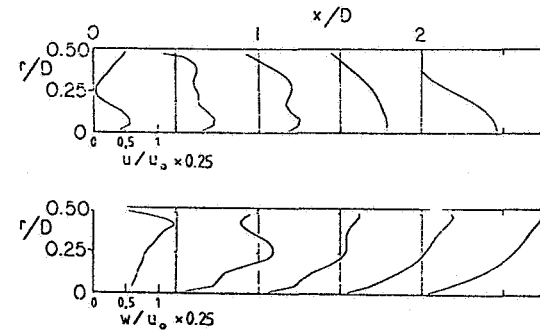
(c)  $\phi = 70$  deg.



(a)  $\phi = 0$  deg.



(b)  $\phi = 45$  deg.



(c)  $\phi = 70$  deg.

Fig. A3 Predicted Velocity Profiles for Flowfield with  $D/d = 1$  Using Standard  $k-\epsilon$  Model

Fig. A4 Predicted Velocity Profiles for Flowfield with  $D/d = 1$  and Strong Nozzle at  $L/D = 2$  Using Standard  $k-\epsilon$  Model

19. Harch, W. H., "Numerical Modeling of Ramjet Combustors", AFWAL-TR-82-2112, Feb. 1983.
20. Hall, M. G., "Vortex Breakdown", Annual Review of Fluid Mechanics, Vol. 4, 1972, pp. 195-218.
21. Back, L. H., and Roschke, E. J., "Shear-Layer Regions and Wave Instabilities and Reattachment of an Abrupt Circular Channel Expansion", ASME Journal of Applied Mech., Sept. 1972, pp. 677-681.
22. Roschke, E. J., and Back, L. H., "The Influence of Upstream Conditions on Flow Reattachment Lengths Downstream of an Abrupt Circular Channel Expansion", J. Biomechanics, Vol. 9, 1976, pp. 481-483.
23. Nozaki, T., and Hatta, K., "Reattachment Flow Issuing from a Finite Width Nozzle", Bulletin of the ASME, Vol. 25, No. 200, 1982, pp. 196-203.
24. Gupta, A. K., Lilley, D. G., and Syred, N., "Swirl Flows", Abacus Press, Tunbridge Wells, England, 1984.

#### Appendix

Predictions given in the bulk of this paper were obtained using the modified  $k-\epsilon$  turbulence model with C formulation as deduced in Ref. 10. Corresponding predictions with the standard  $k-\epsilon$  model were given in Ref. 4 for the  $D/d = 2$  case, with both open-ended and strong contraction nozzle at  $L/D = 2$ . For completeness of the present paper, predictions with the standard  $k-\epsilon$  model for the open-ended and strong nozzle at  $L/D = 2$  are given for the cases discussed in Sections 3.2 and 3.3, for different chamber diameters. Figures A1 and A2 are for the  $D/d = 1.5$  case; Figs. A3 and A4 are for the  $D/d = 1$  case.



APPENDIX L

TURBULENCE MEASUREMENTS IN A COMPLEX  
FLOWFIELD USING A CROSSED HOT-WIRE

(AIAA-84-1604)

# TURBULENCE MEASUREMENTS IN A COMPLEX

## FLOWFIELD USING A CROSSED HOT-WIRE

B. E. McKillop\* and D. G. Lilley\*\*  
Oklahoma State University, Stillwater, Okla.

### Abstract

Measurements of turbulence quantities in a complex axisymmetric nonreacting nonswirling confined flowfield have been made using a crossed hot-wire anemometer. Axial and radial time-mean velocities, directional turbulence intensities, and main Reynolds stress were measured. Associated turbulent viscosity values are deduced throughout. The confined jet is a model of an axisymmetric combustor can, with expansion ratio  $D/d = 2$  and expansion angle  $\alpha$  of 90 deg. Investigations were made with and without a downstream contraction nozzle of area ratio 4 located at  $L/D = 2$ . Measurements indicate that the crossed hot-wire used cannot handle axial flow reversal (without prior knowledge and probe re-orientation) and that the experimental technique is inadequate for the measurement of time-mean radial velocity. Other quantities show a high level of comparability. In common with previous researchers, time-mean and turbulence characteristics with the contraction nozzle at  $L/D = 2$  show little change from that of the corresponding flowfield without a contraction nozzle, for the nonswirling flow cases.

### Nomenclature

A, B, C	calibration constants
$A_m$	axial velocity fluctuation sensitivity coefficient
$A_v$	radial velocity fluctuation sensitivity coefficient
$B_\phi$	$(E_1 A_{v1} + E_2 A_{v2})$
D	confined jet tube diameter
$D_m$	$(E_1 A_{m1} + E_2 A_{m2})$
d	nozzle exit diameter
E	time-mean voltage of hot-wire = $\bar{e}$
e	voltage of hot-wire = $\bar{e} + e'$
K	free jet parameter
L	distance from nozzle exit to contraction nozzle
u	axial velocity component = $\bar{u} + u'$
$\overline{u'v'}$	turbulent Reynolds shear stress
v	radial velocity component = $\bar{v} + v'$
x, r	axial and radial coordinates

\* Graduate Student, School of Mechanical and Aerospace Engineering, Student Member AIAA

\*\* Professor, School of Mechanical and Aerospace Engineering, Associate Fellow AIAA

This paper is declared a work of the U.S. Government and therefore is in the public domain.

Z	effective cooling velocity
$\alpha$	expansion angle
$\phi$	yaw angle
$\nu_t$	turbulent viscosity
$\nu_t^*, \nu_t^+$	nondimensional turbulent viscosity

### Subscripts

1,2	refer to hot-wires 1 and 2
0	value at $x = 0$
rms	root-mean-square value

### Superscripts

( $\bar{\quad}$ )	time-mean average
( $\quad$ )'	fluctuating quantity

## 1. Introduction

### 1.1 Combustor Flowfields

A renewed interest in gas turbine combustor analysis has been initiated by new emphasis on pollutant emission reduction, noise suppression, fuel economy, and performance. The combustor must fulfill several requirements<sup>1</sup> including: burn fuel efficiently; maintain stable combustion over a wide range of operating conditions; uniform distribution of temperature in product gases; minimum size and weight; and minimum pressure drop. Flowfields are complex because of corner and central recirculation regions produced by rapid expansion and perhaps strong swirl imparted to the incoming air. Thus, in general, the flow is a swirling, recirculating, turbulent one and is, therefore, difficult to analyze. The present study emphasizes nonswirling flow and its measurement with a crossed hot-wire anemometer.

The general aim of the on-going research investigation at Oklahoma State University is to provide information on the fluid dynamic aspects of combustor flowfields. The characterization, either in the form of experimental or theoretical analysis, is useful to designers. Theoretical investigators can also compare the experimental data with the data from a numerical solution of the appropriate governing partial differential equations. With this general knowledge, combustor development time and cost can be reduced. Several research methods are being pursued including: flow visualization; computer simulation; and time-mean and fluctuating velocity measurements, with emphasis on nonreacting, steady turbulent flow in axisymmetric geometries. The flow enters through a nozzle of exit diameter  $d$  and proceeds via a sudden expansion into a tube of diameter  $D$ . A swirler may be located immediately upstream of the inlet to the test section, if needed. Also, a contraction

nozzle may be positioned at some downstream location in the tube.

## 1.2 Turbulence Measurement

Several authors have discussed turbulence phenomena in detail and suggested various methods of turbulence measurements.<sup>2-5</sup> The hot-wire anemometer is the most widely used instrument to obtain turbulence quantities. A single hot-wire in a two-dimensional flow can measure the streamwise components of the time-mean velocity and the root-mean-square velocity fluctuation at a particular location in the flowfield when used at a single orientation. By using multi-orientations of a single hot-wire, the three components of the mean and fluctuating velocity vector can be determined.<sup>6-8</sup> The problems associated with this method are that extensive data reduction is required to calculate the desired turbulence quantities and, because the wire has to be positioned several times, the data obtained is not truly simultaneous. Also, the assumptions needed in the data reduction phase are not always valid. A multi-wire probe can be employed using a single orientation to determine flowfield quantities. In a two-dimensional flow, the time-mean velocities, streamwise and cross-stream velocity fluctuations and their cross correlation can be determined with a two-wire probe. A crossed hot-wire probe was used in this study in which the wires were inclined at  $\pm 45$  deg. to the flow direction and parallel to the probe axis. This probe should give more accurate turbulence intensities and cross correlation than a single wire multi-orientation method because it is used at only one orientation with nearly simultaneous data acquisition.

## 1.3 Previous Experimental Studies

Recent Studies at OSU. Research presently being undertaken at OSU involves several methods. Still<sup>9</sup> and movie<sup>10</sup> photography of neutrally-buoyant helium-filled soap bubbles and injected smoke has aided in the visualization of various combustor flowfields. A five-hole pitot probe has been used to measure time-mean velocities at different swirl strengths.<sup>9,11</sup> Turbulence quantities have been determined with a six-orientation single hot-wire technique<sup>12</sup> in swirling and nonswirling flowfields. Predictions of confined swirling flows corresponding to the ones studied experimentally have been achieved using a computer code that solves the appropriate partial differential equations.<sup>13</sup> These predictions<sup>14</sup> have now been supplemented by predictions which include downstream nozzle effects<sup>15</sup> and start computations using realistic inlet conditions<sup>16</sup>

Free Jet. Free jet measurements were made in the present study as a preliminary to the main goal of confined jet measurements. They provide an independent check on the data acquisition and interpretation techniques. Results, discussed at length elsewhere,<sup>1</sup> show good agreement with those of previous works.<sup>17-24</sup>

Confined Jet. Flow separation behind an orifice in an electrically heated tube was investigated by Krall and Sparrow.<sup>25</sup> The peak Nusselt number was presumed to be at the reattachment point. They concluded that the local heat-transfer coefficients in the separated, reattached, redevelopment regions are several times

as large as those for a fully developed flow. Also, they found that the reattachment length was unaffected by Reynolds number in the turbulent range. This result was verified by Phaneuf and Netzer<sup>26</sup> who measured mean axial velocity and wall static pressure behind abrupt pipe steps. It was concluded that the reattachment zone spreads out with increasing Reynolds number and increasing step height, provided the Reynolds number is in the appropriate range.

Back and Roschke<sup>27,28</sup> measured the reattachment length downstream of a pipe step by dye visualization in water flows. A conical contraction section was placed just upstream of a sudden expansion to reduce the boundary layer thickness. Dye was injected through holes positioned along the larger diameter tube at intervals of one step height. Reattachment locations were then observed by inspecting the direction of dye flow. Visual observation of small buoyant particles in a fluid in the redevelopment region was accomplished by Feuerstein et al.<sup>29</sup> They found the reattachment length to be slightly different from that given by Back and Roschke probably due to dissimilar inlet profiles.

Pitot probe and hot-wire measurements in various sudden expansion flowfields were made by Ha Minh and Chassaing.<sup>30</sup> The time-mean axial velocity was determined with both instruments and good agreement was exhibited. A rotating, inclining, single hot-wire technique was employed to measure the Reynolds stresses. One of their expansion ratios matched the one used in the present study but the axial locations of their measurements were not compatible.

Moon and Rudinger<sup>31</sup> and Johnson and Bennett<sup>32</sup> developed laser-Doppler Systems to measure mean velocities and recirculation region geometries, but the expansion ratios differed from the one used in the present experiments.

The experiments of Chaturvedi<sup>33</sup> for nonswirling flow are directly comparable to the results of the present study. Also comparable are six-orientation single hot-wire measurements recently obtained by Jackson and Lilley<sup>34</sup> in the same test facility as in the present study. Mean velocity and pressure downstream of a sudden expansion of a diameter ratio of 2 were measured with a stagnation tube and pitot probe. A single and crossed hot-wire were used to measure the turbulence intensities and turbulent shear stress. Mean velocity was also measured with the single hot-wire.

## 1.4 The Present Contribution

To further develop combustor flowfield prediction techniques, including turbulence modelling, there is a strong need to obtain experimental estimates of the mean and turbulent flow quantities and the turbulent viscosity. In the present study, a crossed hot-wire single orientation technique is employed to measure time-mean velocity, turbulence intensities and Reynolds stress in a combustor simulation confined jet flowfield. Measurements in the confined jet are carried out for nonswirling flow with a sudden expansion, with and without a downstream contraction nozzle.

Section 2 describes the experimental facilities and hot-wire and raw data acquisition instrumentation. Experimental techniques, data reduction scheme and turbulent viscosity formulation are given in Section 3. Measurement procedures and results for confined sudden expansion flows are discussed in Section 4. Some of the turbulence quantities are compared with measurements done by Sami et al.<sup>24</sup> in the free jet and Chaturvedi<sup>33</sup> and Jackson and Lilley<sup>34</sup> in the confined jet facilities. Section 5 draws conclusions and summarizes the main results.

## 2. Experimental Facilities

### 2.1 Idealized Flowfields

Confined flow at abrupt expansions, as in an actual gas turbine combustor, is a typical example of the problem of fluid flow separation from the boundary. A region of reverse flow is caused by this separation at the sudden expansion. This region, called the corner recirculation zone (CRZ), is associated with a large pressure drop which adversely affects the performance of a can-type combustion chamber. Turbulence levels are high on the shear layer between the two regions which indicates that, at this position, good combustion would occur. Reacting flows in can combustors have an area of high heat transfer at the location of the reattachment of the dividing streamline which, if left untreated, could lead to rapid deterioration of the walls of the combustor. A central toroidal recirculation zone (CTRZ) is present only with swirling flow, which is not a subject of the present study.

### 2.2 Free Jet

The free jet facility consists of a seamless contoured nozzle fed by a thermally stabilized compressed air generator which delivers the desired flow rate through a small pressure regulator and a Fisher and Porter Model 10A1735A rotameter. The nozzle has a throat diameter of 3.4 cm and an effective flow management section just upstream. It is necessary to calibrate the crossed hot-wires in a flow of known characteristics. The potential core of the free jet was utilized for this calibration. The sensitivity to angulation (see Section 3.1) was obtained by the use of a rotary table on the jet centerline to rotate the probe inside the potential core from -10 to +10 deg. to the free stream flow direction. An "L" shaped probe bracket holds the probe while it is being calibrated.

### 2.3 Confined Jet

The Oklahoma State University Confined Jet Test Facility is used in this experimental study. It is simulation of an idealized axisymmetric combustion chamber of a gas turbine engine. Figure 1 shows a schematic of the overall facility. Ambient air enters the low-speed wind tunnel through a foam rubber air filter. The air then flows through an axial flow fan driven by a 5 h.p. varidrive motor which allows the flow rate to be varied for different test conditions. Next, the flow passes into a flow conditioning section which reduces the intensity of the turbulence caused by the driving fan. This turbulence management section consists of a perforated aluminum plate, followed by a fine mesh screen, a 12.7 cm length of

packed straws, and five more fine mesh screens. The flow then enters a contoured nozzle designed by the method of Morel<sup>35</sup> to produce a minimum adverse pressure gradient on the boundary layer to avoid local separation and flow unsteadiness. The ratio of the turbulence management cross section to that of the nozzle throat, by area, is approximately 22.5. The nozzle throat diameter  $d$  is 15 cm.

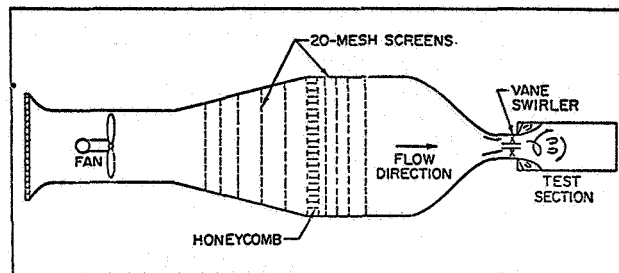


Fig. 1 Schematic of the Overall Experimental Facility

Finally, the flow enters the test section, which is an idealized combustion chamber model. It is composed of a swirler (optional), an expansion block and a long plexiglass tube. The expansion block is a 30 cm diameter disk of wood that has a 15 cm diameter hole centered on its axis and is attached after the swirler. In this study, the swirler is not used and the expansion block is mounted directly on to the throat of the wind tunnel nozzle. The flow expands into a 150 cm long plexiglass tube of diameter  $D$  of 30 cm, thus giving a diameter expansion ratio  $D/d$  of 2. The test section is constructed of plexiglass so as to permit flow visualization and ease of location of measuring probes. Holes are located at multiples of  $x/D = 0.5$  along the length of the tube, so that the hot-wire probe can radially traverse the airflow. A contraction nozzle with an area ratio of 4, shown in Fig. 2, may be positioned downstream of the expansion block to simulate the confining wall of a real gas turbine combustor. The test section does not have film cooling holes or dilution air holes, which do occur in combustors. The ample size of the test section used in this study provides good probe resolution for the hot-wire measurements.

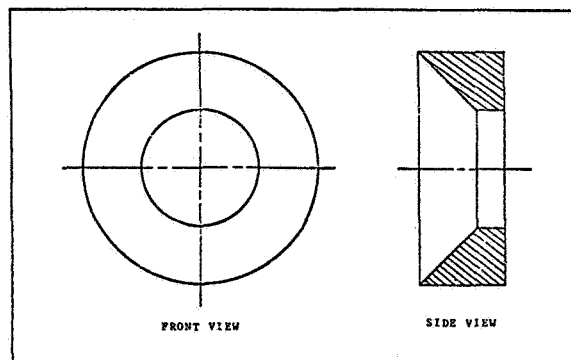


Fig. 2 The Contraction Nozzle with Area Ratio of 4

## 2.4 Hot-wire Instrumentation and A/D Conversion

A crossed hot-wire probe, DISA Type 55P63, is used in this experimental study in which the wires are inclined at  $\pm 45$  deg. to the flow direction and parallel to the probe axis. The probe orientation in the flowfield is illustrated in Fig. 3. Each hot-wire has a separate constant temperature anemometer; the DISA 55M01 main frame with a 55M10 standard bridge anemometer. To obtain the turbulence intensities in the axial and radial directions, it is necessary to instantaneously add and subtract the anemometer voltage outputs, with adder and subtractor circuits constructed of commercially available 741 operational amplifiers. The multiplication of the voltages by a Saicor Model SAI 43 correlation and probability analyzer gives the shear stress. Because the fluctuating signals are small, each signal is amplified by a Hewlett Packard Amplifier with a 20 dB gain. The frequency response of the hot-wires and the associated electronics is approximately 40 kHz based on square wave response tests. The use of linearizers was judged unnecessary from experience in the use of crossed hot-wire anemometry gained previously at Oklahoma State University by researchers such as Morrison<sup>36</sup> and Swearingen.<sup>37</sup>

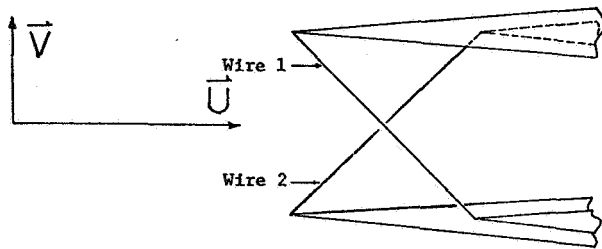


Fig. 3 Hot-wire Orientation

To increase the accuracy of the measurements, a microprocessor with 12-bit analog to digital (A/D) conversion is employed to acquire the data. A schematic of the hot-wire and data acquisition equipment layout is shown in Fig. 4. Because the A/D converter, an Octogon Sys-2, has a maximum input voltage of 2.5 V, the incoming mean voltages are stepped down by a factor of four. The rms signals from the adder and subtractor are changed from AC to DC signals so that the A/D converter can read them.

## 3. Experimental Techniques and Data Reduction

### 3.1 Experimental Techniques

The hot wires are assumed to obey an extension of the familiar King's Law:

$$E^2 = A + BZ^{1/2} + CZ$$

where A, B and C are constants determined a priori by a calibration experiment and Z is the effective cooling velocity. The calibration is accomplished prior to every experiment by placing the crossed hot-wire on the free jet centerline within the potential core region. Writing this equation for

each wire, inversion yields the effective cooling velocities  $Z_1$  and  $Z_2$ , which permit the time-mean axial and radial velocities  $u$  and  $v$  to be deduced with the geometry of Fig. 4.

The instantaneous velocity fluctuations measured from an inclined hot-wire can be defined by the following expression derived by Corrsin and Uberoi<sup>17</sup>:

$$e'/E = (A_m u' \pm A_v v')/\bar{u}$$

where  $A_m$  is the sensitivity coefficient for axial velocity fluctuation and  $A_v$  is the radial velocity fluctuation sensitivity coefficient. This equation can also be written for each wire, and the output from each wire added and subtracted. The crossed hot-wires are matched so that the sensitivity coefficients  $A_m$  and  $A_v$  are approximately the same for both wires and the overheat ratios of the wires are set so that  $E_1 = E_2$ . These simplifications give:

$$e'_1 + e'_2 = D_m u'/\bar{u}$$

where  $D_m = E_1 A_{m1} + E_2 A_{m2}$

and

$$e'_1 - e'_2 = B_\phi v'/\bar{u}$$

where  $B_\phi = E_1 A_{v1} + E_2 A_{v2}$ .

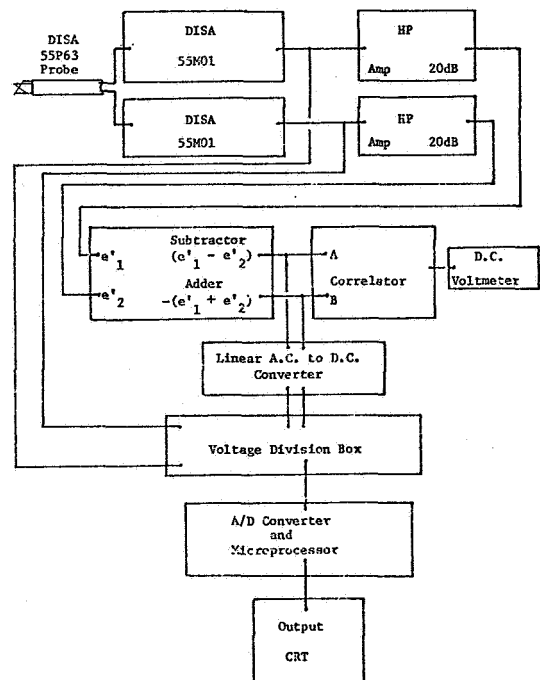


Fig. 4 Instrumentation Layout

To obtain the appropriate  $D_m$  or  $B_\phi$ , the sensitivity coefficients  $A_m$  and  $A_v$  need to be evaluated for each wire. Appropriate calibrations from potential core free jet measurements are used for this, with linear variations of  $D_m$  and  $B_\phi$  with velocity being obtained.<sup>1</sup>

A cross correlator can be used to determine the major shear component of the Reynolds stress tensor in a turbulent shear flow by multiplication of the voltages proportional to  $u'/\bar{u}$  and  $v'/\bar{v}$ . Thus:

$$\overline{u'v'} = (\text{Correlation Output})\bar{u}^2 / (B_{\phi} D_m)$$

with the output from the Honeywell SAI-43A correlator being corrected for hot-wire fluctuating signal amplification.

A computer code was designed to accomplish the reduction of the voltage data from the hot-wires in the technique just discussed. It is described and listed, with a User's Guide and sample output in Ref. 1.

### 3.2 Turbulent Viscosity Formulation

The Boussinesq<sup>38,39</sup> concept asserts that the eddy viscosity is a scalar quantity (much larger than the laminar viscosity except in near-wall regions). It relates turbulent shear stress to time-mean velocity gradients via:

$$\tau_t = -\overline{u'v'} / (\partial\bar{u}/\partial r + \partial\bar{v}/\partial x)$$

and generally varies throughout the flowfield. It is required that the flow is not far from equilibrium (that is turbulence generation equals dissipation locally) and that the turbulence Reynolds number is high. The near-equilibrium assumption has been shown to be approximately correct for a mixing layer<sup>40</sup> and the Reynolds number at which experiments are conducted in this present study are sufficiently large. In the present study, measured turbulent shear stress and time-mean velocity gradients are used to deduce values of eddy viscosity via the Boussinesq concept, with only the main velocity gradient used; axial gradient of the radial velocity are very small in comparison. Appropriate finite central differencing is used for the velocity gradient calculation.

From inverse analysis of experimental time-mean measurements, Hinze<sup>2</sup> states that the turbulent viscosity in a round free jet is approximately constant in the central part of the fully-developed region and given by the relation:

$$\nu_t = 0.00196 K u_0 d$$

where K is a parameter between 5.4 and 6.39. The latter value is used in agreement with earlier measurements.<sup>41</sup> In the free jet, a non-dimensionalized turbulent viscosity  $\nu_t^+$  given by:

$$\nu_t^+ = \nu_t / (6.39 u_0 d)$$

should approach the value of 0.00196 in the fully-developed region. Results of Ref. 1 confirm this. In the confined jet, the simple normalization

$$\nu_t^* = \nu_t / (u_0 d)$$

is used to be consistent with on-going theoretical studies.<sup>42</sup> Its value, corresponding to 0.00196 in the free jet, is 0.0125. Later deduced values will be seen to be below this in low shear regions and above this in high shear regions.

## 4. Results and Discussion

Nonswirling nonreacting confined jet flows are investigated by the use of a crossed hot-wire to measure mean velocities  $\bar{u}$  and  $\bar{v}$ , fluctuating velocities  $u'$  and  $v'$ , and Reynolds stress  $\overline{u'v'}$ . The preceding quantities are normalized with the nozzle uniform axial exit velocity  $u_0$ , determined with the probe from an independent measurement at the nozzle exit face. Radial distribution of turbulent viscosity is also deduced. The Reynolds numbers of the flows under investigation are high enough to ensure that the results are in the Reynolds number independent regime. Prior to any measurements, the crossed hot-wire probes were calibrated in the free jet facility. The voltage divider box and A/D converter were also calibrated by use of a voltage standard. This was to check that no 'drifting' of the electronics had occurred. Measurements were made in a model of an axisymmetric can combustor (confined jet test section) with an expansion ratio  $D/d = 2$ , an expansion angle  $\alpha$  of 90 deg, and axial location increments of 0.5 chamber diameters. The axial location of zero is actually 1 mm downstream of the enlargement face so as to prevent the hot-wire probe from damage. Comparable are measurements by Chaturvedi<sup>33</sup> and Jackson and Lilley.<sup>34</sup> A single hot-wire multi-orientation technique was used by Jackson and Lilley<sup>34</sup> in the same test facility. Also, a confined jet flowfield was investigated with a contraction nozzle of an area ratio of 4 located at  $L/D = 2$ . This nozzle, mentioned earlier, has a 45 deg. slope facing upstream. Time-mean flowfield data for this configuration have been presented previously by Yoon and Lilley<sup>11</sup> using a five-hole pitot probe technique. Tabulated data for both flowfields investigated in the present study are contained in Ref. 1.

### 4.2 Time-Mean Velocities

Figure 5 shows measured values of time-mean axial and radial velocities. A nearly flat axial velocity profile is seen at the entrance of the test section. Comparisons of the time-mean axial velocity with Chaturvedi<sup>33</sup> and Jackson and Lilley<sup>34</sup> show good agreement except in the expected region of recirculation. There are two reasons for this: although a hot-wire anemometer cannot sense flow direction, the previous workers<sup>33,34</sup> plotted some negative values of time-mean axial velocity by deducing direction from earlier pitot probe data; and, because of the "L" shaped probe design the hot-wire are hidden from the recirculating flow by the probe supports. Because the time-mean radial velocity is calculated from the subtraction of two large quantities producing a small number, the profiles shown in Fig. 5 are almost zero at all axial locations. Bruun<sup>43</sup> states that velocities determined by a crossed hot-wire probe have a very strong yaw dependence, particularly  $\bar{v}$ . This also may account for the error in the time-mean radial velocity. Thus, the experimental technique is not adequate for these radial velocity measurements.

### 4.3 Turbulence Intensities

Inspection of the radial distributions of  $u'_{rms}/u_0$  and  $v'_{rms}/u_0$  displayed in Fig. 6 shows similar trends to those found earlier.<sup>33,34</sup> The axial turbulence intensity values are lower than previous measurements, but the radial turbulence intensity values are in good agreement. The axial

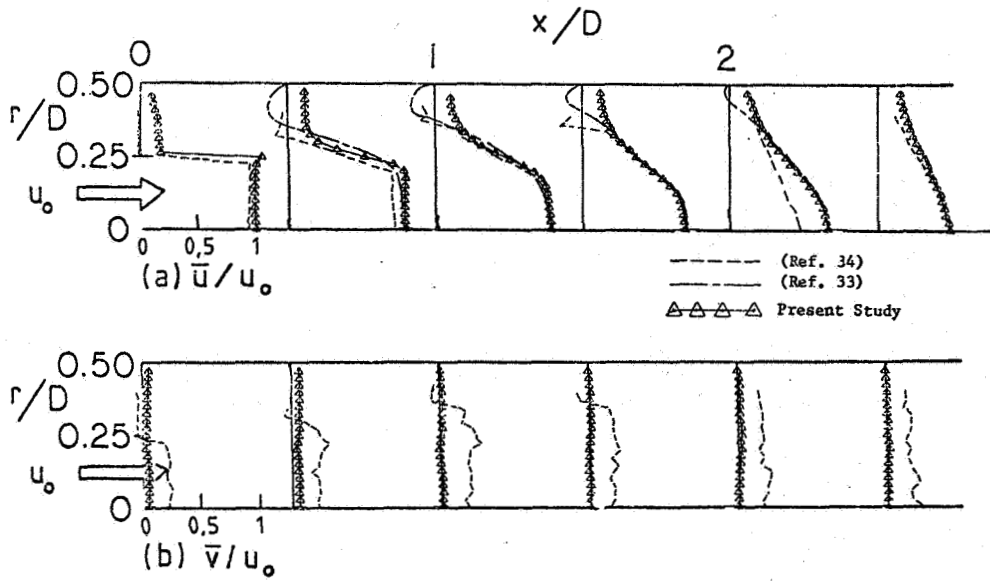


Fig. 5. Confined Jet Radial Distribution of Time-Mean (a) Axial and (b) Radial Velocities

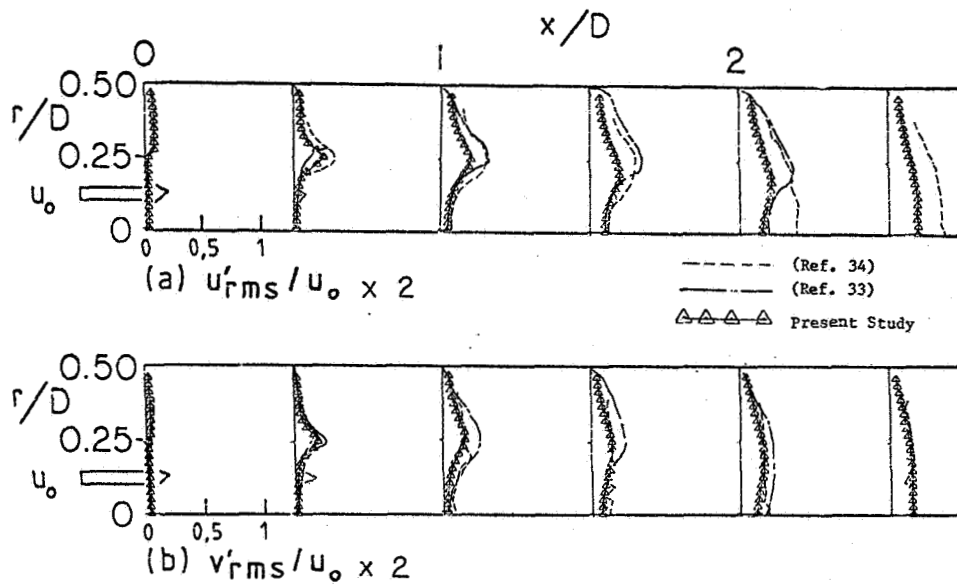


Fig. 6. Confined Jet Radial Distribution of (a) Axial and (b) Radial Turbulence Intensities

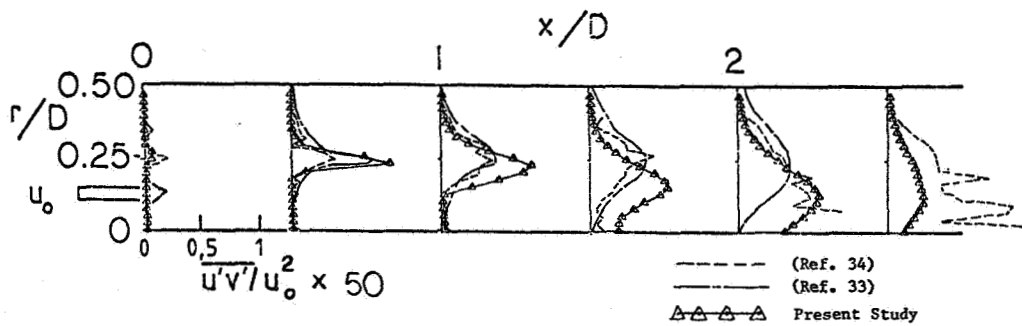


Fig. 7. Confined Jet Radial Distribution of Turbulent Shear Stress

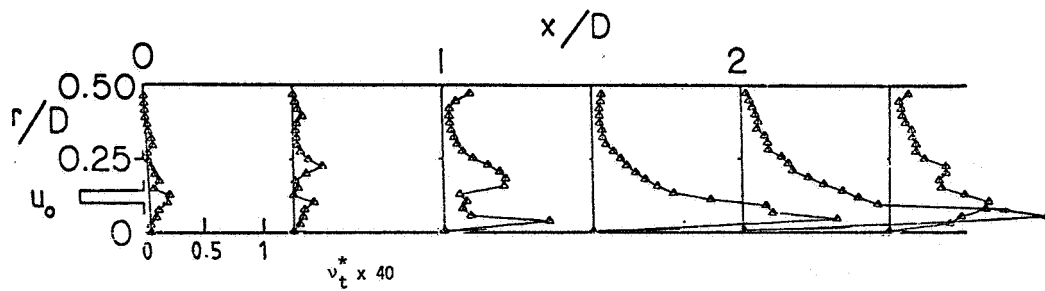


Fig. 8. Confined Jet Radial Distribution of Turbulent Viscosity

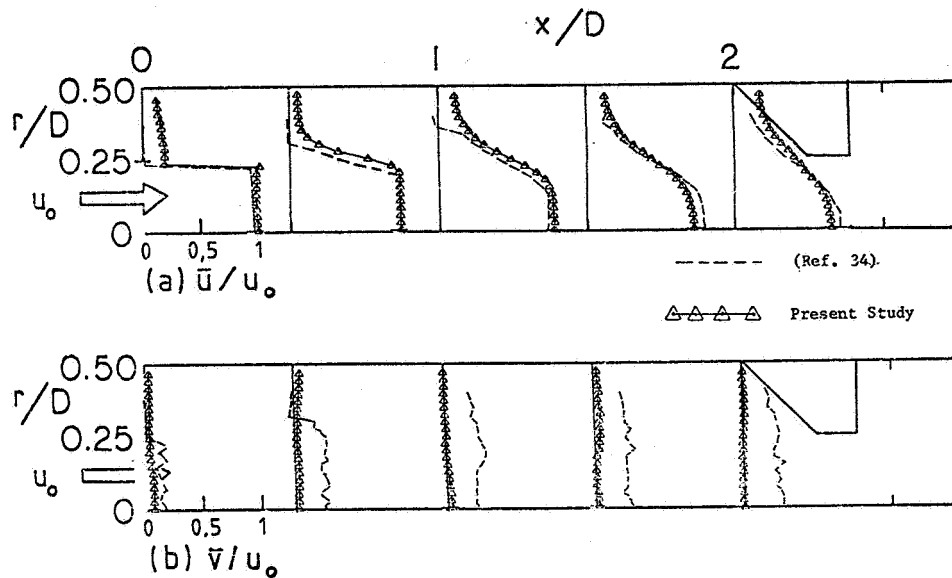


Fig. 9. Confined Jet with Contraction Nozzle Radial Distribution of Time-Mean (a) Axial and (b) Radial Velocities

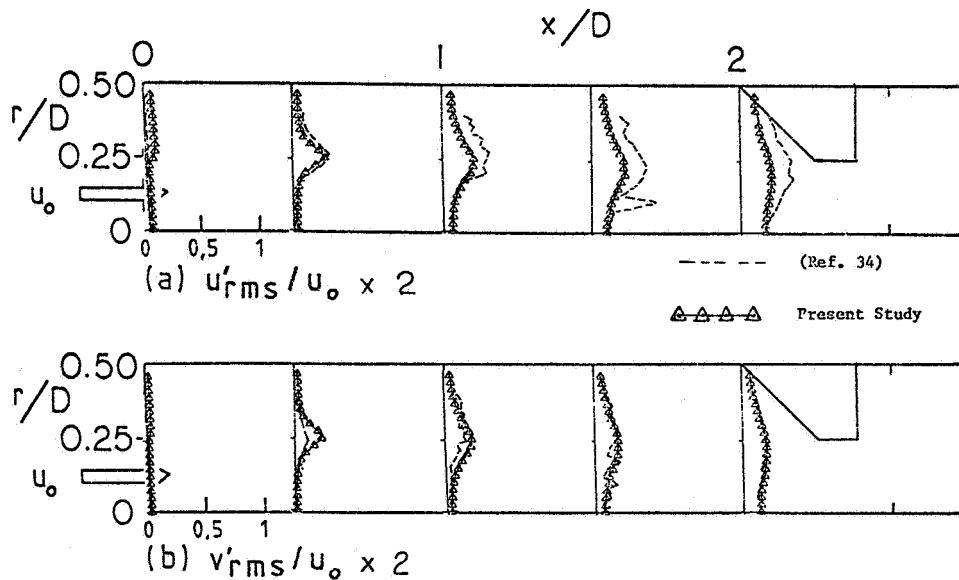


Fig. 10. Confined Jet with Contraction Nozzle Radial Distribution of (a) Axial and (b) Radial Turbulence Intensities



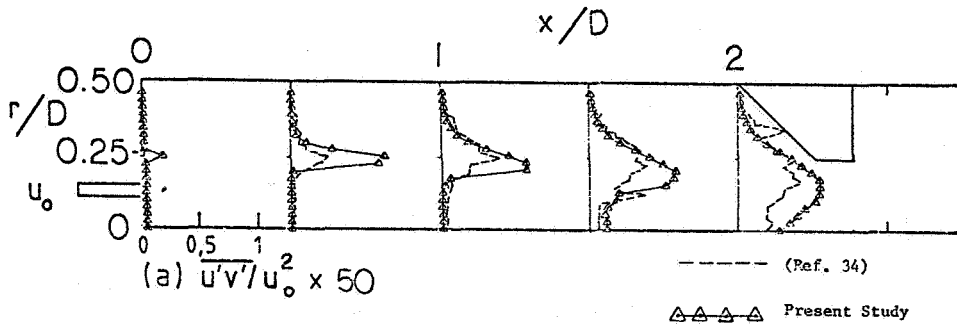


Fig. 11. Confined Jet with Contraction Nozzle Radial Distribution of Turbulent Shear Stress

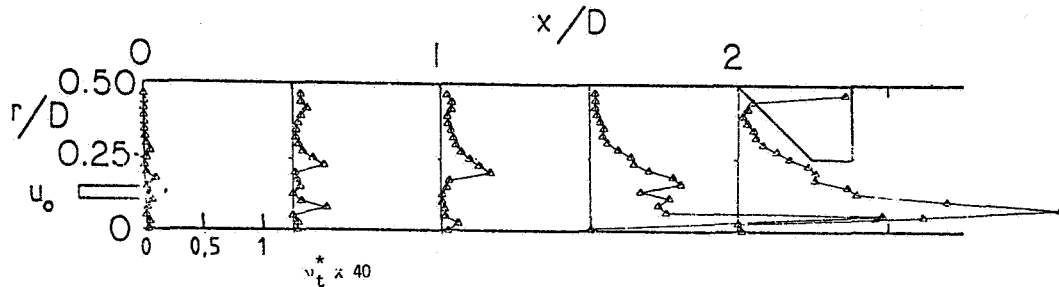


Fig. 12. Confined Jet with Contraction Nozzle Radial Distribution of Turbulent Viscosity

turbulence intensity is slightly larger than the corresponding radial quantity with maximum values on the shear layer between recirculating and nonrecirculating flow. The figure also shows that the radial turbulence intensity is damped to a higher degree than the axial turbulence intensity by the presence of the test facility tube wall.

#### 4.4 Shear Stress

Shown in Fig. 7 is the radial distribution of turbulent shear stress. As can be seen, Chaturvedi's<sup>33</sup> data indicates lower values of shear stress than the present study. Also, results are similar to Jackson and Lilley's<sup>34</sup> with the present measurements having smoother profiles. The shear layer, which is very thin at the entrance to the test section, grows quickly to encompass a large amount of the flowfield. All shear stress values are plotted as positive, although in the vicinity of the recirculation zone, the gradient of the time-mean axial velocity in the radial direction might be positive, inferring negative values of  $\overline{u'v'}$ .

#### 4.5 Turbulent Viscosity

Figure 8 shows the radial distribution of turbulent viscosity. As shown, the turbulent viscosity grows in magnitude while progressing downstream with large peaks near the centerline from  $x/D = 1$  to 2.5. Here the peak reduces because the mean velocity gradient near the centerline has increased. Although the change in mean axial velocity is little at small radial and axial positions, the peak is not seen since the shear stress is correspondingly small. The peaks in the

vicinity or  $r/D = 0.25$  at axial locations of 0.5 and 1.0 give an indication of the position of the contraction nozzle. The expected free jet turbulent viscosity of 0.00196 corresponds to 0.5 on the horizontal axis. As can be seen, the values of viscosity are lower than this expected value in the low shear regions and larger in high shear regions. It must be noted that the turbulent viscosity is the most difficult to ascertain of all the turbulence quantities presented.

#### 4.6 Downstream Nozzle Effects

The measurements of Figs. 5 through 8 for the open-ended flow situation were repeated with the contraction nozzle of area ratio 4 (shown in Fig. 2) located 2 test section diameters downstream of the inlet - a corresponding situation to that used in previous five-hole pitot probe,<sup>11</sup> single-wire hot-wire anemometer<sup>34</sup> and prediction<sup>15</sup> studies. The new figures - Figs. 9 through 12 - illustrate the downstream nozzle effect on the flow parameters measured. As expected from assessment of the previous results, the nozzle effects on the nonswirling flowfield investigated here are minimal.

The time-mean velocities in the confined jet with the contraction nozzle at  $L/D = 2$  are presented in Fig. 9. The profiles show that the results change very little from the identical flowfield without a contraction nozzle, as also found elsewhere.<sup>11,34</sup> Figure 10 presents turbulence intensities and shows little change from the non-contracted counterpart. Turbulent shear stress profiles are presented in Fig. 11. Like the normal stresses, there is insufficient change with

respect to the flowfield without the contraction nozzle to warrant any new discussion. The radial distribution of turbulent viscosity is presented in Fig. 12. As before, the results indicate that the contraction nozzle effects little change. It may be remarked that it is known that a downstream nozzle of area ratio 2 or 4 does affect swirling flow in the test section,<sup>11,34</sup> although the swirl flow cases were outside the scope of the present study.

### 5. Closure

A crossed hot-wire probe has been employed to measure the time-mean and fluctuating velocities and shear stress in nonswirling nonreacting confined jet flows. The turbulent viscosity is also calculated from these results. Measurements were also made in the axisymmetric confined jet test section with an expansion ratio  $D/d = 2$ , an expansion angle  $\alpha$  of 90 deg. and at axial location increments of 0.5 diameters. A contraction nozzle was located at  $L/D = 2$  for some of the measurements. Good agreement with previous workers is to be noted. However, the crossed hot-wire probe cannot accurately measure recirculating flow without prior flow direction knowledge, and deduction of the time-mean velocity is inadequate. Nevertheless, the crossed hot-wire technique gives more accurate results for the turbulent shear stress, and thus turbulent viscosity, than a multi-orientation single-wire technique. Smoother profiles for turbulent shear stress are seen in the present study than in the previous single-wire study. As compared with a free jet, the effects of confinement are: faster development of velocity profiles; higher values of turbulence quantities; and larger time-mean radial velocities. Time-mean and turbulence characteristics with the contraction nozzle at  $L/D = 2$  show little change from that of the corresponding flowfield without a contraction nozzle. This is probably because of the high time-mean axial velocity dominating the central region of the flow-domain, and the accelerating effect of the nozzle only being felt locally.

### Acknowledgments

Gratitude is expressed to National Aeronautics and Space Administration Lewis Research Center and Air Force Wright Aeronautical Laboratories for support via Grant No. NAG 3-74, technical monitor Dr. J. D. Holdeman.

### References

- McKillop, B. E. "Turbulence Measurements in a Complex Flowfield Using a Crossed Hot-Wire". M.S. Thesis, Oklahoma State University, Stillwater, Okla., July 1983.
- Hinze, J. O., "Turbulence", 2nd Edition, McGraw-Hill, New York, 1975.
- Bradshaw, P., "An Introduction to Turbulence and Its Measurement", Pergamon Press, New York, 1976.
- Beer, J. M. and Chigier, N. A., "Combustion Aerodynamics", Wiley, New York, 1972.
- Syred, N., Beer, J. M. and Chigier, N. A., "Turbulence Measurements in Swirling Recirculating Flows", Proc. Salford Symposium on Internal Flows, Int. of Mechanical Engineering, London, England, 1971, pp. B27-B36.
- Dvorak, K. and Syred, N., "The Statistical Analysis of Hot-Wire Anemometer Signals in Complex Flow Fields", DISA Conference, University of Leicester, 1972.
- King, C. F., "Some Studies of Vortex Devices - Vortex Amplifier Performance Behavior", Ph.D. Thesis, University College of Wales, Cardiff, Wales, 1978.
- Jorgensen, F. E., "Directional Sensitivity of Wire and Fiber Film Probes", DISA Information No. 11, Franklin Lakes, New Jersey, May, 1971.
- Rhode, D. L., Lilley, D. G. and McLaughlin, D. K., "Mean Flowfields in Axisymmetric Combustor Geometries with Swirl", AIAA Journal, Vol. 21 No. 4, April 1983, pp. 593-600.
- Lilley, D. G., "Turbulent Combustor Flowfield Investigation", in Combustion Fundamentals Research, NASA CP-2268, March 1983, pp. 101-117.
- Yoon, H. K. and Lilley, D. G., "Five-Hole Pitot Probe Time-Mean Velocity Measurements in Confined Swirling Flows," Paper AIAA 83-0315, Reno, Nev., Jan. 10-13, 1983.
- Janjua, S. I., McLaughlin, D. K., Jackson, T. W. and Lilley, D. G., "Turbulence Measurements in a Confined Jet Using a Six-Orientation Hot-Wire Probe Technique", Paper AIAA 82-1262, Cleveland, Ohio, June 21-23, 1982.
- Lilley, D. G. and Rhode, D. L., "A Computer Code for Swirling Turbulent Axisymmetric Recirculation Flows in Practical Isothermal Combustor Geometries", NASA CR-3442, Feb., 1982.
- Rhode, R. L., Lilley, D. G. and McLaughlin, D. K., "On the Prediction of Swirling Flowfields Found in Axisymmetric Combustor Geometries", ASME Journal of Fluids Engrg., Vol. 104, 1982, pp. 378-384.
- Abujelala, M. T. and Lilley, D. G., "Confined Swirling Flow Predictions", Paper AIAA 83-0316, Reno, Nevada, Jan. 10-13, 1983.
- Sander, G. F. and Lilley, D. G., "The Performance of an Annular Vane Swirler", Paper AIAA 83-1326, Seattle, Wash., June 27-29, 1983.
- Corrsin, S. and Uberoi, M. S., "Spectrums and Diffusion in a Round Turbulent Jet", NASA Report 1040, 1949.
- Kolpin, M. A., "The Flow in the Mixing Region of a Jet", Journal of Fluid Mechanics, Vol. 18, 1964, pp. 529-548.

19. Davies, P. O. A. L., Fisner, M. J. and Barrett, M. J., "Turbulence in the Mixing Region of a Round Jet", *Journal of Fluid Mechanics*, Vol. 15, 1963, pp. 337-367.
20. Wagnanski, I. and Fiedler, H., "Some Measurements in the Self-preserving Jet", *Journal of Fluid Mechanics*, Vol. 38, 1969, pp. 577-612.
21. Rodi, W., "A New Method of Analysing Hot-Wire Signals in Highly Turbulent Flow, and Its Evaluation in a Round Jet", *DISA Information*, No. 17, 1975.
22. Bradshaw, P., Ferris, D. H. and Johnson, R. F., "Turbulence in the Noise Producing Region of a Circular Jet", *Journal of Fluid Mechanics*, Vol. 19, pp. 591-624, 1964.
23. Corrsin, S., "Investigation of Flow in an Axially Symmetrical Heated Jet of Air", *NACA Wartime Report W94*, 1943.
24. Sami, S., Carmody, T., and Rouse, H., "Jet Diffusion in the Region of Flow Establishment", *Journal of Mechanics*, Vol. 27, 1967, pp. 231-252.
25. Krall, K. M. and Sparrow, E. M., "Turbulent Heat Transfer in the Separated, Reattached, and Redevelopment Regions of a Circular Tube", *Journal of Heat Transfer*, Feb., 1966, pp. 131-136.
26. Phaneuf, J. T. and Netzer, D. W., "Flow Characteristics in Solid Fuel Ramjets", Report No. NPS-57Nt74081. Prepared for The Naval Weapons Center by The Naval Postgraduate School, Monterey, California, July, 1974.
27. Back, L.H. and Roschke, E. J., "Shear Layer Flow Regimes and Wave Instabilities and Reattachment Lengths Downstream of an Abrupt Circular Channel Expansion", *Journal of Applied Mechanics*, Sept. 1972, pp. 677-681.
28. Roschke, E. J. and Back, L. H., "The Influence of Upstream Conditions on Flow Reattachment Lengths Downstream of an Abrupt Circular Channel Expansion", *Journal of Biomechanics*, Vol. 9, 1976, pp. 481-483.
29. Feuerstein, I. A., Pike, G. K., and Round, G. F., "Flow in an Abrupt Expansion as Model for Biological Mass Transfer Experiments", *Journal of Biomechanics*, Vol. 8, 1975, pp. 41-51.
30. Ha Minh, H. and Chassaing, P., "Perturbations of Turbulent Pipe Flow", *Proc. of Symposium on Turbulent Shear Flows*, Pennsylvania State University, April, 1977, pp. 13.9-13.17.
31. Moon, L. F. and Rudinger, G., "Velocity Distribution in an Abruptly Expanding Circular Duct", *ASME Journal of Fluids Engineering*, March, 1977, pp. 226-230.
32. Johnson, B. V. and Bennett, J. C., "Velocity and Concentration Characteristics and Their Cross Correlation for Coaxial Jets in a Confined Sudden Expansion; Part II: Predictions", *Proceedings, ASME Symposium on Fluid Mechanics of Combustion Systems*, Boulder, CO, June 22-23, 1981, pp. 145-160.
33. Chaturvedi, M. C., "Flow Characteristics of Axisymmetric Expansions", *Proceedings, Journal Hydraulics Division, ASCE*, Vol. 89, May 1963, pp. 61-92.
34. Jackson, T. W. and Lilley, D. G., "Single-Wire Swirl Flow Turbulence Measurements", Paper AIAA 83-1202, Seattle, Wash., June 27-29, 1983.
35. Morel, T., "Comprehensive Design of Axisymmetric Wind Tunnel Contractions", *ASME Paper 75-FE-17*, Minneapolis, May 5-7, 1975.
36. Morrison, G. L., "Flow Instability and Acoustic Radiation Measurements of Low Reynolds Number Supersonic Jets", Ph.D. Thesis, Oklahoma State University, 1977.
37. Swearingen, J. D., "Crossed Hot-Wire Measurements in Low Reynolds Number Supersonic Jets", M.S. Thesis, Oklahoma State University, 1979.
38. Boussinesq, J., *J. Mem. Pres. Acad. Sci.*, Paris, Vol. 23, 1877, p. 46.
39. Prandtl, L., *Z. Angew. Math. Mech.*, Vol. 5, 1925, pp. 136-139.
40. Bradshaw, P., Cebeci, T., and Whitelaw, J. H., "Engineering Calculation Methods for Turbulent Flow", Academic Press, New York, 1981.
41. Hinze, J. O. and van der Hegge Zijnen, B. G., "Transfer of Heat and Matter in the Turbulent Mixing Zone of an Axially Symmetrical Jet", *Applied Science Res.*, A1, 1949, pp. 435-461.
42. Abujelala, M. T., Jackson, T. W., and Lilley, D. G., "Swirl Flow Turbulence Modeling", Paper AIAA 84-1376, Cincinnati, Ohio, June 11-13, 1984.
43. Bruun, H.H., "Interpretation of X-Hot-Wire Signals", *DISA Information No. 18*, Franklin Lakes, New Jersey, May, 1971.

APPENDIX M

FIVE-HOLE PITOT PROBE MEASUREMENTS OF SWIRL, CONFINEMENT  
AND NOZZLE EFFECTS ON CONFINED TURBULENT FLOW

(AIAA-84-1605)

**FIVE-HOLE PITOT PROBE MEASUREMENTS OF SWIRL,  
CONFINEMENT AND NOZZLE EFFECTS ON CONFINED TURBULENT FLOW**

G. L. Scharrer\* and D. G. Lilley\*\*  
Oklahoma State University  
Stillwater, Oklahoma 74078

**Abstract**

Nonswirling and swirling inert flows are investigated in axisymmetric test sections with expansion ratio 1 and 1.5 and the following geometric parameters: side-wall expansion angle  $\alpha = 45$  and  $90$  degrees, swirl vane angle  $\phi = 0$  (swirler removed),  $45$  and  $70$  degrees, and downstream blockages of area ratios  $2$  and  $4$  located  $2$  diameters from the test section inlet. The time-mean velocity components are obtained, via a five-hole pitot probe, for all the flows studied. The corner recirculation zone is prominent in nonswirling expanding flows, but it decreases when swirl is introduced. The presence of swirl results in the formation of a central recirculation zone. Initially, increases in inlet swirl strength result in an increase in length of this zone. However, increasing to very high swirl strengths results in a shortening and widening of this zone. Placing a downstream nozzle in the flowfield creates an adverse pressure gradient near the wall and a favorable pressure gradient near the centerline. This results in increased axial and swirl velocities near the centerline and decreased velocities near the wall. It also decreases the central recirculation zone length. The degree of the effect increases as the degree of blockage increases. Reduction of the expansion ratio results in a reduction of the central recirculation zone length. The corner recirculation zone length (measured in step heights) does not change appreciably with expansion ratio for ratios greater than  $1$ . Gradual expansion has a minimal effect on the flow.

**Nomenclature**

C	velocity coefficient = $\rho v^2 / [2(p_c - p_w)]$
CRZ	corner recirculation zone
CTRZ	central toroidal recirculation zone
D	test section diameter
d	inlet nozzle diameter
L	downstream blockage location
p	time-mean pressure
Re	Reynolds number
$v = (u, v, w)$	time-mean velocity (in x-, r-, $\theta$ -directions)
V	time-mean velocity vector magnitude

\* Graduate Student, School of Mechanical and Aerospace Engineering, Student Member AIAA  
\*\* Professor, School of Mechanical and Aerospace Engineering, Associate Fellow AIAA

This paper is declared a work of the U.S. Government and therefore is in the public domain.

x, r, $\theta$	axial, radial, azimuthal cylindrical polar coordinates
$\alpha$	side-wall expansion angle
$\beta$	yaw angle of probe = $\tan^{-1}(w/u)$
$\delta$	pitch angle of probe = $\tan^{-1}[v/(u^2 + w^2)^{1/2}]$
$\rho$	density
$\phi$	swirl vane angle = $\tan^{-1}(w_{in}/u_{in})$ , assuming perfect vanes

**Subscripts**

C	central pitot pressure port
d	relating to inlet nozzle diameter
in	inlet conditions
N, S, E, W	north, south, east, west pitot pressure ports
o	value at inlet to flowfield
h	swirl vane hub; expansion step height
p	relating to probe sensing tip diameter

**1. Introduction**

The state of the art in combustor design has been advanced significantly in recent years because of the need for greater fuel efficiency and fuel versatility: engines must be capable of burning cheaper fuels and/or several different types of fuels. Researchers have utilized many different means in order to study the phenomena of combustion: computer simulation;<sup>1-9</sup> instantaneous and time-mean velocity measurements;<sup>2-20</sup> flow visualization;<sup>7-9, 21-24</sup> and heat transfer and temperature measurements.<sup>19, 23, 24</sup> The ultimate goal of research efforts is to develop cost-effective computer programs that accurately describe the process for any combination of physical parameters. However, experimental data for the system to be modeled must be available in order to validate the models used in computer codes.

As part of an on-going research study at Oklahoma State University on 'Investigation of Flowfields Found in Typical Combustion Geometries', studies are in progress concerned with experimental and theoretical research in 2-D axisymmetric geometries under low speed, nonreacting, turbulent, swirling flow conditions. The aim is to characterize the time-mean and turbulence flowfield, recommend appropriate turbulence model advances, and implement and exhibit results of flowfield predictions. The present contribution concentrates on the time-mean flow characterization via the five-hole pitot probe technique and is based on a recently-completed M.S. Thesis,<sup>25</sup>

extending earlier work<sup>10</sup> to more configurational changes.

The effect of confinement and downstream nozzle contraction ratios on swirling flowfields are not yet well explored in the literature. Therefore, to highlight these effects, three expansion ratios  $D/d$  (combustion chamber diameter/jet diameter) and two contraction ratios  $A/a$  (combustion chamber area/contraction nozzle area) were selected. The expansion ratios are 2, 1.5 and 1 while the contraction ratios are 4 and 2. The contraction nozzle is located at  $L/D = 2$  or  $L/D = 1$ , where  $L$  is the distance downstream of the inlet to the flow domain. Data acquisition is via a five-hole pitot probe enabling three time-mean velocity components in the axial, radial and azimuthal directions to be measured. The earlier study<sup>10</sup> investigated the case  $D/d = 2$ ; the present study uses  $D/d = 1.5$  and 1 for comparison purposes. A corresponding flow visualization investigation using photography of neutrally-buoyant helium-filled soap bubbles is also detailed in Ref. 25, although no results are presented in the present paper.

Previous relevant studies are presented in Section 2. Section 3 recalls the facilities and instrumentation employed, along with the procedure for five-hole pitot-probe measurements and data reduction. Results are presented and discussed in Section 4, while Section 5 draws conclusions from the study.

## 2. Review of Previous Studies

Bradshaw and Wong<sup>3</sup> used three different geometric perturbations to study the reattachment of a turbulent shear layer. The study showed that a nonswirling flow reattaches 6 to 9 step heights downstream of separation. It was also observed that the flow just downstream of reattachment bears very little resemblance to a plane mixing layer of any other sort of thin shear, even if the residual influence of the boundary layer is small.

Macagno and Hung<sup>5</sup> used dye injection and still photographs to study a laminar oil flow past a 2:1 diameter expansion. Streamline and vorticity contours are presented. The contours show that the main flow when separation occurs, then moves back to the wall well downstream of the reattachment point.

Time-mean velocity measurements and several means of flow visualization were employed by Rhode<sup>7-9</sup> to study inert nonswirling and swirling flowfields. Photographs, streamline contours and velocity profiles of the flowfield are presented for a  $D/d = 2$  case. A five-hole pitot probe was used by Yoon<sup>10,11</sup> to measure velocities in the same test section, with additionally downstream nozzle effects included. Velocity profiles and streamline contours are presented to illustrate the effects of swirl and geometric parameters on the flowfield. The results of the present study are compared with those obtained by Yoon to determine the effects of swirl, confinement and downstream nozzle on the flowfield.

A nonswirling flowfield, similar to that of Refs. 7 through 11, was studied by Chaturvedi<sup>14</sup> to determine the effect of inlet expansion angle  $\alpha$  on the flow. It was found that the reattachment point

moved downstream from 6 to 9 step heights as the expansion angle was increased from 15 to 90 degrees. The author also suggested that varying the expansion ratio  $D/d$  would not affect the flow near the exit plane  $x/D = 0$ , because the primary effect of the change would be on the mixing process and diffusion after the maximum rate of turbulence production is obtained.

Syred and Dahman<sup>16</sup> studied the effect of confinement on an inert swirling flow. It was found to be complex because of two effects: entrainment rates of swirling jets are very high, which can cause them to "stick" to the wall; decay of swirl velocity is usually uneven across the enclosure. Their study was  $D/d$  ratios of 4 and 2; the present study uses  $D/d$  ratios of 1.5 and 1.

A Laser Doppler Anemometer located the reattachment point for a turbulent, nonswirling flow at 4.5 step heights downstream of the exit plane in a study performed by Yang and Yu<sup>18</sup> with  $D/d = 2.7$ . The authors theorized that the reattachment point was unusually far upstream as a result of a large back pressure caused by a short, rapidly contracting nozzle of area ratio  $A/a = 7.25$  which followed by sudden enlargement. Indeed, most researchers,<sup>2,3,5,6,14,21</sup> found the reattachment point to be 6 to 9 step heights downstream of the exit plane.

## 3. Experimental Equipment and Procedure

### 3.1 The Test Facility

The confined jet test facility is described at length elsewhere.<sup>7-11</sup> It has a variable speed axial flow fan that drives the flow through a settling chamber and into a contraction section designed by the method of Morel<sup>6</sup>. The flow leaves the contraction section via a 15 cm diameter circular nozzle and enters the test section. The test section is a constant diameter plexiglass tube with length greater than 5 tube diameters; this minimizes the presence of end-effects in the measuring region  $x/D < 2.0$ . Test section diameters of 22.5 and 15 cm are used in the present study; a 30 cm diameter test section was used in previous studies. The side-wall angle  $\alpha$  and the swirl vane angle  $\phi$  are variable. No side-wall expansion is used for the smaller tube, while angles of  $\alpha = 45$  and 90 degrees are used for the larger tube. Swirl vane angles of 0 (swirler removed), 45 and 70 degrees are used for both tubes.

Typical operating Reynolds numbers (based on average inlet velocity and inlet diameter) range from 50,000 to 150,000 depending upon fan speed and aerodynamic blockage by the swirl vanes. It has been shown that this is the Reynolds number insensitive region for this facility<sup>7</sup> in terms of nondimensional flow characteristics further downstream.

The effect of a downstream blockage on the upstream flow in the test section is important in combustion aerodynamics. Two blockages of area ratio 2 and 4 are used, with each of the two test sections. Their design is illustrated in Ref. 11, and their side-view contours are seen later in the figures. These blockages when used, are located 2 tube diameters downstream of the inlet plane  $x/D = 0$ .

### 3.2 The Swirler

Swirling jets are commonly used to control the length and stability of the flame in a combustor, and the effects of the degree of inlet swirl on the flowfields and combustion have been extensively studied.<sup>27</sup> Researchers typically use either a vane swirler or a tangential entry mixing chambers to impart swirl to the flow under study; a variable-angle vane swirler is used in the present study. It was constructed at Oklahoma State University according to a preliminary design plan from NASA. The physical features of the swirler are diagrammed in detail in Ref. 28; the performance of the swirler is detailed in Refs. 20 and 29. It may be noted that the ten variable-angle flat blades of pitch-to-chord ratio 0.68 give good turning efficiency, but Sander and Lilley<sup>29</sup> have shown that the idealized  $\phi$  vs.  $S$  relationships are not correct, and nonuniform axial and swirl profiles (with nonzero radial velocity) emanate from the swirler exit.

### 3.3 Five-Hole Pitot Probe Instrumentation

A five-hole pitot probe was chosen as the measuring instrument for this study because the probe is reliable, accurate, and it is capable of measuring both the magnitude and the direction of the time-mean flow velocity. The pitot probe used in this study is a model DC-125-12-CD manufactured by United Sensor and Control Corporation. The accuracy of this particular probe is well-documented and it is has been used extensively on earlier studies.<sup>7-11</sup> After calibration, in use on a radial traverse, the probe is rotated so as to align the probe sensing head with the local flow direction in the  $x\theta$ -plane, hence establishing the yaw angle  $\beta$  of the flow. The total velocity magnitude  $V$  and pitch angle  $\delta$  are then deduced from calibration characteristics. Extensive discussion about the technique appear in Refs. 7 through 11 and 25.

### 3.4 Data Reduction and Accuracy

A Fortran code similar to that developed by Rhode<sup>7</sup> is used to reduce the data. The code uses the radial traverse data and the pitch angle calibration characteristic in conjunction with a cubic spline interpolation technique to obtain the pitch angle  $\delta$ . Then, the velocity coefficient is determined using  $\delta$  and the velocity coefficient calibration characteristic. The absolute velocity is then determined, from which the velocity components are deduced using the pitch and yaw angles, and simple geometry.

It should be noted that the effect of the fluctuating turbulent component of velocity is ignored in relating sensed pressures to time-mean velocities. The additional terms cannot be measured by the instruments in use here, and although the effect on pressure probes is still unknown, the error incurred is likely to be less than five percent except in very high turbulence regions. It should also be noted that the five-hole pitot probe is of questionable accuracy in high shear regions. However, these regions are encountered infrequently in this study. Therefore, the general trends found herein are certainly valid.

## 4. Results and Discussion

Nonswirling and swirling inert flows are investigated in axisymmetric test sections with expansion ratio of 1 or 1.5, which may be equipped with a downstream blockage of area ratio 2 or 4. Time-mean velocity measurements are performed as described in Section 3. The effect of the following geometric parameters on the extent of the flowfield recirculation zones is analyzed: expansion ratio  $D/d = 1$  and 1.5, sidewall expansion angle  $\alpha = 45$  and 90 degrees, swirl vane angle  $\phi = 0, 45$  and 70 degrees, and downstream blockage of area ratio 2 and 4. The nozzle inlet Reynolds numbers employed in this study are high enough to ensure that the flowfields being investigated are independent of the Reynolds number; the Reynolds number corresponding to each flow case is listed in Table 1.

Table 1. Wind Tunnel Fan Speeds and Inlet Nozzle Reynolds Number

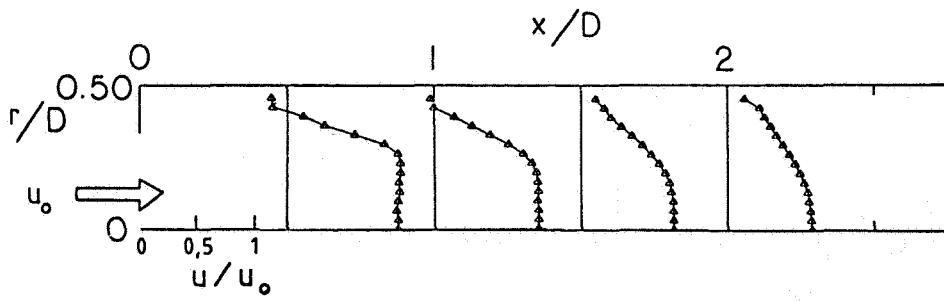
$\phi$	Fan Speed (rpm)	$Re_{(D/d=d_{1.5})}$	$Re_{(D/d=d_{1.0})}$
0	1950	125,000	86,400
45	2600	66,600	64,400
70	2600	28,700	28,000

### 4.1 Effects of Swirl on Open-Ended Flows

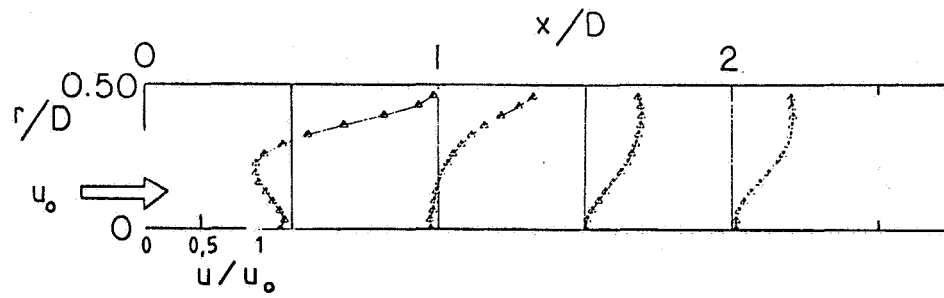
A variable-angle vane swirler is used in the present study to impart a tangential velocity component to the inlet flow. Swirl vane angles of 0 (swirler removed), 45 and 70 degrees are used. Figure 1 parts a through c shows the axial and swirl velocity profiles for  $\phi = 0, 45$  and 70 degrees, respectively, for the test section with expansion ratio  $D/d = 1.5$ . Figure 2 parts a through c, show the corresponding results for the test section with  $D/d = 1$ .

The swirler is removed to obtain results for the nonswirling case. Flow visualization studies<sup>25</sup> show that the corner recirculation zone (CRZ) extends to approximately  $x/D = 1.25$ ; this translates to 7.5 step heights from the exit plane  $x/D = 0$ . Inspection of Figure 1a verifies that the reattachment point is between  $x/D = 1.0$  and 1.5, but the reattachment location cannot be specified based on this figure. Moon and Rudinger<sup>12</sup> used a similar expansion ratio ( $D/d = 1.43$ ) and found the reattachment point at  $x/D = 1.25$  (approximately 8 step heights downstream of the exit plane). This is in good agreement with the present study.

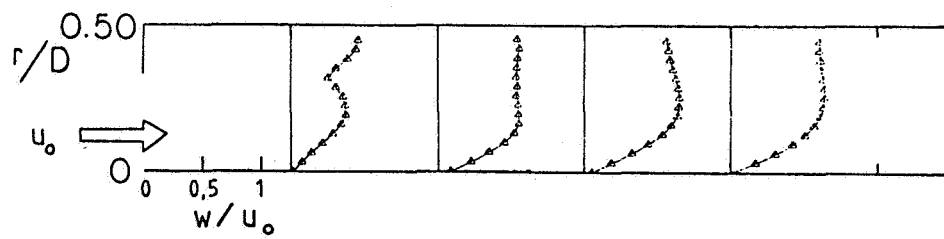
For the intermediate swirl case of  $\phi = 45$  degrees, only a small corner recirculation zone CRZ is observed. The reattachment point is located at about  $x/D = 0.25$ . No CRZ is apparent for the strong swirl flow ( $\phi = 70$  degrees): centrifugal forces dominate this flow. The centrifugal forces in the flow result in the formation of a central toroidal recirculation zone CTRZ and a precessing vortex core, as shown in the photographs of Ref. 25. The precessing vortex core is a region of high swirl, low axial velocity flow along the axis, and relatively constant small diameter. It extends



(a)  $\phi = 0^\circ$



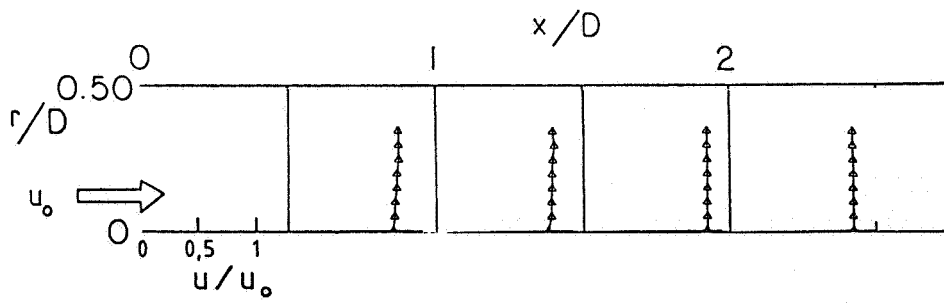
(b)  $\phi = 45^\circ$



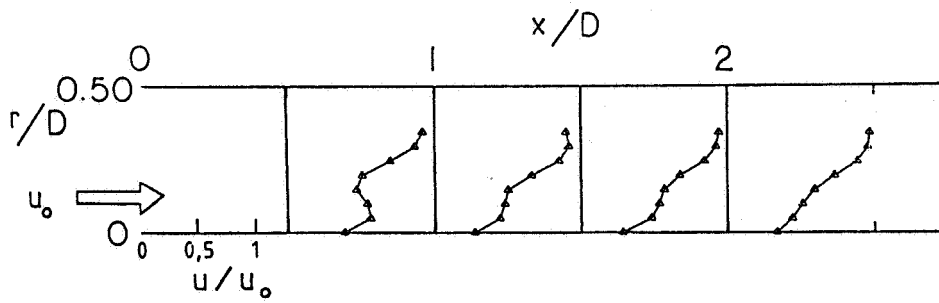
(c)  $\phi = 70^\circ$

Fig. 1. Velocity Profiles for Open-Ended Flows with Expansion Ratio  $D/d = 1.5$  and Expansion Angle  $\alpha = 90^\circ$

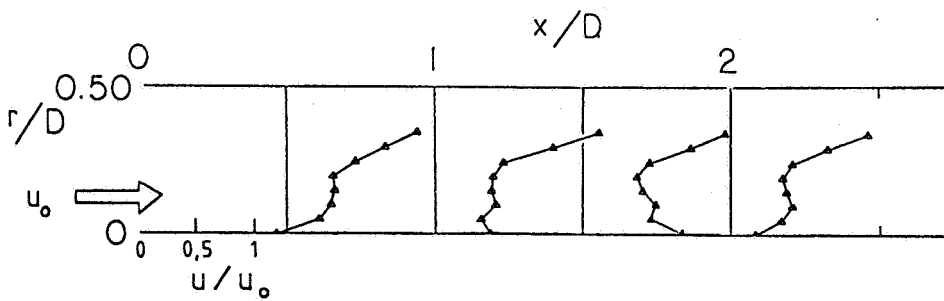
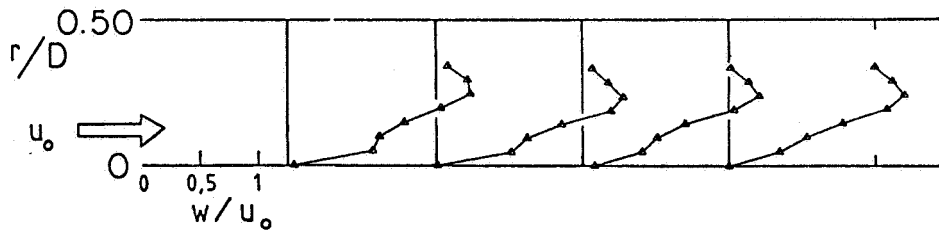




(a)  $\phi = 0^\circ$



(b)  $\phi = 45^\circ$



(c)  $\phi = 70^\circ$

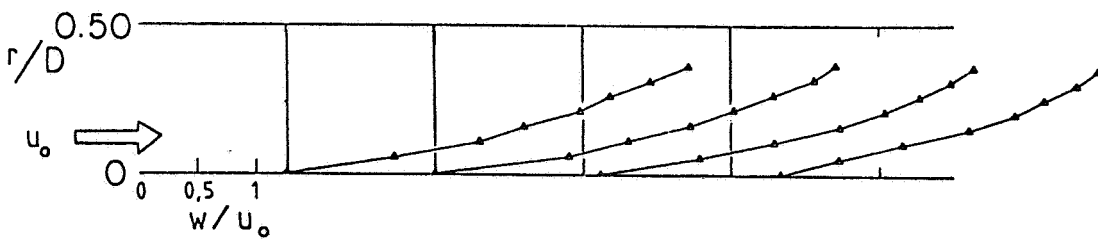


Fig. 2. Velocity Profiles for Open-Ended Flows with Expansion Ratio  $D/d = 1.0$

from the end of the CTRZ to the test section exit. The CTRZ is a wide reverse flow region encountered near the inlet. Further inspection of the flow visualization photographs shows the CTRZ ending at  $x/D = 1.5$  for the moderate swirl case, and ending at  $x/D = 0.75$  for the strong swirl case. Observation of parts b and c of the figure concur with this finding.

The swirl velocity profiles are nearly uniform in the near-wall region but decrease in an almost linear slope to a zero value at the centerline. The radial location of the maximum swirl velocity moves outward for the strong swirl case due to centrifugal effects. The swirl nonuniformity at  $x/D = 0.5$  is due to the insensitivity of the five-hole pitot probe to small velocities, this same result was obtained in similar problems also being encountered in Refs. 7 and 10.

The velocity profiles in Figure 2 parts a, b, and c show how the flowfield of Figure 1 changes when the expansion ratio is reduced to 1.0. The axial velocity in Figure 2a is merely plug flow. Centrifugal effects dominate the axial and swirl profiles of parts b and c of Figure 2: the highest velocities are located farthest from the centerline. The profiles change very little as they move downstream. In addition, there is no CTRZ for the moderate swirl case and only a small CTRZ extending to  $x/D = 0.5$  for the strong swirl case.

Concerning the CRZ, after comparing the present data for  $D/d = 1.5$  with the data of Yoon<sup>10</sup>, Moon and Rudinger,<sup>12</sup> and data tabulated by Sinder and Harsha,<sup>30</sup> it can be seen that the reattachment point for a suddenly expanding nonswirling flow is found to be between 6 to 9 step heights downstream of the inlet regardless of the expansion ratio. Table 2 amalgamates the data, to show the consistency of reattachment point location for  $D/d > 1$ .

Table 2. Corner Recirculation Zone Lengths for Nonswirling Flow

Expansion Ratio (D/d)	CRZ Length in Step Heights
1.43	8
1.5	7.5
1.73	8
2	8
3	6.25

Table 3 and Figure 3 show the variation of CTRZ length with expansion ratio, using the present data and that of Ref. 10. They show no clear trend for moderate swirl: the CTRZ length decreases from 1.6 to 1.5 to 0 diameters as the expansion ratio decreases from 2 to 1.5 to 1. However, there is a steady decrease in CTRZ length for strong swirl: it goes from 1.2 to 0.75 to 0.5 diameters as the expansion ratio goes from 2 to 1.5 to 1. In general, the length of the CTRZ decreases as the expansion ratio decreases, and this effect becomes more pronounced as the swirl strength increases.

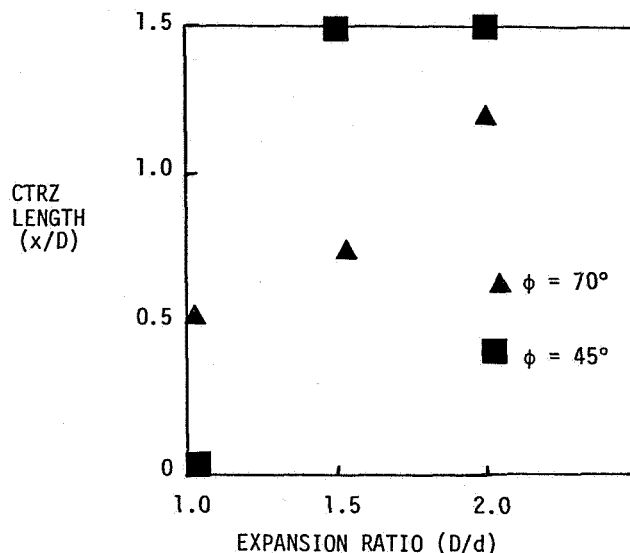


Fig. 3. Central Recirculation Zone Lengths vs. Expansion Ratio for Swirling Flow

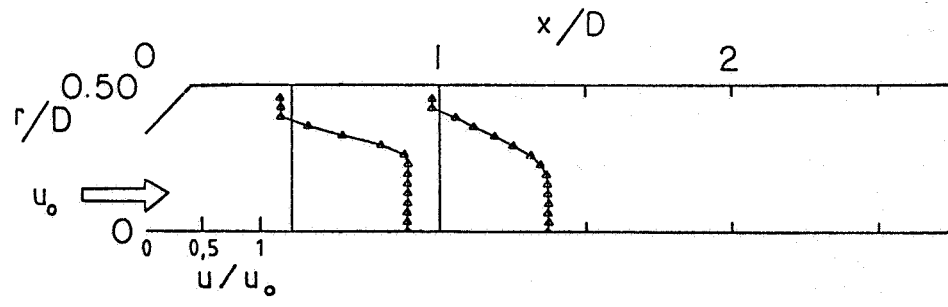
Table 3. Central Recirculation Zone Lengths for Swirling Flow

D/d	$\phi = 45$	$\phi = 70$
1.0	0	0.5
1.5	1.5	0.75
2.0	1.6	1.2

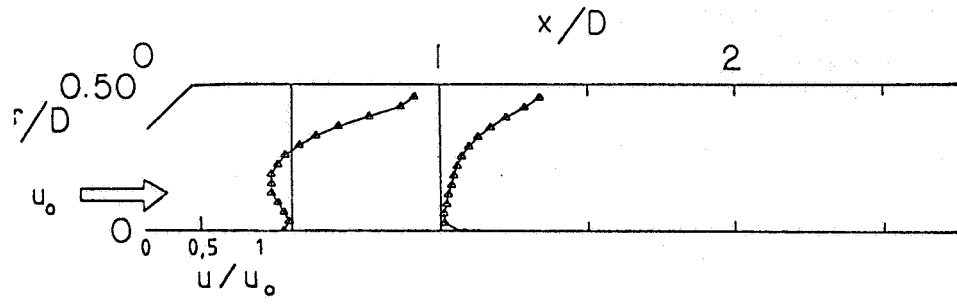
#### 4.2 Effects of Gradual Expansion on Open-Ended Flows

Photography of gradual expansion flows with  $\alpha = 45$  degrees revealed significant effects only near the inlet location. Hence, they were measured only at  $x/D = 0.5$  and 1 for  $\phi = 0, 45$  and 70 degrees. This was, of course, only the case  $D/d = 1.5$  and the velocity profiles are shown in parts a, b and c of Figure 4. Only a small effect of the gradual expansion inlet is felt on the flow. The nonswirling flow measurements plotted in Figure 4a appear to be identical to the corresponding sudden expansion flow data in Figure 1a. Photographs also identify the reattachment point in both case to be at  $x/D = 1.25$ . Swirling flow photographs show no change in CTRZ length with gradual expansion; and the velocity profiles of Figure 4 parts b and c differ from parts b and c of Figure 1 in only one respect: increased near-wall swirl velocity for the gradual expansion case in the upstream region.

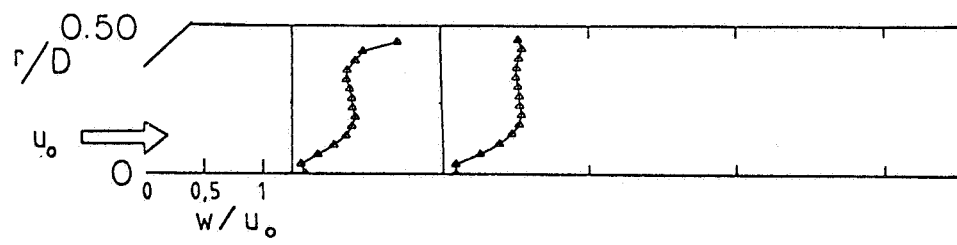
It may be concluded that the major effect of a gradual expansion is to encourage the air to flow along the wall and accelerate axial velocities close to the wall. That effect is diminished when the expansion ratio decreases. Since a gradual expansion does not appreciably alter a flowfield,



(a)  $\phi = 0^\circ$



(b)  $\phi = 45^\circ$



(c)  $\phi = 70^\circ$

Fig. 4. Velocity Profiles for Open-Ended Flows with Expansion Ratio  $D/d = 1.5$  and Expansion Angle  $\alpha = 45^\circ$

it would be redundant to investigate a gradual expansion flow with downstream blockage. Hence blockage effects investigated in Section 3.3 are for the sudden expansion and no expansions cases only.

### 4.3 Effects of Blockages on Flows

To better illustrate the effects of downstream blockages, the data obtained with each blockage in place are compared to the data obtained for open-ended flows. Measurements were taken at the same locations (when necessary) as for the open-ended flows of Section 3.1. The velocity profiles for flows with the small blockage of area ratio  $A/a = 2$  are shown in Figs. 5 and 6, for the cases  $D/d = 1.5$  and 1, respectively. The velocity profiles for flows with the large blockage (area ratio 4) are shown in Figs. 7 and 8. The blockages are placed 2 chamber diameters downstream of the exit plane in each case.

For the nonswirling flow with expansion ratio 1.5, the weak downstream nozzle shortens somewhat the CRZ with reattachment point  $x/D = 1.2$ , but streamlines are altered only at the blockage location itself. Figure 5a shows the velocity profiles at  $x/D = 2.0$  only. The axial velocity is essentially zero near the wall and the centerline region is accelerated, as expected. In addition, a small swirl velocity is induced in the near-wall region. The moderate swirl flowfield in part b of the figure has a shorter CTRZ (it extends to  $x/D = 1.25$ ) and higher axial velocities near the centerline than the corresponding open-ended flow shown in part b of Figure 1. The corner recirculation zone appears to be unaffected by the blockage, but in any case it is very small in length (0.25 diameters). Also, the swirl velocity and the swirl velocity gradient in the radial direction increase slightly with the small blockage in place. When the swirl vane angle is increased to 70 degrees, the CTRZ length decreases to  $x/D = 0.4$  and the precessing vortex core becomes noticeably wider. Figure 5c shows axial velocities that are diminished in the near-wall region and accelerated near the centerline, and swirl velocities that are increased near the centerline in comparison to the velocities shown in Figure 1c. The only change from the moderate swirl case is the wider vortex core.

Decreasing the expansion ratio to 1 does not change the relation between the small-blocked flows and the open-ended flows that is documented above. Figure 6 shows: axial velocities that are diminished near the wall and increased near the centerline; swirl velocities that are increased near the centerline and diminished near the wall for the swirling flows; and a small induced swirl velocity near the wall for the nonswirling flow. The only change is for the strong swirl flow in part c: the centerline axial velocities at  $x/D = 0.5$  and 1 are large and negative, indicating that the CTRZ is longer for the small-blocked flow than for the open-ended flow. This phenomenon does not occur in strong swirl flows for other expansion ratios; it is most likely a result of continuity: the near-centerline velocities are increased and the near-wall velocities are not yet appreciably diminished, thus the centerline flow is reversed to balance the mass flows.

When the data of Figures 5 and 6 are compared to the analogous data of Ref. 10, it is clear that placing a small blockage 2 diameters downstream of the exit plane produces the same changes from the open-ended case regardless of the expansion ratio: the axial and swirl velocities decrease near the wall and increase near the centerline for swirling and nonswirling flows, with the exception of the small induced swirl in the nonswirling flow.

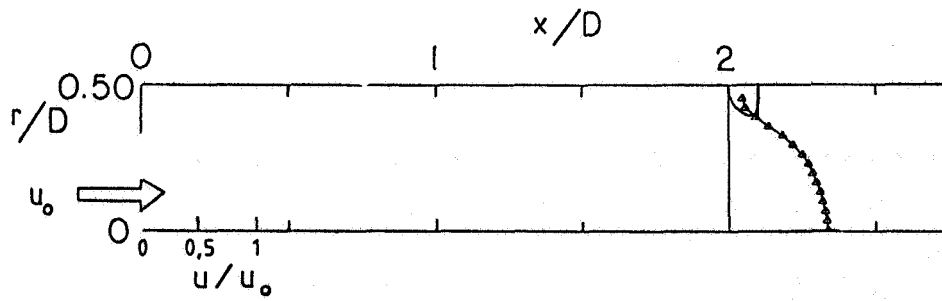
The effect of a stronger downstream nozzle of area ratio 4 is also investigated for swirl vane angles  $\phi = 0, 45$  and 70 degrees on flowfields with expansion ratios of 1.5 or 1. The axial and swirl velocity profiles are shown in Figures 7 and 8 for  $D/d = 1.5$  and 1, respectively. The nonswirling flow of Figure 7a shows a CRZ extending to about  $x/D = 1.2$ , larger centerline velocities than for the unblocked flow and a slight induced swirl in the near-wall region at  $x/D = 2$ . This flowfield is very similar to that of Figure 5a - the slightly blocked flow. The axial velocity profiles of Figure 7b detail the significant effect of the large blockage on the moderately swirling flow. The near-wall velocities are blunted all the way upstream to  $x/D = 0.5$ , and the accompanying centerline acceleration results in the absence of a CTRZ. The swirl velocities shown in the same figure are noticeably greater than those of part b of Figures 1 and 5. Figure 7c shows that there is a negative axial velocity annular region at  $x/D = 0.5$  but it is small; therefore, it is probable that the CTRZ ends near  $x/D = 0.5$ . Again, the centerline axial and swirl velocities are increased and the near-wall axial and swirl velocities are decreased from their unblocked counterparts on account of the presence of the blockage. It should be noted that the centerline axial velocities for the strong swirl flow do not increase nearly as much as for the moderate swirl flow; this is because of the dominance of centrifugal forces, and the lower axial momentum of the strong swirl flow.

Reducing the expansion ratio to 1 results in the flowfield alterations shown in Figure 8 parts a, b, and c. The nonswirling flow of part a exhibits the familiar change: induced swirl near the blockage and centerline acceleration. For the moderate swirl of part b, the velocity profiles are nearly identical to Figure 7b for expansion ratio 1.5: large increase in centerline axial and swirl velocities are diminished near-wall velocities. Again, the strong swirl flow of part c is essentially an exaggerated version of Figure 6c: the centerline axial velocities at  $x/D = 0.5$  and 1.0 are negative; the off centerline axial and swirl velocities are very large; and the axial and swirl velocities diminish near the wall.

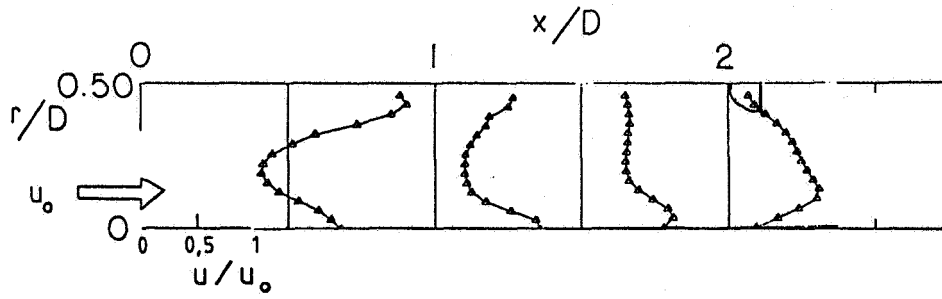
Correlating the present data to that of Ref. 10 for  $D/d = 2$ , it is clear that the effect of a blockage is to: accelerate the axial and swirl velocities near the centerline; diminish those velocities near the wall; and decrease the length of the CTRZ. The effect is greater when the degree of blockage is greater. For strong swirl flows, a blockage increases the length of CTRZ when the expansion ratio is 1. Otherwise (that is,  $D/d > 1$ ) a blockage shortens the CTRZ.

## 5. Conclusions

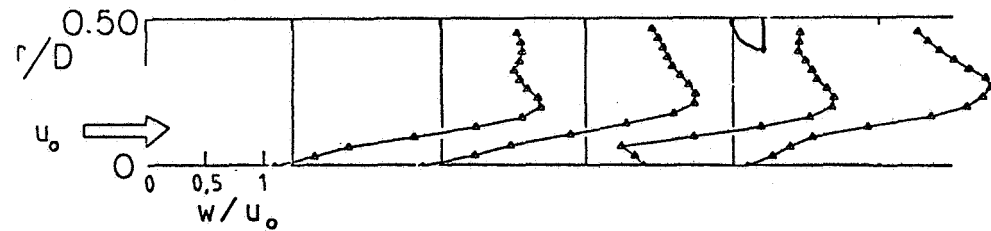
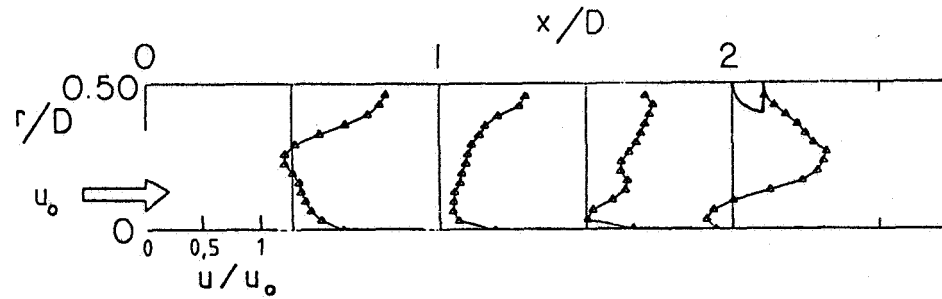
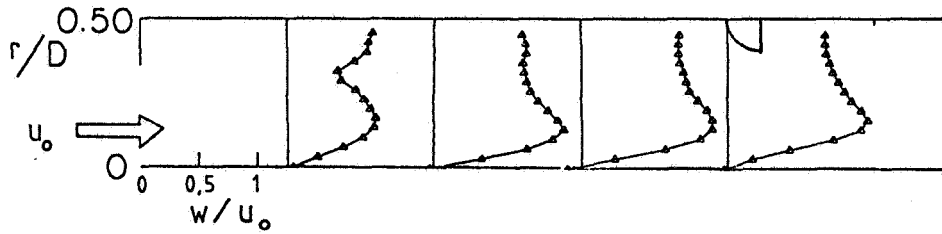
The corner recirculation zone is prominent in nonswirling expanding flows, but it decreases when



(a)  $\phi = 0^\circ$

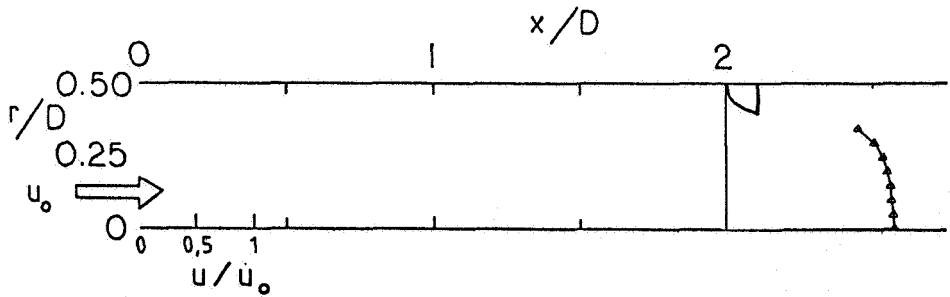


(b)  $\phi = 45^\circ$

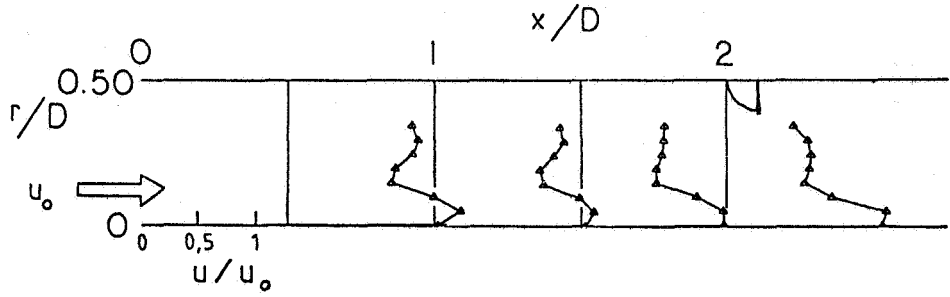


(c)  $\phi = 70^\circ$

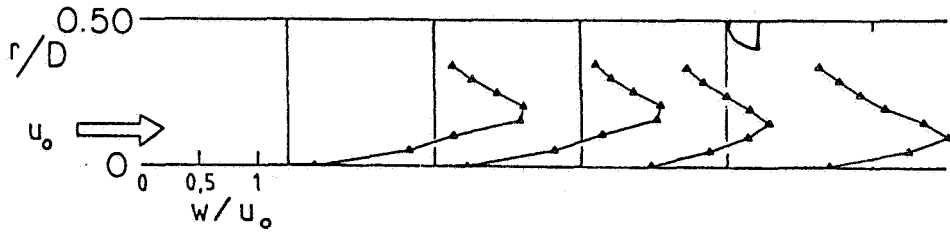
Fig. 5. Velocity Profiles for Flows with Expansion Ratio  $D/d = 1.5$ , Expansion Angle  $\alpha = 90^\circ$  and Small Blockage



(a)  $\phi = 0^\circ$



(b)  $\phi = 45^\circ$



(c)  $\phi = 70^\circ$

Fig. 6. Velocity Profiles for Flow with Expansion Ratio  $D/d = 1.0$  and Small Blockage

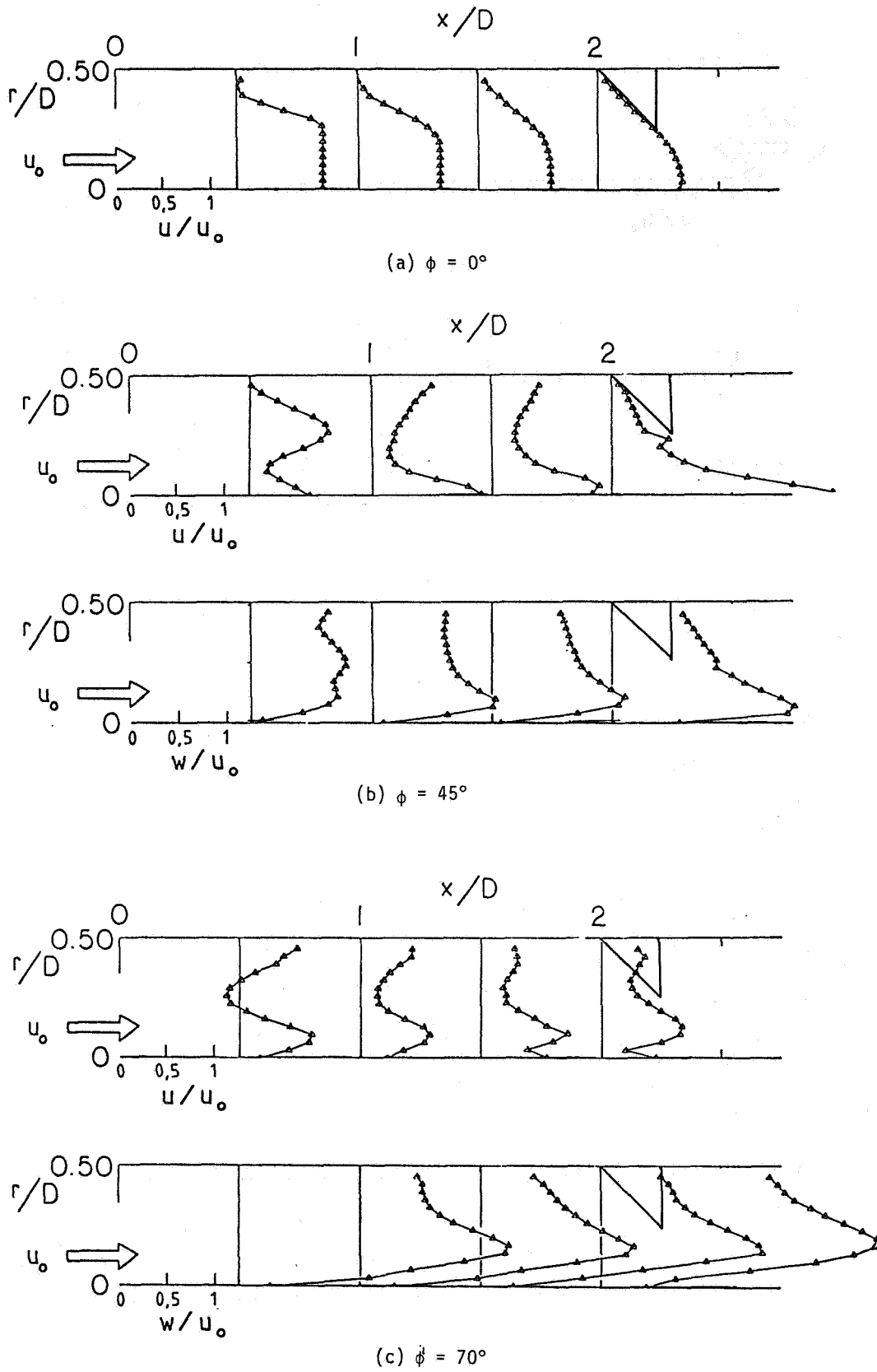


Fig. 7. Velocity Profiles for Flow with Expansion Ratio  $D/d = 1.5$ , Expansion Angle  $\alpha = 90^\circ$  and Large Blockage

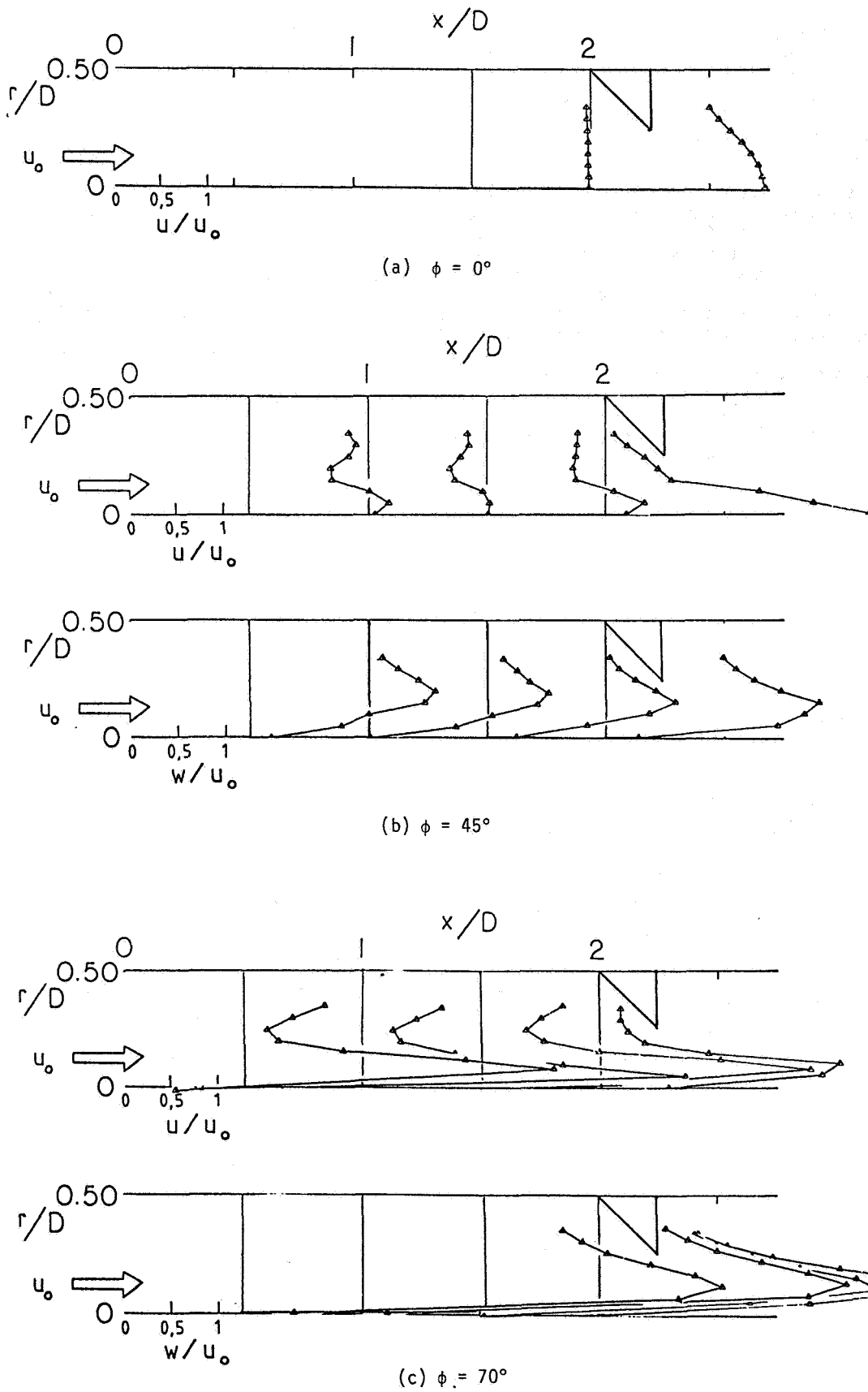


Fig. 8. Velocity Profiles for Flow with Expansion Ratio  $D/d = 1.0$  and Blockage



swirl is introduced and disappears when centrifugal forces predominate. The presence of swirl results in the formation of a central recirculation zone. Initially, increases in  $d$  result in an increase in its length, but increasing  $d$  to very high swirl strengths results in a shortening and widening of this zone.

Placing a blockage in the flowfield creates an adverse pressure gradient near the wall and a favorable pressure gradient near the centerline. This results in increased axial and swirl velocities near the centerline and decreased velocities near the wall. The Blockage also decreases the central recirculation zone length, except for strong swirl flows with no expansion (that is,  $D/d = 1$ ). The degree of the effect increases as the degree of blockage increases.

Reduction of the expansion ratio results in a reduction of the size of the central recirculation zone, as is apparent when the present data are compared previous studies. This central zone vanishes for moderate swirl in a nonexpanding flow. Also, placing a blockage in a nonexpanding, strongly swirling flow increases the narrow central recirculation zone length; an opposite effect is observed for expanding (that is,  $D/d > 1$ ) flows. The corner recirculation zone length (measured in step heights) does not change with expansion ratio for  $D/d > 1$ .

Changing the inlet from sudden to gradual expansion has a minimal effect on the flow.

#### Acknowledgments

The authors wish to gratefully acknowledge NASA Lewis Research Center and Air Force Wright Aeronautical Laboratories for financial support under Grant No. NAG 3-74, technical monitor Dr. J. D. Holdeman. Special thanks are offered to Dr. M. T. Abujelala for assistance with the data reduction and graphics.

#### References

- Abujelala, M. T. and Lilley, D. G., "Confined Swirling Flow Predictions," Paper AIAA-83-0316, Reno, Nevada, January 10-13, 1983.
- Ha Minh, H. and Chassaing, P., "Perturbations of Turbulent Pipe Flow," Proceedings, Symposium on Turbulent Shear Flows, Pennsylvania State University, April 1977, pp. 13.9-13.17.
- Bradshaw, P. and Wong, F. Y. F., "Reattachment of a Confined Turbulent Diffusion Flame Burner," *Journal of Fluid Mechanics*, Volume 52, Pt. 1, 1972, pp. 113-135.
- Hutchinson, P., Khalil, E. E., and Whitelaw, J. H., "Measurement and Calculation of Furnace-Flow Properties," *Journal of Energy*, Volume 1, July-August 1977, pp. 211-219.
- Macagno, E. D., and Hung, Tin-Kan, "Computational and Experimental Study of a Captive Annular Eddy," *Journal of Fluid Mechanics*, Vol. 28, Pt. 1, 1967, pp. 43-64.
- Nozaki, T., and Hatta, Keiji, "Reattachment Flow Issuing From a Finite Width Nozzle (Report 3: Effects of Inclinations of Reattachment Wall)," *Bulletin of the JSEM*, Volume 25, No. 200, February 1982.
- Rhode, D. L., "Predictions and Measurements of Isothermal Flowfields in Axisymmetric Combustor Geometries," Ph.D. Thesis, Oklahoma State University, Stillwater, Okla., Dec. 1981.
- Rhode, D. L., Lilley, D. G., and McLaughlin, D. K., "On the Prediction of Swirling Flowfields Found in Axisymmetric Combustor Geometries," *ASME Journal of Fluids Engng.*, Vol. 104, 1982, pp. 378-384.
- Rhode, D. L., Lilley, D. G., and McLaughlin, D. K., "Mean Flowfields in Axisymmetric Combustor Geometries with Swirl," Paper AIAA-82-0177, Orlando, Florida, Jan. 11-14, 1982.
- Yoon, H. K., "Five-Hole Pitot Probe Time-Mean Velocity Measurements in Confined Swirling Flows," M.S. Thesis Oklahoma State University, Stillwater, Okla., July 1982.
- Yoon, H. K., and Lilley, D. G., "Five-Hole Pitot Probe Time-Mean Velocity Measurements in Confined Swirling Flows," Paper AIAA-83-0315, Reno, Nevada, January 10-13, 1983.
- Moon, L. F., and Rudinger, "Velocity Distribution in an Abruptly Expanding Circular Duct," *Journal of Fluids Engineering*, March 1977, pp. 226-230.
- Janjua, S. I., "Turbulence Measurements in a Complex Flowfield Using a Six-Orientation Hot-Wire Technique," M.S. Thesis, Oklahoma State University, Stillwater, Okla., Dec. 1981.
- Chaturvedi, M. C. "Flow Characteristics of Axisymmetric Expansions," *Proceeding, Journal of Hydraulics Division, ASCE*, Vol. 89, No. HY3, 1963, pp. 61-92.
- Mathur, M. L., and MacCallum, N. R. L., "Swirling Air Jets Issuing from Vane Swirlers. Part 1: Free Jets; Part 2: Enclosed Jets," *Journal of the Institute of Fuel*, Vol. 40, May, 1967, pp. 238-245.
- Syred, N., and Dahman, K. R., "Effect of High Levels of Confinement Upon the Aerodynamics of Swirl Burners," *Journal of Energy*, Vol. 2, No. 1, Jan. - Feb. 1978, pp. 8-15.
- Afrosimova, V. N., "Study of the Aerodynamics of a Furnace Space," *Thermal Engineering*, Vol. 14, Part 1, 1967, pp. 10-15.
- Yang, B. T., and Yu, M. H., "The Flowfield in a Suddenly Enlarged Combustion Chamber," *AIAA Journal*, Vol. 21, No. 1, Jan. 1983, pp. 92-97.
- Owen, F. K., "Laser Velocimeter Measurements of a Confined Turbulent Diffusion Flame Burner," Paper AIAA-76-33, Washington, D. C., Jan. 26-28, 1976.

20. Sander, G. F., "Axial Vane-Type Swirler Performance Characteristics," M.S. Thesis, Oklahoma State University, Stillwater, Okla., July 1983.
21. Abbott, D. E., and Kline, S. J., "Experimental Investigation of Subsonic Turbulent Flow Over Single and Double Backward Facing Steps," *Journal of Basic Engineering*, Sept. 1962, pp. 317-325.
22. Bird, J. D., "Visualization of a Flowfield by Tuft Grid Technique," *Journal of Aeronautical Science*, Vol. 19, 1952, pp. 481-485.
23. Back, L. H. and Roschke, E. J., "Shear Layer Flow Regimes and Wave Instabilities and Reattachment Lengths Downstream of an Abrupt Circular Channel Expansion," *Journal of Applied Mechanics, Transactions ASME*, Vol. 94E, Sept. 1972, pp. 677-81.
24. Runchal, A. K., "Mass Transfer Investigation in Turbulent Flow Downstream of Sudden Enlargement of a Circular Pipe for Very High Schmidt Numbers," *Journal of Heat Transfer, Transactions of ASME*, Vol. 88C, Feb. 1966, pp. 131-136.
25. Scharrer, G. L., "Swirl, Expansion Ratio and Blockage Effects on Confined Turbulent Flow," M.S. Thesis, Oklahoma State University, Stillwater, Okla., May 1984.
26. Morel, T., "Comprehensive Design of Axisymmetric Wind Tunnel Contractions," Paper ASME 75-FE-17, Minneapolis, Minn., May 5-7, 1975.
27. Gupta, A. K., Lilley, D. G. and Syred, N., "Swirl Flows," Abacus Press, Tunbridge Wells, England, 1984.
28. McKillop, B. E., and Lilley, D. G., "A Variable Vane Angle Swirler," Report, Oklahoma State University, Stillwater, Okla., July, 1982.
29. Sander, G. F., and Lilley, D. G., "The Performance of an Annular Vane Swirler," Paper AIAA 83-1326, Seattle, Wash., June 27-29, 1983.
30. Sinder, M. M., and Harsha, P. T., "Assessment of Turbulence Models for Scramjet Flowfields", NASA CR 3643, 1982.

1. Report No. NASA CR-3869		2. Government Accession No.		3. Recipient's Catalog No.	
4. Title and Subtitle  Investigations of Flowfields Found in Typical Combustor Geometries				5. Report Date February 1985	
				6. Performing Organization Code	
7. Author(s)  David G. Lilley				8. Performing Organization Report No. None	
				10. Work Unit No.	
9. Performing Organization Name and Address  Oklahoma State University School of Mechanical and Aerospace Engineering Stillwater, Oklahoma 74078				11. Contract or Grant No. NAG3-74	
				13. Type of Report and Period Covered Contractor Report	
12. Sponsoring Agency Name and Address  National Aeronautics and Space Administration Washington, D.C. 20546				14. Sponsoring Agency Code 533-04-1A (E-2374)	
15. Supplementary Notes  Final report. Project Manager, J.D. Holdeman, Internal Fluid Mechanics Division, NASA Lewis Research Center, Cleveland, Ohio 44135. (Work partially funded by Ramjet Technology Branch, AFWAL.) Appendix A - On the Prediction of Swirling Flowfields Found in Axisymmetric Combustor Geometries by D.L. Rhode, D.G. Lilley, and D.K. McLaughlin; Appendix B - Mean Flowfields in Axisymmetric Combustor Geometries With Swirl by D.L. Rhode, D.G. Lilley, and D.K. McLaughlin; Appendix C - Turbulence Measurements in a Confined Jet Using a Six-Orientation Hot-Wire Probe Technique by S.I. Janjua, D.K. McLaughlin, T.W. Jackson, and D.G. Lilley; Appendix D - Five-Hole Pitot Probe Time-Mean Velocity Measurements in Confined Swirling Flows by H.K. Yoon and D.G. Lilley; Appendix E - Confined Swirling Flow Predictions by M.T. Abujelala and D.G. Lilley; Appendix F - Single-Wire Swirl Flow Turbulence Measurements by T.W. Jackson and D.G. Lilley; Appendix G - The Performance of an Annular Vane Swirler by G.F. Sander and D.G. Lilley; Appendix H - Accuracy and Directional Sensitivity of the Single-Wire Technique by T.W. Jackson and D.G. Lilley; Appendix I - Limitations and Empirical Extensions of the $k-\epsilon$ Model as Applied to Turbulent Confined Swirling Flows by M.T. Abujelala and D.G. Lilley; Appendix J - Swirl Flow Turbulence Modeling by M.T. Abujelala, T.W. Jackson, and D.G. Lilley; Appendix K - Swirl, Confinement and Nozzle Effects on Confined Turbulent Flow by M.T. Abujelala and D.G. Lilley; Appendix L - Turbulence Measurements in a Complex Flowfield Using a Crossed Hot-Wire by B.E. McKillop and D.G. Lilley; Appendix M - Five-Hole Pitot Probe Measurements of Swirl, Confinement and Nozzle Effects on Confined Turbulent Flow by G.L. Scharrer and D.G. Lilley.					
16. Abstract  This is the Final Report on Grant NAG3-74 and discussion is on those activities undertaken during the entire course of research from July 1, 1980 to June 30, 1984. Studies were concerned with experimental and theoretical research on 2-D axisymmetric geometries under low speed nonreacting, turbulent, swirling flow conditions typical of gas turbine and ramjet combustion chambers. They included recirculation zone characterization, time-mean and turbulence simulation in swirling recirculating flow, sudden and gradual expansion flowfields, and further complexities and parameter influences. The study included the investigation of: a complete range of swirl strengths; swirler performance; downstream contraction nozzle sizes and locations; expansion ratios; and inlet side-wall angles. Their individual and combined effects on the test section flowfield were observed, measured and characterized. Experimental methods included flow visualization (with smoke and neutrally-buoyant helium-filled soap bubbles), five-hole pitot probe time-mean velocity field measurements, and single-, double-, and triple-wire hot-wire anemometry measurements of time-mean velocities, normal and shear Reynolds stresses. Computational methods included development of the STARPIC code from the primitive-variable TEACH computer code, and its use in flowfield prediction and turbulence model development.					
17. Key Words (Suggested by Author(s))  Combustor; Swirl; Turbulent flow; Hot wire measurements; Axisymmetric; Pitot probe measurements			18. Distribution Statement  Unclassified - Unlimited STAR Category 07		
19. Security Classif. (of this report) Unclassified		20. Security Classif. (of this page) Unclassified		21. No. of pages 191	22. Price A09